Quantitative basis for the structure and properties of a critically-important pressure vessel steel

Hector Pous Romero
Selwyn College

Department of Materials Science and Metallurgy
University of Cambridge

A dissertation submitted for the degree of
Doctor of Philosophy at the University of Cambridge

May 2014

Preface

This dissertation is submitted for the degree of Doctor of Philosophy at the University of Cambridge. The research reported was conducted under the supervision of Professor H. K. D. H. Bhadeshia in the Department of Materials Science and Metallurgy, University of Cambridge, between April 2011 and June 2014.

This dissertation is the result of my own work and includes nothing which is the outcome of work done in collaboration except where specifically indicated in the text. Neither this, nor any substantially similar dissertation has been or is being submitted for any degree, diploma or other qualification at any other university or institution. This dissertation does not exceed the word limit of 60,000 words.

Some of the work described herein has been published:

H. Pous-Romero, I. Lonardelli, D. Cogswell and H. K. D. H. Bhadeshia. Austenite grain growth in a nuclear pressure vessel steel. *Materials Science and Engineering A*, 567:7279, 2013.

H. Pous-Romero and H. Bhadeshia. PVP2013-97099: Coalesced martensite in pressure vessel steels In *Proceedings of the ASME 2013 Pressure Vessels and Piping Division Conference*, 2013.

H. Pous-Romero and H. Bhadeshia. Coalesced martensite in pressure vessel steels. *Journal of pressure vessel technology*, 136:1-6, 2014.

Hector Pous Romero, June 2014

Acknowledgements

I would like to express my sincere gratitude to my supervisor Professor Harry Bhadeshia for his invaluable support, guidance, inspiration and encouragement during the work and my stay here. Without his motivation and quest for excellence, this work would have never been fruitful. I also acknowledge the valuable input from my industrial supervisors, Daniel Cogswell and Jesus Talamantes. Discussions with staff at Rolls-Royce and Sheffield Forgemasters are also appreciated.

I would also like to thank Professor Mark Blamire for the provision of laboratory facilities in the Department of Materials Science and Metallurgy at the University of Cambridge, and also every member of the Department and staff for being helpful and supportive to me. I would like to thank Steve, Mathew, Ivan, Yan Pei and Lin Sun for the fruitful technical discussions on related matters and their continuos help. All the help and support provided by James, Lucy, Chris, Ed, Tim, Mandla, Subhankar, Wil, Guo Lei and other past and present Phase Transformations and Complex Properties research group members is greatly acknowledged. Last but no least, I would like to express my sincere gratitude to my family and particularly to my wife Andrea for her constant support.

At last, I take this opportunity to express my gratitude for the financial support of Rolls Royce, without its support this work would have not been possible.

Abstract

A particular steel, SA508, that is critically important in the fabrication of nuclear reactor facilities is the subject of this thesis. The ally has been in use since the 1970s but current material and production methods are based largely on empirical understanding. Meeting the required mechanical properties in ever larger pressure vessels is a challenge because of the potential for scatter in properties and consequent difficulties defining a safe design. Such scatter can arise from microstructural variations but surprisingly, most studies conclude that large components made from SA508 Gr. 3 steels are, following heat treatment, fully bainitic.

The research has concentrated on understanding the complex relations between processing, microstructure and mechanical properties. A methodic approach to address experimental observations in which the different stages in the multiple heat treatment, consisting of austenitising followed by water quenching and tempering, are individually investigated is undertaken.

In terms of austenitisation, there is uncertainty on the physical significance of models applied to the coarsening of austenite grains of these steels. For example, some of the published activation energies for grain growth exceed by more than a factor of two, the activation energy for self diffusion of iron. As a result, new data are generated and analysed by creating theory to account for the initial austenite grain size generated when the steel becomes fully austenitic, and any growth during heating to the annealing temperature. The experimental data reflect two regimes of isothermal grain coarsening, with grain boundary pinning dominating the kinetics up to the coarsening temperature, which is proven to be dependent on the amount of pining particles. The precipitates responsible for this pinning have been identified using thermodynamics, high-energy X-rays, transmission electron microscopy and microanalysis as aluminium nitrides. A model to describe austenite grain growth accounting for all these factors has been developed and seems to generalise well on unseen data.

It is demonstrated that the microstructure of SA508 Gr. 3 alloys is far from homogeneous when considered in the context of the cooling rates encountered in practice through a typical component wall section. During the experimental work it has been discovered that at fast cooling rates, $10\,^{\circ}\mathrm{C\,s^{-1}}$, there are circumstances where the adjacent martensitic platelets of a similar orientation can coalesce as the austenite transforms, to produce much coarser structures which are believed to be detrimental to toughness. An examination of published micrographs reveals that such coalesced regions existed but were not noticed in previous studies. The mechanism of coalescence is described and methods to ameliorate the coarsening are discussed.

For slow cooling rates consistent with positions at the mid-wall thickness of large components, allotriomorphic ferrite that is initially expected to lead to a deterioration in toughness, is found in the microstructure for realistic combinations of austenite grain size and cooling rate. Detailed TEM investigation has revealed aligned rows of precipitates inside the allotriomorphic ferrite, consistent with interphase precipitation at the α/γ interface during the course of transformation. Parameters are established to identify the domains in which SA508 Gr. 3 steels transform only into the fine bainitic microstructures. A model is proposed to estimate the level of allotriomorphic ferrite as a function of material composition, austenite grain size and cooling rate.

Tempering effects have also been studied revealing that contrary to common practice, shorter tempering times improve hardness, strength and toughness. Reduction in these properties is linked with an increased precipitation associated with longer tempering times.

Effects of austenite grain size, cooling rate and tempering parameter on mechanical properties have been assessed by means of tensile strength, Charpy impact energy and hardness for 18 different conditions. Material properties have been found to be dependent on the microstructure and present complex relations with the processing conditions. As a general trend, the best properties are found for the fast cooled microstructures containing a mixture of bainite - martensite, within the scope of the experiments reported here. However, experimental findings have confirmed that toughness is not reduced when allotriomorphic ferrite is present in the microstructure when compared to fully bainitic samples with larger grains. Hence, it is proposed that to improve toughness, austenitic grain sizes should be kept to a minimum by austenitising at lower temperatures or short times.

A complex relation between processing, microstructure and properties has been found during the course of this investigation. It is therefore, of great interest to find a reliable method to accurately predict the mechanical properties of large vessels as a function of thermal processing parameters. A methodology is presented that interprets a large quantity of industrially relevant experimental data using neural networks, permuting the determination of the relationship between key processing parameters such as the austenite grain size, cooling rate and tempering parameter, to develop a reliable method for stimating strength and toughness on unseen data.

Abbreviations and nomenclature

PWR	Pressurised water reactor
BWR	Boiling water reactor
HWR	Heavy-water reactor
RPV	Reactor pressure vessel
Gen_i	Generation_i reactor
PWHT	Post-welding heat treatment
DBTT	Ductile-brittle transition temperature
YS	Yield strength
UTS	Ultimate tensile strength
USE	Upper shelf energy
TP	Tempering parameter
HAZ	Heat-affected zone
TP_{eq}	Equivalent tempering parameter
SEM	Scanning electron microscopy
TEM	Transmission electron microscopy
EBSD	Electron backscatter diffraction
EDX	Energy dispersive X-ray
HV	Vickers hardness
MTDATA	National Physical Laboratorys Metallurgical and Thermodynamic Data Bank
DESY	Deutsches Elektronen-Synchrotron facility
MAUD	Materials Analysis Using Diffraction program
STEM	Scanning transmission electron microscopy

P	Probability of finding carbides larger than a given critical size
J	J-factor
e	Energy released during nuclear reaction
m	Mass defect
c	Speed of light
Ae_1	Lower temperature limit of the equilibrium ferrite-austenite phase field
Ae_3	Upper temperature limit of the equilibrium ferrite-austenite phase field
Ac_1	Temperature at which austenite begins to form during heating at a specified rate
Ac_3	Temperature at which transformation of ferrite to austenite is completed during heating at a specified rate
σ	Yield strength
$f_{\mathrm{Mo_2C}}$	volume fraction of $\mathrm{Mo_2C}$
D	Grain size
D_0	Initial grain size
t	Holding time
T	Holding temperature
n	Fitting parameter in grain growth model
C	Fitting parameter in grain growth model
A	Fitting parameter in grain growth model
η	Fitting parameter in grain growth model
Q	Activation energy for grain growth
υ	Boundary and migration velocity
M	Effective interface mobility
G_{int}	Driving force for interface movement
V_m	Molar volume
υ	Grain boundary energy per unit area

R	Universal gas constant
d_c	Critical carbide size
E	Young's modulus
γ_p	Surface energy
σ_p	Principal cleavage stress
ν	Poisson's ratio
d_s	Size of the minimum observable carbide
a	Parameter in the Weibull distribution
b	Shape factor in the Weibull distribution
T_0	Transition temperature
α	Ferrite
α_b	Bainite
α'	Martensite
$95\% CI$	95% confidence interval
σ_x	Standard deviation
N_{LI}	Number of linear intercept lines
$\%\,\mathrm{RA}$	Percent relative accuracy
$\overline{LI}$	Average linear intercept
n_g	Number of measured grains
g	Gravitational acceleration
$a_{\alpha'}$	Martensite lattice parameter
a_γ	Austenite lattice parameter
ε_O	Offset strain
V	Volume fraction
D_{Lim}	Limiting grain size in presence of second phase particles
d	Second phase particles size
f_v	Volume fraction of second phase particles

X_i	Element concentration
$\Delta\mu$	Driving free energy per unit volume for boundary migration
C_1	Constant which contains the interfacial energy per unit area
$\lvert\dot{Q}\rvert$	Heating rate
D_{Ac3}	Grain size when the material becomes fully austenitised
D_p^γ	Prior-austenite grain size
f_{vAlN}	Volume fraction of AlN
$f_{vAlNref}$	Volume fraction of AlN for a reference composition
B_S	Bainite-start temperature
M_S	Martensite-start temperature
$\overline{L}_\gamma$	Austenite grain size
$\lvert\dot{T}\rvert$	Cooling rate
B_{Sr}	Bainite transformation temperature recorded during continuous cooling
M_{Sr}	Martensite transformation temperature recorded during continuous cooling at a certain rate
$Ar3$	Allotriomorphic ferrite transformation temperature recorded during continuous cooling at a certain rate
$Ae3$	Allotriomorphic ferrite equilibrium onset temperature during cooling
V_α	Volume fraction of allotriomorphic ferrite
I	Nucleation rate
$\nu_{\alpha,t}$	Growth rate of phase α at the current time t
T_{max}	Tempering temperature
t_{th}	Isothermal holding time for the tempering stage
t_{eq}	Equivalent time at tempering temperature due to the heating/cooling cycles
H_f	Parameter being fitted with the hyperbolic tangent function
A_h	Fitting parameter in the hyperbolic tangent function

B_h	Fitting parameter in the hyperbolic tangent function
C_h	Fitting parameter in the hyperbolic tangent function
D_h	Fitting parameter in the hyperbolic tangent function
h	Heat transfer coefficient
q	Heat flux across an interface
ΔT_d	Temperature difference between the component and the sink
C_P	Specific heat capacity at constant pressure
ρ	Material density
V_p	Probe volume
A_s	Probe surface area
T_s	Probe surface temperature
T_∞	Sink temperature

Contents

Chapter 1

Introduction

Production of the next generation of nuclear power plants is likely to become a challenge, as emerging countries are installing a fleet of reactors for the first time, while countries such as Sweden, the USA and the UK are seeking to replace or increase their existing capacity. Furthermore, the present trend in the nuclear industry focuses on increasing the lifetime of the nuclear facilities, from the current operational life of 40 years to 60 years, while ensuring and increasing the structural integrity of the components [1–4]. It is therefore, necessary to have overall and detailed information about the properties of materials used in structural components to ensure the reliable fabrication of nuclear reactors.

There are only a few steel grades that have sufficient international experience for approved use in nuclear reactor facilities, partly because the qualification of such materials requires an enormous amount of time-consuming work. In this context low-alloy steels, such as the SA508 type alloy variants, have been the key materials for the manufacture of high integrity components, such as pressure vessels, compressors, and steam generators, over the last 40 years. This is because of the material good balance between strength, toughness and cost. For these components, strength to withstand internal pressure and high fracture toughness to assure safety from momentary shock due to unexpected accidents are the most crucial mechanical properties.

ASTM standards define the requirements for this alloy, in terms of chemical composition, heat treatment and mechanical properties, and SA508 steels require significant processing to achieve the specified mechanical properties. The material is hot forged to break-up the as-cast structure and is subject to a multiple heat treatment consisting of austenitisation followed by water quenching and tempering. Meeting the required mechanical properties in ever larger pressure vessels is a challenge due to the greater section sizes and material heterogeneity inherent to the large ingots required to produce these forgings [4, 5].

Pressure vessels steels are designed to operate at temperatures above the ductile-brittle fracture transition. However, these steels suffer from irradiation embrittlement, which shifts this transition temperature to higher values and the energy for ductile fracture is also reduced [6–9]. This results in a decrease of the operation safety margins, hence there is a higher probability of fast fracture [8–10]. Therefore, a material of high initial toughness and low initial ductile-brittle transition temperature should be adopted for pressure vessels [6, 7, 10].

Although SA508 steels have been in use since the 1970s, there has not been a a deep investigation of the metallurgy, with research focused on certain areas, such as microstructural characterisation after the heat treatment process, while neglecting other aspects, such as austenitising or tempering effects. This means that current materials and production methods are based on empirical understanding.

The purpose of this research was to establish quantitatively, the microstructural changes that occur during the different steps in the heat treatment used to optimise the combination of properties. Work has concentrated on identifying the relations between key processing parameters, microstructure and mechanical properties in order to address experimental observations. Furthermore, several modelling techniques have been used to develop models capable of reproducing the complex microstructural and properties changes that occur during the austenitising, quenching and tempering stages. It is believed that the results may lay the foundations for better safety assessments and lifing procedures.

Chapter 2

Literature Review

2.1 Nuclear energy overview

To trace the history of nuclear power development, it is necessary to look back over seven decades, to the 1930s. In 1934 - the 1938 physics Nobel prize winner - Enrico Fermi was the first to discover the potential of nuclear fission, when he bombarded uranium atoms with neutrons and discovered that the products of this reaction were much lighter than the original uranium [11, 12].

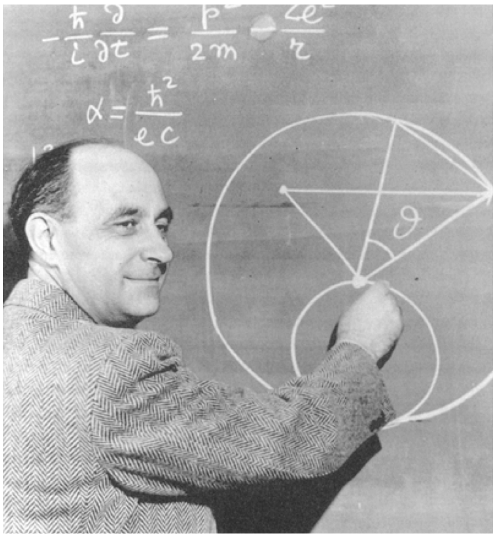

Figure 2.1: 1938 physics Nobel prize winner Enrico Fermi [12].

The concept of nuclear fission involves the decomposition of a heavy particle nucleus, uranium 235 atom (^{235}U), into two or more lighter elements, barium (^{143}Ba) and krypton (^{90}Kr) atoms, when it is bombarded with a small isotope, commonly a neutron. When this reaction takes place the mass of the system changes; the two smaller nuclei will have a lower mass than the original, creating the so called *mass defect* [13, 14].

The amount of energy that is released during the reaction is proportional to the amount of missing matter and can be calculated using the Albert Einstein's famous equation [15]:

$$e = m\,c^2 \tag{2.1}$$

where e is the energy produced, m is the mass defect and c is the speed of light.

For the particular case of fission of uranium 235 the equation is as follows [16]:

$$^{235}_{92}\mathrm{U} + ^{1}_{0} n \rightarrow \left[^{236}_{92}\mathrm{U} \right] \rightarrow ^{143}_{56}\mathrm{Ba} + ^{90}_{36}\mathrm{Kr} + 3^{1}_{0}n \tag{2.2}$$

The three neutrons produced in this nuclear reaction, if they encounter other ^{235}U atoms, can initiate further fission, producing even more neutrons. This results in a cascade called *chain reaction* [13, 14, 16].

Only a few years after the discovery of the nuclear fission, in 1942, a group of scientists led by Fermi at the University of Chicago (USA), created the first controlled, self-sustaining nuclear reaction, of what is today considered to be the world's first nuclear reactor, the *Chicago Pile - 1* [12]. After this scientific milestone, most of the early nuclear research was focused on developing an effective weapon for use in World War II (1939-1945). However, in 1951 the first electricity from nuclear energy was generated in the *Experimental Breeder Reactor I* at Idaho (USA) [12].

The number of nuclear power plants growth rapidly during the 1960s, 1970s, as nuclear energy was seen as a safe and clean alternative to current energy prac-

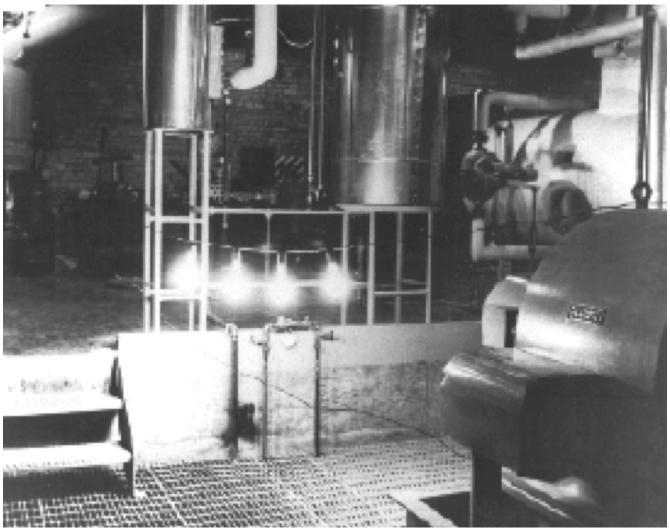

Figure 2.2: The Experimental Breeder Reactor I generating electricity to light four 200 watt bulbs on 1951 [12].

tices. In 1980 there was a total of 253 operating nuclear plants and 230 additionally under construction globally [12, 17]. However, two major disasters, the 1979 accident at the Three Mile Island nuclear power plant in Pennsylvania (USA) and the 1986 accident at Chernobyl (Ukraine) affected the perception of nuclear power [17–20]. After these unfortunate events, the general trend was to a slow down the nuclear programme, with moratoriums on the further construction of nuclear power units and plans to retire and close down existing plants [17, 19].

Recently, due to volatile and increasing fuel costs, concerns about the security of energy supplies and more pressure on global climate change, there is a renewed interest in expanding the nuclear power capacity, particularly for mitigating greenhouse gas emissions. [19, 20].

As per 2013, there were 437 nuclear reactors in operation distributed in 30 countries, producing about 13% of the worldwide electricity demand [3, 19, 21]. It is forecast that by 2030, industrialisation outside Europe and North America, will cause the global energy demand to double to over 30,000 TWh annually, resulting in 108 new units forthcoming (under construction or on order) [2, 18].

Furthermore, over 40 developing countries, distributed from the Gulf to Latin America, have recently approached United Nations officials expressing their interest in starting nuclear power programmes [19].

The power produced by nuclear means is not only for to civil purposes, it is also used in other applications such as the naval industry or defence. The electricity is generated thanks to the energy released during the nuclear fission, which is used to boil water to generate steam through a series of temperature/pressure controlled water cycles, which eventually drive turbine generators [3, 22]

2.2 Nuclear reactors

There has been a constant interest in revising the design of nuclear reactors, with increasing security and efficiency as the key driving factors. At the present, the large majority of existing reactors are classified as Generation II (Gen II), which began operation in the 1960s, Fig. 2.3. This class of commercial reactors is designed to be economical and reliable. It includes the pressurised water reactor (PWR), accounting for two-thirds of the installed capacity worldwide, followed by the boiling water reactor (BWR) with a 21% usage, and the heavy-water reactor (HWR) representing 14% of installed units [1, 2, 20, 21].

Given that PWRs represent the large majority of the nuclear capacity worldwide, materials issues in this type of reactor are of particular interest. Figure 2.4 shows a simplified schematic of a PWR plant showing the major components of the containment building. Among all components, the reactor pressure vessel (RPV), which acts as the primary pressure boundary and containment for the reactor core, is the most life-limiting structural component because replacement of the RPV is not considered a viable option [2, 4, 22].

The latest report from the International Atomic Energy Agency, shows that the international population of nuclear reactors used for utility power generation is ageing rapidly. Since 80 % of the current reactors have been in service for 20 or more years, as seen in Fig. 2.5 [3]. Gen II reactors were originally commissioned with an expected operational life of 40 years. Therefore, many reactor operators

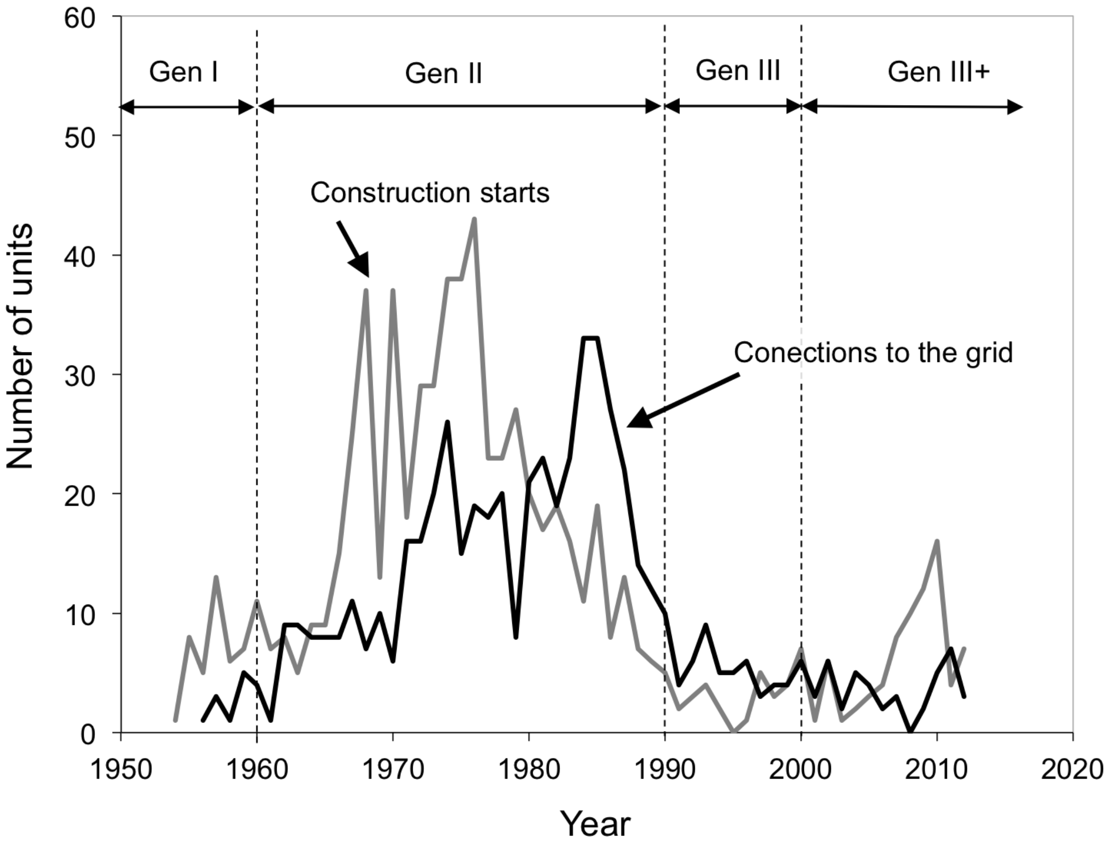

Figure 2.3: Yearly evolution of the number of nuclear plants under construction and being connected to the grid. The design generation type is also included. Adapted from [1–3].

are seeking license renewal to allow them to operate the plants for an additional 20 years [1, 2]. The main concern is to know how long these facilities can be safe, reliable and economically operational. Undoubtedly, the limiting factor is whether structural materials would be able to maintain their integrity beyond their 40 years design life. Hence the lifetime of the current reactor fleet worldwide will ultimately be governed by the performance of materials.

2.3 SA508 Steel

The current trend in the nuclear industry is focused on increasing the lifetime of the nuclear facilities while ensuring and increasing the structural integrity of the

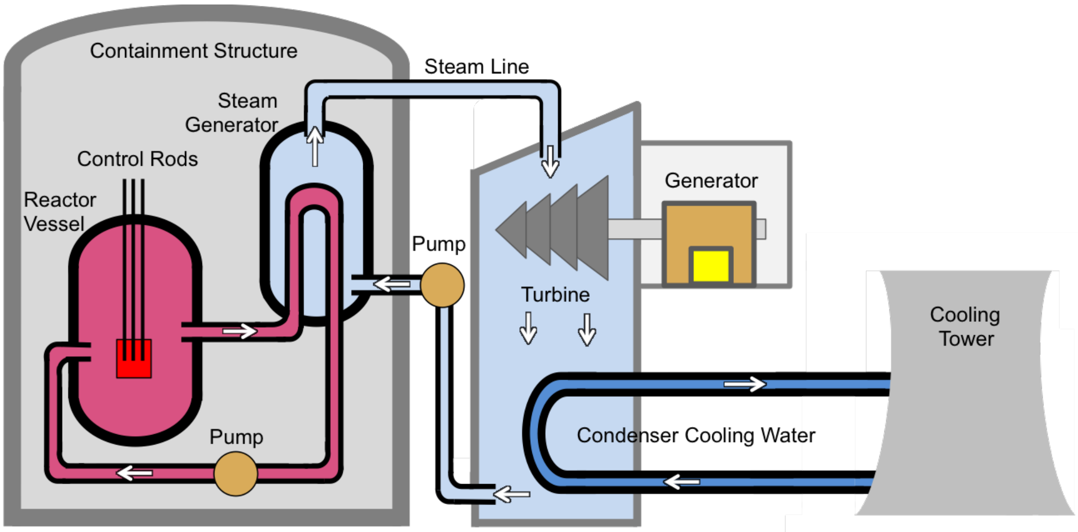

Figure 2.4: Simplified schematic of the major components in the primary and secondary circuits of a PWR. Adapted from [2, 23].

components, as the estimated cost of decommissioning a plant, including used fuel and site restoration, is about \$500 million [21]. A clear example is the increased component design lifetime, of the newly commissioned Gen III+ plants, of 60 years [20]. It is therefore, necessary to have overall and detailed information about the properties of materials used in structural components to ensure the reliable fabrication of nuclear reactors.

SA508 low-alloy steels, are used in key structural components such as pressure vessels, compressors, and steam generators. There are demanding requirements for tensile, toughness and resistance to irradiation embrittlement over the service period. By international standards, SA508 steels are divided into grades depending on their chemical composition, and each grade is additionally sub-divided into classes depending on the applied heat-treatment. The composition range for SA508 according to the ASTM standards is given in Table 2.1 [24].

Currently, the most common material choice for major high integrity vessel production is the SA508 Grade 3, as it presents good strength, toughness and weldability in addition to economy [4, 25]. This is the third generation of steels

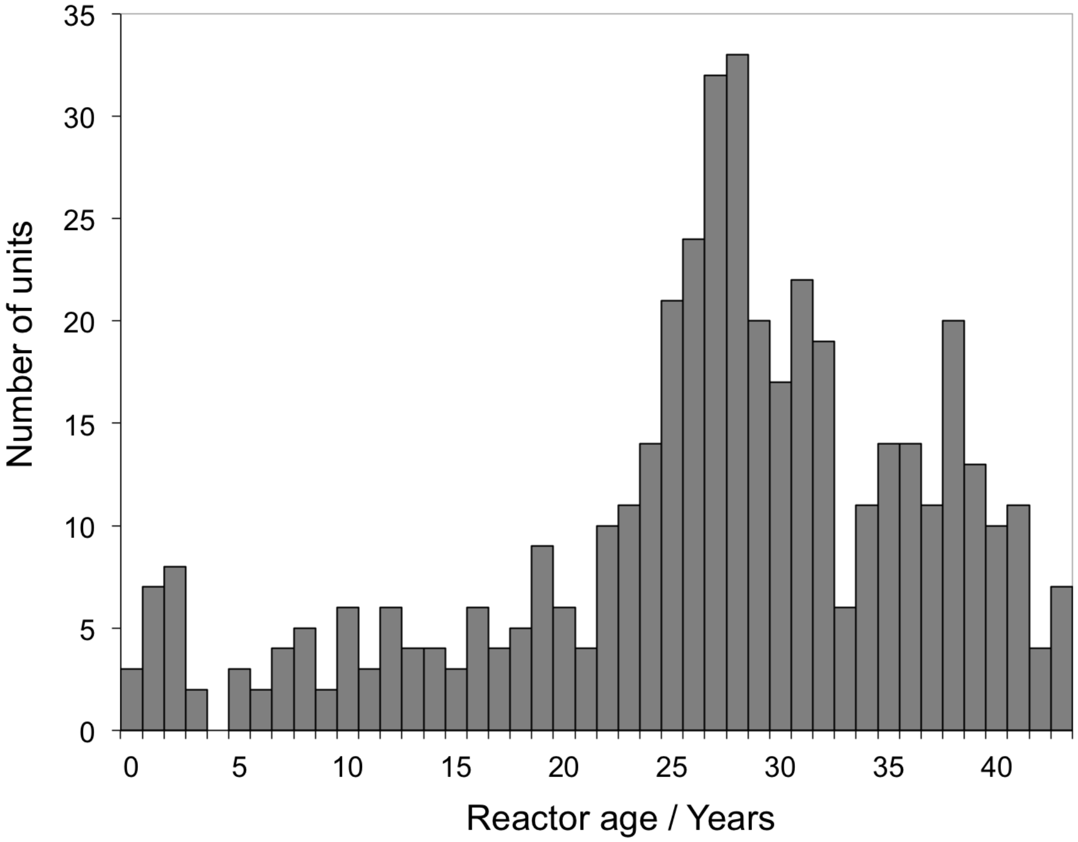

Figure 2.5: Worldwide distribution of nuclear power plants classified by years of commercial operation. Adapted from [3].

for nuclear facilities replacing the former Grades 1 and 2, as it exhibits improved mechanical performance, Table 2.2. The newest development in SA508 steels is Grade 4N, with better strength and toughness. It has significantly different composition from Grade 3 steel, containing higher amounts of Ni and Cr with reduced Mn content, see Table 2.1. These modifications introduce a level of uncertainty to the manufacturers who rely on large and long term experimental datasets in order to gain confidence in the use of the steel [25]. This issue, along with the usual constraints and risks implied on the nuclear industry, such as the possibility of Ni being an element sensitive to irradiation embrittlement, has been the major drawnback/limitation for the extensive use and acceptance of SA508 Grade 4N [9, 26]. Extensive experimental programmes need to take place before commercial implementation in the nuclear industry. The present work focuses on the study of the extensively used SA508 Gr. 3 steel to provide scientific knowledge linking empirical observations to microstructural and property changes.

The ASTM specification allows the use of a relatively large range of compositions (Table 2.1), this has created that different countries, and manufactures, have developed individual compositions, based on their own test programmes [29, 31]. As a result, there is a lack of a standard composition and large variations in the amounts of alloying elements used to produce the SA508 Gr. 3 alloys, in-

Table 2.1: Composition range for ASTM SA508 (wt%) [24].

	Grade 1	Grade 2	Grade 3	Grade 4N
Carbon	≤ 0.35	≤ 0.27	≤ 0.25	≤ 0.23
Manganese	0.40 - 0.90	0.50 - 0.90	1.20 - 1.50	0.20 - 0.40
Molybdenum	≤ 0.10	0.55 - 0.70	0.45 - 0.60	0.40 - 0.60
Nickel	≤ 0.40	0.50 - 1.00	0.40 - 1.00	2.8 - 3.9
Chromium	≤ 0.25	0.25 - 0.45	≤ 0.25	1.25 - 2.00
Silicon	0.15 - 0.35	0.15 - 0.35	0.15 - 0.35	≤ 0.30
Phosphorus	≤ 0.025	≤ 0.025	≤ 0.025	≤ 0.025
Sulfur	≤ 0.025	≤ 0.025	≤ 0.025	≤ 0.025
Vanadium	≤ 0.05	≤ 0.05	≤ 0.05	≤ 0.03

Table 2.2: Mechanical properties for SA508 steels.

	Yield strength / MPa	Tensile strength / MPa	Elongation / %	Ref.
SA508 Grade 1	345	515	16	[27]
SA508 Grade 2	448	611	18	[28]
SA508 Grade 3	468	611	29	[29]
SA508 Grade 4N	581	750	19	[30]

creasing the difficulties and interpretation when comparing material performance. Figure 2.6 shows the large variety of chemical composition, always between the specifications, used in nuclear pressure-vessel steels.

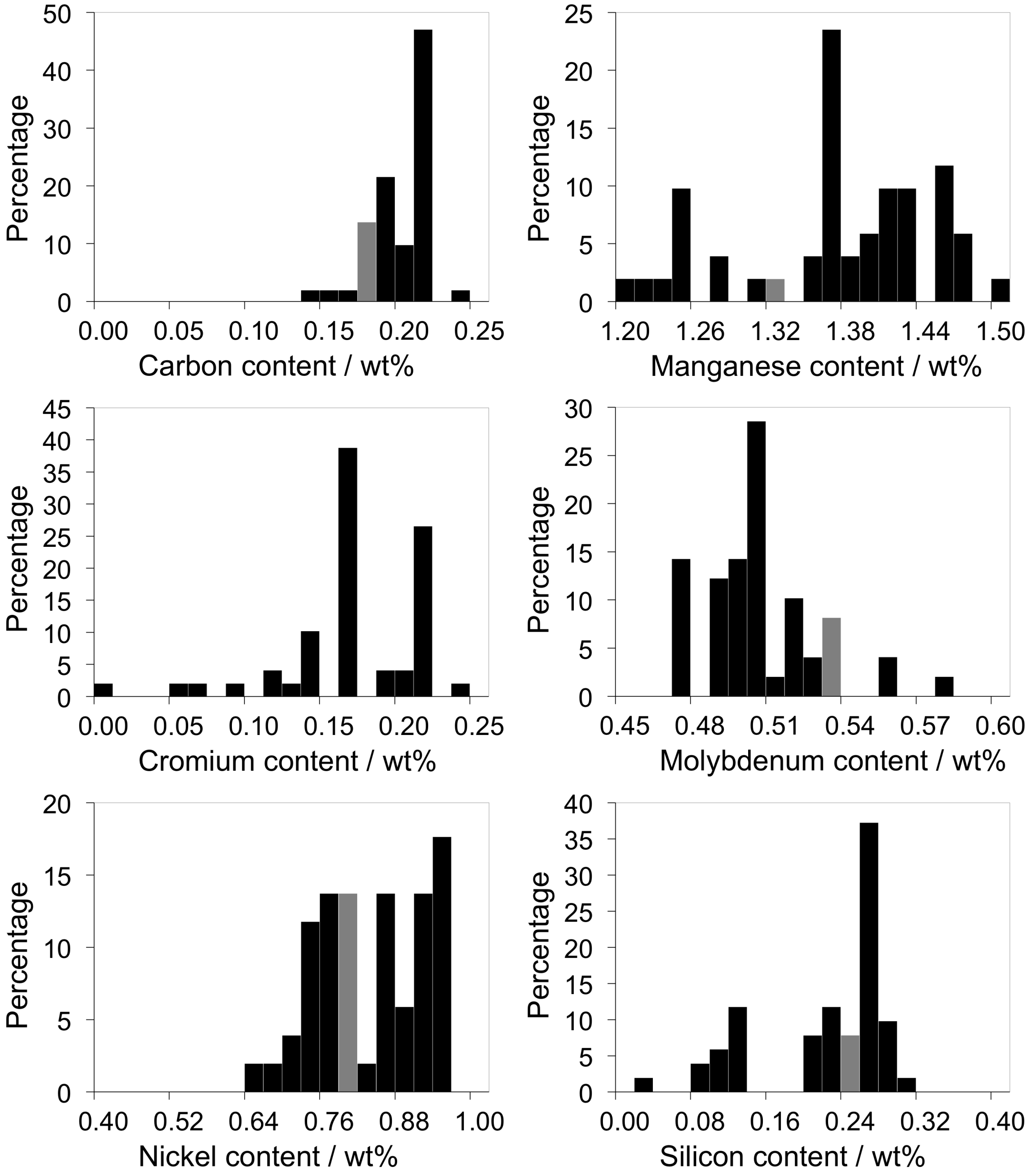

Figure 2.6: Variation in alloying elements for SA508 Gr.3 steels. Grey column represents the range of composition for the alloys studied in the present work. Data from: [25, 28, 29, 31–48].

The most general application for the SA508 Gr. 3 steel is in the RPV, acting as the primary pressure boundary and containment for the reactor core [4]. The design of the RPV has a number of constraints which require the geometry to be complex. Conventional RPVs in the 1950/60s were made of a series of formed plates joined by several weld seams. In contrast, the innovative reactor designs, from the 1970s onwards, are made with large mono-block forgings reducing remarkably the number of welds [4, 6]. The new design is aimed to reduce the processing time, simplify the in-service inspection, ease of maintenance and increase the integrity of the RPV due to the reduction of weld seams [6, 49, 50]. A comparison of the conventional and innovative designs is presented in Fig. 2.7.

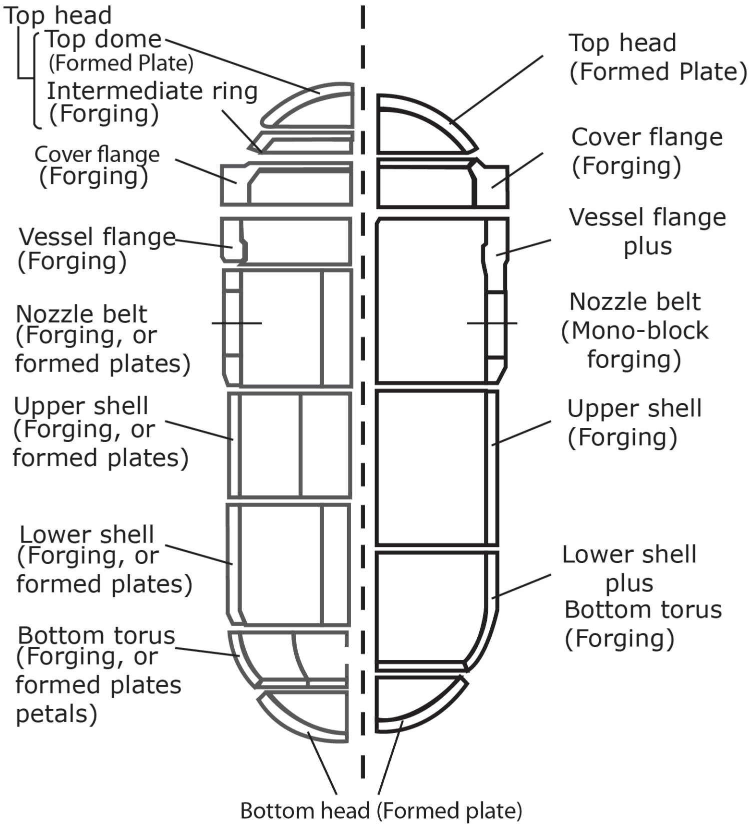

Figure 2.7: Development of pressure vessel design. Left: conventional design. Right: advanced design. Adapted from [6].

The size of the components is the direct result of the power needs of the plant.

The size of the reactor core is dependent on a number of factors, power density, total power and fuel life, being the primary drivers. Since the power capacity demand has increased from 100 MW in the early 1960s, up to 1600 MW nowadays, the size of the the pressure vessel has also enlarged considerably [4, 50]. In the case of the Kashiwazaki Kariwa, Japanese nuclear plant, the RPVs in plants number 6 and 7, are approximately 7 m in diameter and weighing around 900 tonnes, which makes them as the largest pressure vessels in Japan [47]. It is then necessary to increase the thickness of the vessels to satisfy the required strength [7]. Fig. 2.8 shows the relative sizes of civil and marine power plant reactor pressure vessels.

The main reason for the evolution in the size of forging components, is a great demand for increasing plant capacity. Another critical reason is the increase of safety and reliability through the integration of components.

2.4 Manufacture of reactor pressure vessels

The manufacture of RPVs consists of creating a melt by an electric arc method, using scrap steel, which is compositionally selected, with special attention to detrimental residual elements for embrittlement, such as copper, phosphorus or sulphur [4, 51]. Evolution in the steel-making practice has made possible a significant reduction in the content of these impurities as shown in Fig. 2.9. The melt, with required chemistry and weight, is then vacuum stream degassed during ingot pouring into metallic moulds to minimise residual hydrogen, oxygen and nitrogen. This method provides a very high quality ingot, since the final measured amounts of these gases and other inclusions are almost residual, as noted in the levels of nitrogen in Table 2.3.

When thick-wall steel components, as RPVs, are manufactured by vacuum carbon deoxidation, the final grain size is coarse and toughness is compromised. Therefore, many forgemasters have preferred to add aluminum to control grain sizes or use alternative refining techniques in order to manufacture better forging shells for RPV [49].

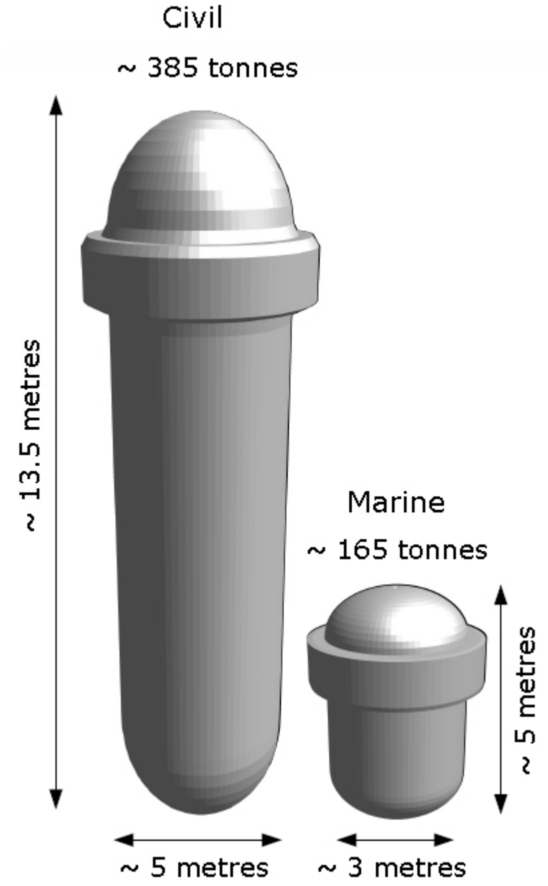

Figure 2.8: Relative sizes of civil and marine power plant RPVs. Adapted from [4].

Chi and Lucas examined the variation in mechanical properties and microstructure of the SA508 Gr. 3 steel depending on different refining processes [35]. Samples were manufactured using three types of refining methods: vaccum carbon de-

Table 2.3: Residual amount of nitrogen measured from different ingots of SA508 Gr. 3 alloy. Values supplied by Sheffield Forgemasters Engineering Ltd.

Nitrogen / wt%										
0.015	0.025	0.018	0.014	0.015	0.022	0.024	0.022	0.020	0.024	0.015

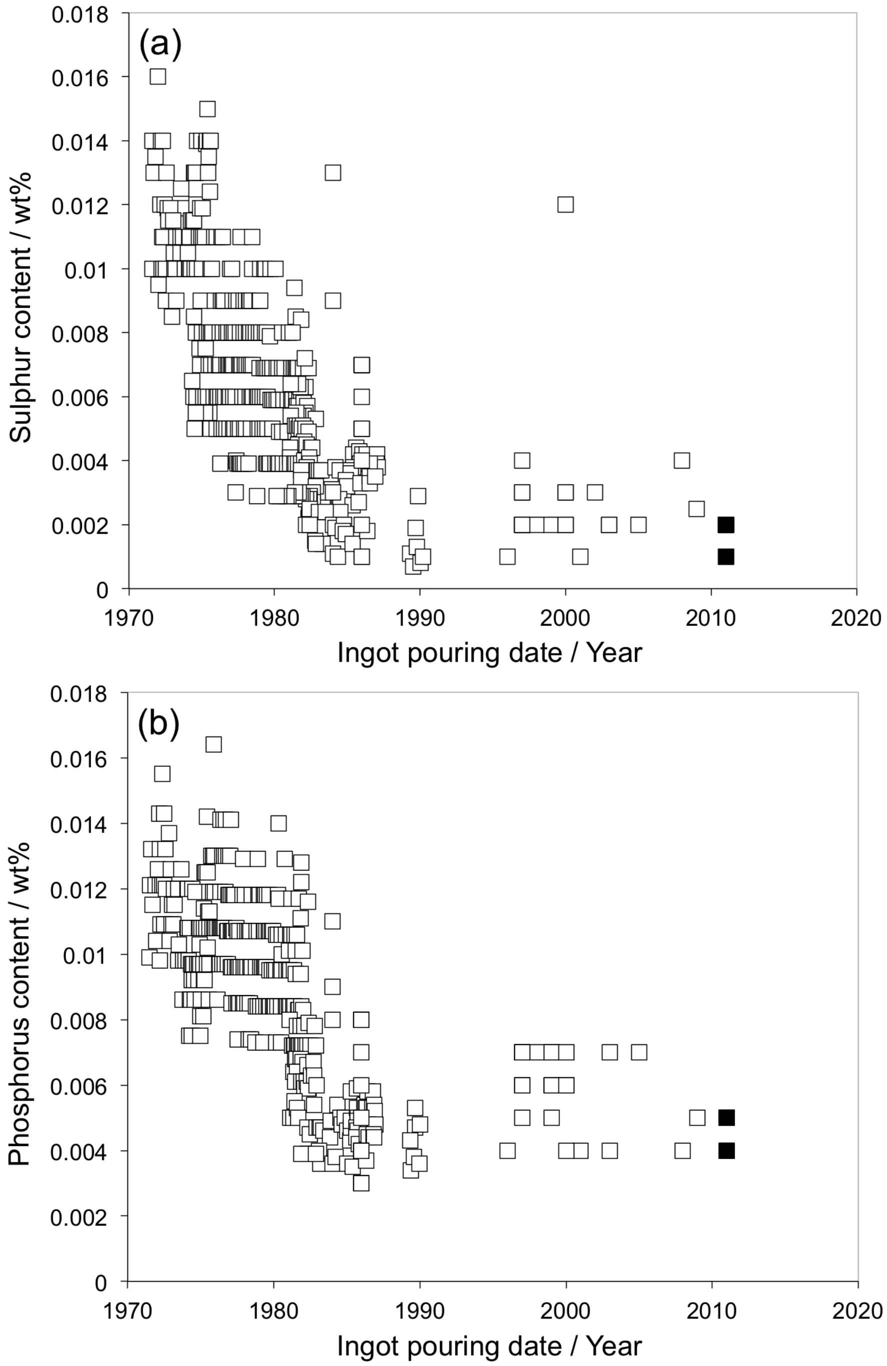

Figure 2.9: Evolution of sulphur and phosphorus content versus ingot pouring year. Black squares represent the amounts of these impurities in the alloys studied in the present work. Adapted from [28, 29, 31–37, 39, 40, 42–45, 47, 51, 52].

oxidation, vacuum carbon deoxidation plus aluminium killing, and silicon killing plus aluminium treated. It is reported that although the materials exhibited basically the same bainitic microstructure, silicon-aluminium treated samples somehow showed better microstructures, from their stable grain size, bainite lath structure, carbide size and distribution. Although, the experimental results are not included in the cited report due to confidentiality, there is a claim that variation in properties such as hardness, tensile and fracture toughness was not significantly different for the variety of refining processes. As pointed out in the report, since the steels were manfactured to meet the code specifications, large differences in properties are not expected. However, they did not conclude that these differences in properties and in microstructure could be due to the variation in composition or in the heat treatments, rather than from the applied refining process [35].

Similar results, where the tensile properties seemed independent of the refining process, with yield strength in the range of 440 ± 15 MPa and ultimate tensile strength in the range of 590 ± 20 MPa, were also obtained by Kim et al. [32]. However, they reported a significant variation in fracture toughness, 426, 574 and 665 MPa $m^{1/2}$, for vacuum carbon deoxidation, vacuum carbon deoxidation plus aluminium killing, and silicon killing plus aluminium treated, respectively. The improvement was attributed to the refining of the austenite grains and the differences in the sulphur contents of the samples. Smaller austenitic grains and lower sulphur contents would increase toughness. As aluminium and silicon were used as deoxidizers, in the silicon killing plus aluminium treated technique, sulphur removal is more effective than in the alternative practices. Therefore, by reducing the sulphur content corresponding inclusions should also be reduced and the fracture toughness improved [32]. Table 2.4 presents the comparison of the content of amount sulphur depending of the refining process.

After the refining process, the high quality ingots are passed to the forging section where the components are forged until the desired geometry is obtained. Forging operations are carried above the Ac_3 temperature, a range of 880 to 1250 °C is commonly used to ensure that the material remains fully austenitic during forming. reheating may be required through out the process. Further machining and welding can be implemented to obtain the final component [4, 53].

Forging, in addition to create the necessary geometry , helps refine the as-cast microstructure by dynamic recrystallisation of the ingot, thus enhancing the mechanical properties relative to the as-cast product. Furthermore, forging should offer sufficient work to break up inclusion clusters and reduce porosity present in the as-cast ingot [4, 53].

The forging procedure for heavy section components used for high integrity applications is similar in the initial stages regardless of the final geometry. To produce the cylindrical (or shell) component of the RPV body, the basic forging steps are as follows:

a - **Cogging**: The ingot is worked along its axis with the purpose of consolidating the central region of the forging which may contain internal voids caused by solidification shrinkage. A study from Kakimoto et al. concluded that a minimum reduction ratio of 75% is required to fully consolidate internal voids, irrespective of their shape (void diameter/height ratio) in ingots [54].

b - **Upsetting**: Upset forging consists of compressing the axial length of the forging. This operation reduces the length of the ingot and increases the cross section. This introduces sufficient work to induce dynamic recrystallisation and break-up any remnants of the cast structure. The forging, after this step, presents the shape of a thick disc.

c - **Trepanning**: The ingot is cored out in the direction parallel to its axis.

Table 2.4: Amount of sulphur in SA508 Gr. 3 alloys from different refining methods [32]

Refining method	Sulphur / wt%
Vaccum carbon deoxidation	0.004
Vacuum carbon deoxidation plus aluminium killing	0.003
Silicon killing plus aluminium treated	0.002

d - **Becking**: This operation consists of increasing the internal bore while reducing the wall thickness of the forging with the help of a thin mandrel bar. This operation is repeated until the size of the bore is such that a large mandrel can be used for the following operations.

e - **Drawing**: At this step the forging is drawn to the final length. Drawing is similar to becking, as it uses a mandrel to forge the ingot and to increase the length of the forging while reducing the wall thickness, although in this operation the bore remains constant. It is common that after the drawing process a supplementary becking operation is used to achieve the required wall thickness and bore of the component. Figure 2.10 shows schematically the steps to forge the cylindrical component of the RPV body.

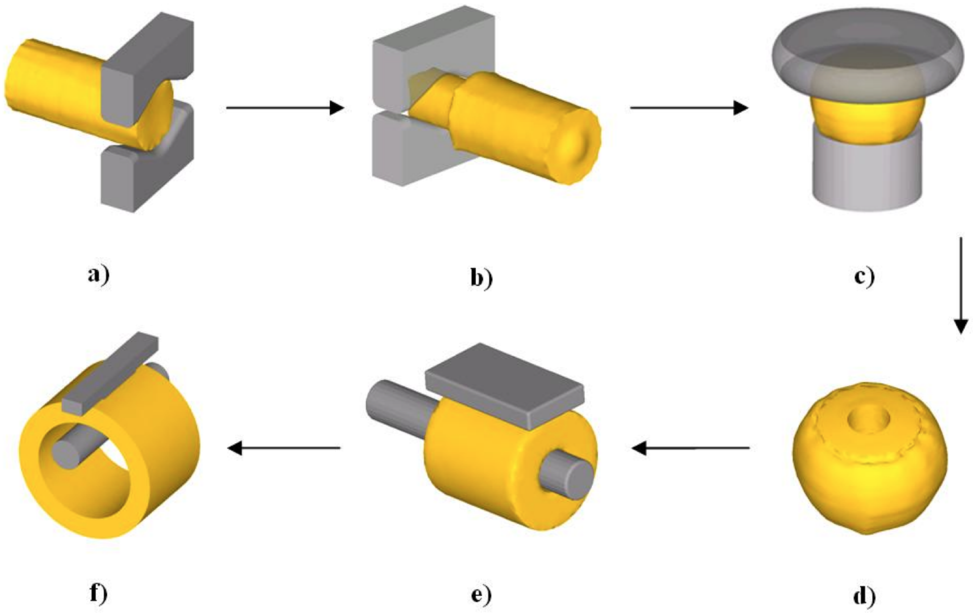

Figure 2.10: Forging procedure of the cylindrical component of the RPV body. a) Initial state b) Cogging. c) Upsetting. d) Trepanning. e) Becking. f) Drawing.

The new RPV design, where components are forged, introduces several advantages as already mentioned. However, this route has a serious setback. It is not possible to cast a large ingot (over 50 tonnes) without macroscopic segregation [10, 55]. The expected types and locations of segregation in a large ingot are known, as seen in Fig. 2.11 . This macro-segregation problem is mitigated by removing the central part of the ingot during the trepanning operation, where the most serious segregation and porosity is accumulated [5, 53].

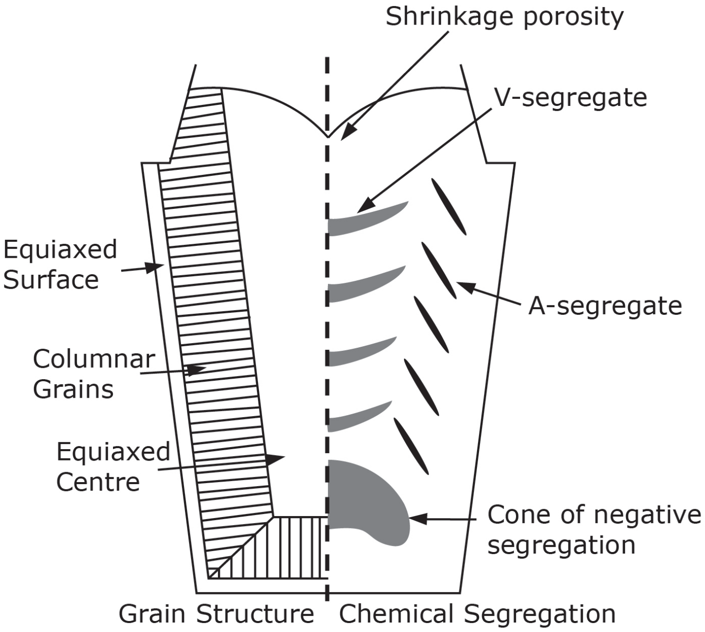

Figure 2.11: Typical macro-segregation pattern for large ingots. Adapted from [10].

Hollow ingot technology was developed in the 1980s as an alternative, when the geometry allows it, to conventional solid ingots on large SA508 Gr. 3 forgings. The use of hollow ingots has resulted in shorter solidification times after casting, consequently, macro-segregation issues are significantly reduced when compared to a conventional ingot [5, 55, 56]. Figure 2.12 shows clear reduction in the radial carbon segregation of a 150 tonne hollow ingot when compared to a 190 tonne solid ingot.

Forged SA508 Gr. 3 components require of heat treatment to achieve the demanding balance of properties, this is performed in two stages, commonly known in industry as *primary* and *quality heat treatment*. The primary heat treatment is carried out directly after all the forging operations with the aim of relaxing all

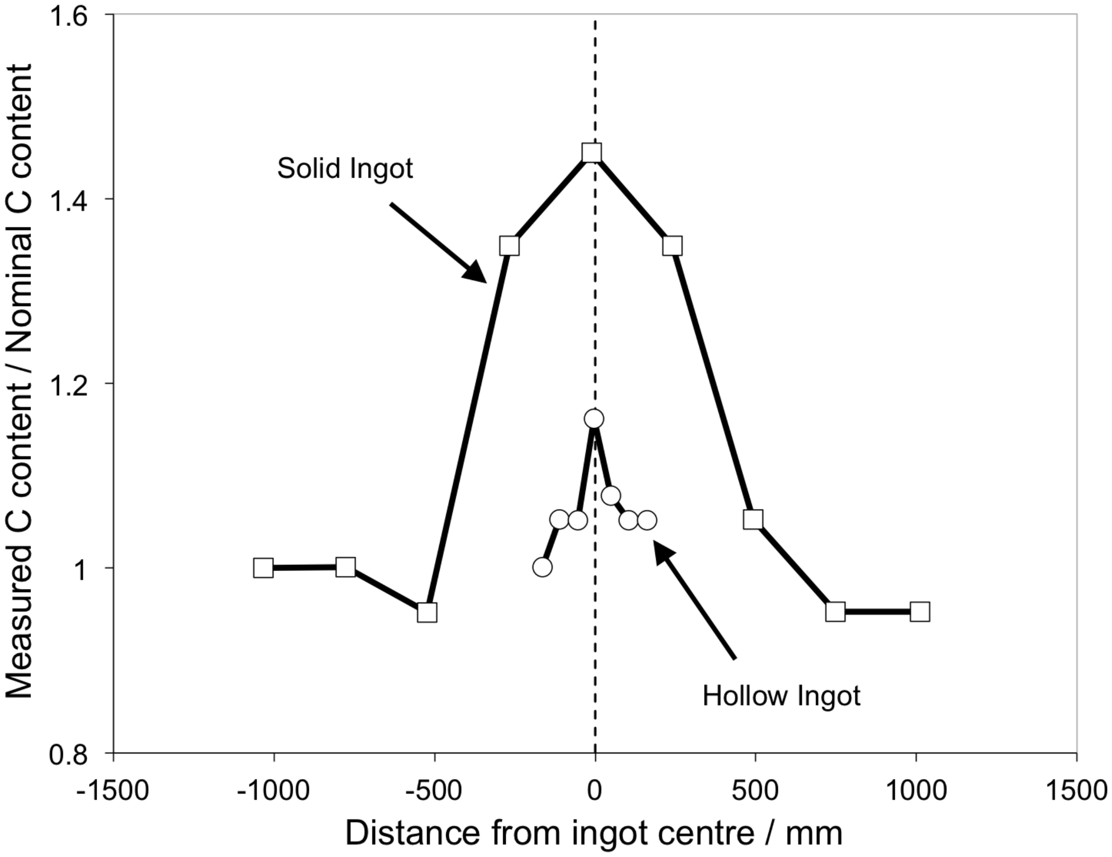

Figure 2.12: Carbon segregation measured in a hollow and a solid SA508 Gr 3 ingot. Adapted from [5].

the strain introduced by hot working, refining the possible coarse grain structures formed during the forging process and to provide sufficient transparency for ultrasonic testing [50, 53, 57]. Cogswell described in great detail the main stages of this primary heat treatment, including the transformation from forging, degassing, homogenisation (optional austenitisation) and tempering [53]. After the last forging operation is complete, the component is air cooled and held between 500 °C to allow for complete phase transformation of the low alloy steel from austenite, and 250 °C to avoid a possible catastrophic through thickness failure of the forging by hydrogen cracking. Upon heating to the homogenisation temperature, degassing will take place by the diffusion of hydrogen to free surfaces, where evaporates to the ambient, when the forging is maintained for a sufficiently long time between 600 - 650 °C. Homogenisation treatment is conducted at temperatures around 900 - 950 °C where complete dissolution of second phase particles should take place. At this point, the forging will be either air cooled or water quenched to allow complete transformation from austenite. An optional second austenitisation, at temperatures ranging from 860 to 890 °C followed by water quench may also be performed to improve through thickness properties and hence attenuation for ultrasonics. Finally the forging is softened to ease machining by tempering in the region of 600 to 650 °C.

After the primary heat treatment, the forging is machined to remove the surface scale formed during previous operations, creating an adequate surface for ultrasonic testing. Following a successful ultrasonic inspection the forging is machined to the near net shape, and undergoes the quality heat treatment to achieve the target properties [50, 53, 57].

Next section will analyse in detail the quality heat treatment of the components and how the microstructure changes through the several steps of the process.

2.5 Quality heat treatment

After fabrication RPV components undergo a controlled heat treatment, to obtain the desired balance in properties, which is determined as a function of the chemistry and vessel thickness [50, 53, 57]. The quality heat treatment consists of austenitisation, followed by quenching in a liquid medium by spraying or immersion. After quenching, the components are tempered [24]. Fig. 2.13 illustrates the heat treatment process with some typical values for temperature and holding times.

The austenitisation in the context of SA508 steels is not specified, but the ASTM code makes a differentiation on the labelling of SA508 Gr. 3 depending on the minimum tempering temperature: 650 °C for Class 1 and 620 °C for Class 2 [24]. Furthermore, SA508 Gr. 3 Class 1 and Class 2 would have specific requirements for tensile and Charpy impact values (Tables 2.5 and 2.6). Com-

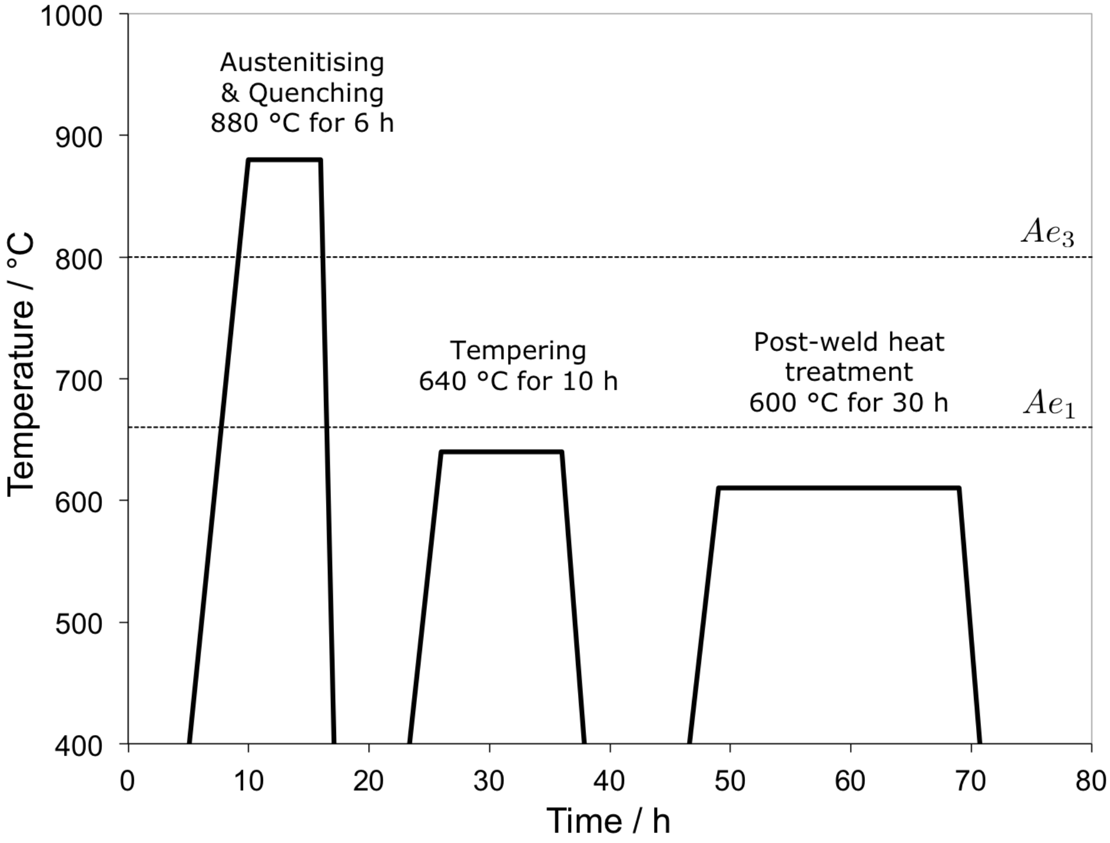

Figure 2.13: Schematic diagram of heat treatment for SA508 Gr. 3 steels with typical values. Equilibrium transformation temperatures Ae_1 and Ae_3 are also shown [40].

monly, SA508 Gr. 3 Class 1 steels are used for RPVs, while Class 2 steels are used for steam generator pressure vessels [47]. Usually after tempering, the sub-elements that form a component are joined by welding and therefore require a post-welding heat treatment (PWHT), at around 610 °C [40, 41, 52].

The holding times for the heat treatment process are determined by the thickness of the vessel. In particular, that for tempering is specified at half hour per 25.4 mm of steel thickness, to obtain homogeneous heat treatment [24]. By contrast, since holding times for austenitising and PWHT are not specified, the holding period will be based on knowledge and expertise from the manufacturer.

Table 2.5: Tensile requirements for SA508 Gr. 3 steels according to ASTM code [24].

	Yield strength / MPa	Tensile strength / MPa	Elongation in 50 mm / %	Reduction of area / %
SA508 Gr. 3 Class 1	≥ 345	550 - 725	≥ 18	≥ 38
SA508 Gr. 3 Class 2	≥ 450	620 - 795	≥ 16	≥ 35

Table 2.6: Charpy impact requirements for SA508 Gr. 3 steels according to ASTM code [24].

	SA508 Gr. 3 Class 1	SA508 Gr. 3 Class 2
Minimum average value of set of three specimens at 4.4 °C / J	41	48
Minimum value of one specimen at 21 °C / J	34	41

It is generally accepted that to achieve the optimum balance between strength and toughness, an accurate selection of the heat treatment and composition are required. Optimisation of the chemical composition is a difficult task, as several aspects have to be accounted for; mechanical properties, weldability, stress relief sensibility, hardenability, irradiation embrittlement, etc.

Kim et al. [41, 48] and Im et al. [46] studied the effect that different alloying elements, particularly carbon, nickel and molybdenum, had on the final properties by comparing a series of optimised compositions, outside the stipulated ASTM range, against a common SA508 Gr. 3 steel. Some of these compositions are presented in Table 2.7. Conclusions from these investigations were similar; the final properties of the alloy depended on the type and amount of cementite (Fe_3C) and molybdenum carbide (Mo_2C) precipitates found in the microstructure [41, 46, 48]. A detailed discussion of the precipitates and other aspects of the microstructure can be found in Section 2.7. Although the purpose of this work is not to develop a new alloy, basic knowledge of the effects of the different alloying elements will be included.

Carbon is an essential element contributing to the hardenability and the strength of the steel, as well as to control cementite and other carbides. Previous investigations have shown that the number of cementite particles is proportional to the carbon content in SA508 Gr. 3 steels and a reduction in carbon mitigates the role of detrimental coarse cementite precipitates, while the strength and hardenability can be maintained and enhanced using substitutional solutes [41, 46, 48]. An increase in molybdenum improves the strength, due to the increased precipitation of fine Mo_2C, which would precipitation harden and reduce the quantity of cementite.

Im et al. developed an empirical equation to relate precipitation hardening to the yield strength (σ, in MPa), and the volume fraction of Mo_2C precipitates ($f_{\mathrm{Mo_2C}}$), as follows [46]:

$$\sigma = 290 + 2660\sqrt{f_{\mathrm{Mo_2C}}} \tag{2.3}$$

This empirical equation assumes a volume fraction of Mo_2C precipitates between 0.3×10^{-3} to 1.3×10^{-3} with an average size of 0.02 µm, and cementite less than 2.6×10^{-3} volume fraction.

To mantain hardenability, Kim et al. proposed nickel as a substitute element for carbon, because it is an austenite stabilizer [41, 48] . By contrast, Im et al. reported that hardenability may be compensated with an increase in total substitutional alloying elements, Mn, Ni and particularly Mo, without stating any specific reason [46].

Increasing the Mo content also improved the fracture toughness due to the

Table 2.7: Comparative of compositions (wt%) and properties of ASTM code, common SA508 Gr. 3 and modified compositions. YS: yield strength, UTS: ultimate tensile strength, DBTT: ductile-brittle transition temperature and USE: upper-shelf energy.

	ASTM Ref. [24]	SA508 Gr. 3 Ref. [46]	Modified 1 Ref. [46]	Modified 2 Ref. [41, 48]
Carbon	≤ 0.25	0.20	0.10	0.10
Manganese	1.20 - 1.50	1.37	0.70	0.70
Molybdenum	0.45 - 0.60	0.48	1.51	0.96
Nickel	0.4 - 1.00	0.91	1.50	2.50
Chromium	≤ 0.25	0.15	0.15	0.14
Silicon	0.15 - 0.35	0.21	0.20	0.20
Phosphorus	≤ 0.025	-	-	-
Sulphur	≤ 0.025	-	-	-
Vanadium	≤ 0.05	-	-	-
YS / MPa	≥ 345	452	607	508
UTS / MPa	550 - 725	601	733	644
DBTT / °C	-	8	-55	-
USE / J	-	272	249	392

formation of Mo_2C fine precipitates and the reduction of coarse cementite particles [41, 48]; additionally, the ductile-brittle transition temperature (DBTT) was shifted to lower temperatures due to an increase in cleavage fracture stress [46]. Nevertheless, this was not observed when the levels of carbon exceed 0.15 wt%, where DBTT was seen to increase with Mo content. When carbon exceed 0.15 wt%, there is insufficient molybdenum to prevent cementite formation [46]. An increase in nickel content also helps to reduce the DBTT by an increase in the cleavage fracture stress [41, 46, 48].

Figures 2.14 and 2.15 summarise the effects that the major alloying elements have on the properties of the material. Figure 2.14 shows that less cementite corresponds to a lower DBTT, due to the increase in cleavage fracture stress. In compositions with the same amount of carbon, those with higher nickel exhibited a lower DBTT. It is clear from Fig. 2.15 that an increase in Mo_2C raises the yield strength at constant carbon concentration.

Although the properties presented in these studies exceed those of current materials (see Table 2.7), due to the lack of information in key areas such as long term irradiation embrittlement, it is unlikely that the alloy modifications will be adopted in industry. Current materials and production methods have been used for decades with empirical understanding of what is required to produce a high quality material. This conservatism makes the introduction of new materials or processes very difficult, and with the problem exacerbated by the limited construction of reactors.

Other minor alloying elements such as, phosphorus and sulphur are incorporated to improve machinability in low alloy steels, and silicon is commonly added as a deoxidant agent in the melting of the steel. Residual elements which are not intentionally added and that cannot easily be removed by from the steel, as copper, tin, arsenic and antimony are generally present as a result of the use of steel scrap. A tight control of residual elements is important, particularly sulphur, copper and tin, as they are known to be responsible for hot shortness during forging. This is the separation of grain boundaries, due to the impurities

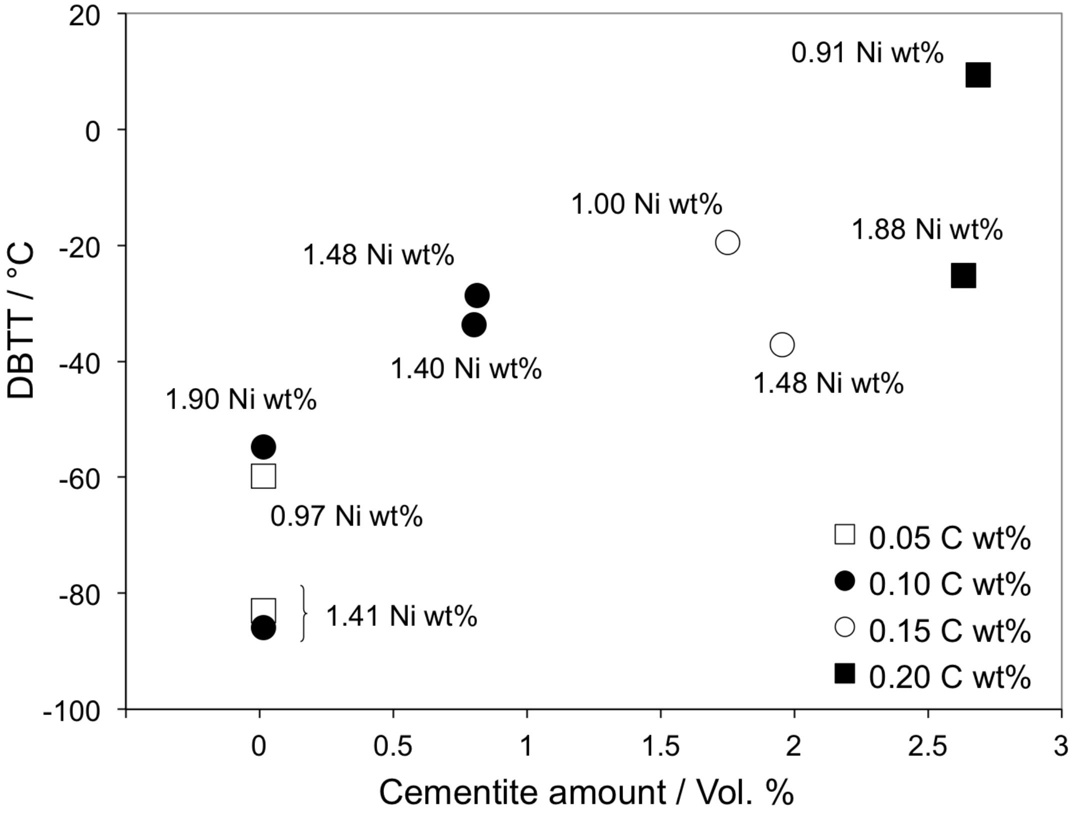

Figure 2.14: Relation between ductile-brittle transformation temperature (DBTT) and calculated equilibrium amount of cementite at 650 °C [46].

or residual elements being in liquid state, at forging temperatures [58–60].

The constant development of melt control, improvements in steel-making and in the casting process has resulted in cleaner steels with less impurities and overall compositions closer to the design specifications. Given that the ASTM code places restrictions on the amounts of constituents, it can be assumed that the forge-to-forge variability of composition has little effect on mechanical properties. The heat treatment applied to the forging following the forming process is the mechanism for achieving the required properties.

The sections that follow analyse the optimisation steps in the quality heat. The microstructure after quenching following austenitisation, will be upper-bainite,

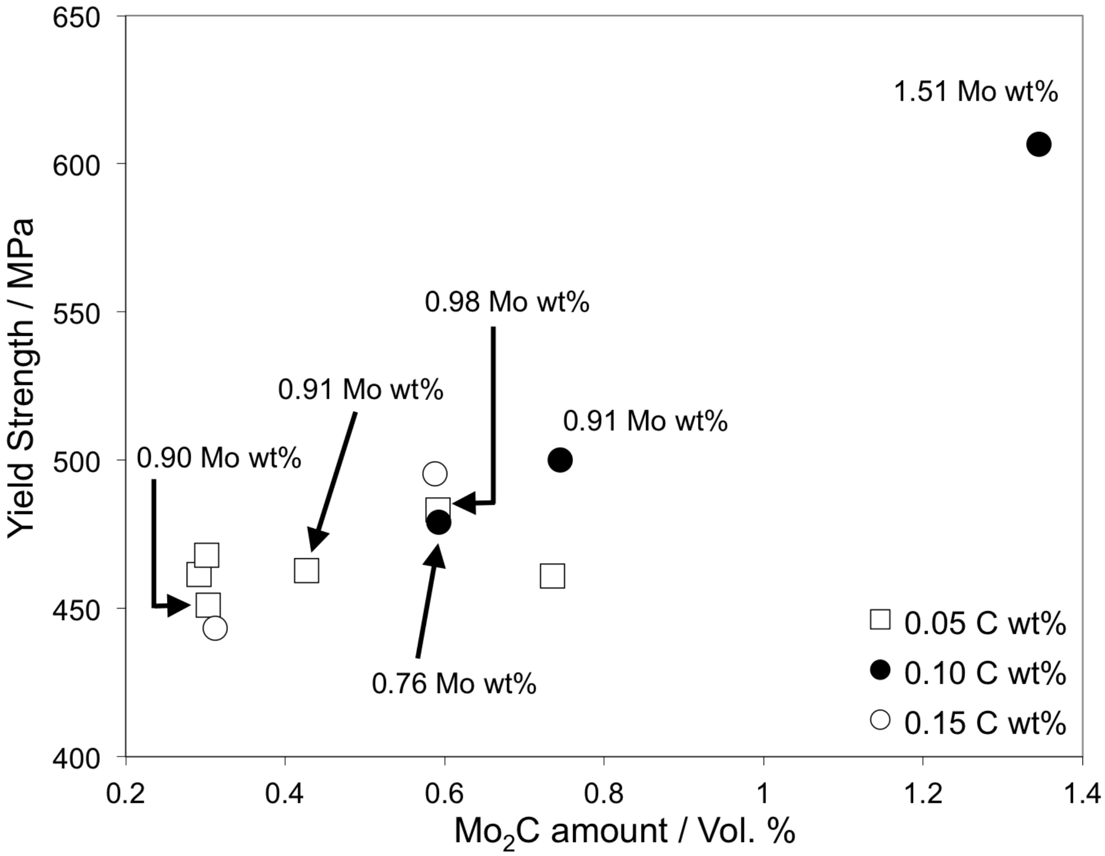

Figure 2.15: Relation between yield strength and calculated equilibrium amount of M_2C precipitates at 650 °C [46].

which is then tempered below the transformation temperature Ac_1, as seen in Fig. 2.13. Martensite may be found in the heat affected zones following welding [52, 61].

2.5.1 Austenitising

Grain size is an important factor to control the strength and toughness of steels. Controlling the austenite grain size enables the bainite to be refined since bainitic laths are arrested at the austenite grain boundaries. The ways to control the austenite grain size of the low-alloy steels can be categorised into austenitisation process control and particle pinning [41].

Pinning utilises small precipitate particles or inclusions, that retard the coarsening of matrix grains by inhibiting the motion of grain boundaries. These particles also define a limiting grain size beyond which the driving force for growth is less than that for pinning [62]. There is a critical balance for precipitates to form and function. Fine particles, closely spaced will produce pining but if they grow too large they will become few, coarse and far apart and will themselves cause quality problems [63].

Pining particles are common in microalloyed steels containing Ti, V, Al and Nb. Niobium is most effective because it has the optimum level of stability in the austenite [64]. However, there has not been any reported evidence of pinning particles in these SA508 Gr. 3 steels. Therefore, the austenitic grain size has to be controlled by monitoring the austenitising process. As previously mentioned, holding times will be influenced by the size of the component, and the ASTM specification does not regulate the austenitising temperature.

In the 1980s, an investigation by Druce on the effect of the austenitisation temperature, and thus austenitic grain size, from 850 °C (22 µm) to 1300 °C (251 µm), on properties of SA508 steels, revealed a clear relation between the temperature and fracture properties of the steel, Fig. 2.16. Charpy impact results proved that as the austenitisation temperature increased there was a deterioration in toughness, as the upper shelf energy (USE) decreased and the DBTT shifted to higher temperatures. Thus the toughness and austenite grain size are inversely proportional [65].

Since ductile fracture in these steels is due to void nucleation and coalescence, Druce suggested that voids initiated preferentially at second phase particles, such as sulphides, with weak interfaces [37, 41, 45, 46]. Hence the reduction in USE at higher austenitising temperatures could be related to the amount of sulphur taken into solution and available for subsequent precipitation during quenching, then providing more ductile void nucleation sites. However, no proof was presented of sulphide particles at fracture surfaces. Moreover, the predicted sulphur solvus in austenitic iron for a manganese content of 1.4 wt% shows no significant change in solubility between 850 to 1000 °C, Fig. 2.17 [66]. Consequently this reasoning

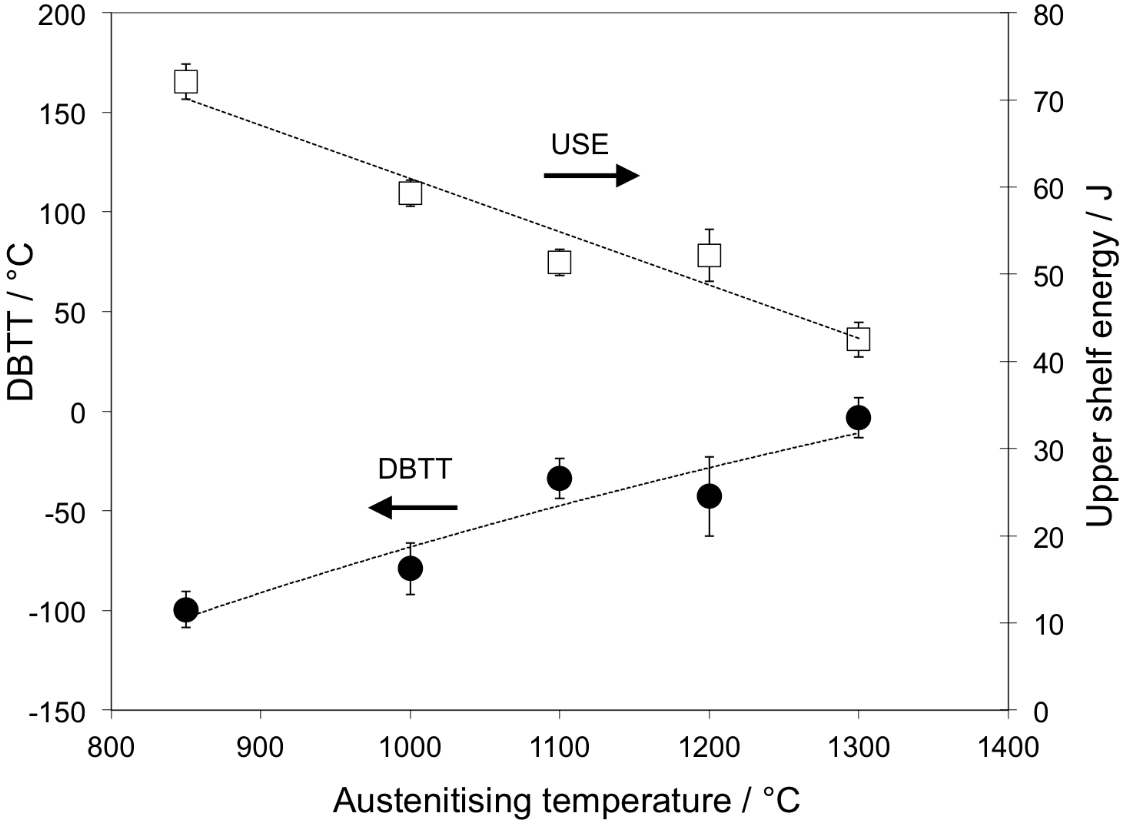

Figure 2.16: Effect of austenitising temperature on upper shelf energy (USE) and ductile-brittle transition temperature (DBTT). Austenitisation time 1 h. Adapted from [65].

would not explain the observed decrease in USE at austenitisation temperatures in the range 850 to 1000 °C.

In addition to that, more recent investigations proved that during ductile fracture, voids are formed at elongated cementite/matrix interfaces or the fracture of a coarse carbides develops into a void. Voids or microcracks are hardly formed at fine carbides [37, 41, 45, 46]. Figure 2.18 shows a scanning electron micrograph of the cross-sectioned area beneath the fracture surface showing void nucleation at coarse carbides.

It was tentatively explained that the observed change in DBTT is controlled

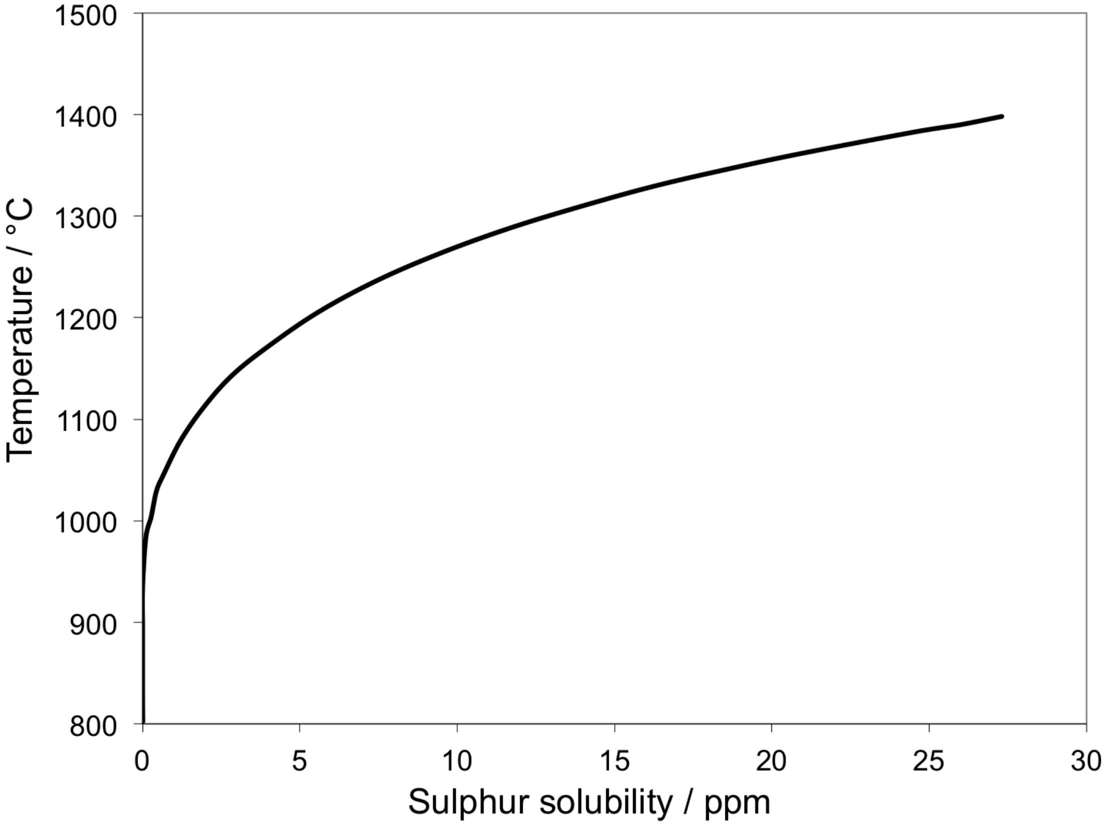

Figure 2.17: Predicted sulphur solubility in 1.4 Mn wt% austenitic iron [66].

by a combination of microstructural element size, grain boundary precipitate structure and interfacial segregation of phosphorus. However, no microstructural analysis supported this argument [65].

A recent study from Lee at al. contradicts the findings from Druce, concluding that the austenite grain size does not affect the transition property T_0 in the cleavage fracture toughness of SA508 Gr. 3 steels (temperature at which the fracture toughness is $100\,\mathrm{MPa\,m^{1/2}}$), which is influenced by the carbide size. As T_0 temperatures in the range of -$72 \pm 3\,^{\circ}\mathrm{C}$ are reported for samples with austenite grain sizes from 25 to 110 µm. Since the cleavage fracture in pre-cracked specimens is controlled by the initiation of micro-cracks in the second phase particles, consequently the transition property, T_0, is nearly irrelevant to the facet and grain

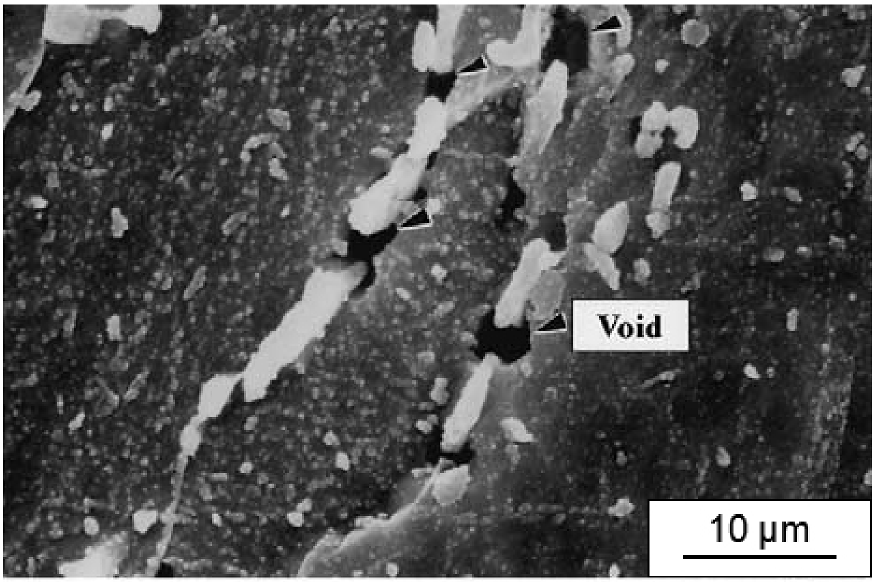

Figure 2.18: Cross-sectioned area beneath the fracture surface showing void nucleation at coarse carbides. Tensile test specimen, tested in the brittle region (- 75 °C) [45].

size [67]. It is important to mention, that the steel used by Druce had a higher level of sulphur, 0.005 wt.%, compared to the much cleaner modern steels with levels of sulphur around 0.002 wt.%.

Lee at al. also reported that the yield strength and the ultimate tensile strength (UTS) are reduced when austenitising at high temperatures, as the austenite grain size increases. A reduction in yield strength from 473 to 416 MPa, and a drop in UTS from 631 to 577 MPa are reported for grain sizes of 25 and 110 µm, respectively [67]. This effect is linked to the strengthening effect by grain refinement. Due to the disordered nature of grain boundaries and the misorientation angle between grains, the bare barriers to dislocation movement. This causes the dislocations to pile up at the grain boundary, creating a stress field that will repel further dislocations, thus increasing the strength of the material.

In the heat treatment of large components, such as RPVs, the heating and cooling rates are limited by the size of the vessel, with typical wall thickness between 200 and 700 mm [4, 39]. Studies on the effects of the heating rate during austenitisation have demonstrated that it has no significant influence on yield strength, which at heating rates of 0.005 and 0.5 °C s^{-1} are 458 and 468 MPa respectively [40]. In contrast, the same change in heating rates shifts the DBTT towards lower temperatures, between 20 to 30 °C, while maintaining the same level of USE, as illustrated in Fig. 2.19 [40]. Unfortunately, no metallurgical explanation was given in the study for these findings.

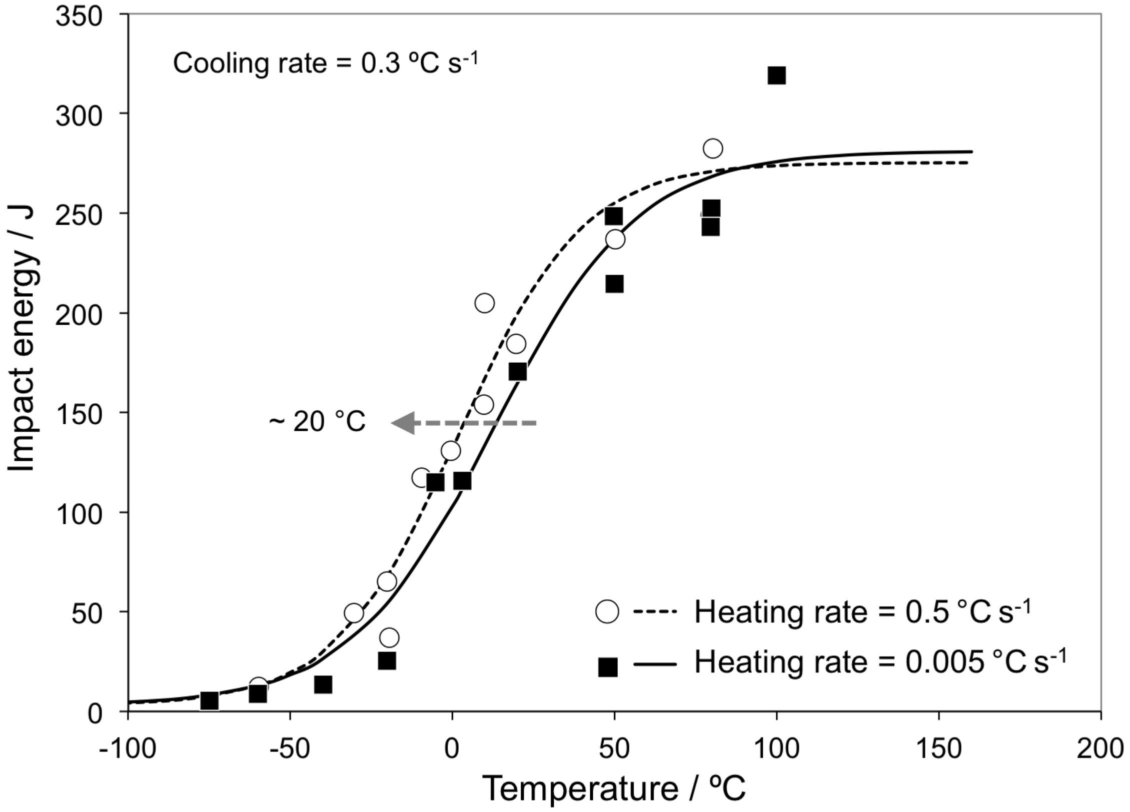

Figure 2.19: Charpy impact energy vs. temperature curves for different heating rates. Adapted from [40].

The forgings are quenched in highly agitated water following austenitisation, and the cooling rate has a much greater influence on the properties of this pressure vessel steel, as it dictates the extent of transformation into bainite [4, 32, 40, 47, 68]. Figure 2.20 illustrates a continuous cooling transformation diagram including cooling curves typical for thick forgings [68].

The fast-cooled regions transform into finer microstructure than those cooled slowly, due to a change in transformation mechanism from diffusional to displace [4]. The latter microstructures are desired since the steel is severely tempered, above at 620 °C for many hours [24]. The martensitic or bainitic regions remain relatively fine during this process and hence ensure the required level of toughness. The precipitation of carbides such as those rich in molybdenum also tends to be more uniform in regions where the initial microstructure obtained on cooling is itself fine, i.e., the products of displacive transformation.

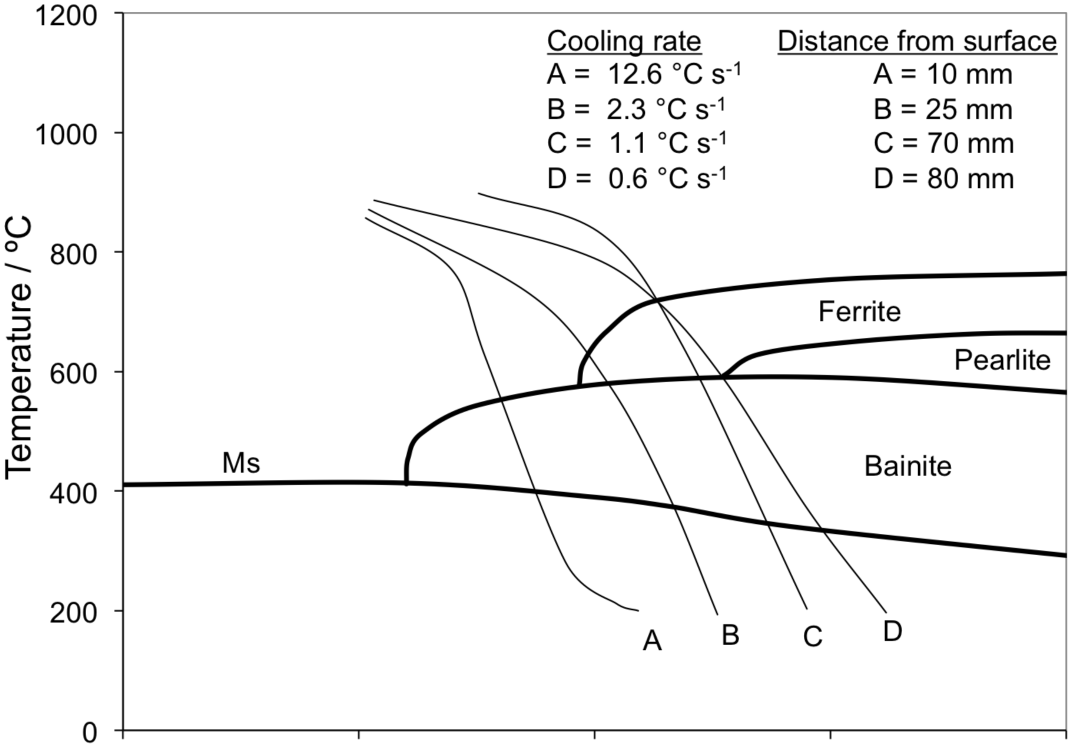

Figure 2.20: Measured cooling rates at various thickness locations [68].

Cooling rates of approximately $0.3\,^\circ\mathrm{C\,s^{-1}}$ are common at the 1/4 thickness position in the practical manufacturing process of commercial nuclear RPV [40], and it has been reported that the cooling rate at the 1/2 depth of a a 340 mm wall thick component is just about 0.2 °C s^{-1} [69]. Studies of the effect of the cooling rate, particularly where cooling rates have been measured accurately, on the resultant microstructure after quenching are scarce. Kim et al. studied the effects of slow cooling rates on the transformation behaviour of SA508 Gr. 3 steels, concluding that cooling rates above 0.17 °C s^{-1} lead to bainitic microstructures [32]. However, this study did not include the possible effects that the austenite grain size may have on the hardenability of the steel, which as will be shown later in the findings of this thesis, has a great effect on the hardenability of SA508 Gr. 3 steels.

Empirical results have shown that by increasing the cooling rates from austenitisation temperatures, from 0.3 to 1.7 °C s^{-1} there is a reduction in transition temperature by 10 to 20 °C [32, 40]. Furthermore, the Charpy impact energy is also improved with faster cooling rates, as seen in Fig. 2.21 [32]. It is suggested, that to secure toughness in SA508 Gr. 3 steels, the recommended minimum cooling rate from the austenitising temperature should be 0.25 °C s^{-1} [32].

These empirical observations have driven the nuclear industry to enhance the cooling rates of large components upon quenching in water. In order to increase the quench efficiency, the overall weight of the forging should be reduced to minimise the thermal mass of the component, and position the forgings to allow steam bubbles to escape readily [53, 57].

2.5.1.1 Model for austenite grain growth

The austenite grain size influences hardenability and consequently determines the final properties of the steel [70–72].

Grain growth is driven by the decrease in free energy due to the reduction in total grain boundary area per unit volume [73]. Grain boundaries are defects in the crystal structure so there is a thermodynamic driving force to eliminate them.

Beck et al. determined experimentally that grain growth, during isothermal

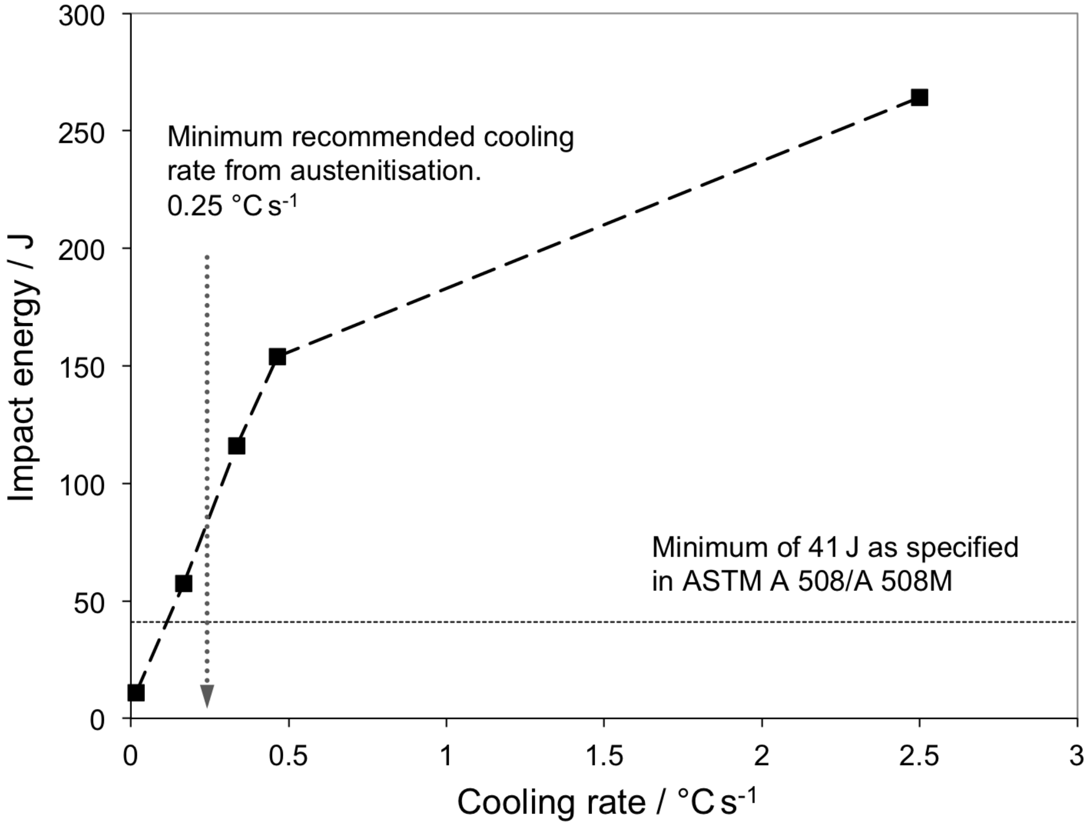

Figure 2.21: Charpy V-notch impact energy at 4.4 °C versus cooling rate for SA508 Gr. 3 steel. Adapted from [32].

holding, is described by the following relation [72, 74]:

$$D^n - D_0^n = Ct \tag{2.4}$$

where D is the grain size, D_0 the initial grain size, t the holding time and n and C are fitting parameters.

The equation can be made more explicit by writing [75]:

$$D^n - D_0^n = A \exp\left(-\frac{Q}{RT}\right)t \tag{2.5}$$

where Q is the activation energy for grain growth, R the universal gas constant and A is a fitting constant depending on the material. The origin of this equation is essentially that the rate of change in grain size depends directly on the amount of grain surface per unit volume that remains within the material.

The majority of models describing the austenite grain growth are based on equation 2.5. Recently, Lee et al. suggested the use of a simplified empirical model [71]:

$$D = A \cdot \exp\left(-\frac{Q}{RT} \right) \cdot t^n \tag{2.6}$$

That has the implicit assumption that the initial grain size term can be neglected, as it is assumed that this is much smaller than the final grain size.

Table 2.8 summarises published models describing isothermal austenite grain growth.

Other models based on thermodynamic data have also been proposed [70, 83]. Fu et al. suggested one for grain growth of austenite in microalloyed steels [70], where the austenite grain size (D), at time t_i with time step (Δt) as a function of boundary velocity (v) can be written as:

$$D\{t_{i+1}\} = D\{t_i\} + \frac{(v_i + v_{i+1})\Delta t}{2} \tag{2.7}$$

where, $v = MG_{int}/V_m$, M is the effective interface mobility, G_{int} the driving force for interface movement and V_m the molar volume.

Yoshie et al. proposed a semi-empirical model to calculate the grain growth of cast C-Mn steel [83]:

$$D^2 - D_0^2 = 4\,\upsilon\,V_m\,M\,t \tag{2.8}$$

where υ the grain boundary energy per unit area.

Table 2.8: Summary of empirical models describing austenite grain growth.

Steel type	Model	n	η	A	Q / kJ mol^{-1}	Ref.
Rolling C-Mn	$D^n - D_0^n = A\exp\left(-\frac{Q}{RT}\right)t$	10		3.87×10^{32}	400.0 for $T > 1000\,°\mathrm{C}$	[75]
Rolling C-Mn	$D^n - D_0^n = A\exp\left(-\frac{Q}{RT}\right)t$	10		5.02×10^{53}	914.0 for $T < 1000\,°\mathrm{C}$	[75]
Forged Waspaloy disc	$D^n - D_0^n = A\exp\left(-\frac{Q}{RT}\right)t$	3		2×10^{26}	595.0	[76]
C-Mn	$D^n - D_0^n = A\exp\left(-\frac{Q}{RT}\right)t$	7		1.45×10^{27}	400.0	[77]
C-Mn-V	$D^n - D_0^n = A\exp\left(-\frac{Q}{RT}\right)t$	10		2.60×10^{28}	437.0	[77]
C-Mn-Ti	$D^n - D_0^n = A\exp\left(-\frac{Q}{RT}\right)t$	4.5		4.10×10^{23}	435.0	[77]
Micro-alloyed	$D^n - D_0^n = A\exp\left(-\frac{Q}{RT}\right)t$	5		1.60×10^{32}	716.9	[78]
Medium C-Nb	$D^n - D_0^n = A\exp\left(-\frac{Q}{RT}\right)t$	2.5		1.03×10^{16}	397.7	[79]
C-Mn	$D^n - D_0^n = A\exp\left(-\frac{Q}{RT}\right)t$	4.1		1.72×10^{21}	$352.2 + 21.8X_{\mathrm{C}} + 19.9X_{\mathrm{Mn}} + 7.2X_{\mathrm{Cr}} + 7.4X_{\mathrm{Ni}}$ [a]	[72]
Low C-Mn	$D^n - D_0^n = A\exp\left(-\frac{Q}{RT}\right)t$	2		4.27×10^{12}	278,8	[80]
Low alloy	$D = A\exp\left(-\frac{Q}{RT}\right)t^{\eta}$		0.211	76.67×10^{3}	$89.1 + 3.6X_{\mathrm{C}} + 1.2X_{\mathrm{Ni}} + 1.4X_{\mathrm{Cr}} + 4.0X_{\mathrm{Mo}}$ [a]	[71]
Ultrahigh-strength 300M	$D = A\exp\left(-\frac{Q}{RT}\right)t^{\eta}$		0.17	4.04×10^{6}	132.0	[81]
Pressure vessel	$D - D_0 = A\exp\left(-\frac{Q}{RT}\right)t^{\eta}$		0.211	76.67×10^{3}	93.0	[82]

---

[a] where X_i is the concentration of the element in wt%

The problem with these empirical models is that they usually cannot be generalised to other steels.

2.5.2 Tempering

It is stipulated by the ASTM standards that the tempering treatment should be performed over 620 °C for 30 min or more per 25.4 mm of the maximum section thickness [24].

The tempering stage is performed to soften the quench material by trading strength for ductility. Temperature and time are often expressed together via an empirical tempering parameter (TP) due to Larson-Miller parameter [47, 68, 84]:

$$\mathrm{TP} = T(\log t + 20) \times 10^{-3} \tag{2.9}$$

where, T is the temperature in Kelvin and t the time in hours.

TP is useful for manufactures as a method to compare the effect of different heat treatments, made at different temperatures for different lengths of time. The TP range normally varies between 18.8 K h (620 °C for 10 h) to 19.6 K h (660 °C for 10 h), for the most common tempering processes for large RPV forgings [40–42, 46].

There are limited data available of the tempering effects on the mechanical properties and microstructure of SA508 Gr. 3 steels. However, some general trends from the work of Haverkamp et al. and from Suzuki et al. can be obtained [47, 68]. Figure 2.22 shows the effect of TP on the tensile and impact properties of SA508 Gr. 3 steel.

Increasing the TP from 19.1 to 19.4 K h will cause a reduction of yield strength of 36 MPa and a decrease in tensile strength from 601 to 558 MPa [47]. In contrast, absorbed energy increases steadily up to reaching a maximum value at a relatively early state of tempering, decreasing significantly afterwards. These empirical observations have limited the tempering parameter to less than 19.4 K h, the value at which the impact energy reaches its maximum [47, 68].

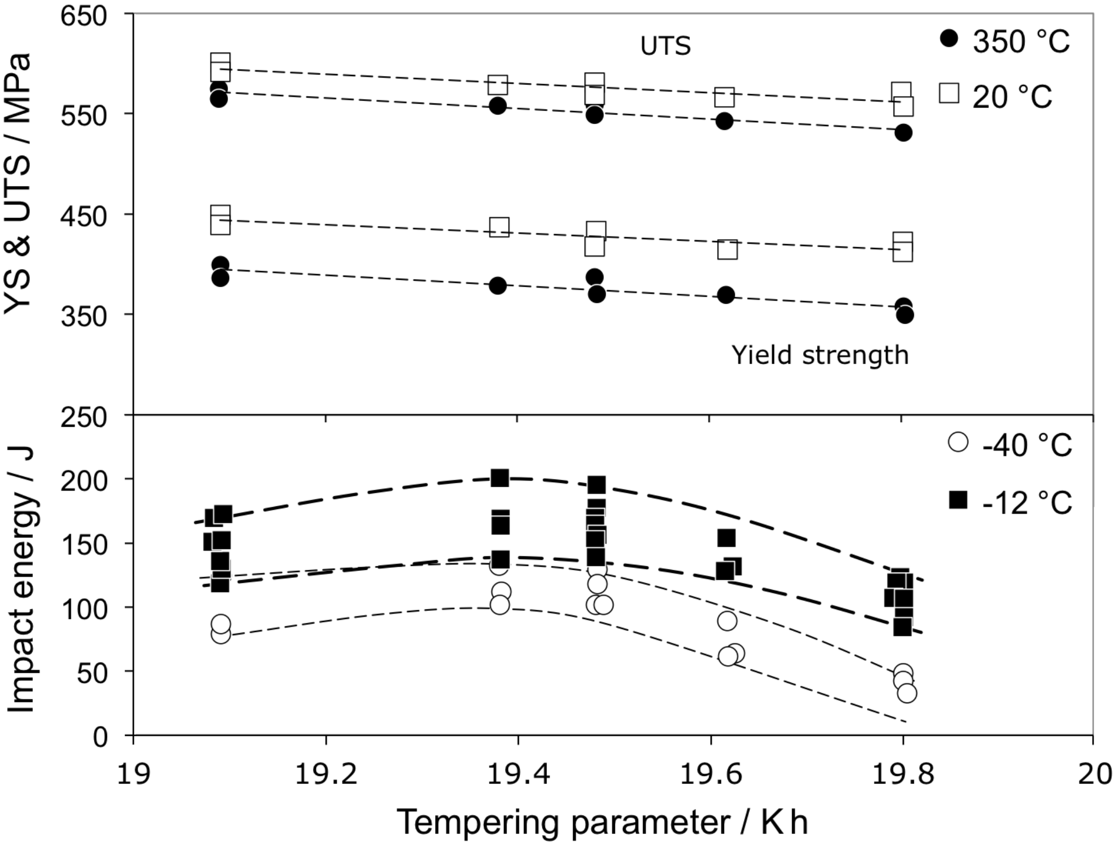

Figure 2.22: Effect of temper parameter on the tensile and impact properties of SA508 Gr. 3 steel. Adapted from [47].

An analysis of the consequences of temper intensity on the microstructure revealed that the reason why SA508 Gr. 3 is sensitive to over-tempering, where properties deteriorate due to the excessive precipitation of Mo_2C in the bainitic ferrite [68]. The solidification induced segregation of Mo may affect the impact values due to higher rate of Mo_2C precipitation [68]. Figure 2.23 shows the inverse relation between measured molybdenum microsegregation and the impact energy.

By studying the Mo_2C precipitation state, Haverkamp et al. found that the detrimental influence on the toughness diminished, when the needle shape of the

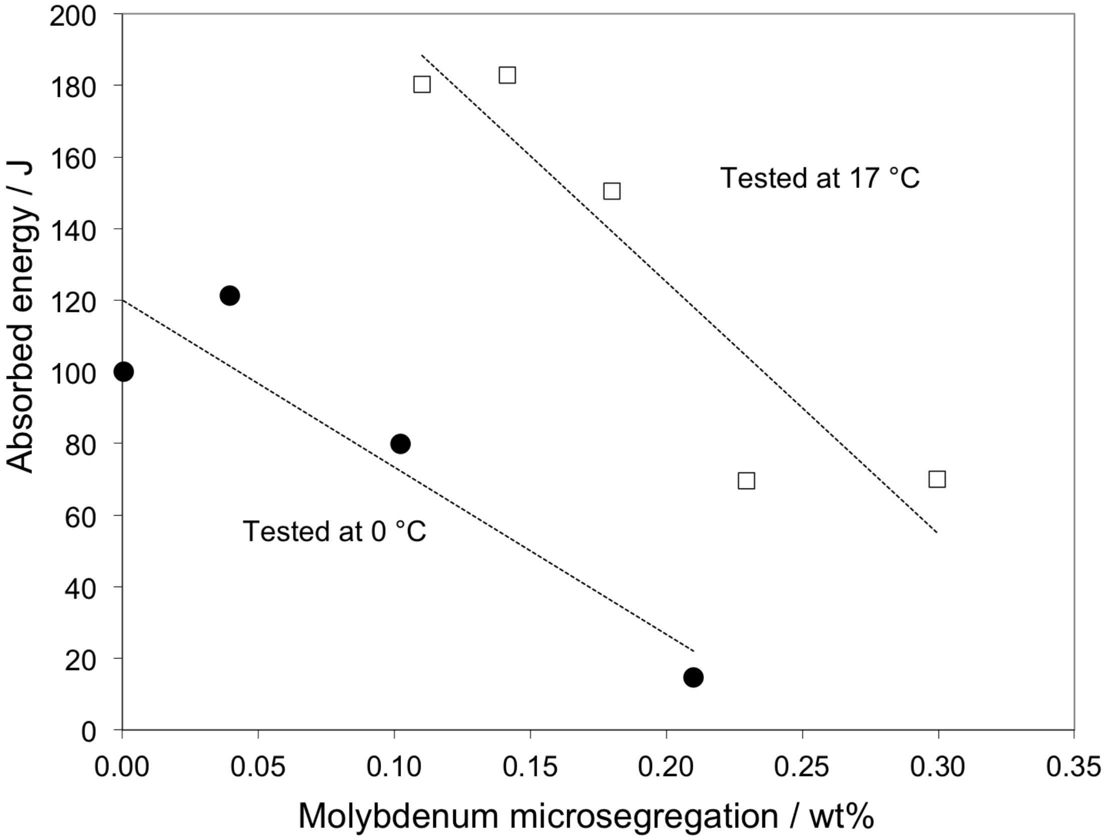

Figure 2.23: Influence of measured Mo microsegregation, measured as deviation from the ladle analysis, on impact absorbed energy. Average Mo content was 0.5 wt%. Adapted from [68].

Mo_2C precipitates decreased [68]. It was also speculated that there is a possible relation between the more compact morphology and a specific amount of aluminium in the composition, due to a probable relation between AlN and Mo_2C. However, the report did not present any proof, even for the existence of the AlN precipitates in the studied pressure vessel steel. Best values of impact energy were obtained at levels of 0.2 wt% of aluminium [68].

In contrast to the austenitisation stage, material properties during tempering are not sensitive to the heating and cooling rates. However, SA508 Gr 3 steels may be susceptible to temper embrittlement during slow cooling through the susceptible temperature range, 350 - 550 °C, resulting in a loss of toughdness characterised by the development of intergranular fractures in the brittle fracture surface [5, 85]. Temper embrittlement is caused by the presence of specific impurities in the steel, which segregate to austenite grain boundaries during heat treatment. The main embrittling elements are phosphorous, antimony, tin and arsenic [85, 86]. Temper embrittlement can be prevented by accelerated cooling from the tempering temperature and/or close control of residual elements during steelmaking to extremely low levels [5, 85, 86].

The requirement for a temper embrittlement resistant steel is commonly expressed by the J-factor [87]:

$$\mathrm{J} = (\mathrm{Mn} + \mathrm{Si})\ (\mathrm{P} + \mathrm{Sn}) \times 10^4 \tag{2.10}$$

where the different elements are expressed in wt%

Commercial specifications require a J-factor of less than 150 for the risk of temper embrittlement to be considered low [87].

After the tempering stage, the forging is then finish machined and prepared for welding to other forgings which form the vessel.

2.6 Post-welding heat treatment

Welding is essential in the assembly of RPV components. Even when low-alloy steels with excellent mechanical properties are developed, their mechanical properties may deteriorate after welding. The welding process will mainly affect the area near to the fusion zone, known as the heat-affected zone (HAZ). Microstructural changes such as grain coarsening, carbide precipitation, and martensite formation generally occur and cause a deterioration in toughness and an increase in sensitivity to brittle fracture [41, 48, 52]. Sufficient fracture toughness in the HAZs and the quantitative evaluation of that toughness are both important to the safe operation of nuclear reactor structures.

According to the distance from the fusion line, the HAZ, in a single pass weld, can be divided in regions according to the welding thermal cycles. Composed of a coarse-grained region reheated above 1100 °C, a fine-grained region reheated between 900 °C and 1100 °C, a partially transformed region reheated between 700 °C and 900 °C, and a tempered region reheated below 700 °C [52]. The most embrittlement seems to occur in the intercritically reheated coarse-grained region located near the bond. This zone, is only partly reaustenitised during a subsequent thermal cycle. In some steels a concentration of austenite stabilisers, such as carbon, can occur in the regions that are reaustenitised and, upon cooling, these locations transform into hard microstructures associated with poor toughness [48, 52, 88].

In a multipass weld, the HAZ microstructure changes with thermal cycles, depending on the number of welding passes and peak temperatures, in a complicated manner, making quantitative analyses difficult. Effects of a multi-pass weld HAZ can be found elsewhere [52, 61]. The work in this thesis will only concentrate in the single pass weld and therefore, in the intercritically reheated coarse-grained region, near the weld fussion line, since this vulnerable area is commonly used to assess the properties of materials/processes [41, 48]. Values for submerged arc welding conditions in SA508 Gr. 3 steels and thermal cycle conditions for simulation of the coarse-grained HAZ are included in Tables 2.10 and 2.11.

The typical microstructure of the HAZ before post-welding heat treatment (PWHT) consists mostly of martensite with a coarse austenite grain size, between 200 and 400 μm. These large grains are produced by the high peak temperatures recorded during welding, commonly around 1350 °C [41, 48, 52]. Kwon et al. identified and quantified the amount of phases in the HAZ, Table 2.9.

The key microstructural factor affecting tensile and impact properties of the HAZ is the martensite fraction, and as the volume fraction of martensite increases, hardness and strength increase, but the fracture toughness decreases [52, 61]. Experimental results shown in Fig. 2.24 prove that martensite in excess of 18 vol%

causes the impact energy to be reduced by half compared with the base material [52].

To reduce and redistribute the residual stresses introduced by welding and thus increase the low values of toughness, RPVs undergo a PWHT. Times and temperatures, limited below the original tempering temperature of the steel (higher temperatures could change the microstructure from what is required), are based on knowledge and expertise from the manufacturer. A common process condition for PWHT is 600 °C for 30 h [28, 42, 89]. After PWHT, the mostly martensitic microstructure is transformed into tempered martensite and the total carbide quantity increases, from 2 to 4 vol.%, because of the additional carbide precipitation during PWHT [41, 48, 52]. Most of the carbides precipitated at this stage are mainly fine Mo_2C [41]. Figure 2.25 compares the microstructure of the HAZ before and after PWHT.

Experimental observations from Kim et al. demonstrated that fracture toughens and tensile strength after PWHT are controlled by the amount of precipitates [52]. An increase in the number of precipitates was found to increase the strength at the expense of toughness, Fig. 2.26. The cause of increase of tensile properties is due to the precipitation hardening effect of the Mo_2C precipitated during the PWHT [41, 46, 48]. Similarly, the reduction in absorbed energy was due to the effect of over-precipitaion of Mo_2C [68]. Table 2.12 summarises the change in properties before and after PWHT. Since the most vulnerable region

Table 2.9: Volume percentage of phases (error range ± 1 %) [61].

	Volume of phases / %			
Specimen	Ferrite	Martensite	Austenite	Carbides
Base material	97	0	0	3
HAZ before PWHT	11	87	0	2
HAZ after PWHT	96	0	0	4

Table 2.10: Submerged arc welding conditions for SA508 Gr. 3 steels [41].

Process	Wire diameter / mm	Current / A	Voltage / V	Travel speed / cm min^{-1}	Preheat temperature / °C	Interpass Temperature / °C
SAW	4	500 - 600	28 - 32	30 - 40	121	200

Table 2.11: Thermal cycle simulation conditions for intercritically reheated coarse-grained HAZ [48].

	First Pass				Second Pass		
Specimen	Heating rate / °C min^{-1}	Holding temperature and time / °C, s	Cooling rate / °C	Interpass temperature / °C	Heating rate / °C min^{-1}	Holding temperature and time / °C, s	Cooling rate / °C min^{-1}
HAZ	9000	1350, 10	780	200	9000	700, 10	780

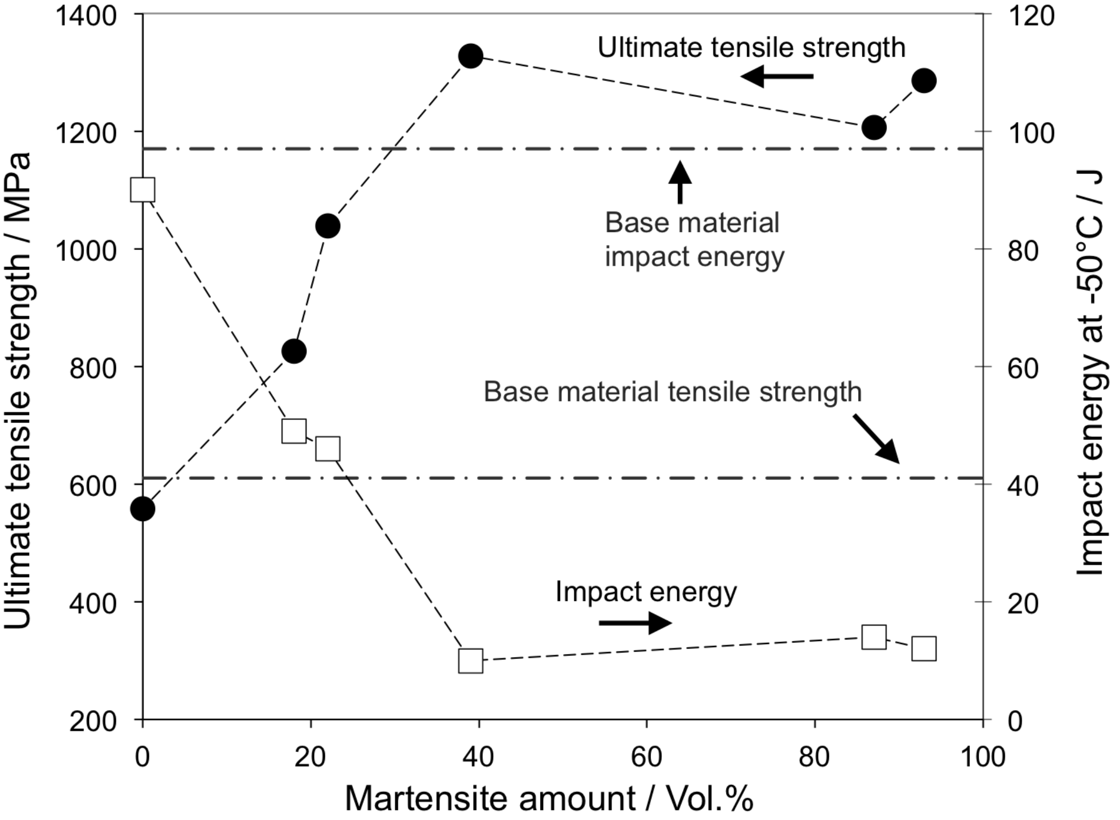

Figure 2.24: Martensite volume percent versus ultimate tensile strength and absorbed energy in the HAZ before PWHT [52].

in the HAZ shows similar impact toughness, lower DBTT and higher tensile values than the base metal, it is commonly assumed that SA508 Gr. 3 steels can be joined safely by welding.

The effects that the PWHT have on properties, has commonly based on the analysis of the HAZ. However, there are no available data on how the PWHT is affecting the base material on SA508 Gr 3. The study of the effects that long PWHTs have on properties of base materials is already being considered for other types steels, such as the 2.25Cr - 1Mo steel grade [90]. Therefore, this is a practice that should also be applied to SA508 Gr 3 steels, as the thermal effects of a PWHT may deteriorate the material performace.

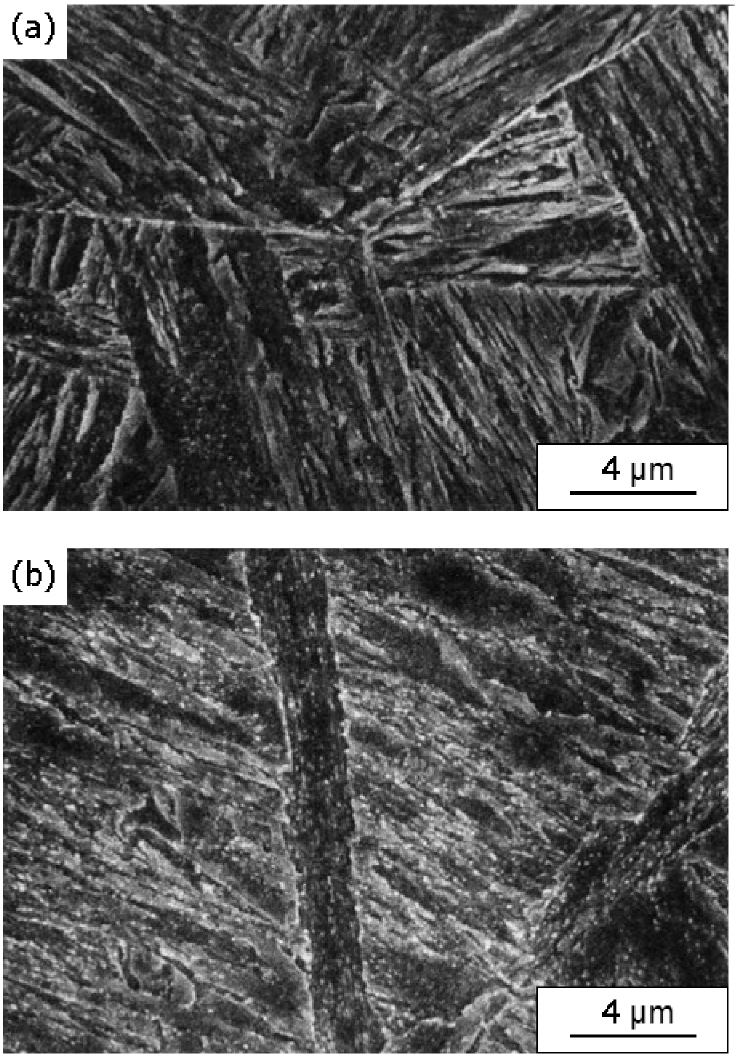

Figure 2.25: SEM image of martensitic HAZ microstructure before (a) and after (b) PWHT [48].

Similar to the TP, an equivalent tempering parameter (TP$_{eq}$) can be defined to asses the consequences of multiple heat treatments. For a given temperature temperature (T_1), for a time (t_1), to calculate the equivalent (t_{eq}) of a treatment at any temperature as [90]:

$$t_{eq} = 10^{\frac{20\,(T_2-T_1)}{T_1}+\frac{T_2}{T_2\log(t_2)}} \tag{2.11}$$

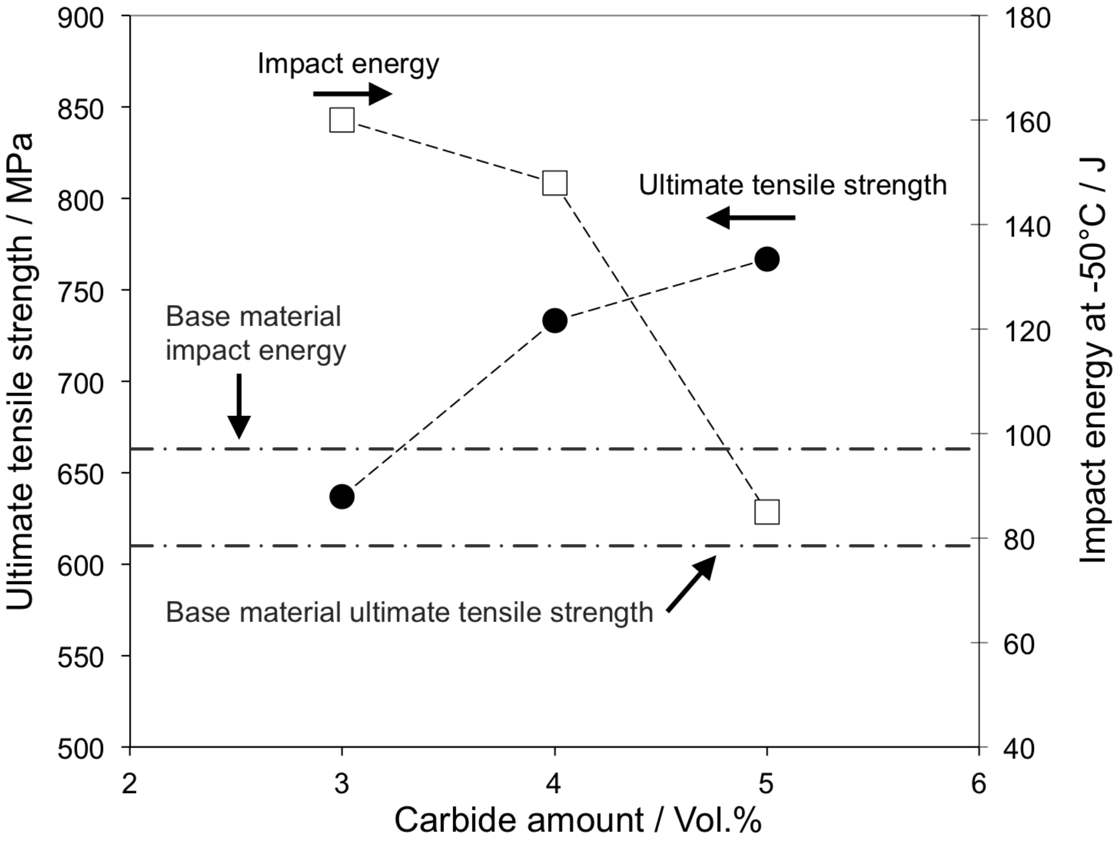

Figure 2.26: Carbide volume percentage versus ultimate tensile strength and absorbed energy in the HAZ after PWHT [52].

where T_1, t_1 are the initial temperature in Kelvin and the time in hours and T_2, t_2 for a subsequent treatment.

Table 2.12: Summary of change in properties before and after PWHT [41, 52].

Specimen	USE / J	DBTT / °C	Tensile strength / MPa
Base material	276	8	610
HAZ before PWHT	67	-18	1206
HAZ after PWHT	203	-69	749

The equivalent time can be used in the following equation to obtain the TP_{eq} [90]:

$$\mathrm{TP}_{eq} = T_1 \left[20 + \log \left(\sum_{i=1}^{n} t_{eq} \right) \right] \times 10^{-3} \tag{2.12}$$

where the temperature is in Kelvin and the time in hours.

2.7 Microstructure

There have been many microstructural characterisations of SA508 Gr. 3 steels, all concluding that the quality heat treatment leads to tempered upper-bainite [25, 35, 37–41, 43–48, 67, 68]. Furthermore, the strength and impact properties of this steel are sensitive to the resulting carbides. Fe_3C usually forms along grain or lath boundaries and Mo_2C is distributed inside the laths [25, 35, 37–41, 43–48, 67, 68]. Fig. 2.27 shows a typical SEM image of a SA508 Gr. 3 steel.

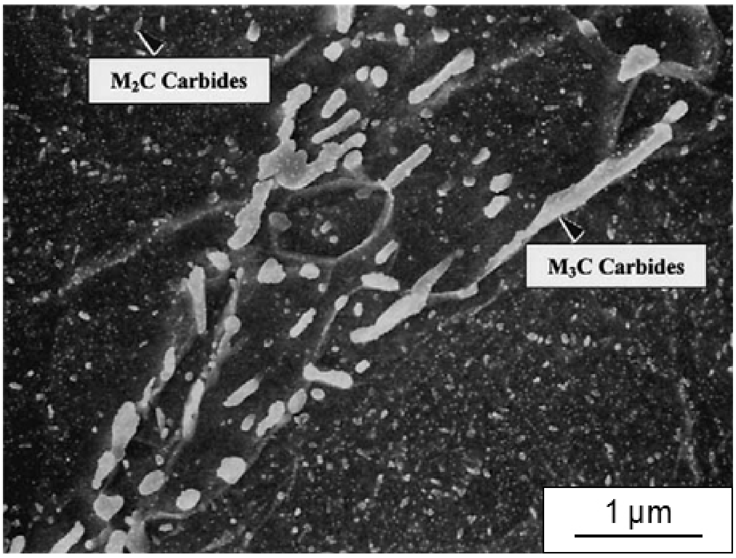

Figure 2.27: SA508 Gr. 3 steel showing typical tempered bainite microstructure. “M” stands for metal atoms [45].

Cementite occurs as long rods (about 0.3 µm thick and 3 µm long) and as spheres (between 0.2 - 0.3 µm in size) [38, 46]. While smaller Mo_2C carbides are mostly present as fine needles (about 0.02 µm thick and 0.3 µm long), but have also been reported with more compact shapes [38, 46, 68]. Fig. 2.28 shows the size distribution of 1428 measured carbides obtained from SEM micrographs.

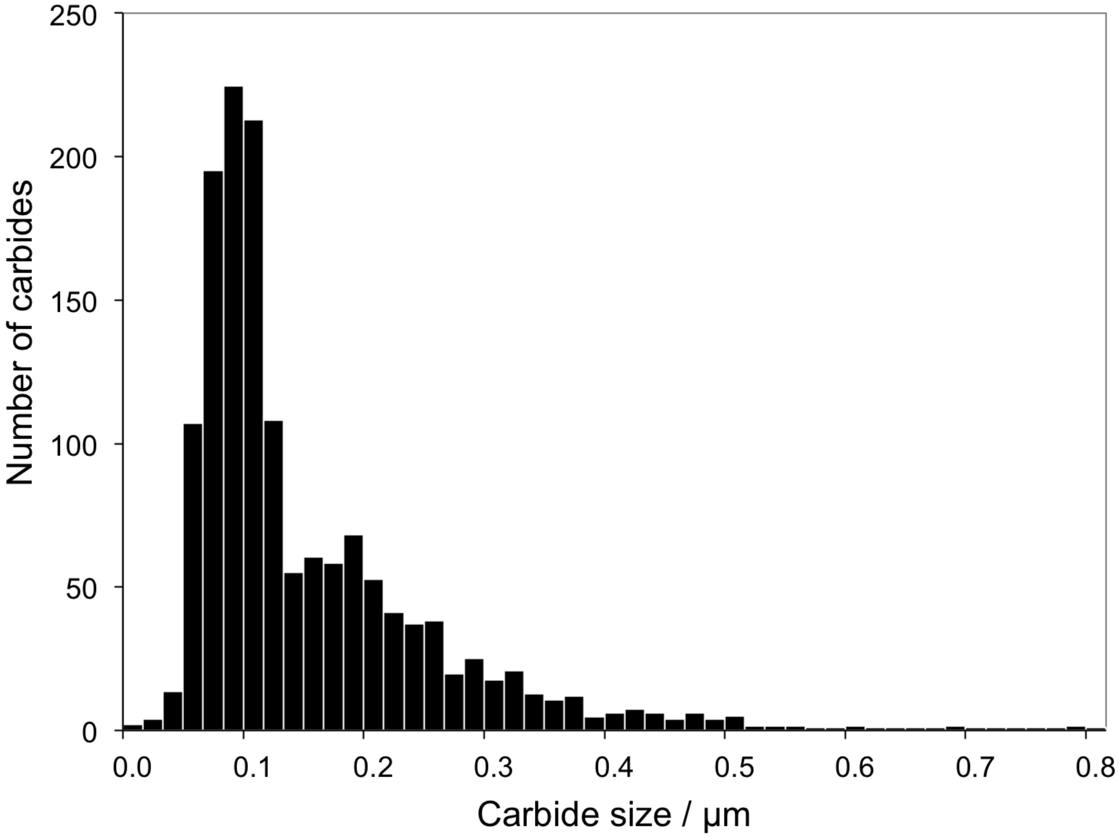

Figure 2.28: Carbide size distribution of SA508 steel. Adapted from [45].

It is generally accepted that brittle fracture is due to cleavage, while ductile fracture is caused by void coalescence in low alloy steels [45, 46]. At temperatures below the DBTT micro-cracks form at carbides and propagate into the matrix creating the fracture [40, 41, 67]. At temperatures above DBTT fracture is due to the coalescence of either voids formed at carbide/matrix interfaces or formed due to fracture of carbides [41, 45].

The toughness in the ductile - brittle transition region of SA508 Gr 3 steels has been reported to be dependent on the probability of finding carbides larger than a critical size in front of a crack tip. The *critical carbide size* is defined as the size of carbides, at a given temperature, that can cause cleavage fracture when micro-cracks formed within the carbides could propagate into the adjacent ferrite matrix [45, 67].

This critical carbide size (d_c) for a particular temperature can be estimated by using the Irwin and Orowan modification to the famous Griffith equation, which accounts for plastic deformation, as follows [45, 67, 91]:

$$d_c = \frac{4\,E\,\gamma_p}{\pi(1-\nu^2)\,\sigma_p^2} \tag{2.13}$$

where γ_p is the surface energy, $7\,\mathrm{J\,m^{-2}}$ from [92], ν is the Poisson's ratio, E is the Young's modulus and σ_p is the principal cleavage stress, which can be obtained by finite element analysis [45, 67, 93].

Lee et al. showed that the probability (P) of finding carbides larger than a given critical size (d_c) followed the Weibull distribution as given by [45]:

$$P(\text{size} > d_c) = \exp\left[-\left(\frac{d_c - d_s}{a}\right)^b\right] \tag{2.14}$$

where d_c is the critical carbide size in µm, d_s is the size of the minimum observable carbide in µm, a is a parameter in the Weibull distribution and b is the shape factor in the Weibull distribution.

Figure 2.29 compares the Weibull distribution after regression analysis for the carbide size distribution of SA508 Gr. 3 with two different tempering processes, showing that the probability of discovering a precipitate larger than the critical size, able to propagate micro-cracks into the matrix to cause cleavage fracture, is significantly reduced as the carbide critical size increases.

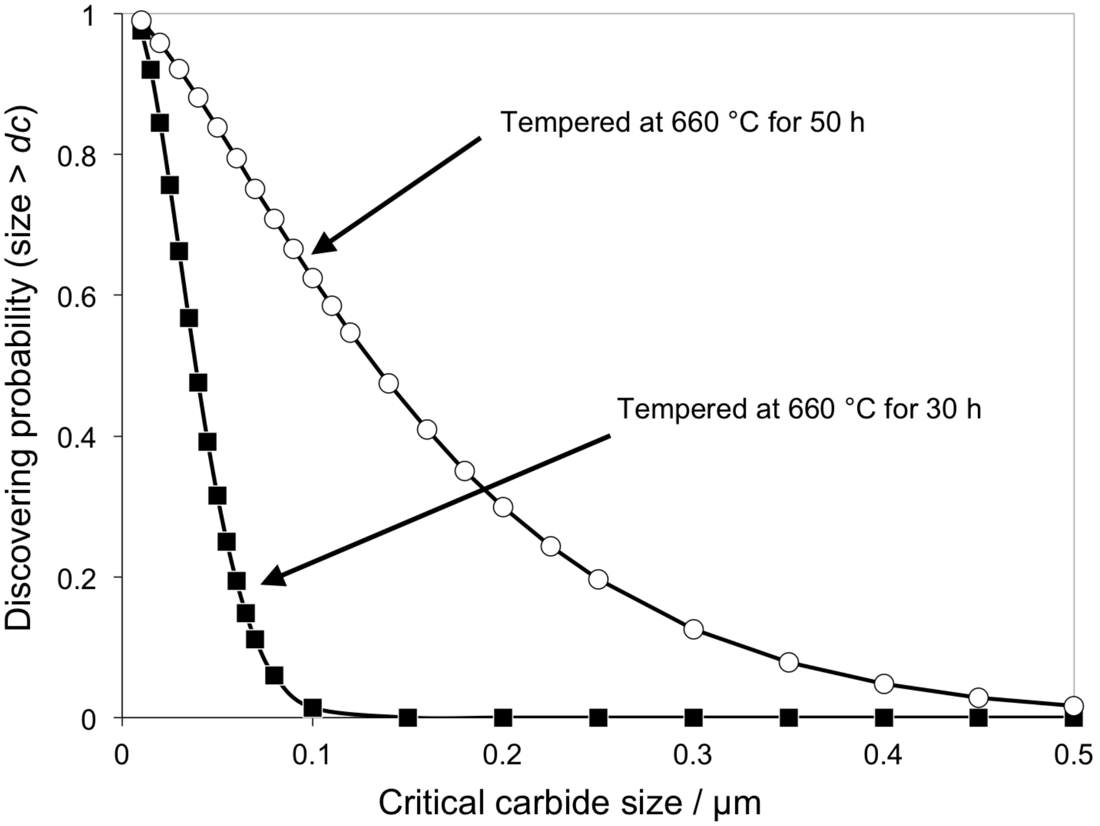

Figure 2.29: Weibull regression analysis for the carbide size distribution showing the probability of discovering a precipitate larger than the critical size. Austenitised at 880°C for 6 h. Adapted from [67].

Figure 2.30 demonstrates an inversely proportional relationship between the probability of finding a carbides larger than the critical size, $(d_c - d_s)^b$, and the transition temperature T_0. As the critical carbide size increases, the probability of finding a precipitate larger than d_c near the crack tip decreases. Hence there is a improvement in fracture toughness in the ductile - brittle transition region by shifting the transition temperature T_0 to lower temperatures.

It is then concluded, that the toughness behaviour of SA508 Gr. 3 steels in the transition region is controlled by the probability of finding a sufficiently large carbide near of a crack tip. Therefore, it is recommended to reduce the number of coarse carbides Fe_3C to improve toughness is the ductile - brittle transition re-

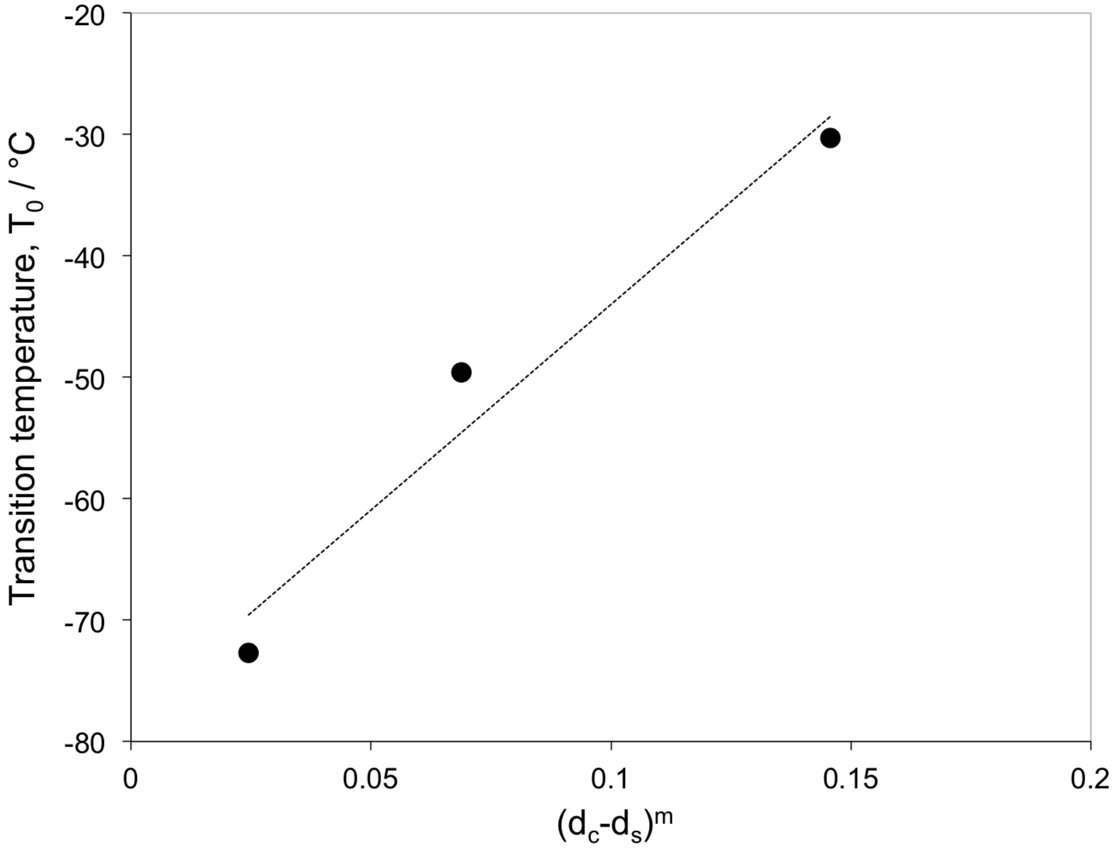

Figure 2.30: Effects of carbide size distribution on the transition temperature T_0, of SA508 steels. Adapted from [67].

gion [45, 67].

To summarise the effects of the microstructural features in SA508 Gr. 3 steels, it has been concluded that coarse rod type and spherical type cementite present in inter-lath region are considered as major detrimental microstructural features to the toughness of this type of bainitic alloys [38, 46, 94]. By contrast it is assumed that Mo_2C carbides have no effect on the fracture process of these pressure vessel steels as these precipitates are extremely fine and it is hard for them to form microcracks or voids [45]. As previously mentioned, M_2C carbides act as precipitation hardening particles [41, 46, 48]. The mechanical properties of the SA508 Gr. 3 steels will then be influenced by the amount of these particles. Larger amounts of M_2C carbides will result in improved mechanical properties.

2.7.1 Through-thickness properties

As previously mentioned, there is a general agreement that the final microstructure after quenching during the quality heat treatment is bainite [25, 35, 37–41, 43–48, 67, 68]. However, RPVs are large components, the wall thickness varies between 200 and 700 mm, so in spite of the water quenching, the cooling rate following austenitisation during the quality heat treatment should vary significantly as a function of depth relative to the surface. Such variations introduce gradients of microstructure [4, 5, 32, 40, 47, 68]. A location-dependent microstructure may appear and, consequently, through-thickness variations of mechanical properties. The question then arises whether the desired microstructures, and hence properties, are in fact present in regions where the cooling rate is slowest.

Previous investigations on the microstructure as a function of thickness in the range 160 and 300 mm wall thickness, have reported that the microstructure is uniformy bainitic [29, 43, 47, 95]. Only Byun et al. reported martensite near the surface, although the report does not include metallographic evidence. The microstructures of two components with wall thickness 250 mm were reported to contain "ferrite", assumed to be allotriomorphic ferrite, in the mid wall of one of the components although metallographic evidence was not provided [43]. There was no explanation why, in two components with the same thermal history, austenitisation, water quench and tempering, and identical thickness, allotriomorphic ferrite was found only in one of them.

Hardenability depends on both, composition and austenite grain size. The compositions for the two components studied in [43] are very similar, furthermore, the material with allotriomorphic ferrite has somewhat higher carbon and nickel concentrations 0.21 vs. 0.17 wt.% and 0.92 vs. 0.82 wt.%, respectively [43]. Therefore, the presence of allotriomorphic ferrite could have been influenced by a finer austenite grain size. As it will be shown later in the thesis, the austenite grain size has a profound influence on the hardenability of SA508 Gr 3 steels.

Table 2.13 summarises the observed differences in microstructures at representative through-thickness positions, of large components with wall thickness varying from 160 to 250 mm.

Table 2.13: Microstructures at representative locations through the thickness (T). α_b: bainite, α': martensite, α: ferrite [43].

Normalised location	Component thickness 210 mm	Component thickness 250 mm	Component thickness 250 mm	Component thickness 160 mm
0 T	$\alpha' + \alpha_b$	$\alpha' + \alpha_b$	α'	α'
0.25 T	α_b	α_b	α_b	α'+ α_b
0.5 T	α_b	α_b	$\alpha_b + \alpha$	α'
0.75 T	α_b	α_b	α_b	$\alpha' + \alpha_b$
1 T	$\alpha' + \alpha_b$	$\alpha' + \alpha_b$	$\alpha' + \alpha_b$	α'

The through-thickness mechanical properties of SA508 Gr. 3 steel are roughly symmetrically distributed from the midpoint of the wall, as seen in Fig. 2.31 [29, 43, 95]. The reported differences in hardness, yield and tensile strength are within the range 5-16% lower at the midpoint [43].

As properties vary depending on the distance from the wall surface. Byuna et al. concluded that the cooling rate gradient during water quenching from austenitisation temperature was the most important cause for inhomogeneous distributions of mechanical properties and that the magnitude of the variations were dependent on the material as well as the wall thickness [43].

2.8 In service conditions

The core of a nuclear reactor presents an exceptionally harsh environment for materials due to the combination of high temperature, high stresses, a chemically aggressive coolant, intense radiation flux, total number of neutrons received per time unit, all of which exert operational burdens on structural materials.

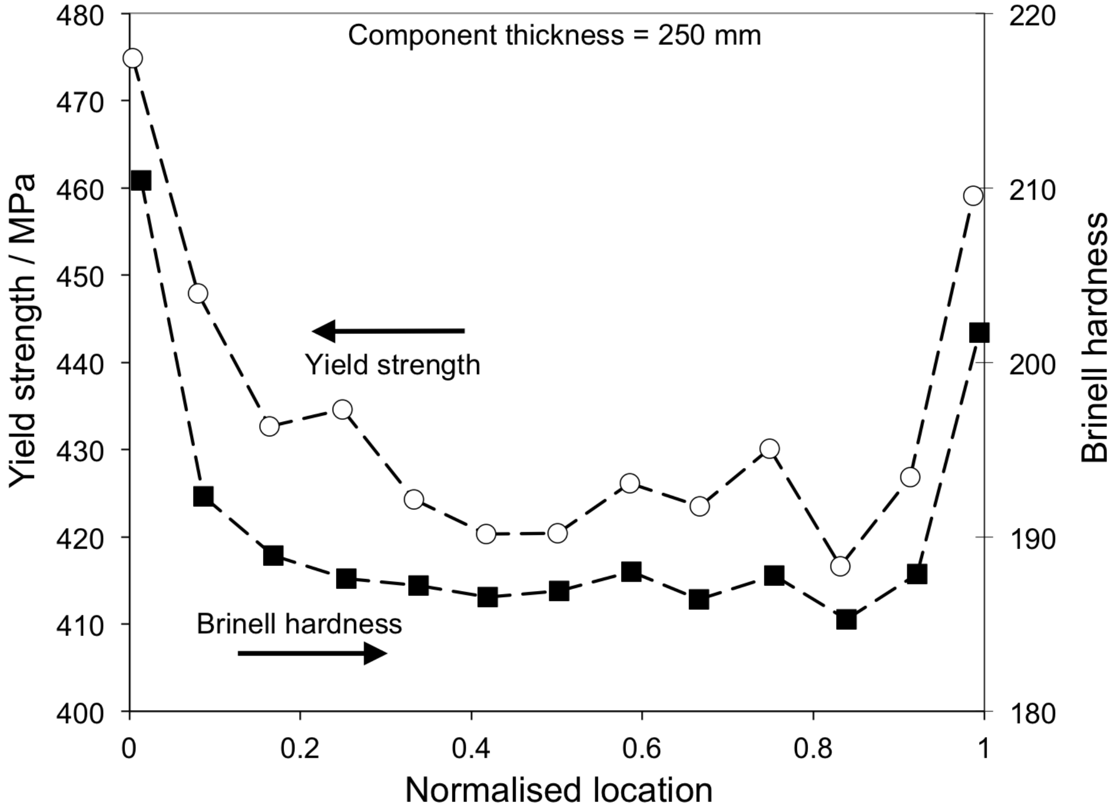

Figure 2.31: Distribution of through-thickness properties. Adapted from [43].

SA508 Gr. 3 steel forgings are currently used for applications in reactors designed to operate at pressures of 15.5 MPa and temperatures of approximately 300 °C during normal operation [96, 97]. And there is no time limit for the operation of components made of SA508 as long as the operating temperatures are maintained below 371 °C, whence creep deformation is negligible [98].

Pressure vessels are designed to operate at temperatures above the onset of upper shelf energy, where the absorbed impact energy of the material can reach values in the region of 300 J, and the fracture toughness is well above 350 $\mathrm{MPa\,m^{1/2}}$, in order to avoid brittle fracture [6, 7, 38–40]. At normal operating temperatures (288 °C), the tensile strength is reduced to 396 MPa from 448 MPa at room temperature [28].

Regulations require very low RPV failure probabilities both for normal operation and postulated accident events, and hence large safety margins between service conditions and material properties are implemented. However, as the SA508 Gr 3 is sensitive to irradiation-induced embrittlement, operation margins with respect to both the temperature and pressure are reduced. The reduction in operation safety margins may directly lead to sudden fast fracture of RPVs [8–10].

2.8.1 Irradiation Embrittlement

There is clear evidence that SA508 steels are severely affected by neutron irradiation [6, 26, 99–101]. This is a complex process, as it increases the number density of point defects, enhances the diffusivity of all atoms and induces phase transformations and microvoids [6, 26, 99]. The radiation sensitivity of pressure vessel steels is determined partly by its chemical composition. Excessive phosphorus, copper and nickel are known to enhance irradiation embrittlement [26, 99–101].

Fig. 2.32 shows the detrimental consequences of irradiation embrittlement on the fracture toughness of SA508 Gr. 3 steels, leading to a reduction in the USE and increases in the DBTT.

At the present time, there is no a complete theory, which would make possible the prediction of irradiation effects with plant in service conditions. The development of an unified theory of radiation embrittlement is rather difficult because of the complicated interaction of metallurgical factors and irradiation conditions, as well as the presence of synergism of residual impurities and alloying elements. Therefore, the nuclear industry relies on exhaustive surveillance programmes to monitor radiation damage on SA508 Gr 3 steels, in which surveillance capsules, containing mechanical property specimens and neutron dosimeters, are placed inside the RPV and periodically removed for evaluation [9, 26, 99–102].

During the 1960s and 1970s when the surveillance programmes were estab-

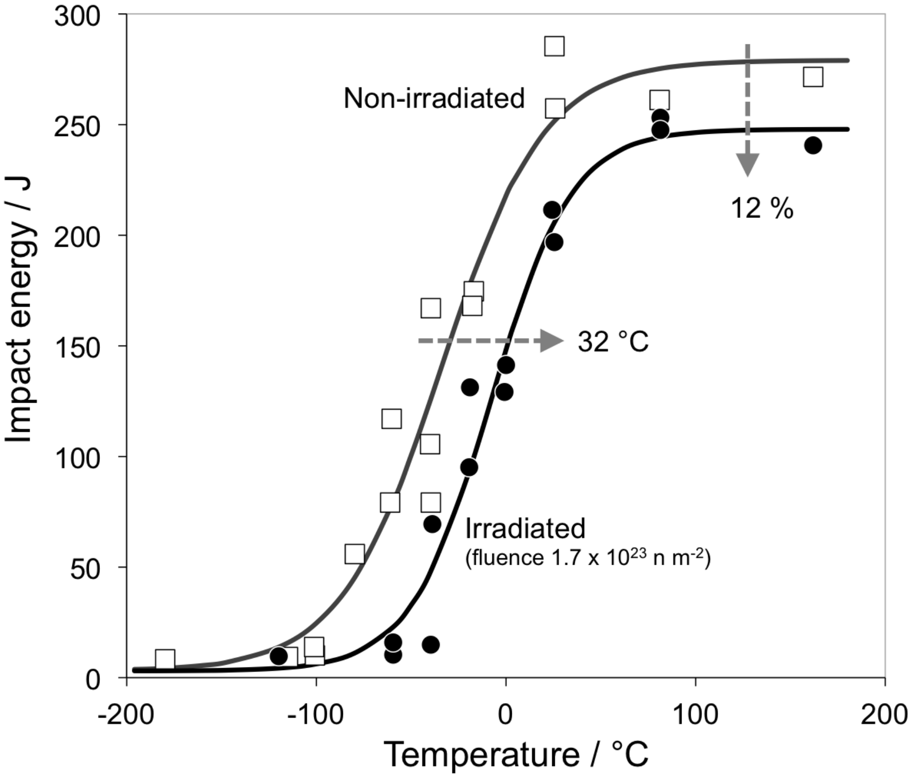

Figure 2.32: Effect of irradiation on the Charpy impact energy of SA508 Gr. 3 steels. Adapted from [97].

lished, fracture mechanics indicated the testing of very large specimens, with thickness similar to the RPV, to accurately assess the structural integrity. Since specimens of this size could not be placed in the water gap between the fuel and the inner diameter of the RPV, it was decide to use much smaller Charpy specimens [103]. Consequently, and although impact (empirical value of energy absorbed) and fracture toughness (unstable crack propagation) tests provide different data, due to the small specimen dimension and testing simplicity, impact Charpy testing has been extensively used to indicate toughness [29, 40, 41, 46–48].

Under normal operation circumstances, even after the deterioration of properties by irradiation, the safety margin between service conditions and material properties is quite large. However, there are particular unpredictable circumstances, such as pressurised thermal shocks, caused by a rapid and severe cool-down in the primary coolant system, where large tensile stresses develop on the inner wall of the vessel due to internal pressure and thermal stresses caused by the cooling, that poses a threat to structural integrity. For embrittled RPVs, these stresses could be high enough to initiate a running crack that may propagate all the way through the vessel wall causing a catastrophic failure [97, 104–106].

Chapter 3

Experimental

3.1 As-received material

The steel discussed in this work is SA508 Gr. 3 from an unspecified part of a forged nuclear pressure vessel, supplied by the industrial sponsor. The three slightly different SA508 Gr. 3 commercial-steels studied are listed in Table 3.1. Alloys A and C in their as–received state had been subjected to multiple heat treatments: austenitisation between 860 and 880 °C for approximately 12 h, water quenched and tempered between 635 and 655 °C for 10 h. Steel B in its as-received condition comes from the bottom of an ingot with no further heat treatment. The range of temperatures and times is due to the thermal gradients in thick samples, which makes the temperature at a particular location uncertain. Alloy A was supplied in 30 mm diameter, 90 mm long rods, Alloy B in 200×100×20 mm flat sheet, and Alloy A in 200 mm diameter, 200 mm long cylinders. As received materials were then machined to obtain the desired shape for experiments.

3.2 Microstructural observations

Samples for microstructural observations were ground, starting with 240-grit silicon carbide grinding paper and increasing progressively up to 2500-grit. The polishing stage was carried out with diamond paste of 6 μm and 1 μm grade. For orientation imaging using the electron back-scattered diffraction (EBSD) tech-

Table 3.1: Full chemical compositions of as-received SA508 Gr. 3 steels (wt%).

	C	Mn	Ni	Mo	Cr	Si	Cu	P	S	Co	Al	V	Nb	Ti	Sb	As	Sn	N
Alloy A	0.17	1.315	0.785	0.53	0.27	0.22	0.04	0.004	0.002	0.01	0.015	0.000	0.004	0.002	0.002	0.005	0.006	0.007
Alloy B	0.17	1.390	0.760	0.50	0.22	0.24	0.04	0.005	0.002	0.00	0.025	0.004	0.004	0.002	0.000	0.006	0.006	0.011
Alloy C	0.17	1.320	0.760	0.51	0.20	0.23	0.02	0.005	0.001	0.06	0.019	0.004	0.004	0.002	0.002	0.003	0.004	0.010

nique, samples were finish-polished using a 0.25 µm colloidal silica. When necessary, samples for optical microscopy and scanning electron microscopy (SEM) were mounted using a hot mounting press at 150 °C and 2 bar pressure.

3.2.1 Optical micrography

Optical microscopy of the specimens was conducted using a Zeiss Axiotech optical microscope with attached QImaging MicroPublisher 3.3 RTV camera. The magnification range varied from 50 to 1000×. Bright field imaging was used but when better information could be obtained dark field imaging was also applied. Samples were etched with 2% nital.

Thermal etching

Austenite grain boundaries were revealed by thermal etching. A prepolished sample is heated to form grooves at the intersections of austenite grain boundaries with the polished surface in an inert atmosphere or vacuum [107]. These grooves define the austenite grain boundaries which can consequently be observed without further metallographic preparation.

For optical observations, a 5 mm wide flat-surface was prepared along the longitudinal axis of cylindrical samples (⌀8 mm × 12 mm) by grinding and polishing.

3.2.2 Grain size measurements

The linear intercept method was used with data obtained from four different fields of the sample and a total of 72 linear intercept lines. The average value was taken as the linear intercept. The reported error corresponds with the 95% confidence interval, which was obtained according to the ASTM standard specification, as follows [108]:

The 95% confidence interval (95% CI) from the linear intercept measurement was calculated:

$$95\%\,CI = 1.96 \times \frac{\sigma_x}{\sqrt{N_{LI}}} \tag{3.1}$$

where σ_x and N_{LI} are the the standard deviation of the values obtained and the number of linear intercept lines respectively.

The percent relative accuracy (% RA) was then obtained:

$$\%\,\mathrm{RA} = \frac{95\%\,CI}{\overline{LI}} \times 100 \tag{3.2}$$

where $\overline{LI}$ is the average linear intercept obtained.

The ASTM specification allows for a maximum % RA of 10% [108]. In the present work, calculated values of % RA were below 8.5%.

The grain size distributions were obtained using the image analyzer software ImageJ [109]. For statistically meaningful results, a maximum error of 5% was allowed in the distribution. The error in the grain size distribution will be function of the number of measured grains (n_g), and can be calculated as follows:

$$Error = \frac{1}{\sqrt{n_g}} \tag{3.3}$$

3.2.3 Scanning electron microscopy

Microstructural features were imaged and chemically characterised by energy dispersive X-ray (EDX) analysis, using a JEOL 5800 LV, with an operating voltage of 15 kV and a working distance of 10 mm. Samples were etched with 2% Nital to reveal the microstructure. Initial EBSD analysis used a Camscan MX2600, images were taken at an operating voltage of 25 kV, a working distance of 30 mm and a tilt angle of 70 °.

3.2.4 Transmission electron microscopy

Samples were sectioned using spark erosion as thin discs (500 - 250 µm) each of diameter 3 mm. Discs were manually ground to an approximate thickness of 50 µm using 600 and 2500 grit silicon paper. Finally, electropolishing was used to finish-thin both sides of the specimens using a solution of 5% perchloric acid, 25% glycerol and 70 % ethanol. The voltage, current and temperature were, 37 V, 26 mA and 10 °C respectively. TEM investigations were carried out by using a JOEL 200CX and a Tecnai F20 with an incorporated EDX detector.

3.3 Mechanical testing

3.3.1 Hardness

Hardness was measured using Vickers hardness testing equipment. A pyramidal indenter was pressed into the surface of the material with a constant load of 20 kg for 20 s. After retrieving the load, the square indent, was measured and converted to Vickers hardness using standard tables. A minimum of five indentations were made at each specimen. The average of the measurements is given as the HV and the standard deviation of the data is presented as the error.

3.3.2 Tensile

Tensile testing was performed externally at Sheffield Forgemasters International Ltd, following the ASTM-370 standard [110]. Parameters recorded during testing include yield strength (by using the offset method at 0.2% strain), the UTS, the elongation, the reduction of area and the Young's modulus. Tensile tests were carried out at room temperature and at 354 °C at a controlled strain rate of 0.012 min^{-1} until the yield strength and then at 0.25 min^{-1} through to break. High temperature testing was performed at Exova. Dimensions of the tensile specimens are summarised in Table 3.2

Table 3.2: Tensile round test specimen dimensions [110].

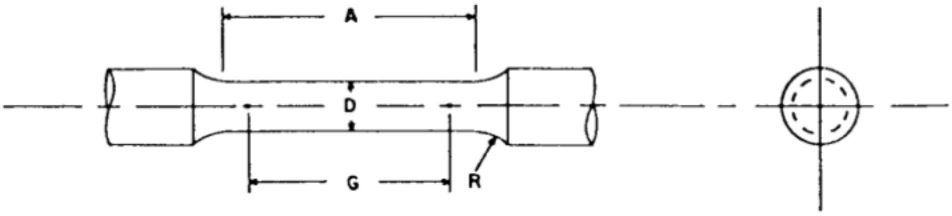

	Dimension / mm
Gauge length (G)	25 ± 0.10
Gauge diameter (D)	6.25 ± 0.12
Radius of fillet (Minimum) (R)	5
Length of reduced section (Minimum) (A)	32

3.3.3 Charpy impact testing

To compare effects on toughness due to different heat treatments, Charpy V-notch impact testing was performed complying with the ASTM E23 standard [111]. Impact tests were performed over the temperature range -196 to 250 °C.

The Charpy test uses a swinging pendulum to strike a constrained test piece in order to establish the amount of energy absorbed by the test piece during failure. The basic set up can be seen in Fig. 3.1. At the starting position (A) the pendulum only has potential energy. It is function of the mass of the hammer (m) and the starting high (H). When the pendulum is released, the hammer moves downwards, hits the specimen and swings to a new maximum high (h). Exactly at the first reversal point (B) the hammer has only potential energy. The energy absorbed by the specimen is the difference of these two potential energies and can be calculated as follows:

$$\text{Impact energy} = (m \times g \times H) - (m \times g \times h) \tag{3.4}$$

where g is the gravitational acceleration.

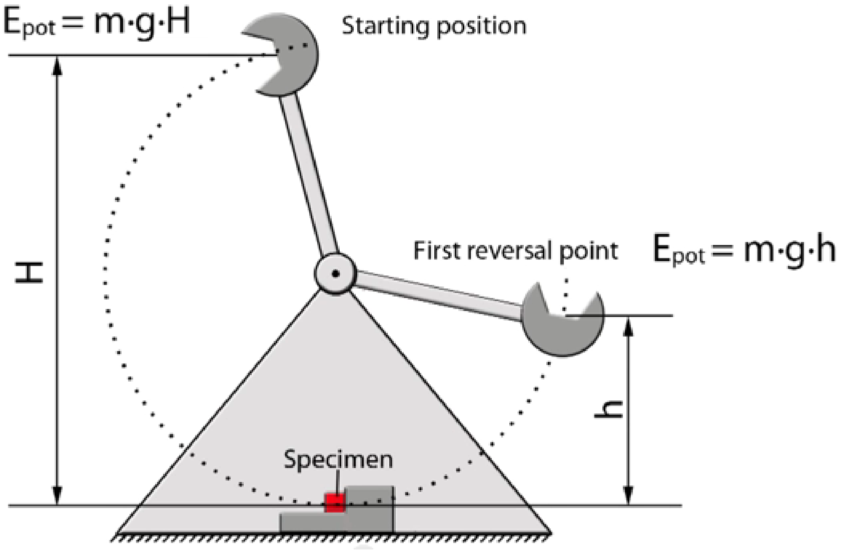

Figure 3.1: The basic Charpy impact testing set up.

3.4 Thermodynamic calculation

Thermodynamic calculations were carried out to estimate the phase equilibria; using the National Physical Laboratory's Metallurgical and Thermodynamic Data Bank (MTDATA) software. By calculating and minimising the Gibbs free energy of the studied system, an estimation of the composition and equilibrium fractions of the phases present can be obtained. The reliability of the results depends on the available data for the subsystems involved in the calculations [112].

In the present work MTDATA version 4.73 with, PLUS, TCFE and SUB SGETE databases were used.

3.5 Heat treatment

3.5.1 Austenitisation

To investigate the effects of the austenitising process parameters (time and temperature) on the austenite grain growth, thermal etching prepared samples (⌀ 8 mm × 12 mm), were heated at temperatures from 840 °C to 1150 °C, and held between 10 min and 13 h.

Heat treatment was carried using a Thermecmaster thermomechanical simulator. The samples undergo a controlled heat treatment, where temperature, dilation, extension and load are recorded with time. Temperature is controlled at ± 2 °C due to the use of a feedback control system connected to a Type S thermocouple which is spot welded to the surface of the sample. This set up enables heating rates up to 50 °C s^{-1} and by using a direct jet of helium towards the sample rapid cooling rates can also be achieved. Samples sit inside an evacuated chamber, maintained at vacuum pressures higher than 1 Pa, a minimum value designed to avoid too much oxidation at high temperature on polished surfaces [113].

Following austenitisation, samples were continuously cooled to obtain martensite at cooling rates from 0.1 to 665 °C s^{-1}. Dilatometric analyses were performed in samples cooled up to 40 °C s^{-1}. For cooling rates above 40 °C s^{-1} samples were water cooled with temperature monitored by thermocouples attached at several locations. The heating rate for the experiments was 5 °C s^{-1}.

Some samples were sealed individually in silica tubes with argon to study the effects of very high austenitisation temperatures in the austenitic grain growth. Samples were heated up to 1200 °C and held for up to 48 h in a Carbolite furnace. These samples were water quenched, with the silica tubes broken inside the water.

3.5.2 Salt bath

Large steel samples (⌀ 200 mm × 20 and 30 mm) used for the mechanical properties programme were heat treated in salt baths at temperatures up to 965 °C for a maximum of 23 h. Heat treatments were carried out externally at Summitglow Ltd.

Salt bath is used for the immersion of components in molten salt preheated at the desired temperature. Since the parts are immersed in the molten salt, air is not in contact with the work piece avoiding the scaling, oxidation and decarburisation. Heat transfer into the components is rapid, much faster than with radiation or convection methods, due to direct contact to the surface; furthermore the heat is more uniformly distributed across the piece. Figure 3.2 compares the heating curves of a ⌀ 200 mm × 20 mm component heated in a vacuum furnace and in a salt bath up to 880 °C.

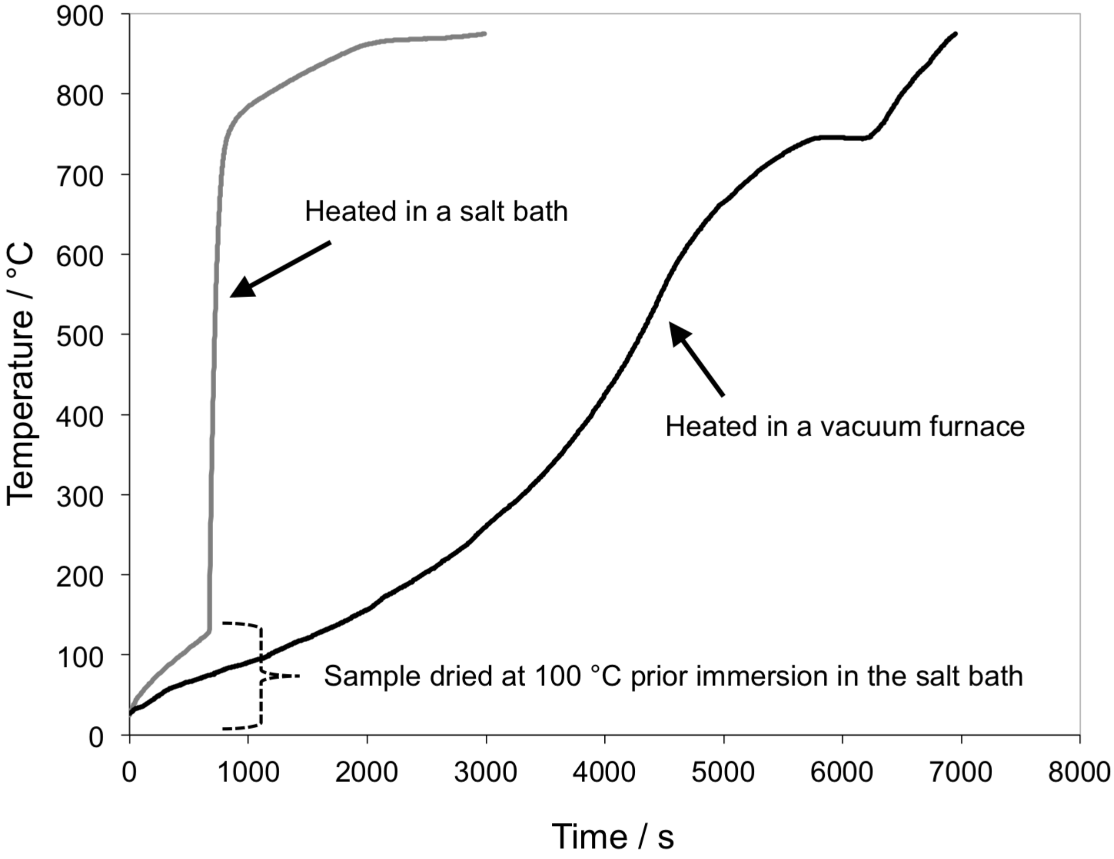

Figure 3.2: Heating curves for the case of vacuum furnace and salt bath.

3.6 Dilatometry

Dilatrometry measures the shrinkage or expansion of specimens during heat treatment and is one of the most powerful techniques for the study and analysis of transformations in steels, as it permits in situ measurement of the reaction in terms of dimensional changes due to phase transformations [114].

Table 3.3: Values for determination of transformation temperatures with the offset method. Austenite and martensite lattice parameters calculated for the steel alloys in this work using equations in Ref. [115].

	Martensite lattice parameter ($a_{\alpha'}$) / nm	0.28737
	Austenite lattice parameter (a_{γ}) / nm	0.35815
Alloy A	Offset strain	1.10594×10^{-4}
Alloy B	Offset strain	1.10481×10^{-4}
Alloy C	Offset strain	1.10520×10^{-4}

Methods for the dilatometric determination of the transformation temperatures of steels are discussed, with emphasis on the noise in the experimental data. For this reason, in the present work the offset method is used to calculate the transformation temperatures, since this technique enables independent investigators to reach identical conclusions given the same set of data. A detailed explanation of this method can be found elsewhere [115].

Given that the austenite unit cell contains four iron atoms and that of martensite two per cell, the offset strain (ε_O) corresponding to a particular value of martensite volume fraction (V) is given by [115]:

$$(1 + \varepsilon_O)^3 = a_\gamma^{-3}[2Va_{\alpha'}^3 + (1 - V)a_\gamma^3] \tag{3.5}$$

where a_γ is the lattice parameter of the austenite and $a_{\alpha'}$ is the lattice parameter of the martensite.

In the present work, a transformation strain due to 1 vol.% martensite was set as the value of the offset at which the transformations were measured. Values for the offset strain and the austenite and martensite lattice parameters are given in Table 3.3. The error associated to the deduction of the transformation temperature with this method is ± 12 °C [115].

3.7 Diffraction techniques

3.7.1 X-ray diffraction

The crystal structure of polished and lightly etched samples was characterised by X-ray diffraction (XRD) using an automated Philips PW1820 $\theta/2\theta$ geometry diffractometer, with CuKα radiation, with a wavelength of the incident X-ray beam of 1.5406 Å, operated at 40 kV and 40 mA. Analysis were performed from 2θ = 40 - 120°, with step size of 0.05° and step time of 4 s, at room temperature. TOPAS version 3 software was used to identity peaks position and phases, quantitative phase analysis was calculated by Rietveld methods.

3.7.2 Synchrotron

High-energy X-rays diffraction analysis were performed at the DESY facilities in Hamburg. Disk like samples, ⌀8 mm × 1 mm, were tested in the P02 beam line with wavelengths of 0.20812 and 0.20692 Å, 60 keV and a beam size of 1.2 × 1.0 mm. Transmission diffraction patterns were recorded using a flat 2D solid state detector, mounted perpendicular to the incident beam behind the sample. The sample to detector distances were modified between 1000 and 1500 mm to increase as much as possible the spatial resolution.

The collected image data were entered into the program MAUD (Materials Analysis Using Diffraction), a Rietveld code written in Java [116]. The tiff images with 32 bit dynamic range are entered using an image manager and then integrated over 360°. The integrated data are then used as spectral data for the Rietveld refinement.

Chapter 4

Results and discussion

As previously discussed, the objective of this study was to understand how the microstructural changes associated with the steps in the quality heat treatment (austenitisation, quenching and tempering) affect the mechanical properties of the material and give scientific interpretations to the empirical knowledge of this pressure vessel steel.

4.1 As-received material

Optical microscopy is of limited use in characterising the fine details of these pressure vessel steels, since the scale of the microstructural features is not resolvable at the magnifications available. Figure 4.1 shows the optical micrographs for the three alloys used in this study.

Alloy A presents remnants of dendritic structure, where secondary dendritic arms are visible with associated preferential areas of precipitation. Alloy C presents a typical microstructure for this type of steels commonly reported as bainite. Alloy B shows the largest grain size in its as-received condition as the material comes from the bottom of an ingot with no subsequent heat treatment.

Precipitate morphology and composition for the as-received condition were investigated by scanning electron microscopy for Alloy A. Two morphologies could

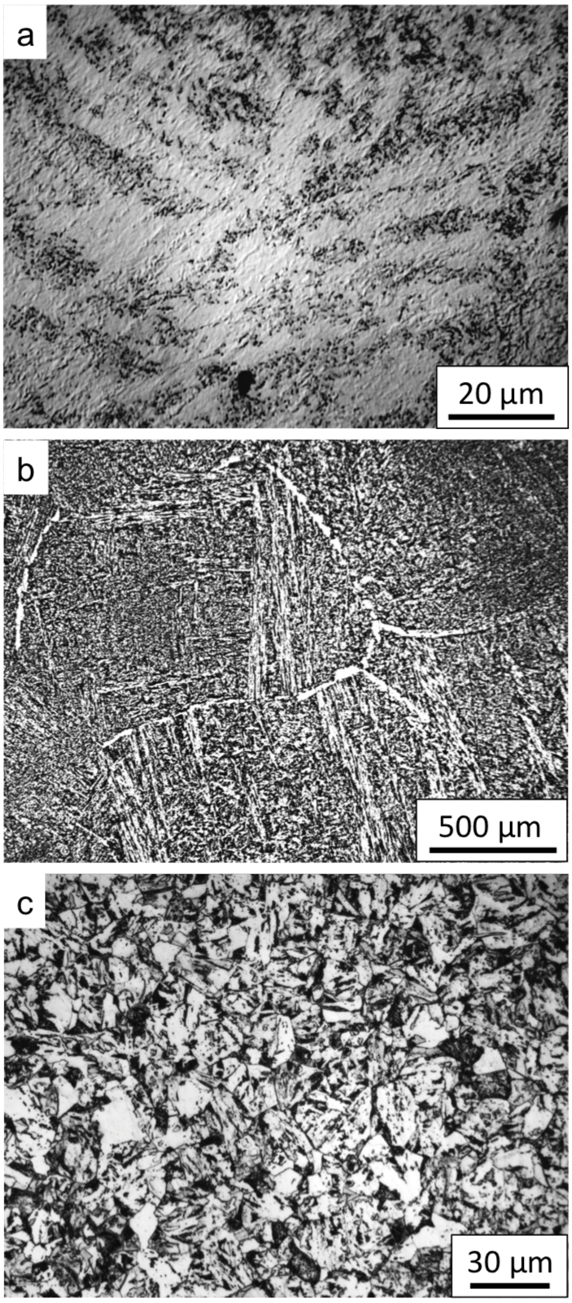

Figure 4.1: Micrographs of the as-received SA508 steel.

be resolved, elongated particles located in regions of intense precipitation and round particles more uniformly distributed, Fig. 4.2. Table 4.1 summarises the average sizes of the precipitates.

Table 4.1: Precipitate size and morphology characterisation by SEM.

Precipitate morphology	Dimensions / μm
Elongated	Length: 0.6 ± 0.4; Thickness: 0.2 ± 0.1
Round	Diameter: 0.1 ± 0.01

Table 4.2: Composition of different areas of as-received samples in wt%.

	Cr	Mn	Ni	Mo	Si	Fe
Intensely precipitated areas	0.43 ± 0.06	2.19 ± 0.31	0.83 ± 0.12	1.41 ± 0.74	0.27 ± 0.04	94.85 ± 1.18
Sparsely precipitated areas	0.25 ± 0.09	1.04 ± 0.19	0.67 ± 0.14	0.57 ± 0.13	0.27 ± 0.05	97.20 ± 0.31

Accurate compositional characterisation of the precipitates, especially the smaller particles, is not possible using SEM techniques as the spread of the incident beam within the sample is relatively large as seen in Fig 4.3. Several area analysis scans have been performed to reveal differences between the regions with intense precipitation, Table 4.2. As expected, solute concentrations are higher in the heavily precipitated regions.

TEM analysis is required to identify the different types of precipitates. Initial analysis of as-received Alloy A samples reveal a complex microstructure with multiple precipitates. The material seems to contain dislocations in spite of the tempering, but it is also clear that many of the dislocation arrays are organised, as would be expected following annealing, Figure 4.4a. The bainitic boundaries are mostly unchanged, in other words, they are roughly of the sub-micrometre thickness, although there is some evidence for localised equiaxed grains, Fig. 4.4b. This is related to the large density of particles that prevent coarsening/recrystallisation

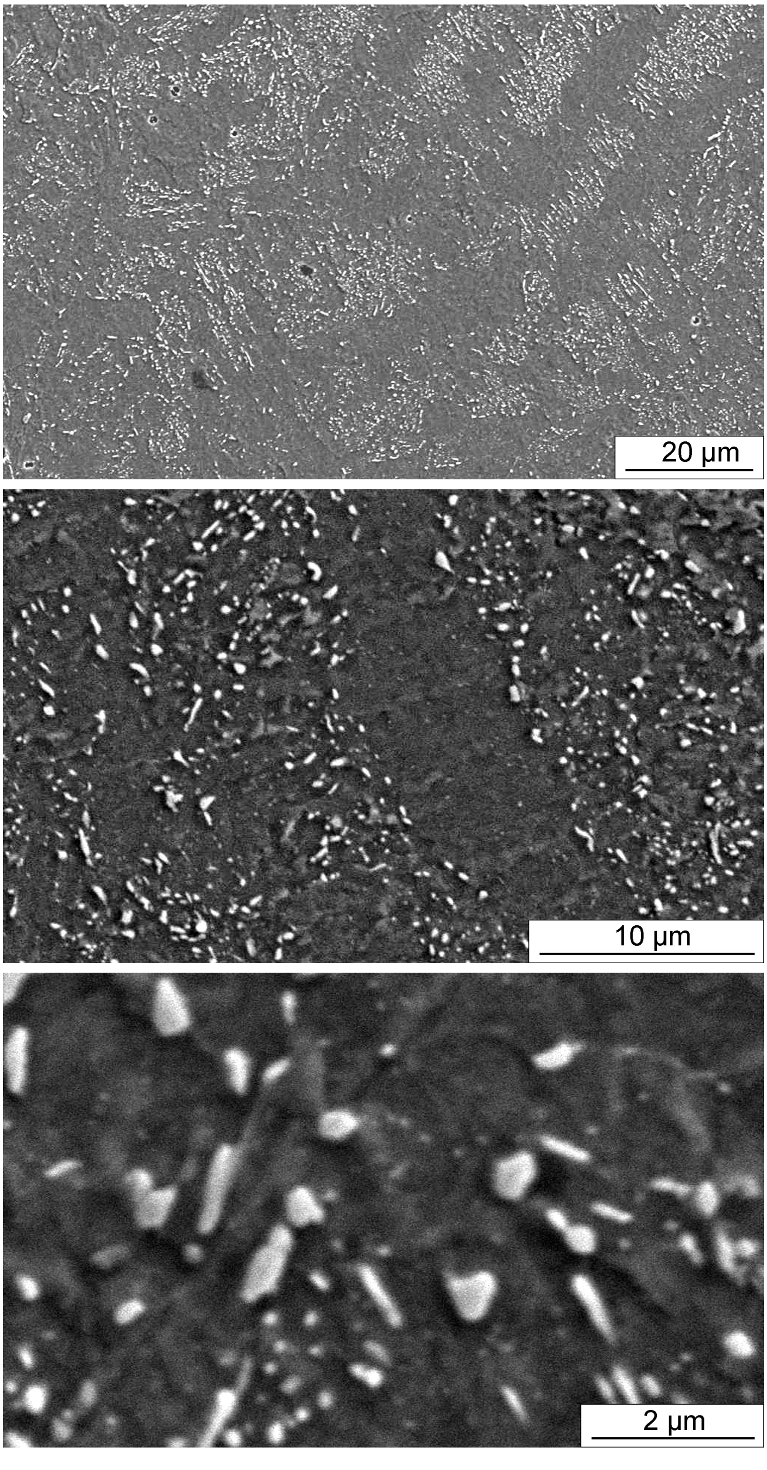

Figure 4.2: Micrographs of the as-received Alloy A.

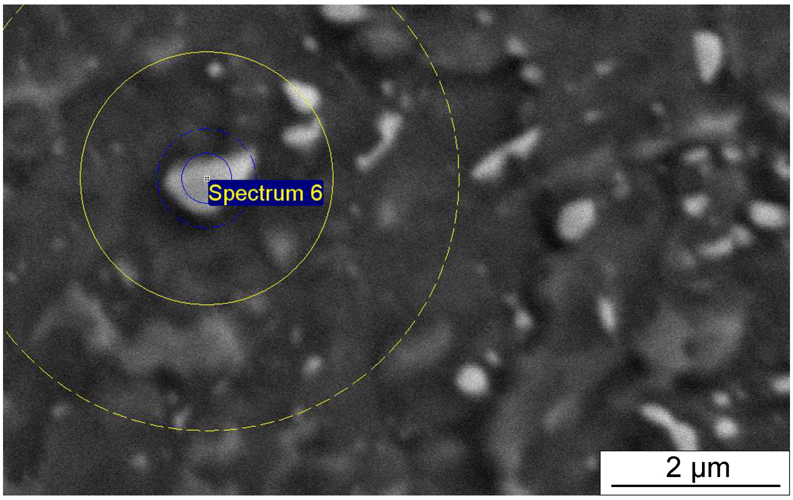

Figure 4.3: EDX analysis error in the compositional characterisation of precipitates. Blue and yellow circles represent the regions over which X-ray information is collected.

of the structure. Micrograph Fig. 4.4c shows clear evidence of boundary pinning.

Figures 4.4a and 4.4b are clear examples of the typically reported bainitic-microstructure of SA508 Gr. 3 alloys, where long rods, commonly Fe_3C, are found along the lath boundaries and fine needle-like shaped precipitates, Mo_2C, distributed inside the laths.

Diffraction pattern analysis proves the existence of cementite particles in the microstructure as seen in Fig. 4.5. Unfortunately, the presence of the smaller Mo_2C was not revealed in the TEM diffraction pattern.

Scanning transmission electron microscopy (STEM), compositional mapping and energy dispersive X-ray analysis established the molybdenum content of the needle-like precipitates, Fig. 4.6.

Figure 4.7 compares the compositional characterisation of the precipitates, confirming cementite as the long rod precipitates at the lath boundaries and the molybdenum carbides as the needle-like inter-lath precipitates.

Hardness measurements for the as-received alloys, of 185 ± 4 HV and 192 ± 7 HV

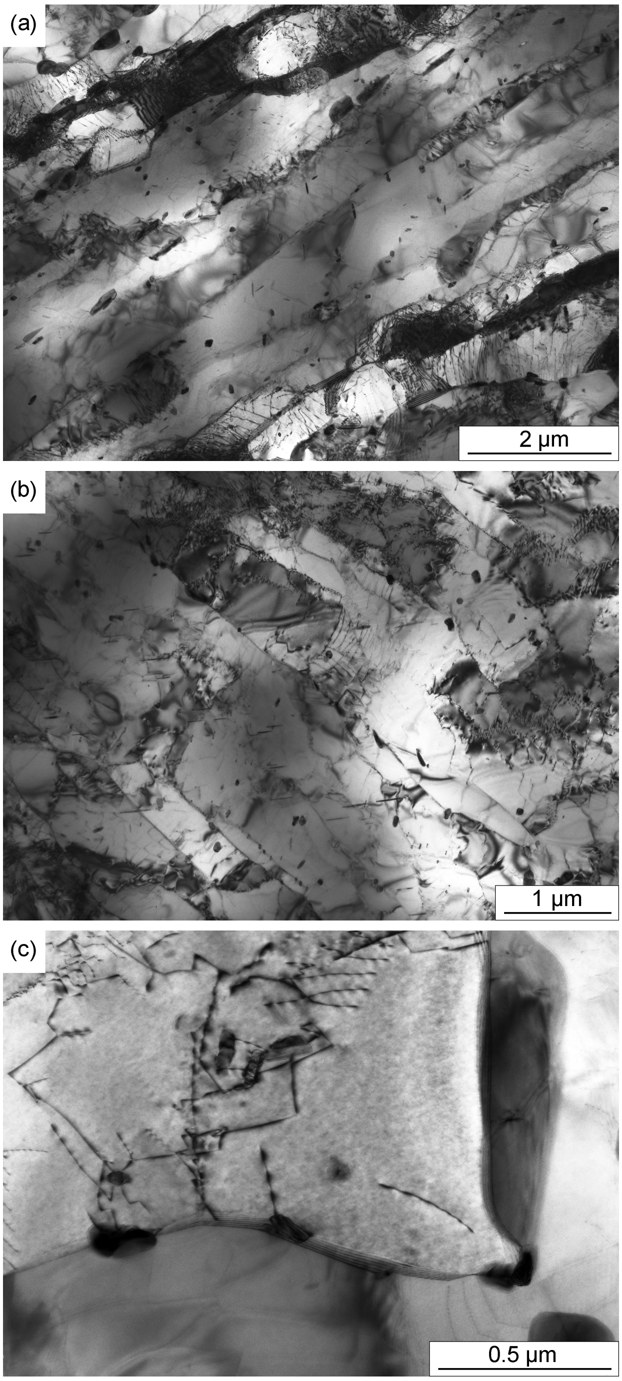

Figure 4.4: TEM micrographs as-received material. a) High density of organised dislocation arrays. b) Bainitic boundaries at sub-micrometre thickness. c) Evidence of boundary pinning.

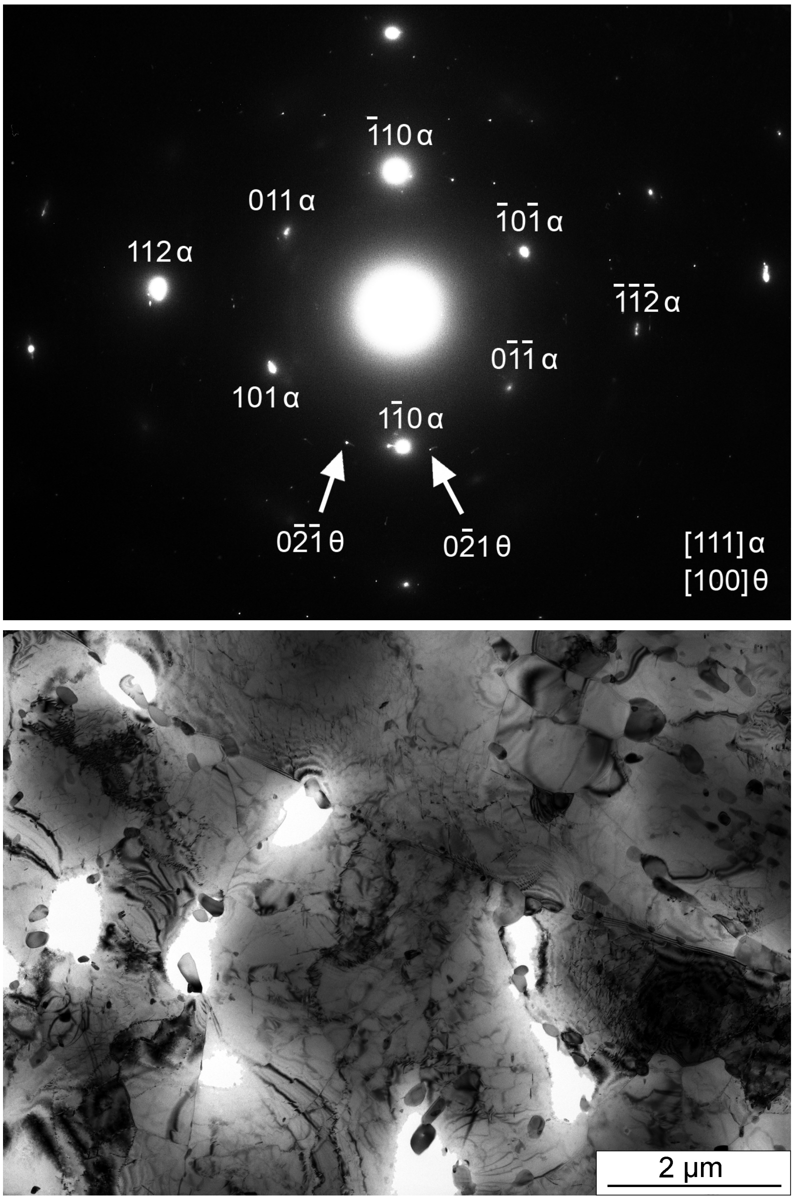

Figure 4.5: Diffraction pattern as-received SA508 Gr. 3 steel, showing ferrite (α) and cementite (θ).

for Alloys A and C respectively, are in agreement with values for SA508 Gr. 3 steels after the quality heat treatment reported in the literature of 196 ± 5 HV [43, 44, 52]. As Alloy B has not been subjected to a severe tempering the hardness in the as-received condition is significantly higher, 220 ± 5 HV.

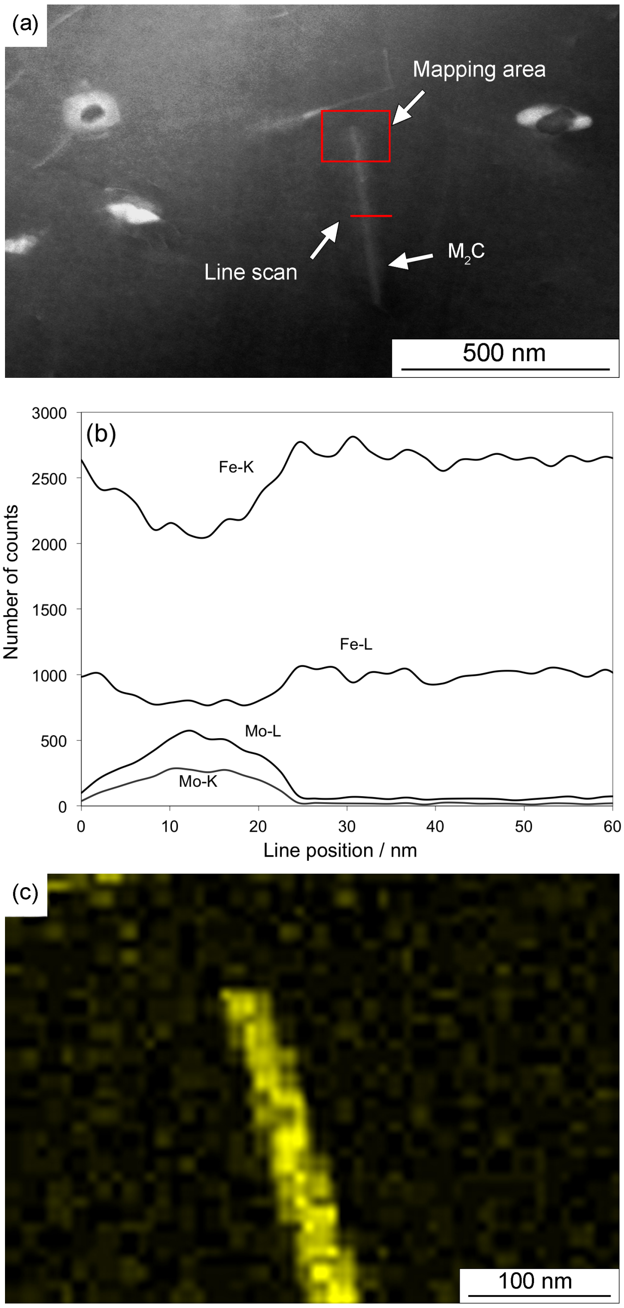

Figure 4.6: a) Needle-like shaped M_2C precipitate. b) Compositional variation of Mo and Fe across the line of scan. c) Mo compositional mapping, showing large amounts of Mo in the needle-like precipitate.

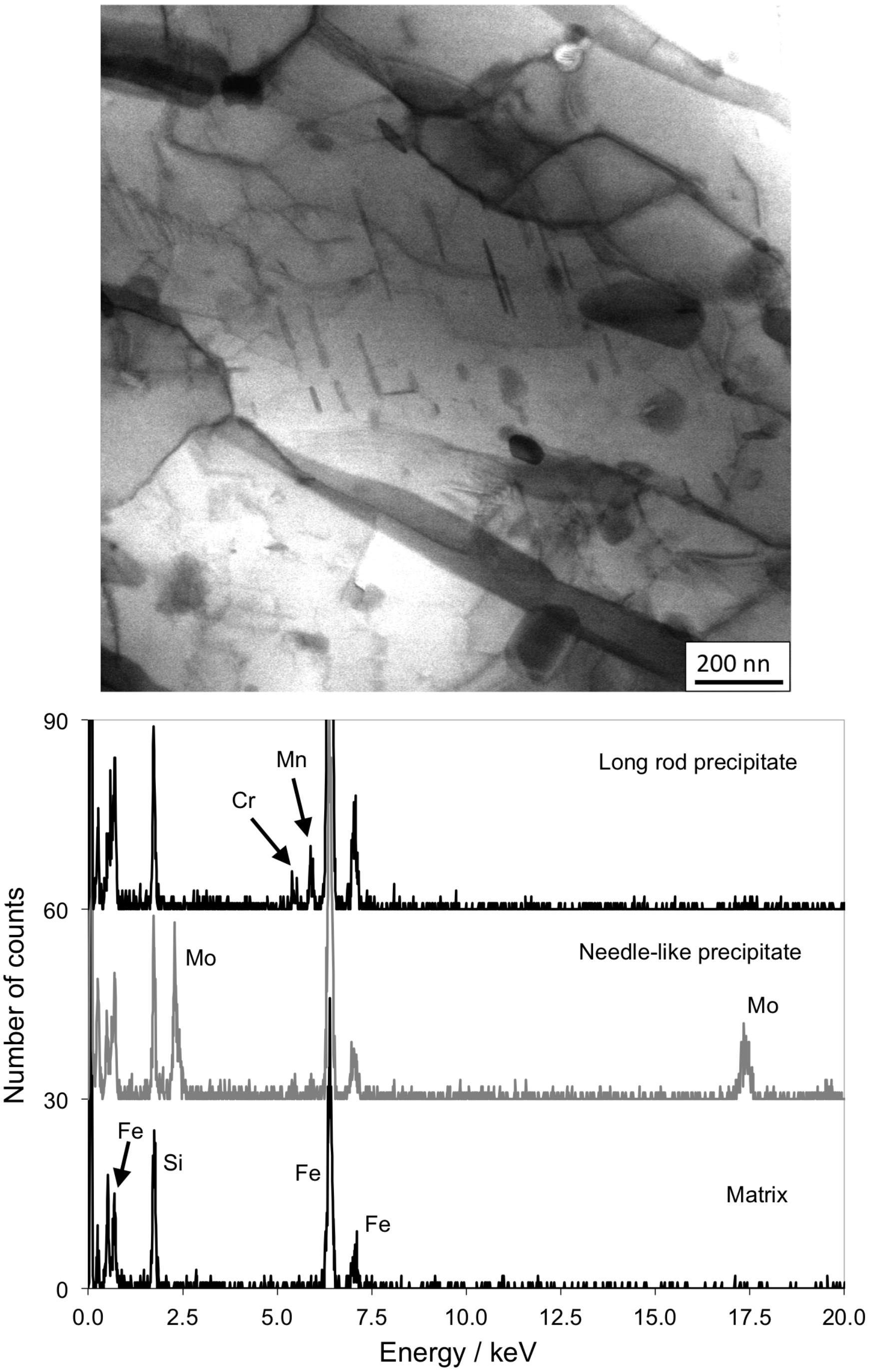

Figure 4.7: STEM EDX analysis of precipitates in Alloy A.

4.2 Austenitising

The first step in the quality heat treatment of nuclear pressure vessels is to heat the component into the fully austenitic region.

Table 4.3: Marshalls reagent composition. Parts A and B are mixed in equal quantities.

Part	Composition
A	5 ml sulphuric acid; 8 g oxalic acid; 100 ml water
B	30% solution hydrogen peroxide

There is a lack of information on the austenitising process of SA508 Gr. 3 steels, a key feature of the heat treatment. An understanding of this is important in achieving the optimum austenite grain size, which in turn influences the hardenability and consequently determines the final properties of the steel [70–72]. Therefore, the influence that the processing parameters, holding temperature and time, have on the austenite grain size need to be understood.

4.2.1 Revealing austenite grain boundaries

It was necessary to find a suitable technique to reveal austenite grain boundaries after different austenitising conditions.

4.2.1.1 Chemical etching

Saturated picric acid solutions have been reported as a suitable technique to reveal austenite grain boundaries in low alloy steels [71, 117]. However, due to safety regulations this etchant cannot be used at the University of Cambridge without a lot of difficulty and tedious procedures. An alternative to picric acid is Marshall's reagent (Table 4.3) which has been applied successfully to reveal austenite grain boundaries in steels [118]. As seen in Fig. 4.8 this etchant reveals features inside the grains, but is not able to clearly delineate grain, discarding chemical etching as a method to reveal prior-austenite grain boundaries.

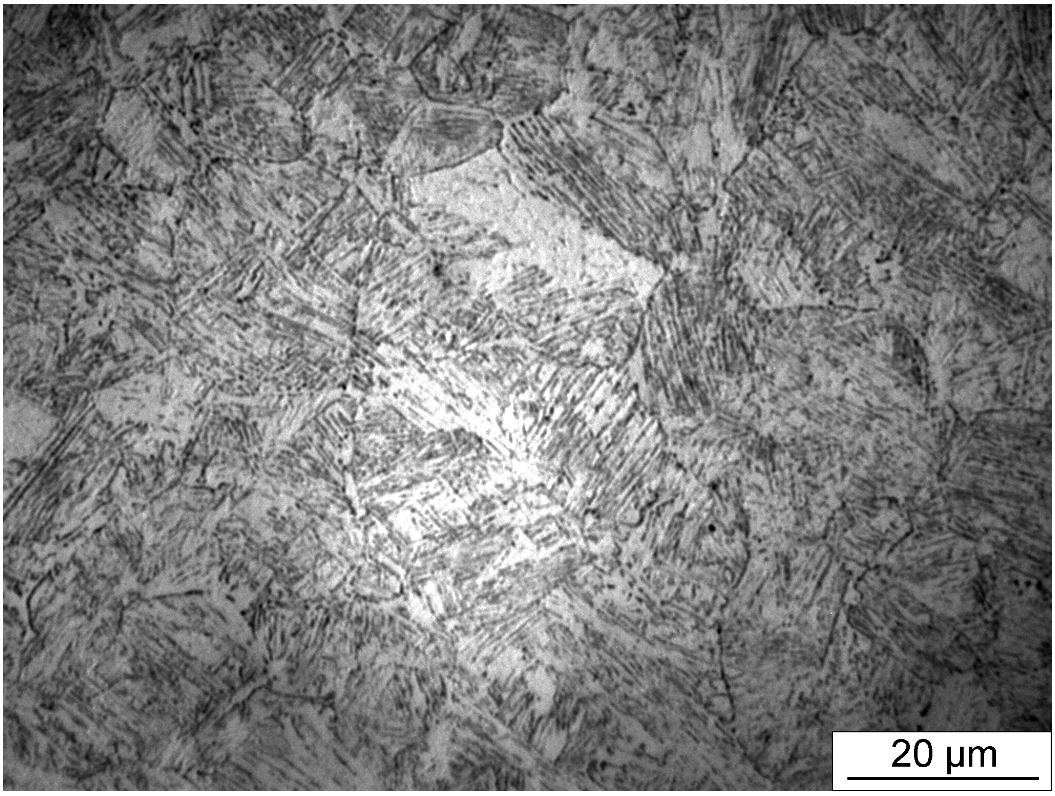

Figure 4.8: Unclear delineation of grain boundaries with Marshall's reagent on SA508 Gr. 3 steel.

4.2.1.2 Electron back-scattered diffraction

EBSD is based on the acquisition of diffraction patterns from the sample to identify the crystallographic orientation relative to the sample frame of reference. Grain size analysis uses changes in crystallographic orientation between neighboring grid points of greater than a defined minimum, typically 10 °, to determine the position of grain boundaries [119, 120].

In EBSD analysis, the results are very dependent on sample preparation. Figure 4.9 shows poor sample preparation resulting in low values of indexation, with black dots in the areas where the crystallography was not resolved. Furthermore, due to the apparatus characteristics significant and accurate results can be very time consuming. Therefore, this method is not efficient, to reveal austenite grain boundaries when large quantities of data are required.

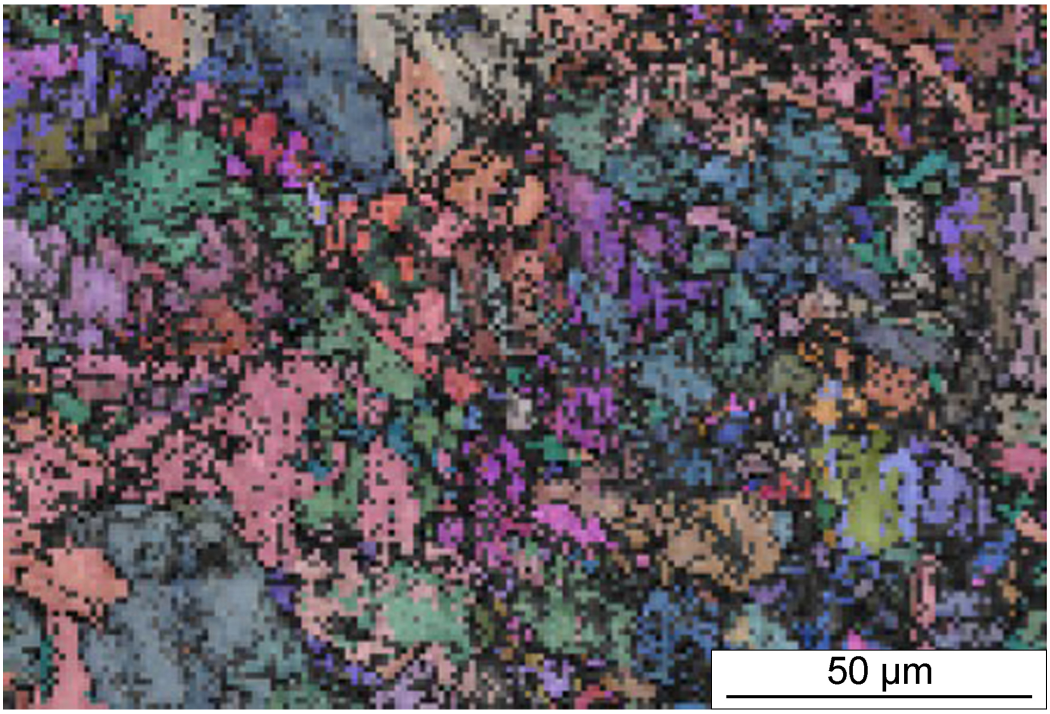

Figure 4.9: EBSD micrograph of SA508 steel austenitised at 910 °C for 10 h.

4.2.1.3 Thermal etching

Thermal etching has been reported as a suitable technique to reveal austenite grain boundaries [107, 113]. However, there may be a possible inhibition of the motion of grain boundaries by the thermal grooves. Work by Mullins, more than 50 years ago, associated the presence of ghost traces[1], with a spasmodic sliding of the thermal grooves [121]. This effect is associated with austenite grain mobility, which decreases as the grain size increases; hence ghost traces are more likely to appear at long austenitisation times or high temperatures. When the ghost traces occurred, differences between the inner and outer grain size on the sample surface could be found. García de Andrés et al., in recent work, examined whether the surface grooves resemble the grain boundaries in the bulk of the materials. They concluded that the measurement of austenite grain size is not significantly affected by the spasmodic advance of grain boundary associated with the presence of ghost traces in the thermal etching procedure [107].

---

[1] Thermal grooves produced at the grain boundaries in positions they formerly occupied.

Thermal etching was found to be a suitable technique to reveal the austenite grain boundaries in SA508 Gr. 3 steel. Furthermore, the fact that ghost lines are not observed and that this technique also shows the bainitic laths arrested at the thermal grooves, indicates that the real grain size is being revealed, Fig. 4.10.

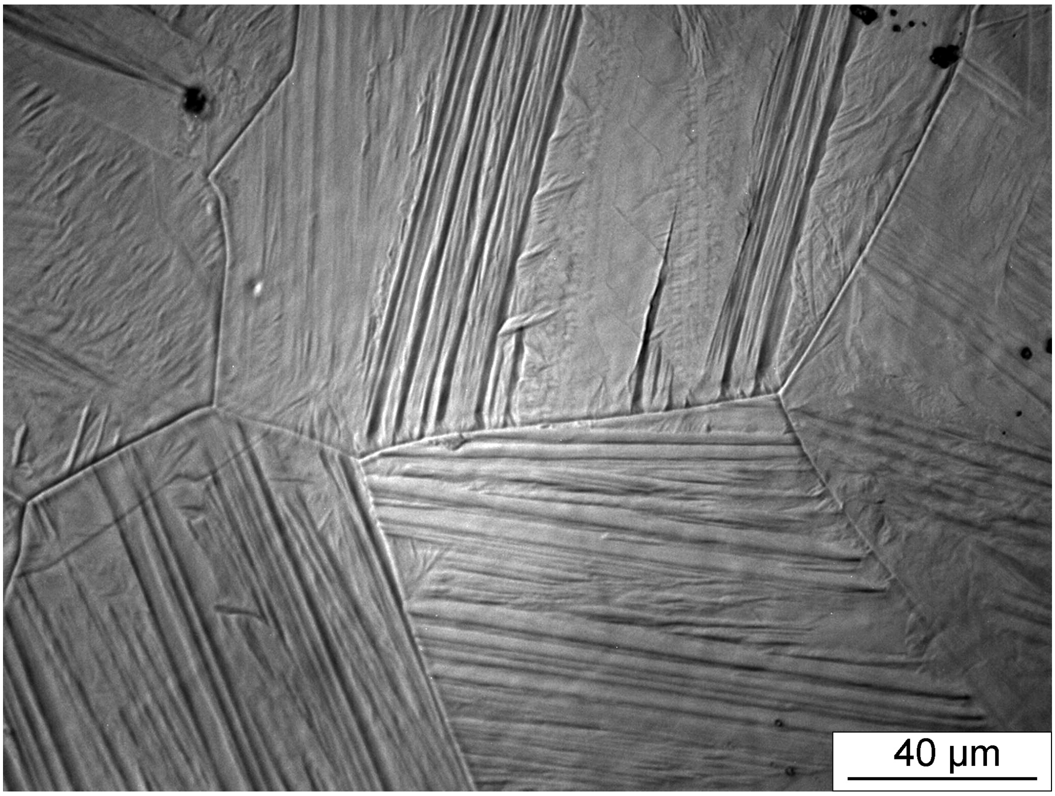

Figure 4.10: Thermal etching micrograph revealing austenite grain boundaries and bainitic laths arrested at the austenite grain boundaries. Sample austenitised at 1150 °C for 10 min.

For these reasons, thermal etching was selected as the technique of choice to reveal the austenite grain boundaries for the different heat-treatment conditions.

4.2.2 Austenite grain growth behaviour

A total of 65 tests were performed across the three SA508 Gr. 3 alloys at different austenitisation conditions to study the effects of time and temperature on austenite grain growth. Test temperatures were selected, with the aid of thermodynamic calculations using MTDATA, to heat the samples into the fully austenitic region, Fig 4.11. From these calculations, equilibrium transformation temperatures, Ae_1 and Ae_3, are 660 °C and 803 ± 6 °C, respectively. A large range of holding times was selected to study the austenite grain growth covering industrial austenitisation times.

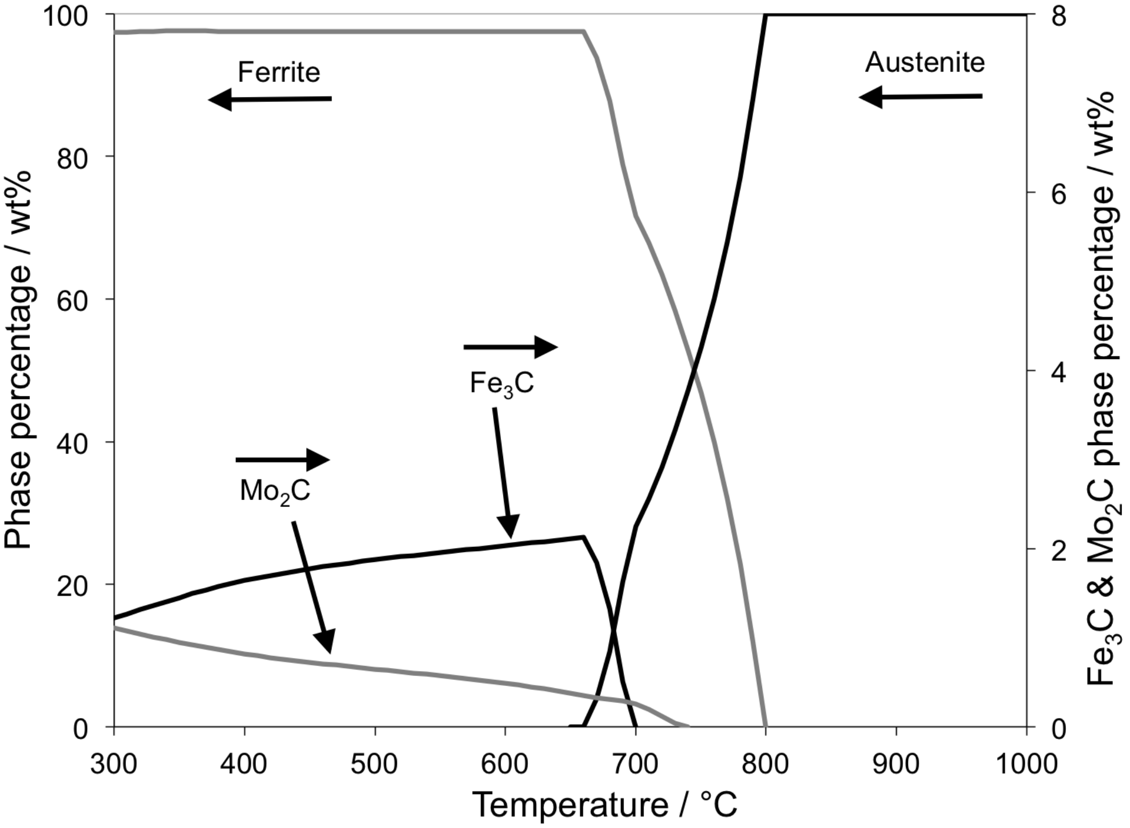

Figure 4.11: Equilibrium phase diagram of SA508 Gr. 3 Alloy A. Only ferrite, austenite, Fe_3C and Mo_2C were allowed to exist. Components: C, Mn, Si, Ni, Cr, Mo and Fe.

Initial experimental results of Alloy A on the austenite grain growth behaviour as a function of temperature are presented in Fig. 4.12. There is a moderate increase of grain size for temperatures up to 910 °C, e.g. ∼13 µm increase after 12 h at 910 °C. However, at 940 °C the size increases significantly, doubling when compared with the lower temperature results. Fig. 4.13 presents thermal etching images revealing the differences in austenite grain growth kinetics. A recent work from Lee et al. on SA508 Gr 3 steels reported, but did not investigate, a very similar phenomenon with reported grain sizes of 25 μm for austenitisation temperatures of 880 °C during 6 and 8 h and a much larger 60 μm after holding at 960 °C for 8 h [67].

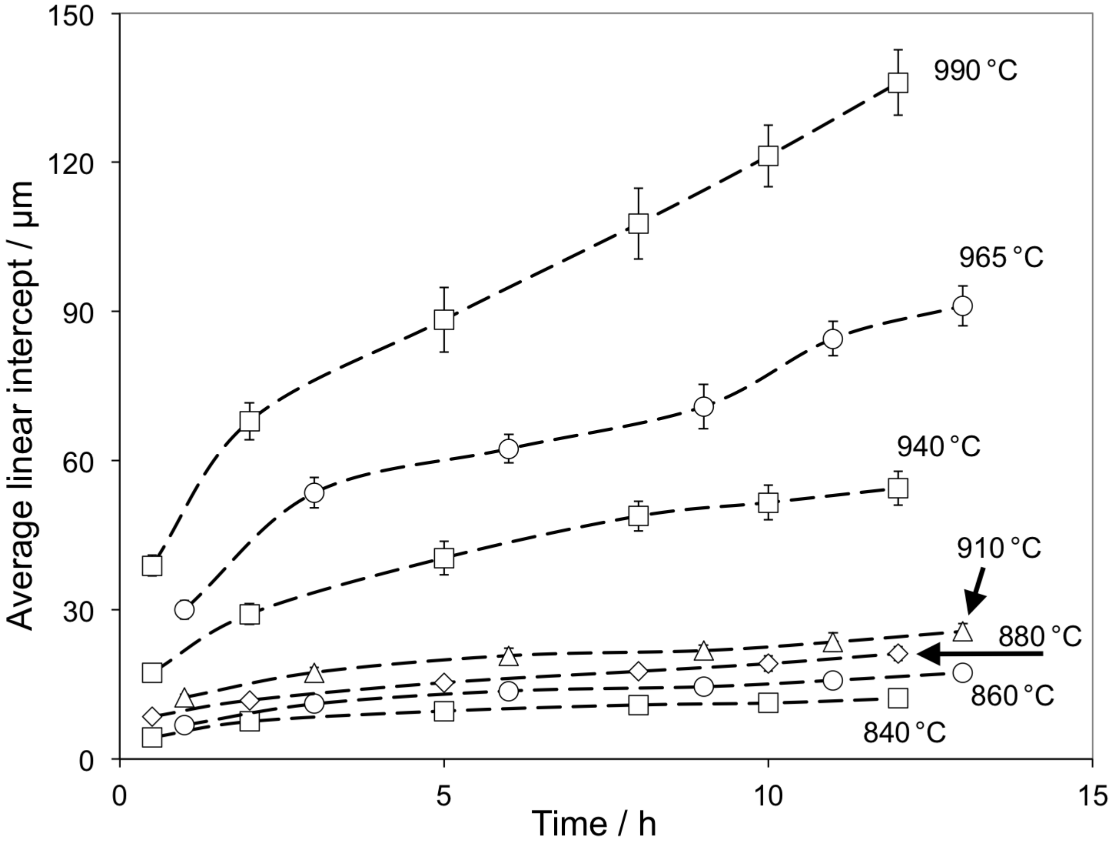

Figure 4.12: Isothermal grain growth behaviour of austenite in Alloy A.

The sudden change in grain growth behaviour, observed here at 940 °C, is typical of cases where a distribution of pinning particles dissolves, permitting a reduction in Zener drag. These particles, if they exist, have not been reported in the nuclear pressure vessel steel of the type studied here in the context of the austenitisation heat treatment (for example in [25, 35, 37–41, 43–48, 67, 68]).

To investigate further the possibility of pinning particles consistent with the austenitisation temperatures studied, a phase diagram calculation was conducted

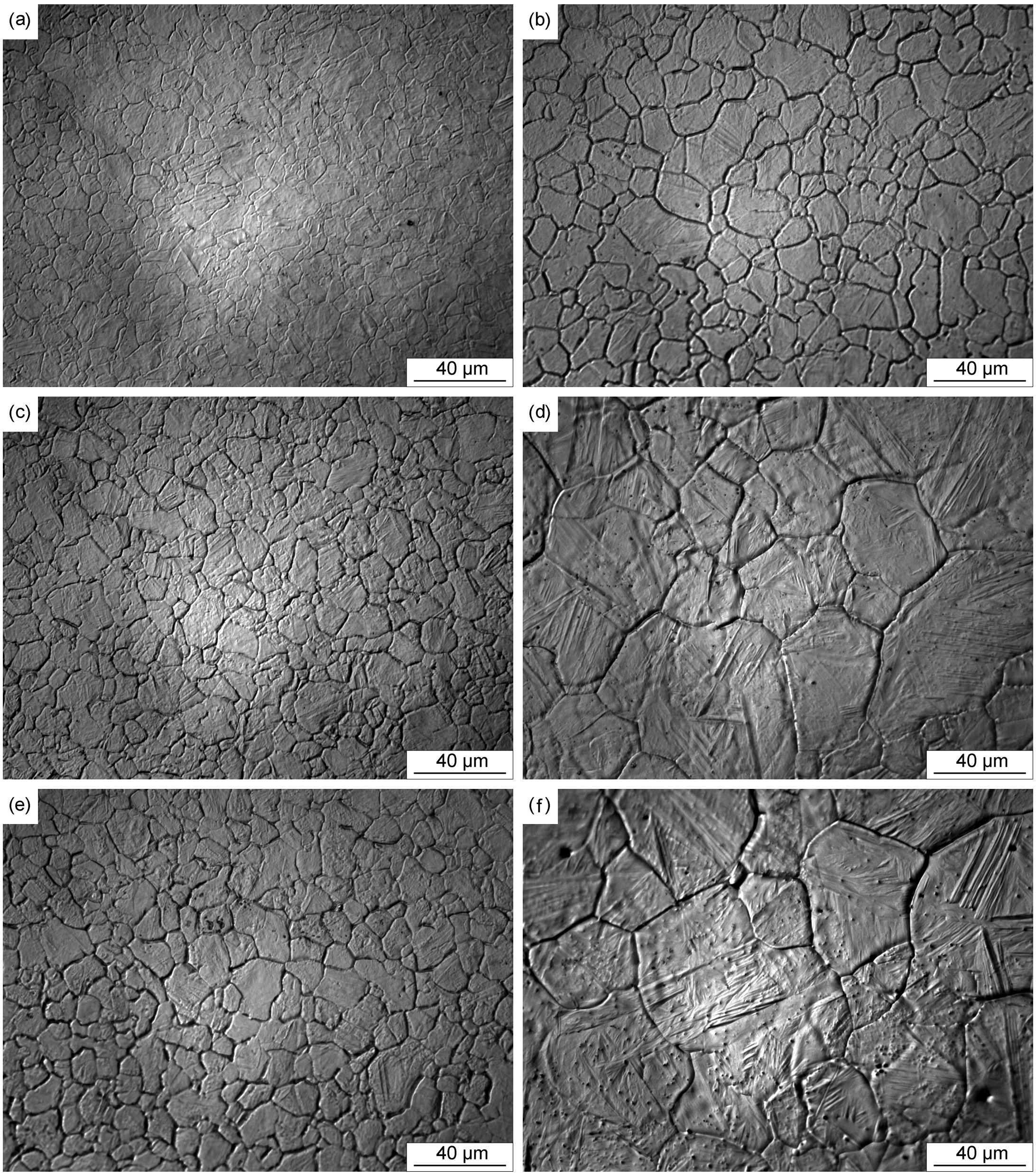

Figure 4.13: Effects of austenitising condition in grain size of Alloy A. a) 840 °C for 30 min; b) 940 °C for 30 min; c) 840 °C for 5 h; d) 940 °C for 5 h; e) 840 °C for 12 h; f) 940 °C for 12 h

using MTDATA, based on the detailed chemical composition of the steel studied and permitting all the possible phases in the database. The results suggest three possibilities for precipitates stable in the temperature range of interest: AlN, MnS and TiNbCN, none of which have been observed experimentally in the steel under consideration. It is significant, however, that it is only the aluminium nitride which exhibits a significant decrease in weight fraction at temperatures around 940 °C, decreasing by a 13% from 910 to 940 °C and a total of 50% in the studied range of temperatures from 840 to 990 °C, Fig. 4.14. This decrease correlates well with the observed change in growth kinetics and as will be seen later, these calculations led to further verification experiments.

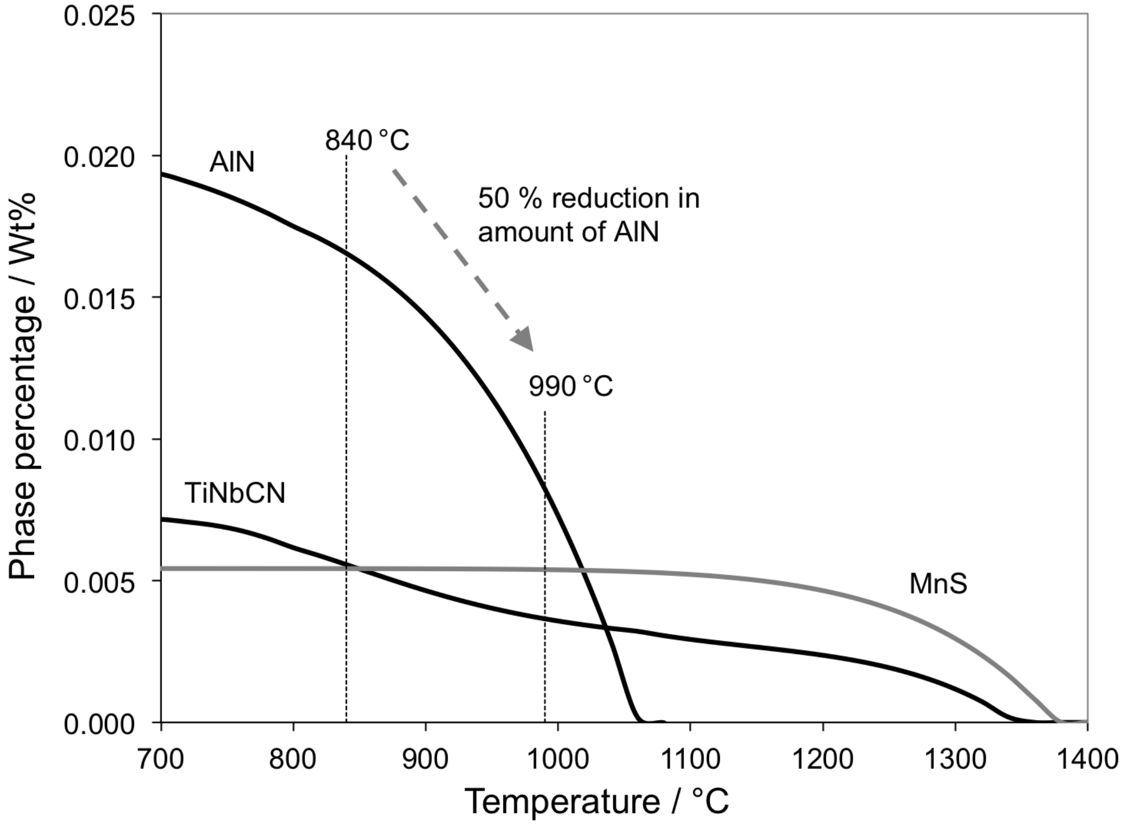

Figure 4.14: Phases in equilibrium at the austenitising temperatures in SA508 Gr. 3 Alloy A.

Table 4.4: Lattice parameters of hexagonal AlN.

a / nm	c / nm	Ratio c / a	Ref.
0.311	0.4978	1.601	[123]
0.312	0.499	1.599	[124]
0.311	0.4975	1.600	[124]
0.311	0.4978	1.601	[125]
0.311	0.4975	1.600	[126]
0.3110 ± 5	0.4965 ± 8	1.596	[127]

4.2.3 AlN in SA508 Gr 3 steels

Aluminium nitride occurs as a white translucent crystalline material of density 3.2 $\mathrm{g\,cm^{-3}}$. The equilibrium crystallographic structure of AlN is hexagonal of the Wurtzite structure with 2 mol / unit cell [122, 123]. Table 4.4 summarises published data on the lattice parameters for AlN in austenite. A summary of the properties and effects of AlN in steel can be found in the extensive review by Wilson and Gladman [122].

The most significant effect of AlN precipitates in steel is in austenite grain size control. There is clear evidence to this effect for low-alloy steels unrelated to the nuclear industry, of the relationship between the austenite grain size and the pinning effect of AlN precipitates [128, 129]. The behaviour reported is similar to that observed here, grain growth retarded by Zener drag at relatively low temperatures, between 950 - 1100 °C with very little grain growth ~40 μm after 10 min. This is followed by a large acceleration when the nitride is rendered ineffective by partial or complete dissolution at elevated temperatures, a fast grain growth of ~200 μm after 10 min was reported at 1150 °C; wt% levels of Al and N were 0.04 and 0.0052, respectively [128]. This response is in contrast to the gradual increase in grain coarsening rate as temperatures are increased in steels without aluminium [129]. The transition between gradual and sudden changes in growth rate is often designated loosely by the term *coarsening temperature*[1] [129].

To analyse the effect of high austenitising temperatures on SA508 steel, Alloy A samples were heated to 1150 °C for 10 min. The measured austenite grain size was 126 ± 10 µm. This coarse size is in agreement with the expected enlargement of austenite at high temperatures due to the suggested complete dissolution of AlN [122, 128, 129]. These experimental observations for the dissolution temperature of AlN coincide with reported values for the complete solution of AlN, as seen in Fig. 4.15. It has been found that AlN dissolves quickly at temperatures between 1000 and 1100 °C causing a drastic decline in the local pinning forces which may give rise to more pronounced abnormal growth [130].

However, it has been proven that grain coarsening temperatures occur at temperatures below those required for solution of the precipitate particles, and as function of aluminium content, Fig. 4.16 [129]. This effect is due to the reduction in the amount of particles and hence the decrease in the pining force exerted giving rise to grain coarsening. From this figure, it can be seen that the predicted grain coarsening temperature for Alloy A which contains 0.0145 wt% Al, corresponds with a temperature is in the region of 940 °C, which is consistent with the experimental data presented in Fig. 4.12. Although, it is emphasised that this temperature should be also influenced by the amount of nitrogen not only the aluminium.

AlN is slow to precipitate during cooling through the austenite range from solution treatment temperatures, being largely retained in solution at all cooling rates in the austenite range, and is even relatively slow to precipitate in the ferrite during cooling. Consequently AlN is largely precipitated during subsequent reheating and holding to austenitising temperatures [122, 129]. This precipitation is fairly rapid, thus complete precipitation has been observed after 10 min at 950 °C [122].

Kinetic analysis of AlN precipitation reveals that precipitation in austenite

---

[1] Coarsening temperature: that at which there is a rapid growth in grain size.

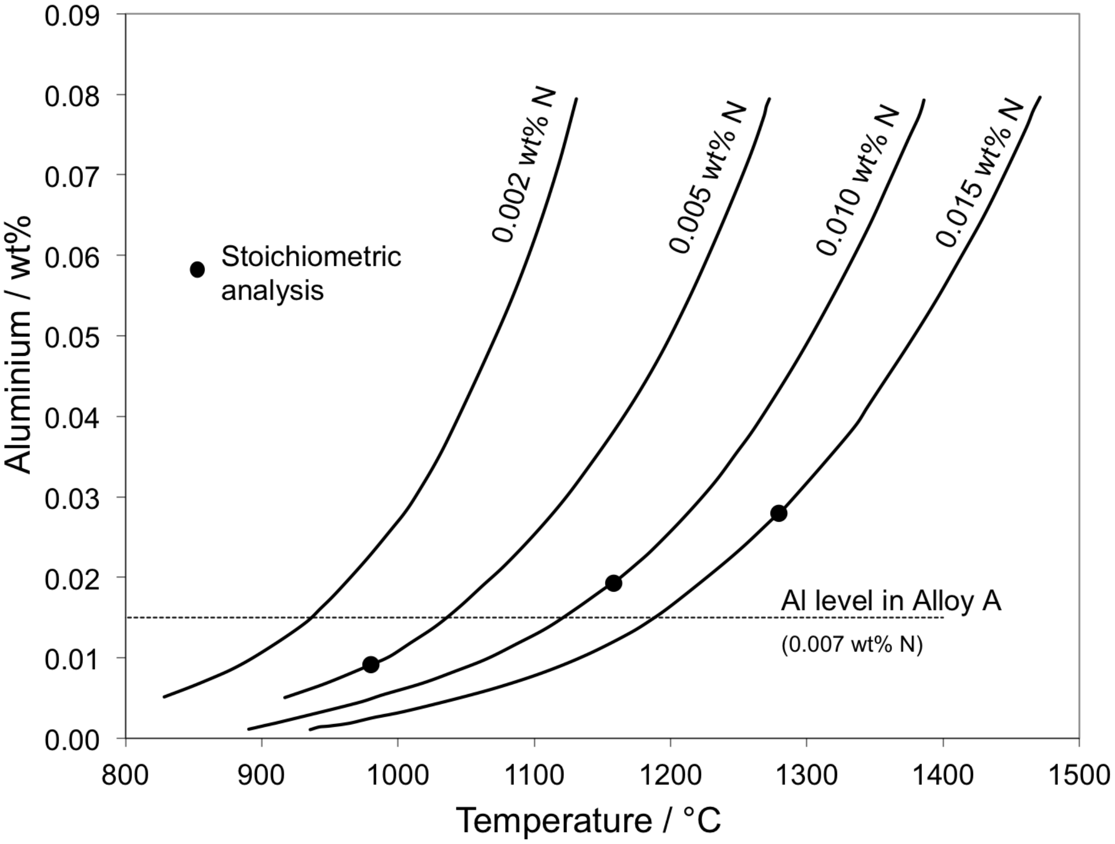

Figure 4.15: Effect of Al and N content on temperature of complete solution of AlN. Adapted from [122].

occurs predominantly at grain boundaries due to the considerable volumetric misfit (71 - 77%) between the AlN and the steel matrix [122, 123, 131, 132], Fig. 4.17. Therefore grain size control is achieved by the grain boundary pinning effect of AlN particles.

Analysis of the morphology of austenite grains reveals mostly equiaxed grains at all temperatures. At temperatures up to 910 °C there is an homogeneous distribution in grain sizes, Fig. 4.13. A change to a bimodal size distribution is observed at 940 °C and also a broadening of the range of grain sizes, which is more marked at long austenitising times, Fig. 4.18. Since 940 °C represents a temperature where the role of AlN is diminishing, the bimodal size distribution may reflect localised reductions in pinning forces associated with the heteroge-

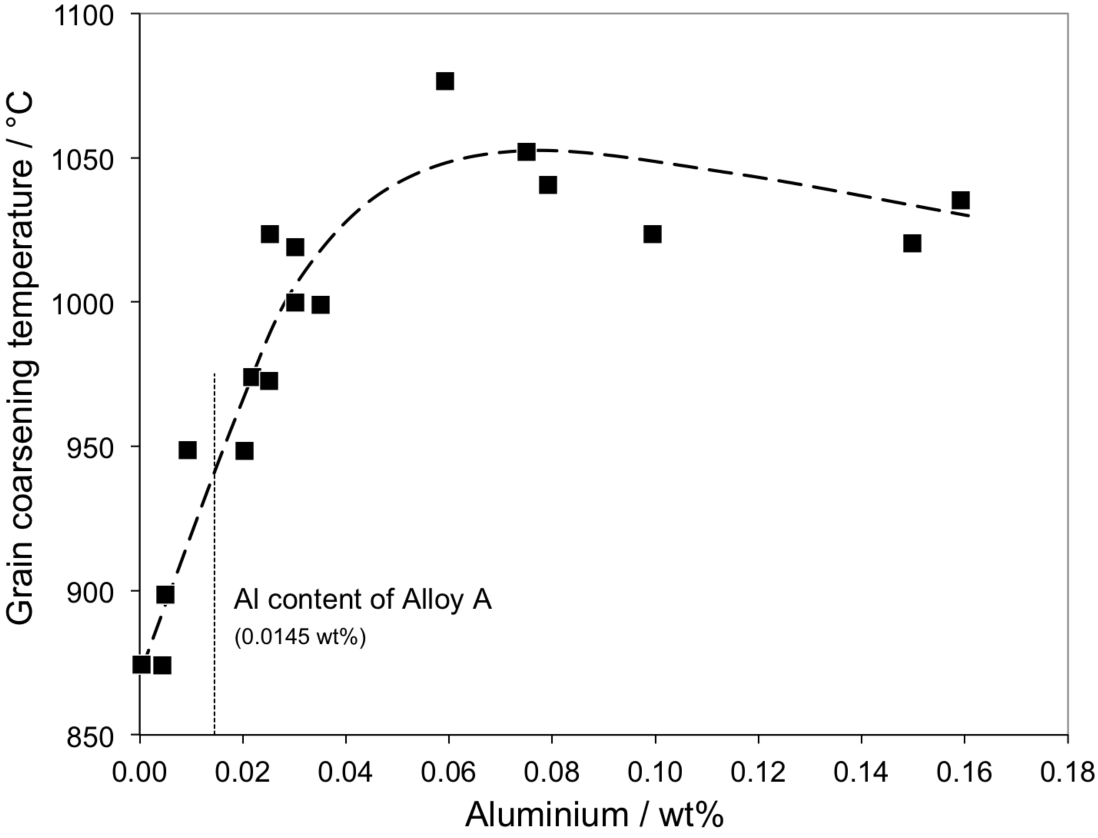

Figure 4.16: Effect of Al content on grain coarsening temperature. Adapted from [129].

neous dissolution of the nitride. Therefore, some grains coarse while others remain pinned.

All these phenomena support the hypothesis of AlN acting to pin boundaries in the SA508 Gr. 3 steel. However, it is necessary to prove the existence of these particles.

Routine X-ray diffraction failed to detect the expected minute quantities of fine AlN < 0.02 wt%, so high-energy X-ray transmission analysis was performed instead. In this case the recorded data present a much higher intensity compared with conventional XRD techniques, 20×10^3 counts compared with 1600×10^3 counts, for the largest peaks. This increases the resolution of the technique, allowing for smaller peaks to be resolved.

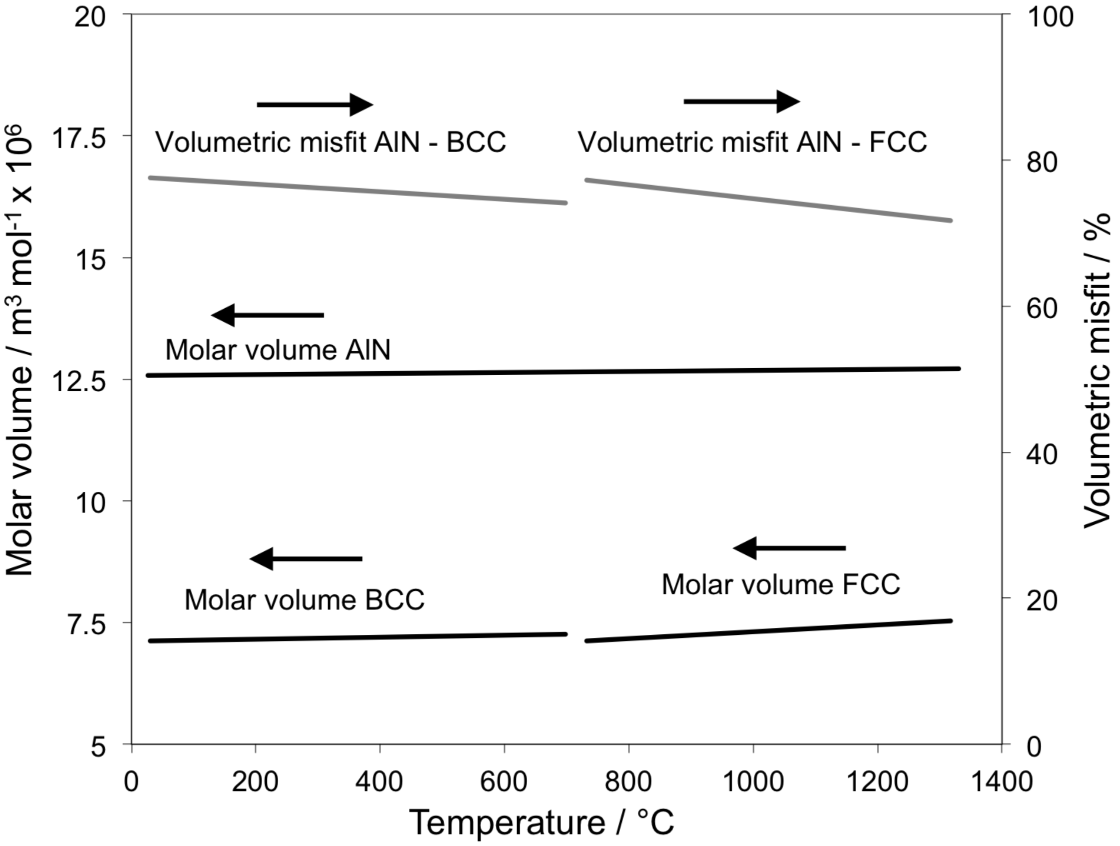

Figure 4.17: Molar volumes of the phases body-centered cubic (BCC), face-centered cubic (FCC) and AlN including the calculated volumetric misfit. Adapted from [123, 131, 132].

Figure 4.19a shows the full spectra for the analysis of the as-received Alloy A, where two large peaks of ferrite are differentiated. Figure 4.19b shows a magnified section of the spectra where the weaker but significant contributions from AlN can be resolved. These peaks are very small, due to the low amount of AlN, but are independent from the other peaks, and in particular that at $2\theta = 6.5°$ is very clear. Therefore it can be concluded that AlN precipitates are present in this nuclear pressure vessel steel. The spectrum also reveals cementite and Mo_2C precipitates in the steel. Quantitative Rietveld analysis is only possible for cementite which is 2.2 ± 0.5 vol%. Nevertheless, the identification of AlN

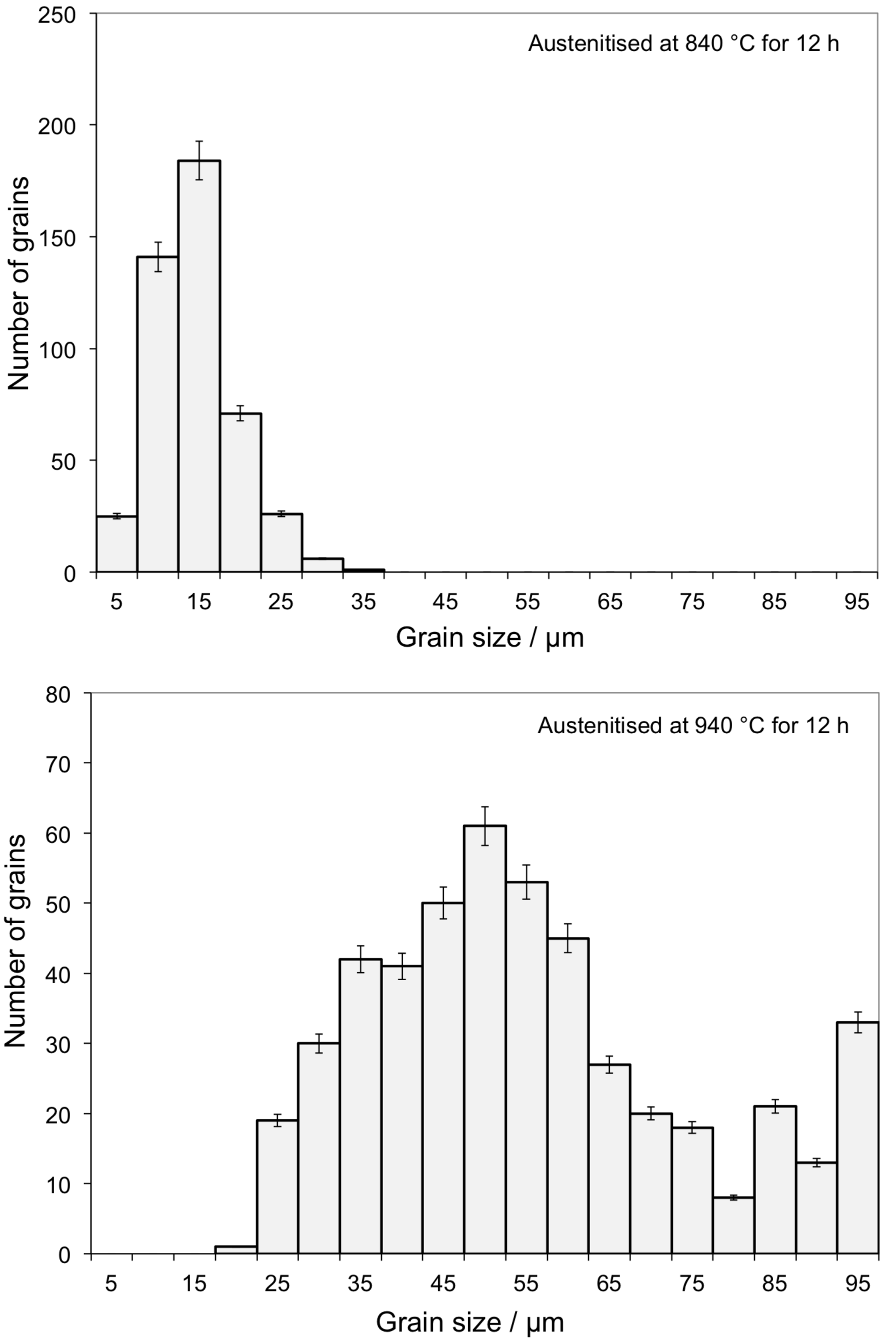

Figure 4.18: Grain size distribution of SA508 Alloy A at different austenitising conditions.

which remains stable at elevated temperatures where austenite grains are driven to grow, is significant and possibly first time that the presence of these precipitates in this steel has been established conclusively.

Indirect techniques have proved the existence of AlN in this pressure vessel steel. However, a direct observation is needed to confirm that these particles are located at grain boundaries and thus impeding grain growth.

Depending of the heating treatment and processing conditions AlN precipitates have been found in different shapes and sizes, from dendritic with several hundred micrometres in length, to finely precipitates of less than 5 nm [122].

Zener derived a model to determine the grain size in presence of second phase particles, as follows:

$$D_{Lim} = \frac{4}{3} \times \frac{d}{f_v} \tag{4.1}$$

where D_{Lim} is the limiting grain size, and d and f_v are the size and volume fraction of second phase particles, respectively.

This model presents several assumptions, such as that the particles are spherical, monosized, randomly distributed, and do not coarsen. However, it can be used to have a rough estimate of the size of the AlN present in the nuclear pressure vessel steel. Using the Zener equation, with the known data of grain size and volume fraction of AlN at 840 °C, the expected size of AlN particles is around 12 nm.

Due to the predicted small size of these particles the only viable technique to observe the precipitates is by means of transmission electron microscopy. Since AlN particles are expected to be found at grain boundaries, in order to increase the probabilities of finding the precipitates, TEM analysis are performed to samples austenitised at low temperature for short time, 840 °C for 30 min, in order to maximise the amount of grain boundary in the sample under investigation.

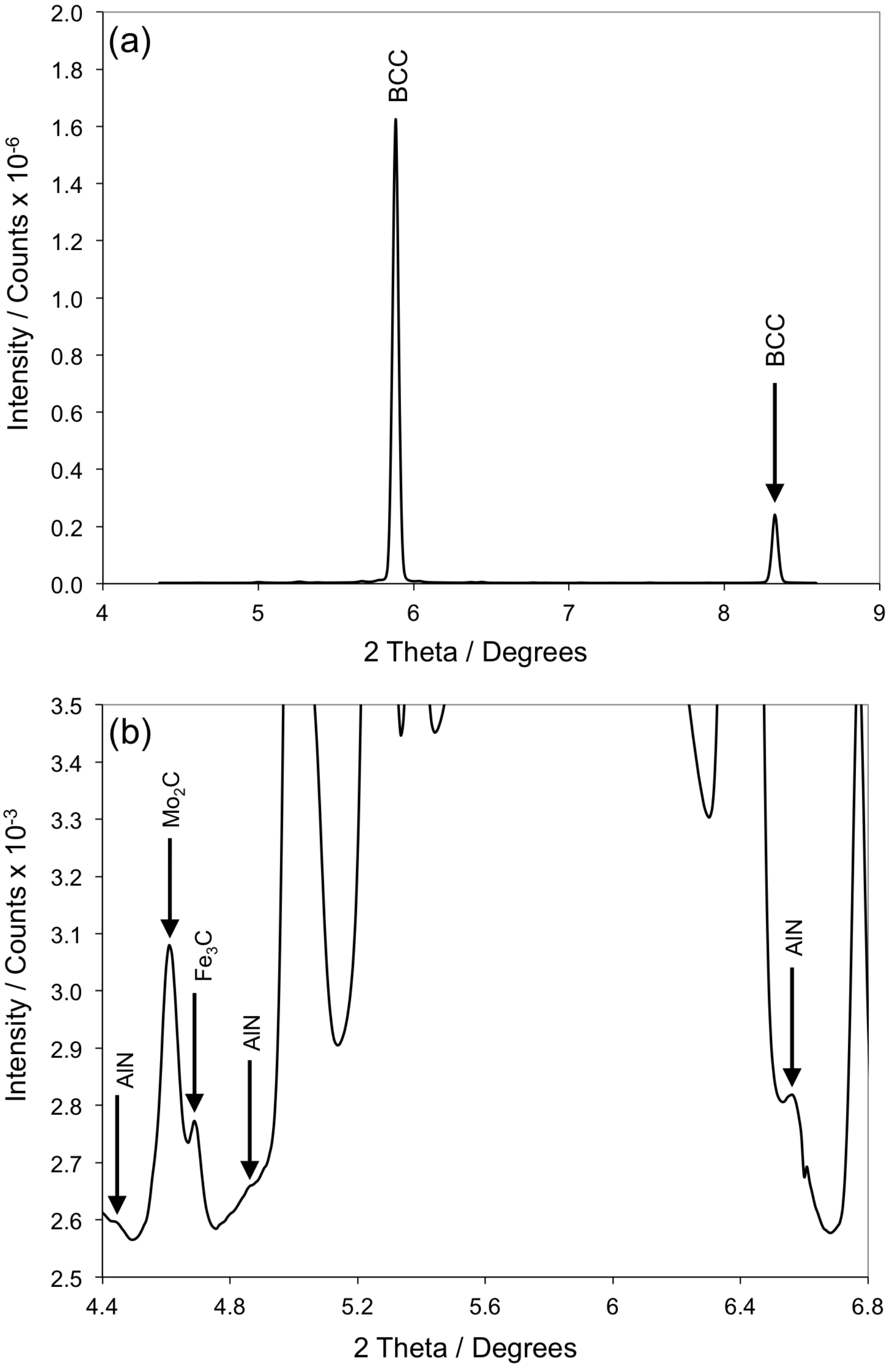

Figure 4.19: Synchrotron high-energy X-ray spectra for as-received Alloy A. a) Full spectra. b) Magnified area showing AlN, Mo_2C and cementite peaks.

Table 4.5: Aluminium and nitrogen levels of the studied alloys in wt%.

	Al	N
Alloy A	0.015	0.007
Alloy B	0.025	0.011
Alloy C	0.019	0.010

Figure 4.20 clearly reveals grain boundary precipitates in the form of hexagonal cylinders consistent with the hexagonal crystal structure of AlN. Furthermore, energy dispersive X-ray analysis confirmed that these particles are rich in aluminium, Fig. 4.21. These observations together with the thermodynamic calculations serve as a strong indicator that the particles represent AlN which is responsible for Zener pinning the austenite grain boundaries in SA508 Gr. 3 steels.

4.2.3.1 AlN effects on austenite grain size

As previously presented in Table 3.1 the compositions for the three alloys in the present work are very similar in major elements. However, there is a difference in the levels of Al and N, Table 4.5. MTDATA calculations confirm that the small differences in Al and N which might appear minor, are in fact very relevant to promote the formation of AlN, as seen in Fig. 4.22. The calculated amount of AlN in Alloy B doubles that of Alloy A at 940 °C, temperature at which this alloy experiences a sudden coarsening behaviour. Consequently, at 940 °C the nitride is still retarding grain growth in Alloy B, and the temperature has to be raised to 965 °C to observe the abrupt coarsening behaviour, as presented in Fig. 4.23.

Synchrotron high-energy X-ray spectra for as-received Alloy B, confirms again the existence of AlN in this alloy. Fig 4.24 shows the identified peaks for AlN, which in this case are more prominent than for Alloy A. This may be a confirmation of the higher amount of these particles as predicted in MTDATA.

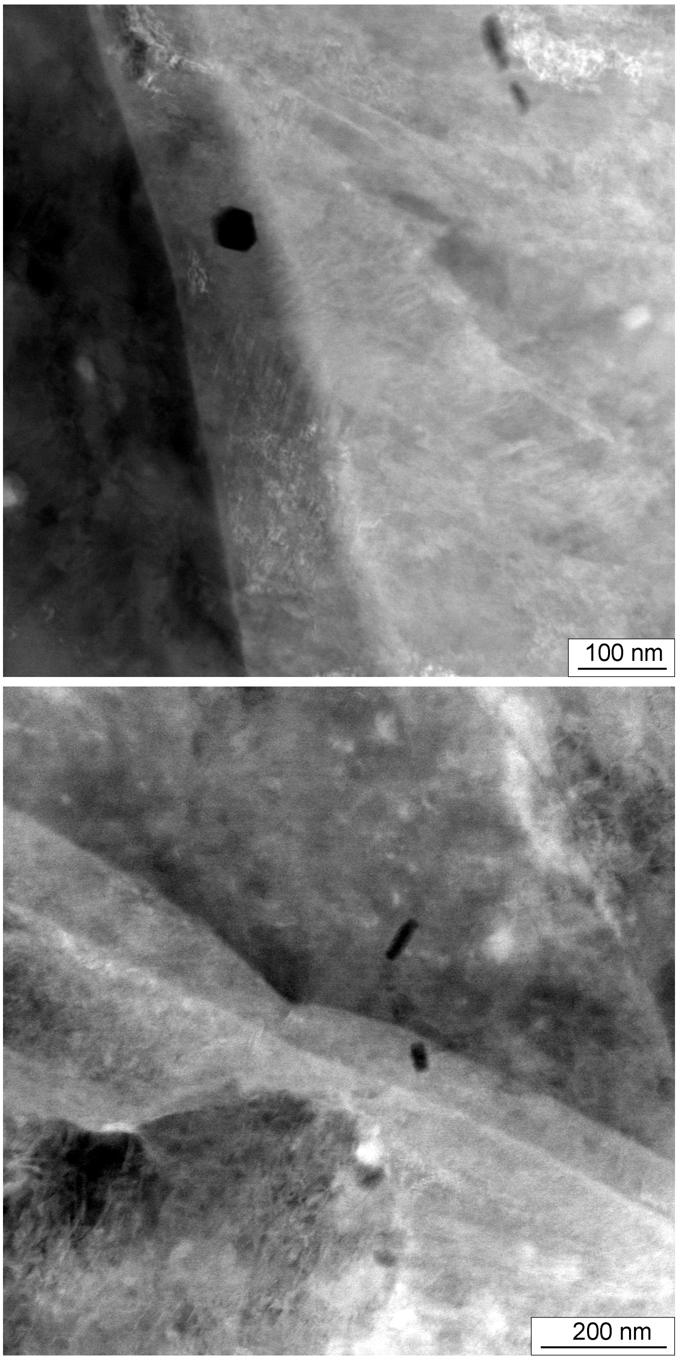

Figure 4.20: STEM micrograph of SA508 Gr. 3 Alloy A austenitised at 840 °C for 30 min, showing grain boundary precipitates.

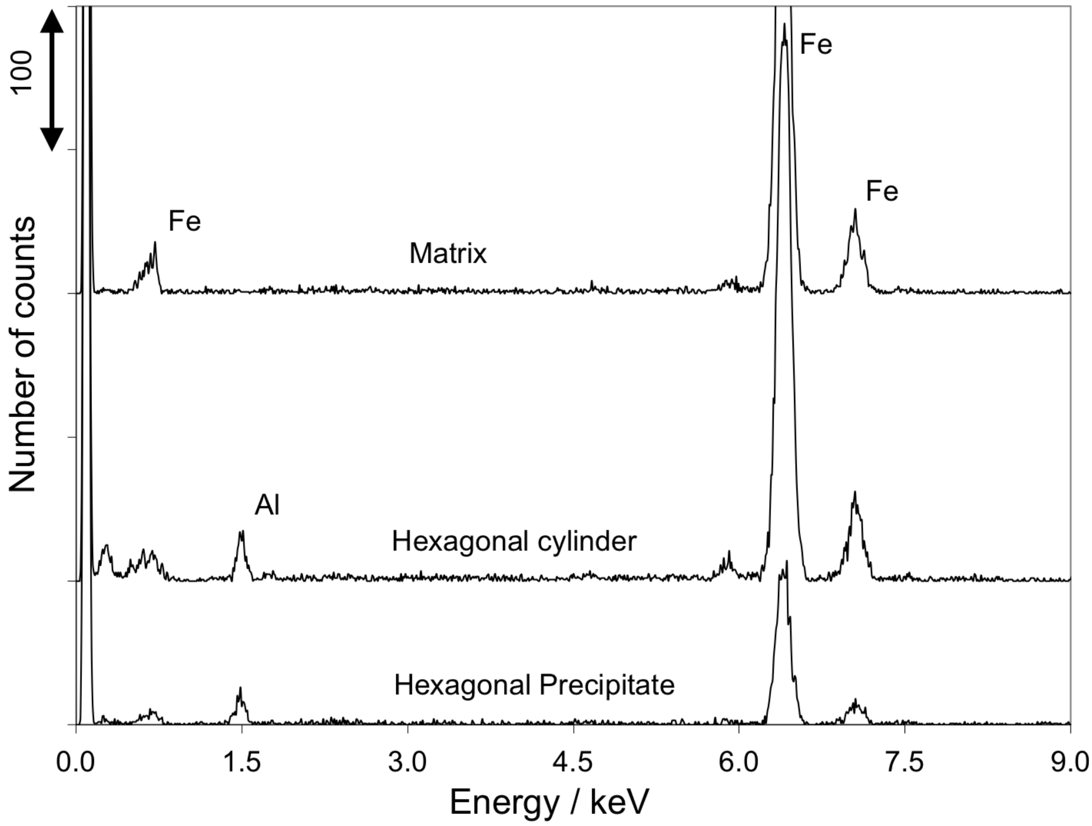

Figure 4.21: EDX analysis of grain boundary precipitates.

As seen in Fig 4.16, Gladman and Pickering proposed that the amount of aluminium would govern the coarsening temperature [129]. However, when combining measured coarsening temperature data from that investigation with data from Alloys A and B from this work and the MTDATA calculated amount of AlN a clear relationship can be observed, as presented in Fig. 4.25. This proves, that the coarsening temperature will be a function of the amount of AlN at a certain temperature, and as the amount of these precipitates increases, the range of austenitisation temperatures at which grain growth is retarded by Zener drag increases. In other words, the material has to be heated to higher temperatures in order to observe a sudden change in grain growth behaviour.

The effect of AlN controlling the coarsening temperature has been explained.

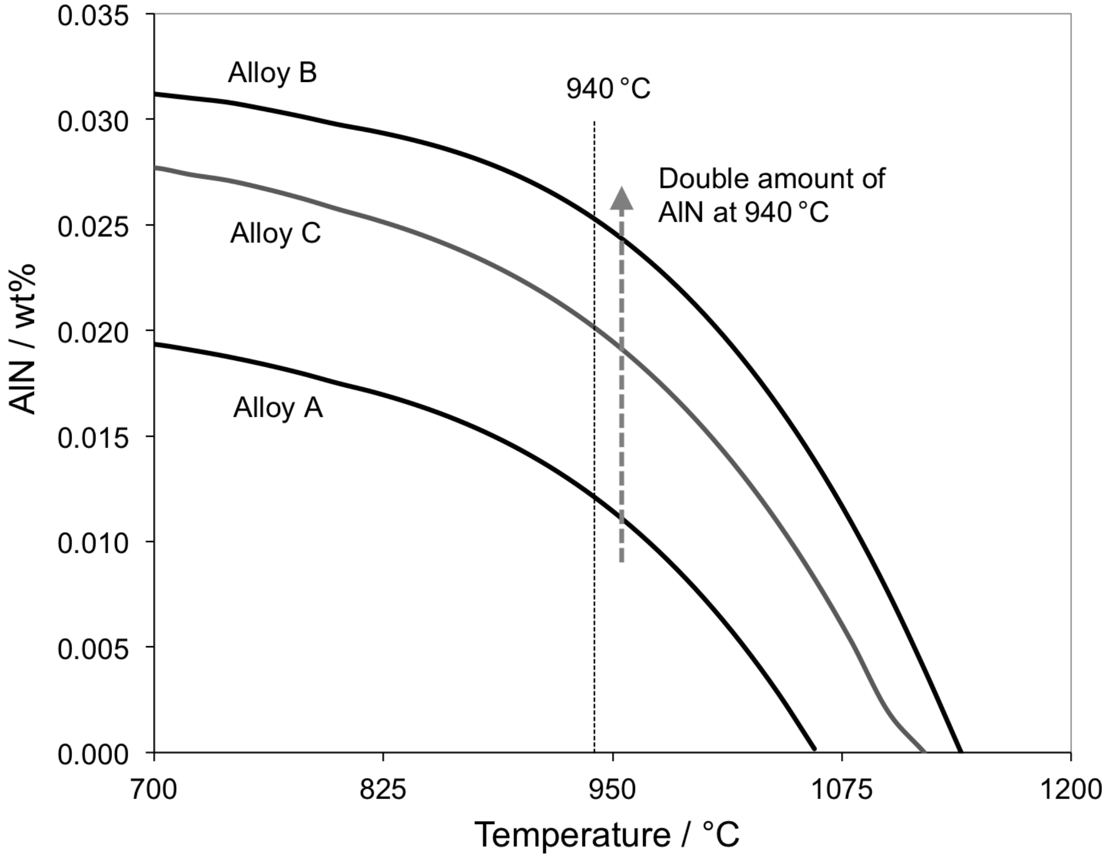

Figure 4.22: Calculated quantity of AlN in the three alloys.

Next step is to understand the role that these pining particles are having on the two distinct austenite grain growth behaviours identified, **above** and **below** the coarsening temperature.

As expected, experimental results show that above the coarsening temperature, alloys with different amounts of AlN present very similar grain sizes. At temperatures over the coarsening temperature the amount of particles is not sufficient to pin austenite grain grain boundaries, therefore the grain size in not affected by the levels of aluminium and nitrogen in the alloy. This occurrence can be seen in Fig. 4.26.

Table 4.6 shows the austenite grain sizes after several hours at temperatures

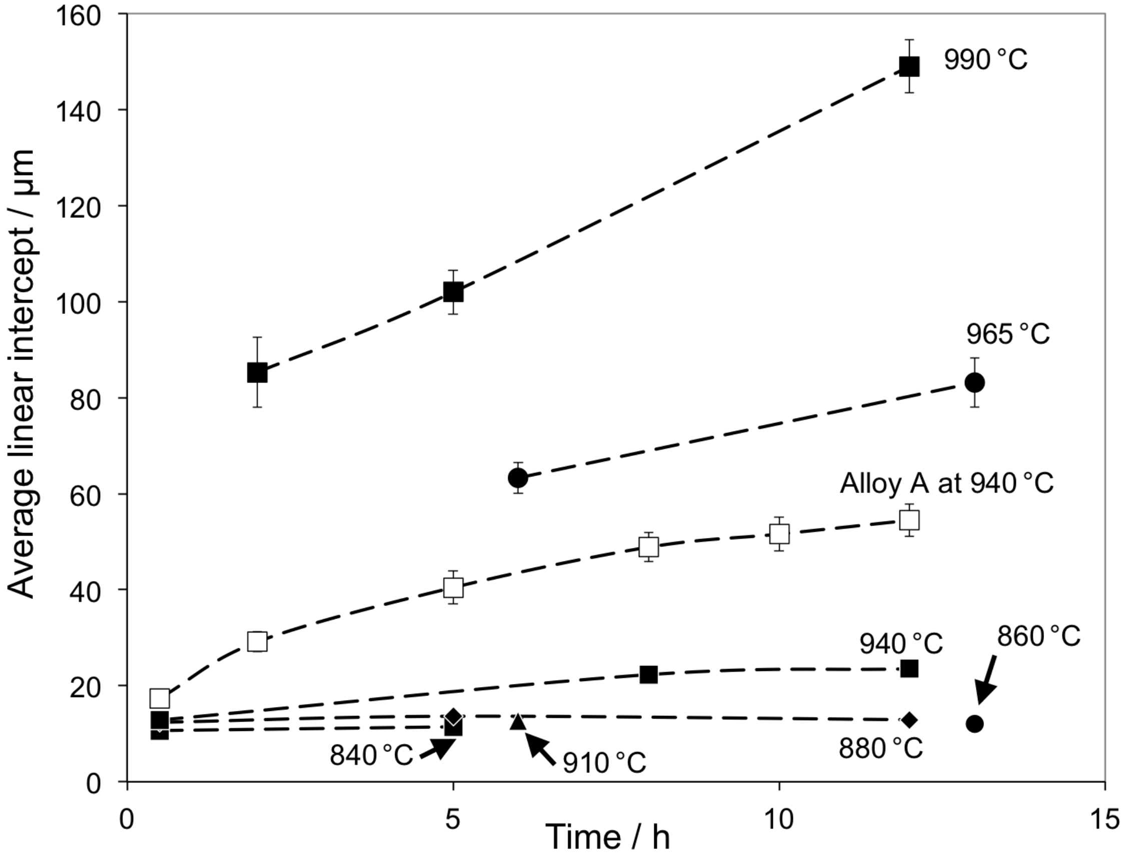

Figure 4.23: Austenite grain size evolution of Alloy B. Grain sizes at 940 °C for Alloy A are added for comparison.

below the coarsening temperature. The differences observed between the alloys are consistent with the calculated amount of AlN, Fig. 4.22, alloy A with the least AlN exhibiting the largest grain sizes. This is particularly marked at longer austenitising times, since Alloys B and C with larger amounts of AlN reach the limiting grain size sooner than Alloy A, as seen in Fig. 4.27. Therefore, it can be concluded that the main factor controlling the austenite grain size on SA508 Gr 3 alloys is the amount of AlN, which will dictate a limiting grain size at austenitisation temperatures below the coarsening temperature.

From these results, it is recommended that to avoid coarsening of the austenite grains and to maintain higher levels of toughness, austenitising temperatures

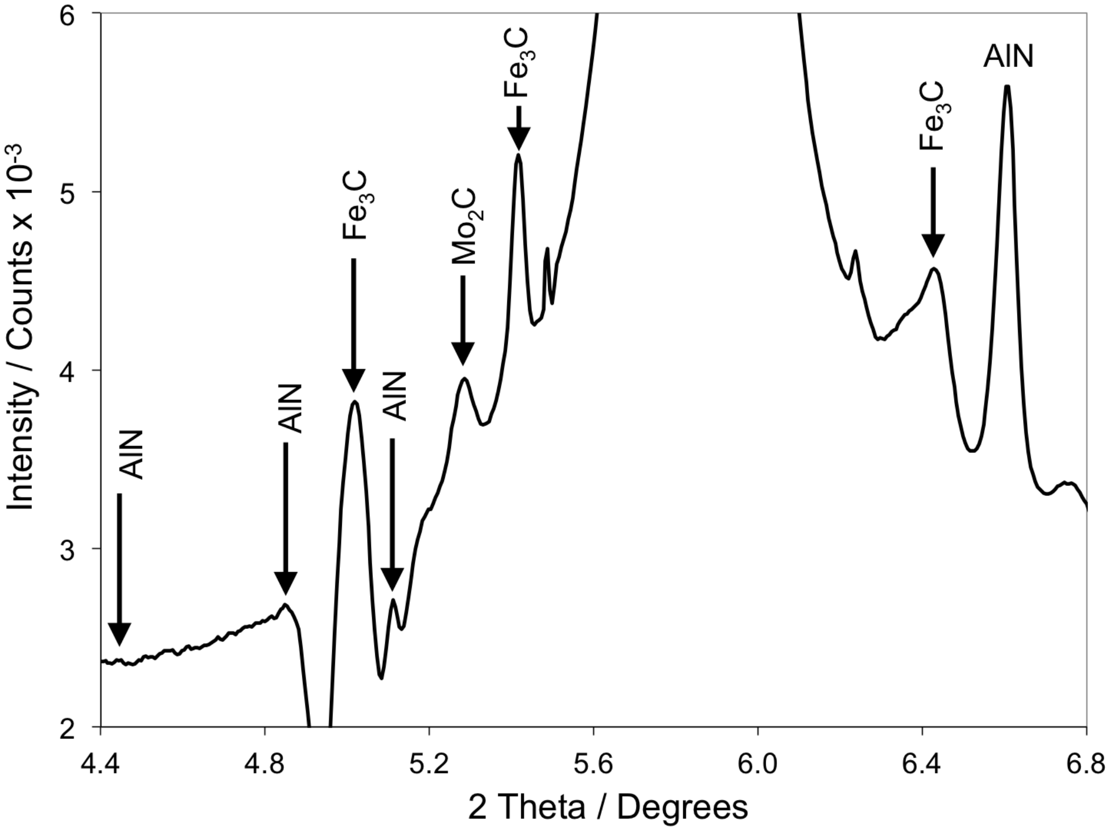

Figure 4.24: Synchrotron high-energy X-ray spectra for as-received Alloy B showing AlN, Mo_2C and Fe_3C peaks.

should be maintained below the coarsening temperature which will be function of the levels of Al and N in the alloy.

4.2.4 Modelling austenite grain growth

Sun et al. in an investigation of the hot deformation behaviour of SA508 Gr. 3 steels, reported an empirical equation to model the coarsening behaviour of the austenite, as follows [82]:

$$D = 20 + 76671 \exp\left(\frac{-93020}{RT}\right) t^{0.211} \tag{4.2}$$

where D is the grain size in microns, R the universal gas constant (8.314 J mol $^{-1}$ K $^{-1}$),

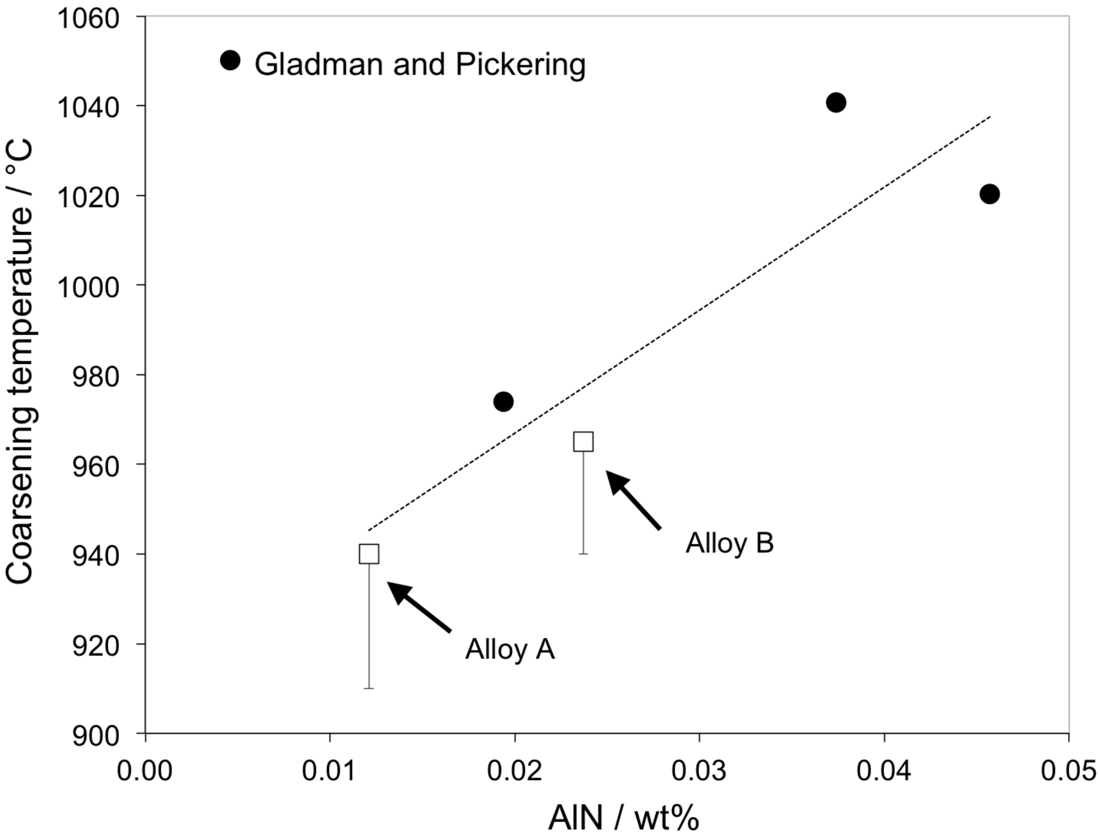

Figure 4.25: AlN effect on coarsening temperature with data from the present work and from the literature [129]. Error bars on the data from the present work are for the uncertainty of finding the coarsening temperature at temperatures between the ones tested.

T the holding temperature in Kelvin and t the holding time in seconds.

However, the authors did not include any data to verify the accuracy of the proposed model. By comparing experimental austenite grain sizes with the calculated values from Eq. 4.2, there is clear evidence that this empirical model does not properly represent the complicated austenitic grain growth behaviour of SA508 Gr. 3 steels, Fig. 4.28.

The previous model is based in an empirical equation proposed in the work of Lee et al. after the analysis of austenite grain sizes from 16 low alloy steels

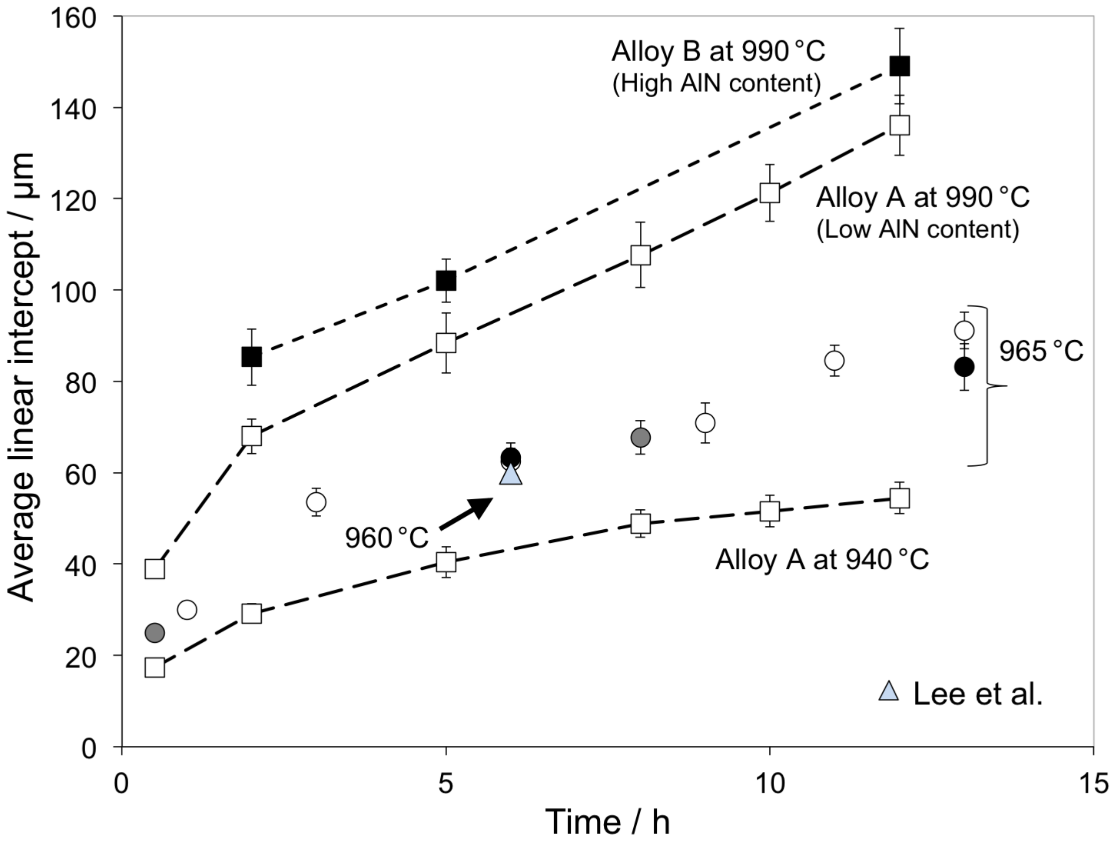

Figure 4.26: AlN effect above the coarsening temperature. Data from the literature also included [67]. White colour Alloy A. Black colour Alloy B. Grey colour Alloy C.

containing different amounts of C, Cr, Ni, and Mo, so: [71]:

$$D = 76671 \exp\left(\frac{-89098+3581X_C+1211X_{Ni}+1443X_{Cr}+4031X_{Mo}}{RT}\right)t^{0.211} \quad (4.3)$$

where D is the grain size in microns, R the universal gas constant (8.314 J mol $^{-1}$ K $^{-1}$), T the holding temperature in Kelvin, t the holding time in seconds and X_i is the concentration of the element in wt%

However, the composition of SA508 Gr. 3 steels is outside of the bounds of the investigation from Lee et al, hence the applicability of this model to these nuclear pressure vessel steel should not be adopted. Table 4.7 gives the range of

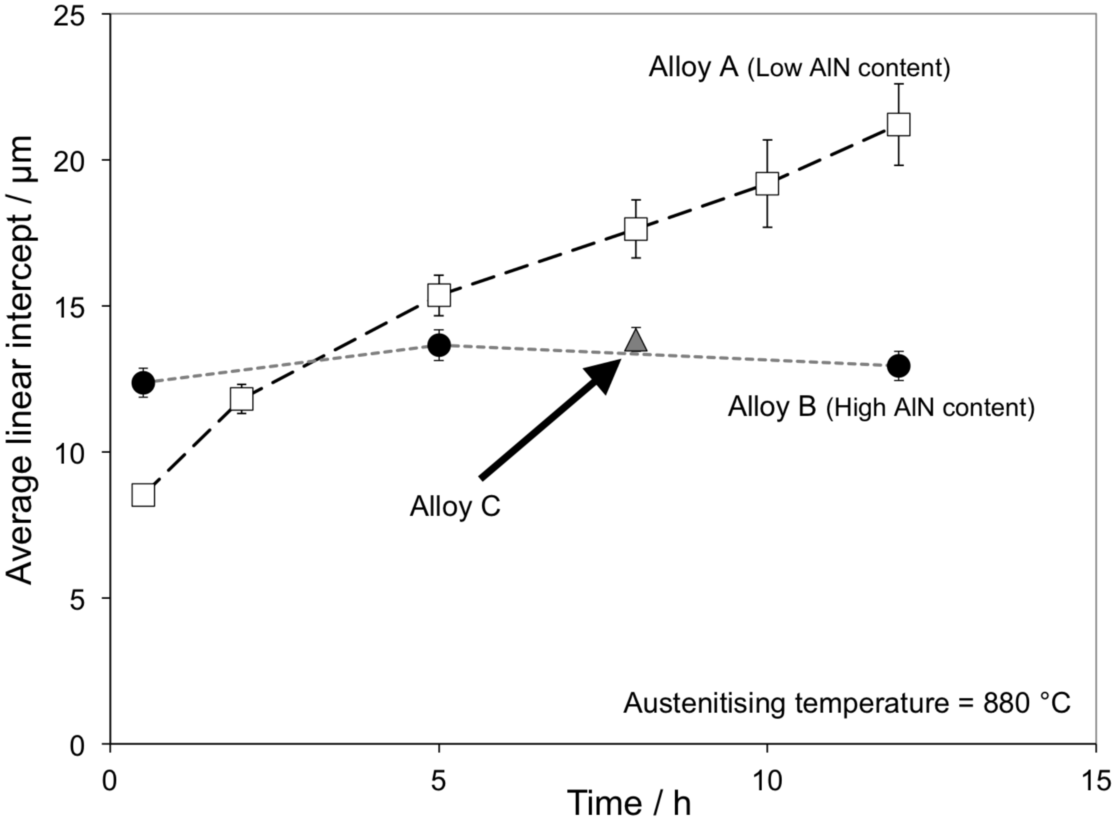

Figure 4.27: AlN effect below the coarsening temperature. White colour Alloy A. Black colour Alloy B. Grey colour Alloy C.

compositions studied in the mentioned work.

As demonstrated, previous models for austenite growth have usually been based on empirical and semi-empirical equations, which may be inadequate for extrapolating to other kinds of steels or time-temperature domains, Table 2.8 is a compilation of published models describing the isothermal growth of austenite grains and it is evident that the parameters n, the time exponent, and Q, the activation energy for boundary motion, vary widely in their magnitudes. Therefore, a more general model, based on physical principles, is proposed for the evolution of the austenite grain structure of SA508 Gr. 3 steel, taking account of the complete heat cycle involved in the generation of the grains.

Table 4.6: Mean lineal intercept representing the austenite grain size. The uncertainties in grain size measurements have been rounded up to integers.

Temperature / °C	Time h	Alloy A Grain size / µm	Alloy B Grain size / µm	Alloy C Grain size / µm
840	0.5	4 ±1	11 ±1	10 ±1
840	5	10 ±1	11 ±1	
860	13	17 ±1	12 ±1	
880	0.5	9 ±1	12 ±1	
880	5	15 ±1	14 ±1	
880	8	18 ±1		14 ±1
880	12	21 ±1	13 ±1	
910	6	21 ±2	13 ±1	

Table 4.7: Range of compositions in wt% analysed in the work of Lee et al. [71]. Composition of SA508 Gr. 3 added for comparison.

	C	Mn	Si	Ni	Cr	Mo
Min.	0.15	0.73	0.20	0.00	0.00	0.00
Max.	0.41	0.85	0.25	1.80	1.45	0.45
SA508 Gr 3	$\leq$ 0.25	1.20 - 1.50	0.15 - 0.35	0.40 - 1.00	$\leq$ 0.25	0.45 - 0.60

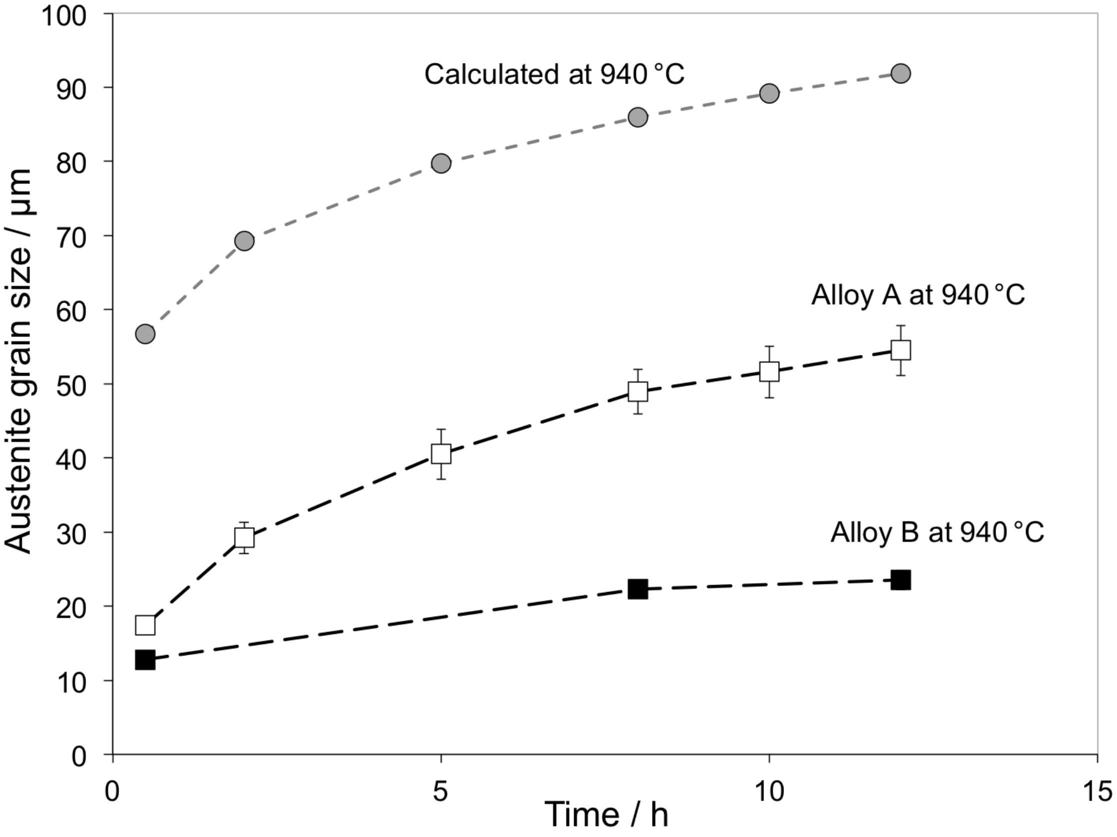

Figure 4.28: AlN effect below the coarsening temperature. White and black colours represent Alloys A, B respectively.

Martin and Doherby studied grain growth in a thin sheet of material where the thickness was much less than the average grain size, so that all the grain boundaries remained normal to the sheet surface [133]. The migration velocity (v) was found to be proportional to the driving force as:

$$v = M\,\Delta\mu \tag{4.4}$$

where M is the mobility of the boundary, $\Delta\mu$ the driving free energy per unit volume for boundary migration.

It is generally accepted that the grain growth is inversely proportional to the driving force, an approximation justified at the rather small driving forces involved in grain growth: [133, 134]:

$$\Delta\mu = C_1\left(\frac{1}{D}\right) \tag{4.5}$$

where D is the grain size and C_1 is a constant which contains the interfacial energy per unit area.

If grain growth occurs in the presence of stable precipitates acting as pinning particles, as it has been demonstrated for SA508 Gr 3 alloys, Eq. 4.5 becomes [135]:

$$\Delta\mu = C_1\left(\frac{1}{D} - \frac{1}{D_{Lim}}\right) \tag{4.6}$$

where D_{Lim} is a grain size limited by particle pinning, representing the point where the driving force for growth equals the opposing pinning force.

If the boundary velocity is written as dD/dt, and the temperature dependence of the mobility is expanded as $M \propto \exp\left(-\frac{Q}{RT}\right)$, then it follows that [135]:

$$\frac{dD}{dt} = A\exp\left(-\frac{Q}{RT}\right)\left[\frac{1}{D} - \frac{1}{D_{Lim}}\right] \tag{4.7}$$

where t is the time, T the temperature, Q an activation energy for grain growth, R the universal gas constant and A is a constant which includes C_1.

On integration from time zero, to a time t, this gives [135]:

$$\begin{split} -DD_{Lim} - D_{Lim}^2 \ln\left(1 - \frac{D}{D_{Lim}}\right) + D_0 D_{Lim} + D_{Lim}^2 \ln\left(1 - \frac{D_0}{D_{Lim}}\right) \\ = A\exp\left(-\frac{Q}{RT}\right)t \end{split} \tag{4.8}$$

where D_0 is the initial grain size which must be known as a function of temperature; a common approximation is to set it to zero or to assume the same initial grain size for all the austenitisation temperatures [72, 79]. This may not be reasonable for the present work since nuclear pressure vessels are large components which take time to reach the desired austenitisation temperature. To resolve this, it is recognised that the very first austenite grain size is defined when the steel becomes fully austenitic at the temperature Ac$_3$, and that there may be subsequent grain growth during heating to the isothermal austenitisation temperature.

Assuming a continuous heating curve, it can be expressed as a sum of short time isothermal holding as is shown in Fig. 4.29

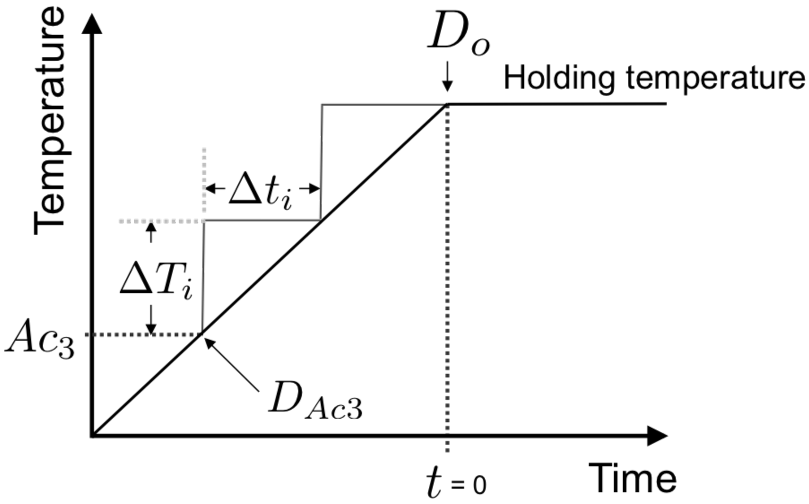

Figure 4.29: Continuous heating curve expressed by a sum of isothermal holdings. Where D_{Ac3} is the austenite grain size at Ac$_3$, D_0 the initial austenite grain size at holding temperature, Δt_i time interval and ΔT_i is temperature difference.

Growth during continuous heating between the Ac$_3$ and heat treatment temperature can be considered as a series of n isothermal steps (Δt_i) with each successive step at a slightly greater temperature (ΔT_i). The definition of $D_0 \geq D_{Ac3}$ is then the size at the point where the isothermal austenitisation temperature is reached:

$$
\begin{split}
-D_0 D_{Lim} - D_{Lim}^2 \ln\left(1 - \frac{D_0}{D_{Lim}}\right) + D_{Ac3} D_{Lim} + D_{Lim}^2 \ln\left(1 - \frac{D_{Ac3}}{D_{Lim}}\right) \\
= \sum_{i=1}^{n} A \exp\left(-\frac{Q}{RT_i}\right) \Delta t_i
\end{split}
\tag{4.9}
$$

Since the heating rate can be expressed as: $|\dot{Q}| = \Delta T_i \,/\, \Delta t_i$, Eq. 4.9 can be rearranged as a function of the heating rate:

$$
\begin{split}
-D_0 D_{Lim} - D_{Lim}^2 \ln\left(1 - \frac{D_0}{D_{Lim}}\right) + D_{Ac3} D_{Lim} + D_{Lim}^2 \ln\left(1 - \frac{D_{Ac3}}{D_{Lim}}\right) \\
= \sum_{i=1}^{n} A \exp\left(-\frac{Q}{RT_i}\right) \frac{\Delta T_i}{|\dot{Q}|}
\end{split}
\tag{4.10}
$$

During heating, the time at which the sample is at each temperature and the difference between the successive temperatures can be set arbitrarily to approach zero in order to maximise accuracy. The grain size D_0 will be the result of integrating over the range of temperatures from Ac$_3$ to the holding temperature (T):

$$
\begin{split}
-D_0 D_{Lim} - D_{Lim}^2 \ln\left(1 - \frac{D_0}{D_{Lim}}\right) + D_{Ac3} D_{Lim} + D_{Lim}^2 \ln\left(1 - \frac{D_{Ac3}}{D_{Lim}}\right) \\
= \frac{A}{|\dot{Q}|} \int_{Ac3}^{T} \exp\left(-\frac{Q}{RT}\right) dT
\end{split}
\tag{4.11}
$$

Rearranging Eqs. 4.8 and 4.11, the proposed austenite grain growth model becomes:

$$
\begin{split}
-D D_{Lim} - D_{Lim}^2 \ln\left(1 - \frac{D}{D_{Lim}}\right) + D_{Ac3} D_{Lim} + D_{Lim}^2 \ln\left(1 - \frac{D_{Ac3}}{D_{Lim}}\right) \\
= A \exp\left(-\frac{Q}{RT}\right) t + \frac{A}{|\dot{Q}|} \int_{Ac3}^{T} \exp\left(-\frac{Q}{RT}\right) dT
\end{split}
\tag{4.12}
$$

This model proposes a more rigorous approach to grain growth as the final grain size will be function of three different factors, the grain size when the material becomes fully austenitided, D_{Ac3}, which can be experimentally measured and is the same independently of the final holding temperature, the grain growth during heating to the holding temperature and the isothermal growth.

To exploit this equation, it is necessary to know the limiting grain size, D_{Lim}, as a function of temperature which is not constant since the fraction of AlN will change with temperature. Therefore, D_{Lim} was assumed to be the largest grain size measured at each temperature plus the error in the grain size measurement; e.g the austenite grain size measured for Alloy A at 940 °C after 12 h is 54 ± 3 μm, so $D_{Lim} = 57\,\mu$m. The values for 990 °C were not included since the grain sizes did not seem to reach a limiting value in that case (Fig. 4.26).

As previously discussed, the austenite grain growth model is based on D_{Ac3}, the austenite grain size at Ac_3. To reveal D_{Ac3} by thermal etching, samples were heated under vacuum to the Ac_3 temperature and then, rapidly-cooled to room temperature. Dilatometric experiments have been used to identify the Ac temperatures. During continuous heating, samples expand linearly as the temperature is increased, it is common to take the first onset of contraction to correspond to the start temperature of austenite formation (Ac_1) and the second onset of expansion corresponding with the full austenitisation of the sample (Ac_3), as seen in Fig. 4.30. The experimentally established Ac_1 and Ac_3 temperatures for the case of Alloy A are 760 and 823 °C, respectively. The measured D_{Ac3} grain sizes for the three alloys are given in Table 4.8.

Effects of the prior-austenite grain size (D_p^γ) on the austenitic grain size at Ac_3 during transformation to austenite is analysed later in Section 4.2.6.

The two unknowns in the proposed model for austenite grain growth (Eq. 4.12) are the activation energy for grain growth (Q), and the material property A. Previous models obtain the values for these parameters in a relative manner. An initial value for one of the parameters is obtained and using that value the other parameters are subsequently calculated [79]. This methodology presents the in-

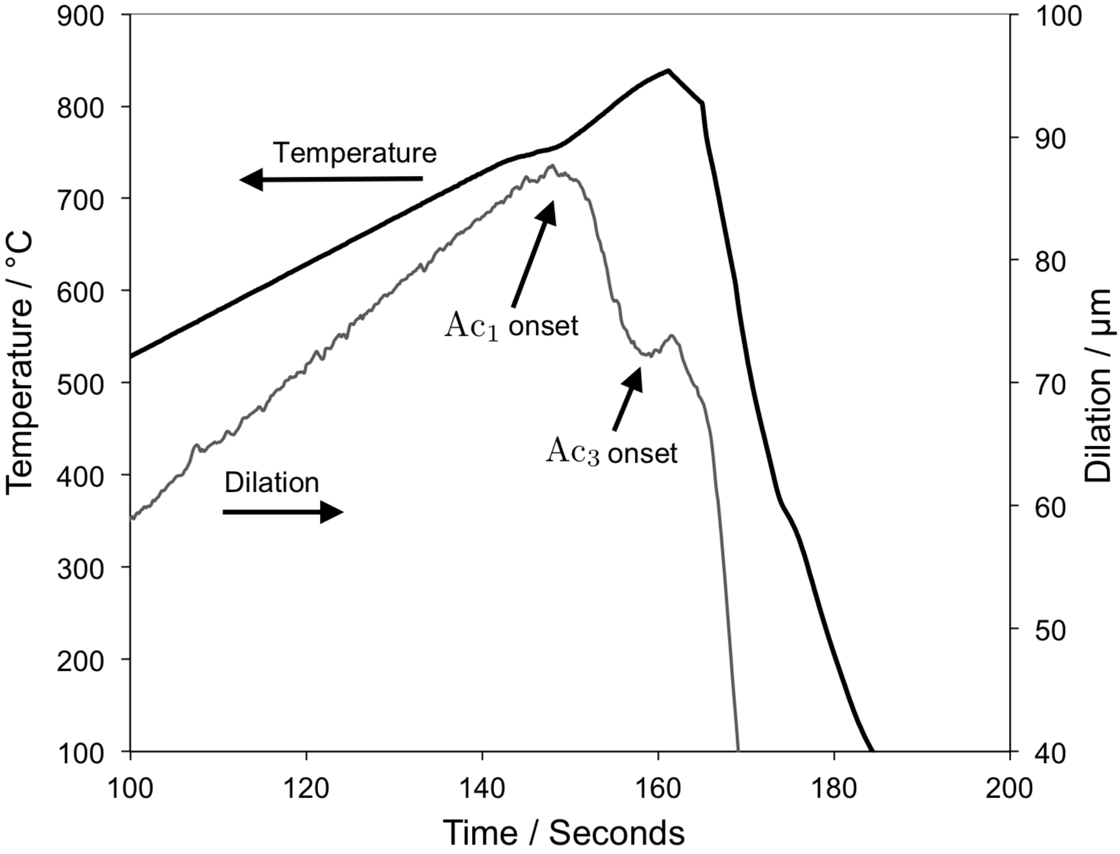

Figure 4.30: Alloy A, Ac_1 and Ac_3 from dilatometric tests

convenience that different models constants may be obtained depending on the value given to that first parameter, using the same set of data. Therefore, a more independent approach is presented here.

By applying natural logarithms and rearranging Eq. 4.12, the unknowns Q and A are independently separated, so as to permit linear regression, as a function

Table 4.8: Measured austenite grain size at Ac$_3$ temperatures. The uncertainties in grain size measurements have been rounded up to integers.

	Alloy A	Alloy B	Alloy C
D_{Ac3} / μm	3 ± 1	8 ± 1	5 ± 1

of an assumed value of Q:

$$\overbrace{\ln\left[-DD_{Lim}-D_{Lim}^2\ln\left(1-\frac{D}{D_{Lim}}\right)+D_{Ac3}D_{Lim}+D_{Lim}^2\ln\left(1-\frac{D_{Ac3}}{D_{Lim}}\right)\right]}^{\text{Y}}$$
$$= \ln A + \overbrace{\ln\left[\exp\left(-\frac{Q}{RT}\right)t + \frac{1}{|\dot{Q}|}\int_{Ac3}^{T}\exp\left(-\frac{Q}{RT}\right)dT\right]}^{\text{X}} \tag{4.13}$$

The activation energy can then be fixed by the value of Q which gives the maximum correlation between X and Y, Fig. 4.31. By applying this methodology the calculated value of Q is 250 kJ mol^{-1}; the physical significance of this is considered next.

Theoretically, the activation energy for the transfer of atoms across a general grain boundary should be about half that for self-diffusion [134]. The activation energy for iron diffusion in austenite is 286 kJ mol^{-1} [136] so that the expected Q should be about 143 kJ mol^{-1}, unlike the 250 kJ mol^{-1} deduced above. Large activation energies are also reported in many studies, as listed in Table 2.8. There is a dearth of explanations in the past, but one possibility is that there is a non-linear relationship between driving force and boundary velocity [72, 74], but as stated previously, the driving force for grain growth is very small, much smaller than for example in solid–state phase transformations in steels, where the linear relationship applies well, for example [137]. It was felt instead that the usual analysis methods do not account sufficiently for uncertainties, which may lead to over-fitting of the experimental data.

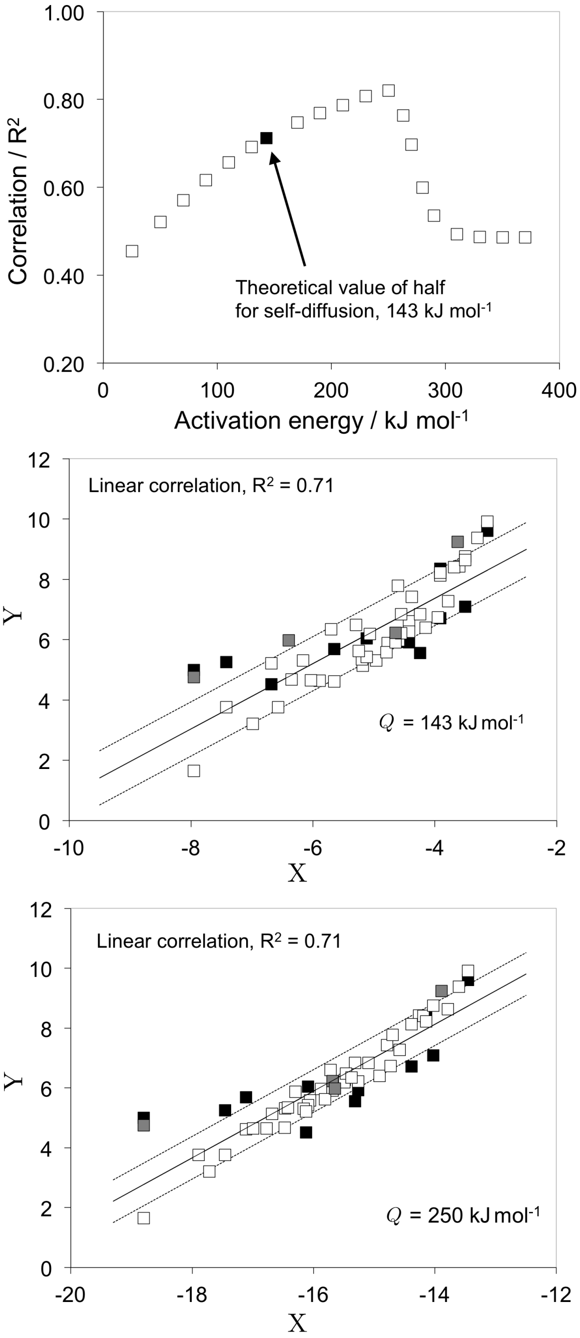

Figure 4.31: Variation of correlation with different values of activation energy for grain growth, Q. X and Y as defined in Eq. 4.13. Dotted lines represent the error between the linear regression line and the data. White, black and grey colours represent Alloys A, B and C respectively.

The over-fitting problem was assessed by introducing the variable X as input and Y as output (based on a particular Q) as defined in Eq. 4.13, into a Bayesian neural network [138–140] with a single hidden unit in order to emulate linear regression. The method provides measures of over-fitting by using only half of the randomly chosen training data to create the model, and then testing the model on the unseen test data. The error in predicting the test data should be similar to that obtained for the training data in order to conclude optimum fitting. Indeed, both the training and test errors should lie within the maximum and minimum bounds of the experimental error in the grain size measurement. Judging from Fig. 4.32, it is evident that the value of $Q = 190\,\mathrm{kJ\,mol^{-1}}$ represents an optimal fit to the experimental data, with either higher or lower values violating the criteria described. The conclusion must therefore be that very large values of Q reported in the literature are not justified by the experimental errors in the grain size data, and that the $190\,\mathrm{kJ\,mol^{-1}}$ is consistent with the theory that the activation energy for grain boundary motion should be about half that for self-diffusion.

The final grain growth equation for SA508 Gr. 3 steel therefore becomes:

$$\begin{aligned}&-DD_{Lim} - D_{Lim}^2 \ln\left(1 - \frac{D}{D_{Lim}}\right) + D_{Ac3}D_{Lim} + D_{Lim}^2 \ln\left(1 - \frac{D_{Ac3}}{D_{Lim}}\right) \\ &= \exp\left(1.003 \ln\left[\exp\left(-\frac{Q}{RT}\right)t + \frac{1}{|\dot{Q}|}\int_{Ac3}^{T} \exp\left(-\frac{Q}{RT}\right)dT\right] + 16.099\right)\end{aligned} \tag{4.14}$$

where the grain sizes are in μm, T is in Kelvin, t in seconds, the activation energy for grain growth $Q = 190{,}000\,\mathrm{J\,mol^{-1}}$ and $|\dot{Q}|$ is the heating rate in $\mathrm{K\,s^{-1}}$. The error associated with this model is 8 μm, calculated as the root mean square error [141].

In order to utilise Eq. 4.14 to predict the grain size for different austenitising conditions, numerical approximation methods have to be used. In the present work, the Newton's iterative method has been applied, as follows [142]:

$$D = D - \frac{f_{(D)}}{f'_{(D)}} \tag{4.15}$$

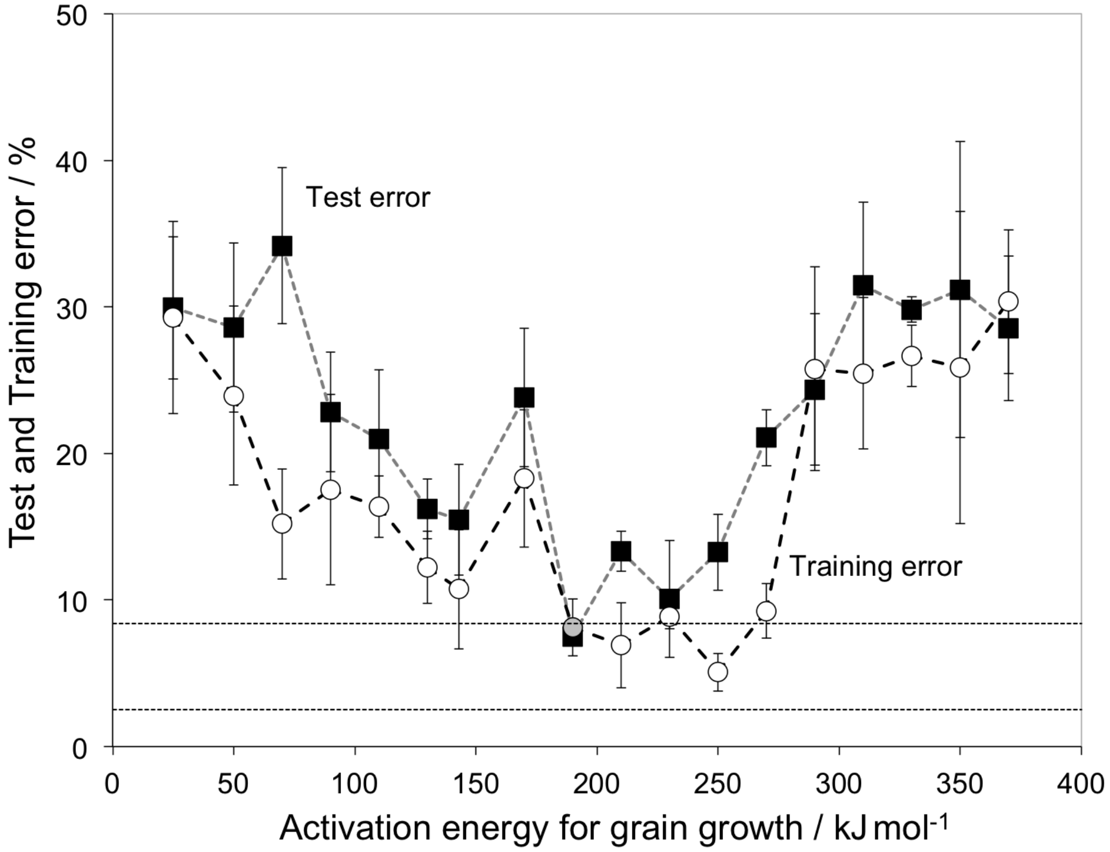

Figure 4.32: Effect of variation of activation energy for grain growth in the test and training errors. Dotted lines represent the maximum and minimum experimental errors from the grain size measurements.

where D is the grain size and f the function as defined in Eq. 4.14.

Fig. 4.33a shows a comparison between experimental data and the proposed equation showing reasonable agreement for the three studied alloys. Furthermore, by considering the effect of the pinning particles on retarding the austenite grain size by introducing the limiting grain size, D_{Lim}, in the model, the very different grain growth behaviours of Alloy A and Alloy B, due to the difference in levels of AlN, can be represented by the same model, as seen in Fig. 4.33b

Given that the theoretical approach leads to a physically meaningful Q, accounts for the initial grain size and the heating rate to the isothermal holding

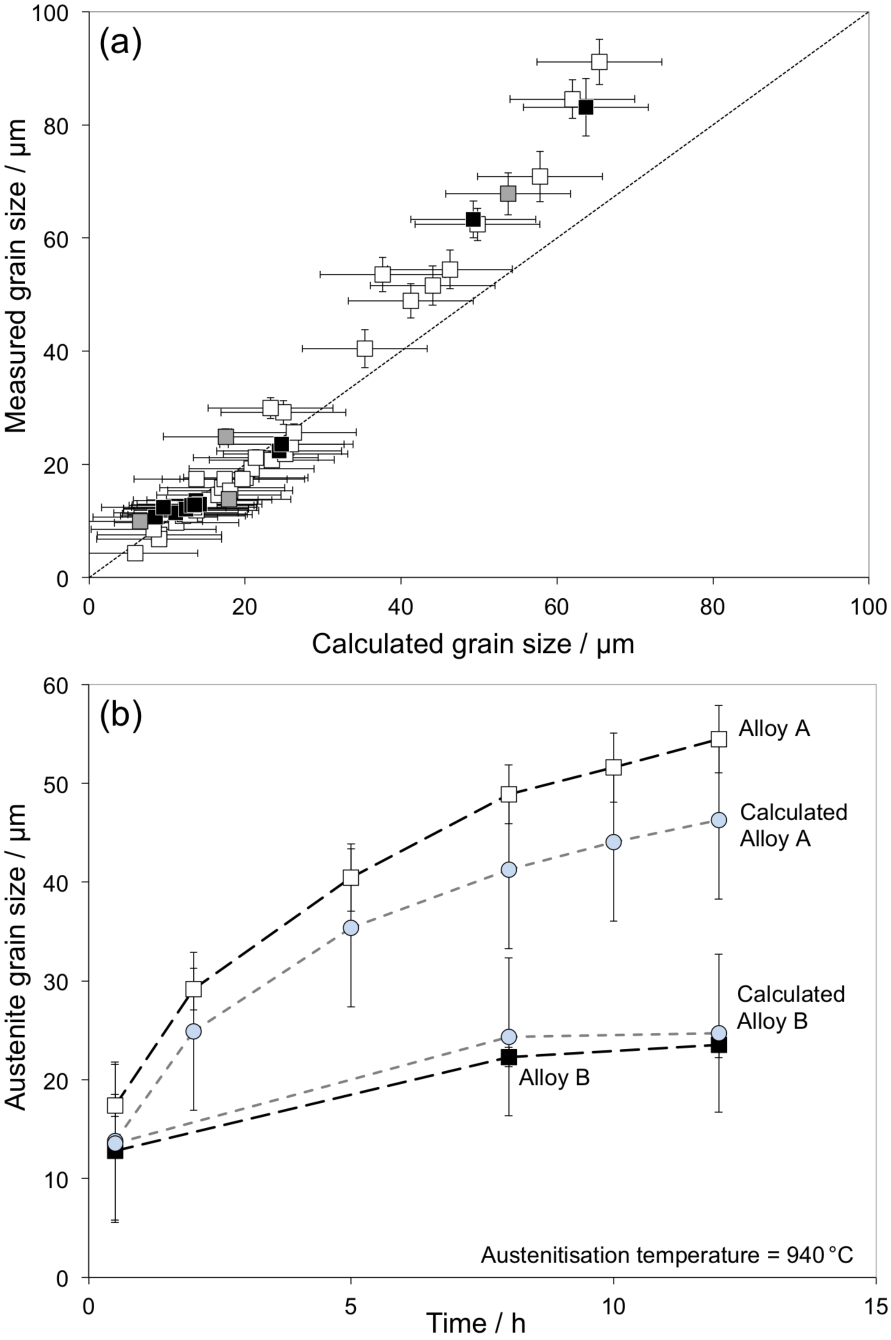

Figure 4.33: Comparison of calculated and measured austenite grain sizes. White, black and grey colours represent Alloys A, B and C respectively.

Table 4.9: Measured and calculated austenite grain sizes for unseen data.

Alloy	Temperature / °C	Time / h	Measured grain size / µm	Calculated grain size / µm
Alloy A	925	1	18 ± 1	17 ± 8
Alloy A	925	3	25 ± 2	25 ± 8
Alloy A	925	5	32 ± 2	32 ± 8
Alloy A	925	13	48 ± 4	42 ± 8
Alloy A	1200	48	221 ± 19	240 ± 8

temperature, test were designed to assess the ability of the model to generalise on unseen data. Grain sizes were measured for five new austenitising conditions; Table 4.9 shows that reasonable agreement is obtained between the measurements and predictions.

4.2.5 Limiting grain size

As graphically represented is Fig. 4.34, grain growth in this nuclear pressure vessel steel presents a relatively fast growth during the initial stage when $D << D_{Lim}$, and then as the the average grain size approaches the limiting grain size, the coarsening process becomes gradually retarded until reaching D_{Lim}.

It has been demonstrated that the limiting grain size varies with the temperature and with the level of AlN, being a determinant factor influencing the austenite grain size. D_{Lim} is a fundamental input for the developed model in the present work. This limiting grain may be experimentally determined, as it has been done here. However, in order to broaden the applicability of the newly developed model to alloy design stages, a function to predict the limiting grain size needs to be found.

As presented in Eq. 4.1, Zener developed a model to estimate the limiting grain size in presence of pinning particles. This simple model was posteriorly modified

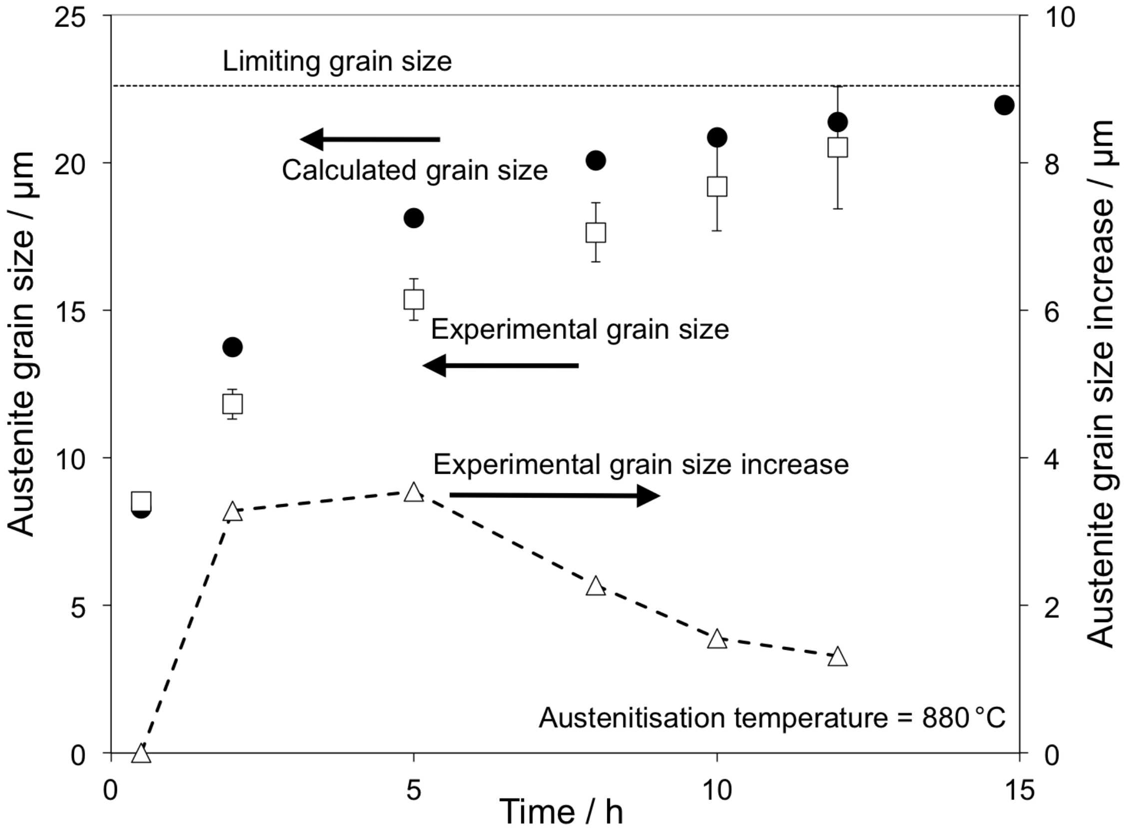

Figure 4.34: Effects of limiting grain size on grain growth kinetics for Alloy A. Error in the calculated grain size not included for clarity.

by Gladman to account for more realistic cubo-octahedron shaped grains, as follows [133]:

$$D_{Lim} = \frac{r}{3\,f_v} \times \left(\frac{3}{2} - \frac{2}{1.5}\right) \tag{4.16}$$

where D_{Lim} is the limiting grain size, and r and f_v are the radio and volume fraction of second phase particles, respectively.

Figure 4.22 showed that the dissolution temperatures for AlN (∼ 1100 °C) are higher than the temperatures being considered for the grain growth model (up to 965 °C). Hence it is reasonable to assume that the size of the AlN particles do not change during the austenitising process. So, modifying Eq. 4.16, to account for a stable precipitate size and the differences in volume fraction of AlN at the temperature of interest between alloys as a ratio, the following function is obtained:

$$D_{Lim} = \frac{1}{3\, f_{vAlN}} \times \left(\frac{3}{2} - \frac{2}{1.5}\right) \times \frac{f_{vAlN}}{f_{vAlNref}} \tag{4.17}$$

where f_{vAlN} and $f_{vAlNref}$ are the volume fraction of AlN for the composition of concern and the volume fraction of AlN for a reference composition, which in this case is Alloy A, at the temperature of interest, respectively. From this equation, the linear correlation between D_{Lim} and the amount of AlN can be found, as presented in Fig. 4.35.

An entirely empirical equation based on Fig. 4.35 is proposed to predict D_{Lim} in SA508 Gr. 3 steels:

$$D_{Lim} = 0.904 \times \frac{1}{3\, f_{vAlN}} \times \left(\frac{3}{2} - \frac{2}{1.5}\right) \times \frac{f_{vAlN}}{f_{vAlNref}} - 120.209 \tag{4.18}$$

The error associated with this model is 10 µm, calculated as the root mean square error [141].

This equation may be used to predict the limiting grain size during design stages and prior the quality heat treatment to proportionate the best austenitising condition, by simply considering the levels of Al and N in the alloy. Additionally, by using the large databases of experimental data from industrial manufactures a more robust model could be obtained following this approach.

Additional test were designed to assess the ability of the grain growth model, using values of the D_{Lim} as calculated from Eq. 4.18, to generalise on unseen data. Table 4.10 shows acceptable agreement between the measurements and predictions.

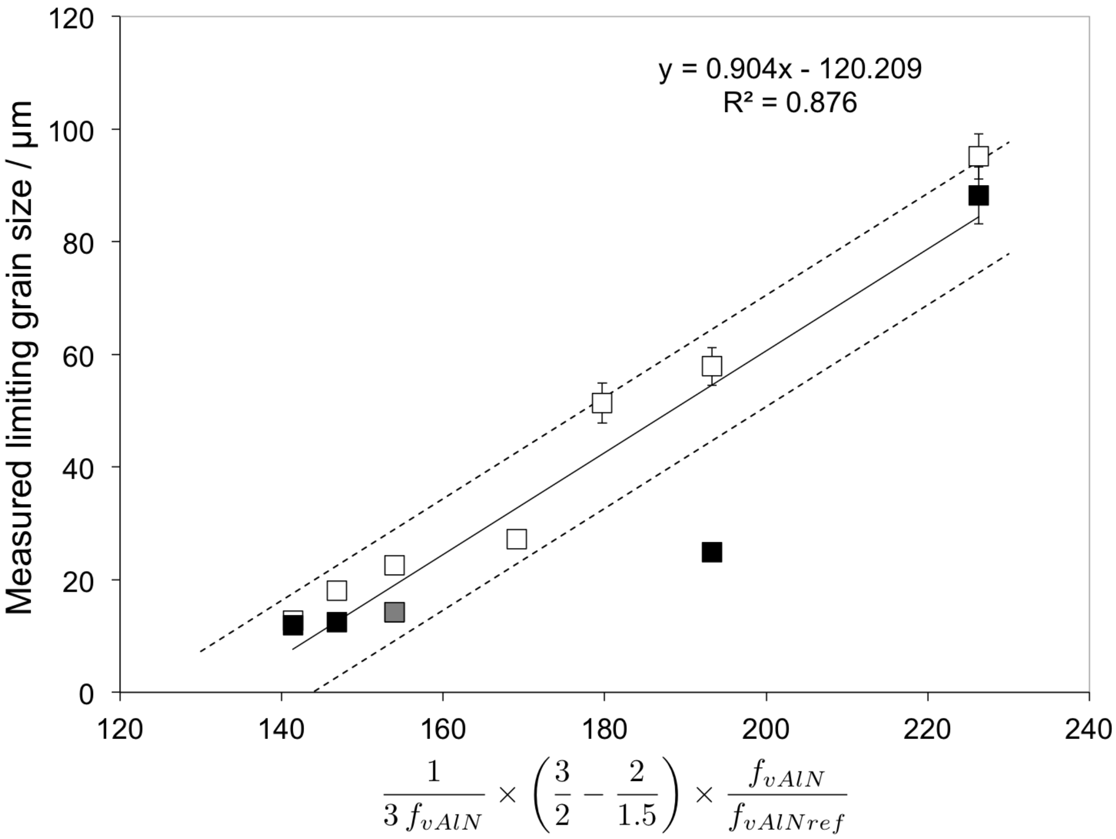

Figure 4.35: Relation between volume fraction of AlN on limiting grain size. Dotted lines represent the error between the linear regression line and the data. White, black and grey colours represent Alloys A, B and C respectively..

4.2.6 Prior-austenite grain size and relationship to the size at Ac$_3$

In the proposed grain growth model, the final austenite grain size is function of the initial size of the austenite grain when the sample is fully austenitised at Ac$_3$ (D_{Ac3}), the growth during heating from Ac$_3$ to the holding temperature and growth during the isothermal holding. Consequently, understanding the effect that the prior-austenite grain size (D_p^γ) has on that at Ac$_3$ during transformation to austenite is crucial.

To reveal the influence of the D_p^γ on D_{Ac3}, four different initial grain-sized mi-

Table 4.10: Calculated austenite grain sizes for unseen data using the calculated limiting grain size as input in the develop model for austenite growth.

Alloy	Temperature / °C	Time / h	Calculated D_{Lim} / µm	Calculated grain size / µm	Measured grain size / µm
Alloy C	840	0.5	8 ± 10	6 ± 8	10 ± 1
Alloy C	940	0.5	55 ± 10	14 ± 8	19 ± 1
Alloy C	965	0.5	84 ± 10	17 ± 8	25 ± 1
Alloy C	965	8	84 ± 10	54 ± 8	68 ± 4

Table 4.11: Measured prior-austenite grain sizes and D_{Ac3} grain sizes.

Material	Prior-austenite grain size / μm	D_{Ac3} grain size / μm
Material A	As received	3 ± 1
Material A	126 ± 10	4 ± 1
Material A	221 ± 19	5 ± 1
Material B	2605 ± 319	8 ± 1

crostructures have been analysed. To analyse the effect of very large D_p^γ grains, as-received material from Alloy B with no further heat treatment has been also tested. Experimental results show that D_p^γ in fact has little effect on D_{Ac3}, as seen in Figs. 4.36 and Table 4.11.

Austenite forms by a nucleation and growth process in steels, with both processes being sensitive to the starting microstructure. Previous investigations have reported that austenite nucleation is favoured at the prior austenite grain boundaries in martensitic and bainitic structures, while at ferritic structures nucleation is predominant at ferrite grain boundaries and austenite nucleates mainly at ferrite-pearlite interfaces as well as the interface between pearlite colonies. However, 'intragranular' nucleation at lath boundaries or at ferrite sub-boundaries has also been reported [143, 144]. Consequently, it is important to understand

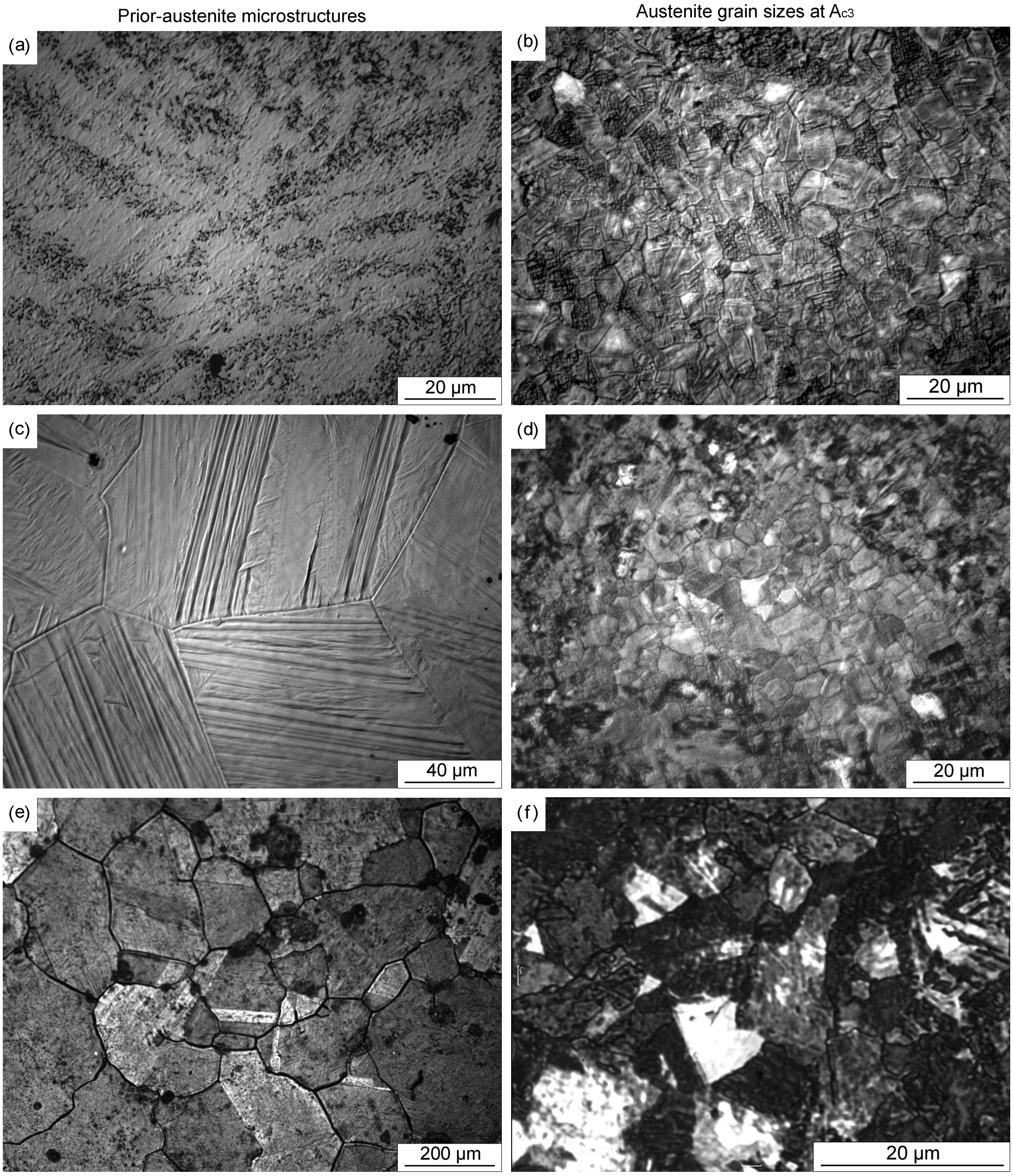

Figure 4.36: Effects of initial microstructure on D_{Ac3}. a) As received microstructure. b) D_{Ac3} from as received microstructure. c) Grain size 126 µm. d) D_{Ac3} from the grain size of 126 µm. e) Grain size 221 µm. f) D_{Ac3} from the grain size of 221 µm

where austenite nucleate in this nuclear pressure vessel steel to fully comprehend the relationship between D_p^γ on D_{Ac3}.

Comparing the dilatometric curves, from the different prior-austenite grain sizes for Alloy A, it is clear that as the D_p^γ is reduced, the transformation temperatures are retarded, as seen in Fig. 4.37. This and the fact that D_{Ac3} is significantly smaller than the initial D_p^γ, suggests that new austenite grains do not initiate exclusively at the prior-austenite grain boundaries.

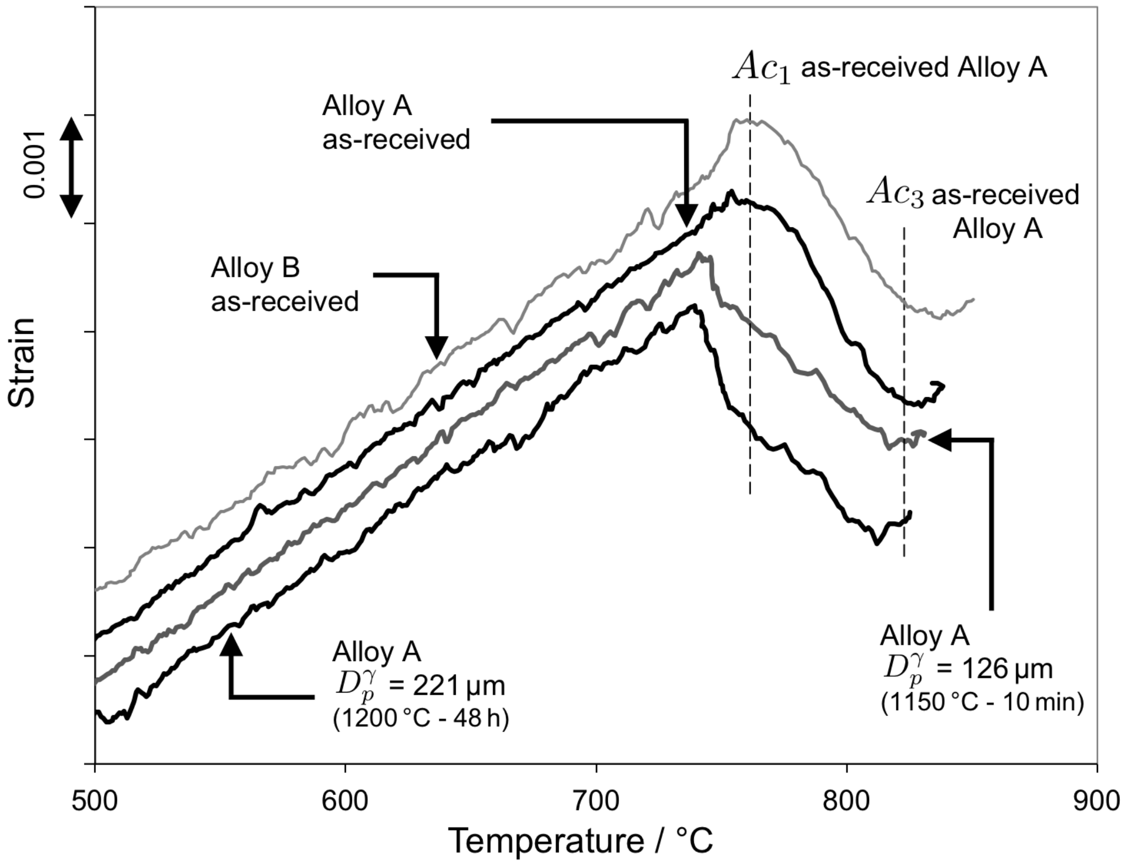

Figure 4.37: Dilatometric curves for the different prior-austenite grain sized microstructures, D_p^γ. Dilatometric curve for Alloy B included for comparison.

To reveal where the austenite starts to nucleate during reheating of the steel, samples were heated into the austenitic region and rapid cooled before fully transforming into austenite. Microstructural analysis of the partly transformed samples proves that austenite nucleates not only at prior-austenitic grain boundaries but also intragranulary as seen in Fig. 4.38. It is also evident in that austenite grains decorate the prior austenite grain boundaries. An estimation of the D_{Ac3} can be made by measuring the grains adjacent with other two, since their growth is restricted by the neighboring grains and their size will remain unchanged up to reaching the fully transformation temperature, Ac_3. The measurement of these grains reveals a value similar to the D_{Ac3} reported in Table 4.11, of $4 \pm 1\,\mu\mathrm{m}$.

These findings suggest that the initial prior-austenitic structure has little effect in the phase transformation during reheating to austenite and then on the austenitic grain size once the sample becomes fully austenitised.

4.2.7 Secondary recristallisation

It has been discovered during the course of the experimental work that there are circumstances in which there is an exaggerated grain growth of individual grains, as presented in Fig. 4.39. It has been reported that on steels containing pinning particles, as it is the case for the SA508 Gr 3 steels studied here, it is frequent to find a bimodal grain size distribution with a few abnormally large grains. This phenomenon, known as *secondary recrystallisation*, occurs when the average grain size has reached the limiting grain size due to pinning particles. At this moment all the grains are pinned, hence the driving force is balanced by the pinning force. If a grain boundary tears itself from these particles, the rate of growth for that particular grain will accelerate while others grains remain pinned, creating a very large grain relative to the fine grained matrix [129, 145, 146].

This occurrence has not been previously reported in the context of SA508 Gr. 3 steels, hence an experimental plan is designed to comprehend this phenomenon. Samples from the three alloys studied were austenitised at 880 °C for 8 h, a temperature below the grain coarsening temperature. Optical microstructural observations revealed exaggerated grain growth of individual grains in Alloys B and C while the grain size distribution of Alloy A remained more homogenous, Fig. 4.40.

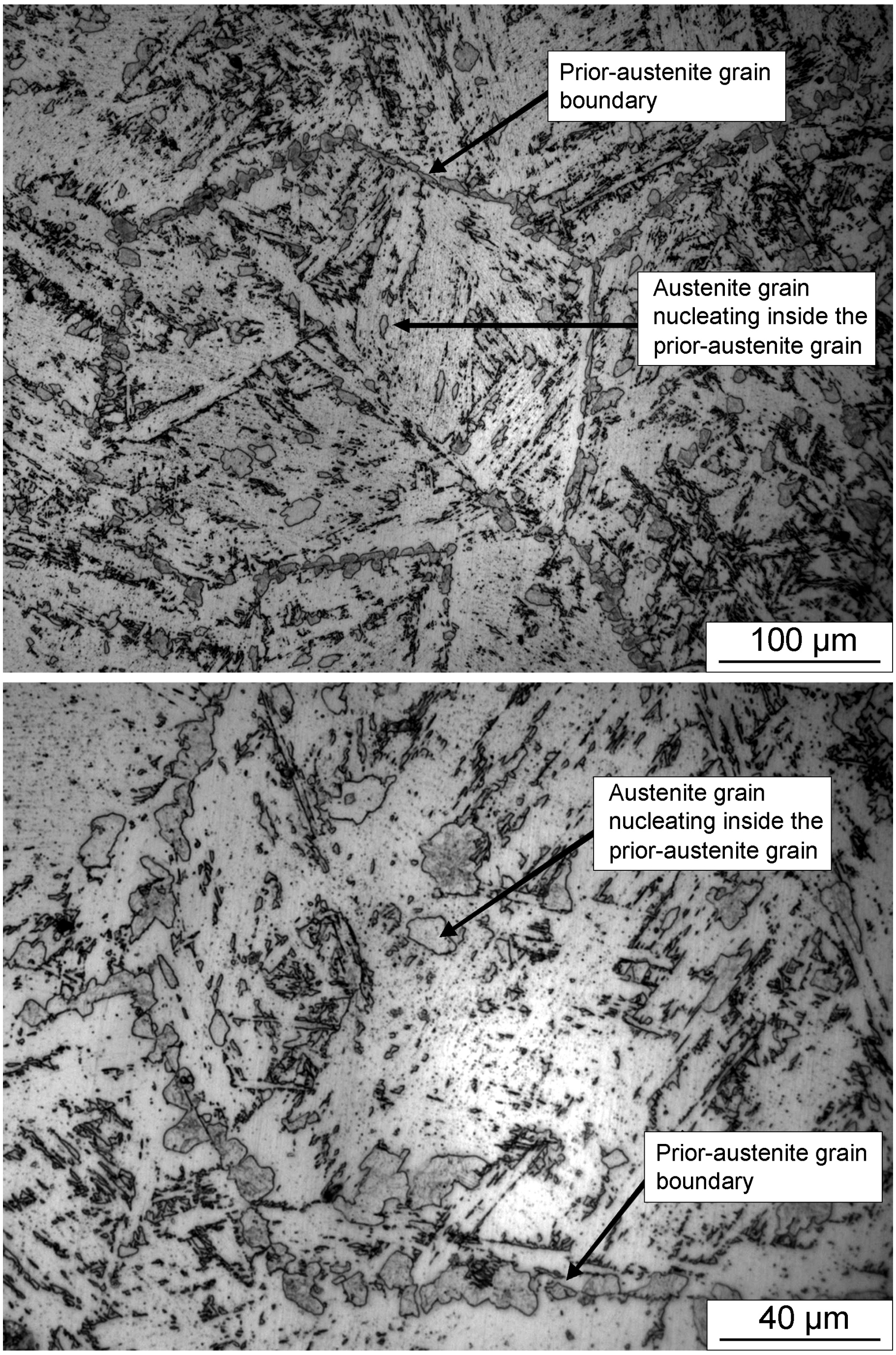

Figure 4.38: Micrographs at different magnifications of austenite nucleation sites during reheating.

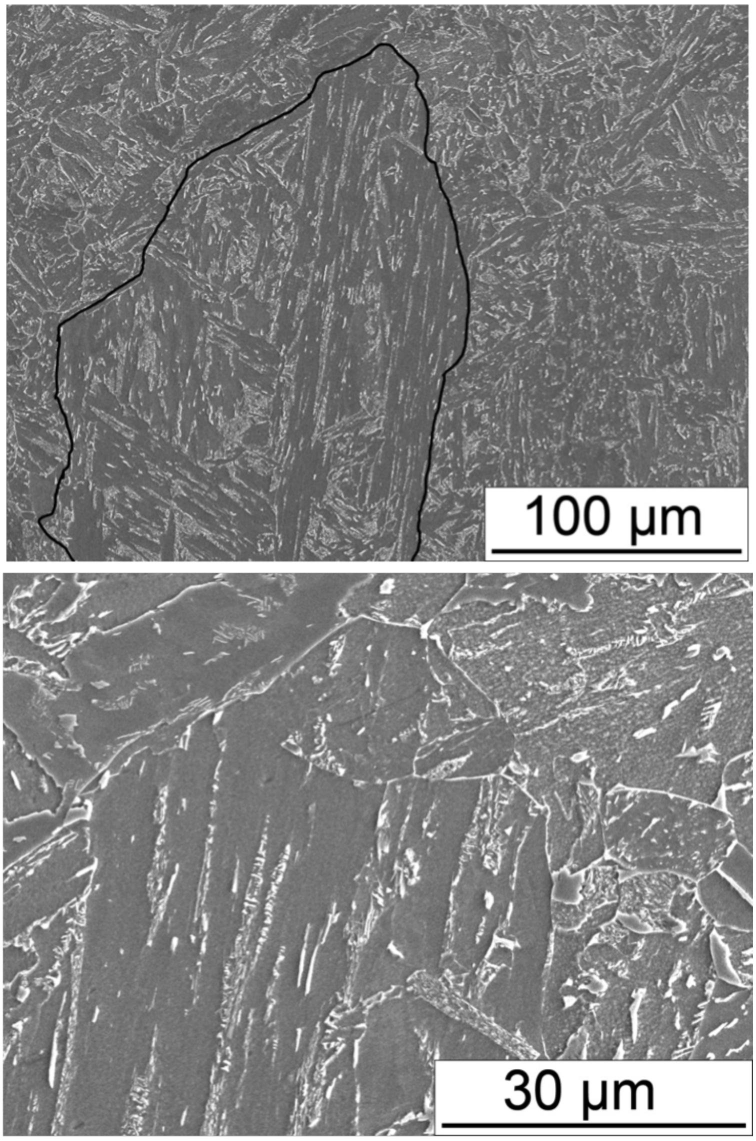

Figure 4.39: SEM micrographs showing exaggerated grain growth of Alloy C austenitised at 880 °C for 8h. Some grain boundaries have been highlighted to evidence the large grain size difference.

At austenitisation temperatures of 880 °C, grain sizes in Alloys B and C have already reached the limiting grain size at 8 h, by contrast grains in Alloy A can still grow a further fews microns, Fig. 4.40d. These empirical observations confirm that the large growth of single grains found in Alloys B and C is due to the secondary recristallysation. Consequently, it is proposed that to avoid the occurrence of these few disproportionally large grains, which may affect the local properties of the component, the level of AlN in the alloy should be reduced, by controlling the amount of Al and N, to increase the limning grain size.

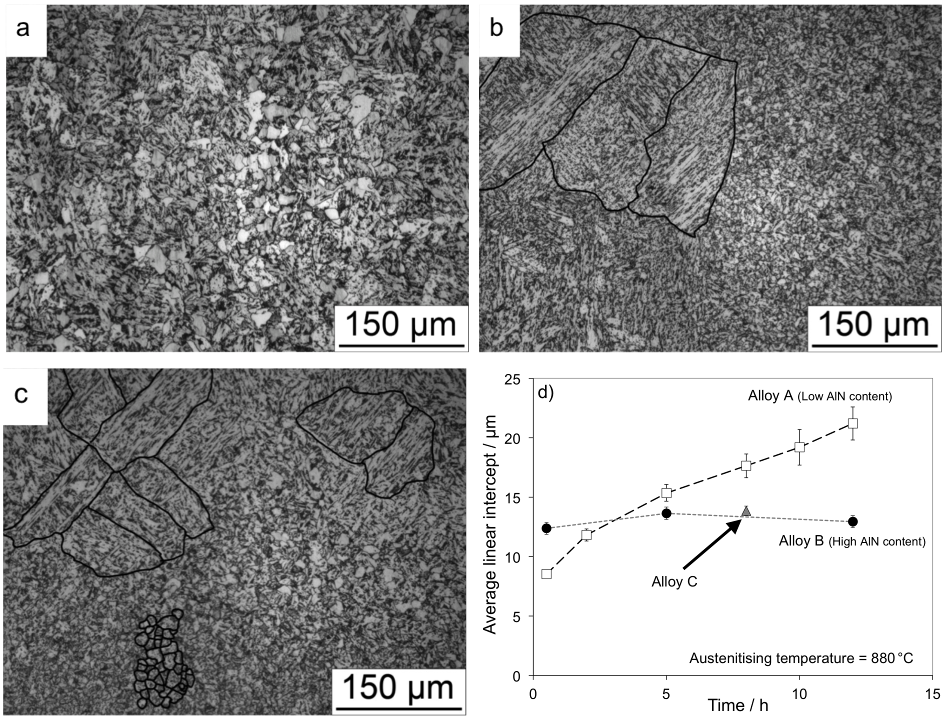

Figure 4.40: Optical micrographs showing exaggerated grain growth. a) Alloy A austenitised at 880 °C for 8h. b) Alloy B austenitised at 880 °C for 8h. c) Alloy C austenitised at 880 °C for 8h. d) Grain size evolution at 880 °C. Some grain boundaries have been highlighted to evidence the large grain size difference.

4.3 Quenching from austenitisation temperatures

As previously discussed, components are water quenched after the austenitising process during the final quality heat treatment. The general agreement is that the resultant microstructure is bainite [25, 35, 37–41, 43–48, 67, 68]. However, RPVs are large components, so in spite of the water quenching, the cooling rate following austenitisation should vary significantly as a function of depth relative to the surface. A location-dependent microstructure may appear and, consequently, through-thickness variations of mechanical properties. Figure 4.41 presents the measured cooling curve of a 320 mm thick SA508 Gr. 3 component during water quenching, where a rate of 0.2 °C s^{-1} is recorded at the mid-wall of the component.

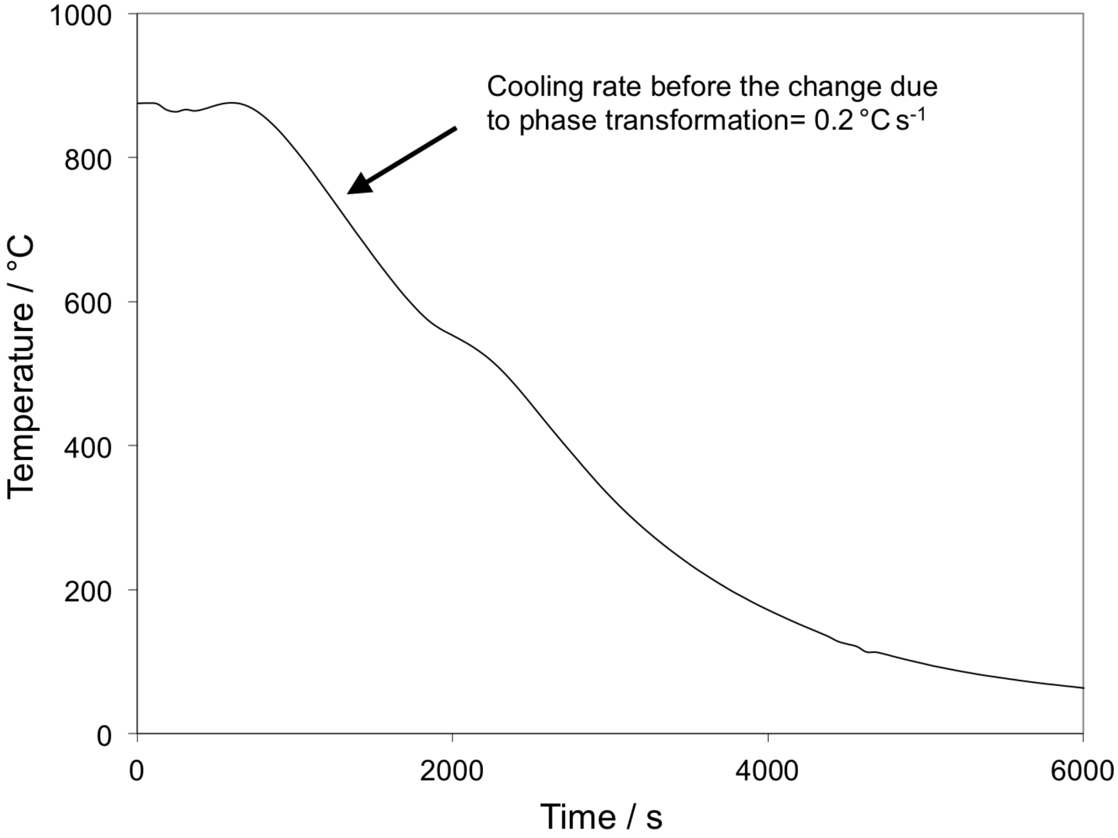

Figure 4.41: Measured cooling curve using thermocouples attached to the mid-wall position of a 320 mm thick SA508 Gr. 3 component. Data courtesy of Rolls Royce Plc.

Such variations may introduce gradients of microstructure, and the atomic mechanisms by which the structure is generated [4, 5, 32, 40, 47, 68]. Structures generated by displacive transformation are preferred because they tend to be fine in scale and are subjected to severe tempering that relieves any excess carbon to precipitate desirable carbides. In an early study from Kim et al. it was reported that cooling rates of 0.2 °C s^{-1} lead to fully bainitic microstructures [32]. However, with a drive for more power, modern pressure vessels can be 700 mm in thickness [10]. The question then arises whether the desired microstructures, and consequently properties, are in fact present in regions where the cooling rate is slowest.

Previous studies in SA508 Gr. 3 did not consider an adequate range of cooling rates and also did not include the effects that the grain size may have on the hardenability of the steel. Therefore the purpose of the present section is to undertake a detailed characterisation of SA508 Gr. 3 steels to establish the conditions under which different microstructures might be generated.

To fully understand the phase transformation behaviour of SA508 Gr. 3 during cooling from austenitisation temperatures, dilatometric and microstructural characterisation has been carried covering a full range of cooling rates, from $0.1\,°\mathrm{C\,s^{-1}}$ to represent the mid-wall of the largest components up to to $30\,°\mathrm{C\,s^{-1}}$ to simulate the fast cooled regions near the external wall. Additionally, by austenitising the samples to different conditions, the role of grain size prior to transformation has also been considered.

Figure 4.42a shows the dilatometric curves for Alloy A during continuous cooling from 0.1 to $30\,°\mathrm{C\,s^{-1}}$, revealing a much more complex behaviour than the commonly assumed bainitic structure, resulting in a larger range of microstructures. By comparing the experimental transformation temperature with the calculated using MUCG83 (Table 4.12), it can be seen that at low cooling rates allotriomorphic ferrite is formed, when exceeding $1\,°\mathrm{C\,s^{-1}}$ the transformation is fully bainitic, while at cooling rates of $10\,°\mathrm{C\,s^{-1}}$ and above the material becomes fully martensitic. At intermediate cooling rates, $7\,°\mathrm{C\,s^{-1}}$, the final microstructure at room temperature is a mixture of bainite and martensite. Hardness measurements also confirm a distinctive change in values for the different transformations, Fig. 4.42b.

It is common practice to use image analysis to determine the volume content for the different phases. However, in this work dilatometric analyses performed during cooling were used to determine phase fractions, by comparing the strain due to transformation, against the linear thermal expansions of austenite and ferrite recorded on the same plot so that whole samples were characterised.

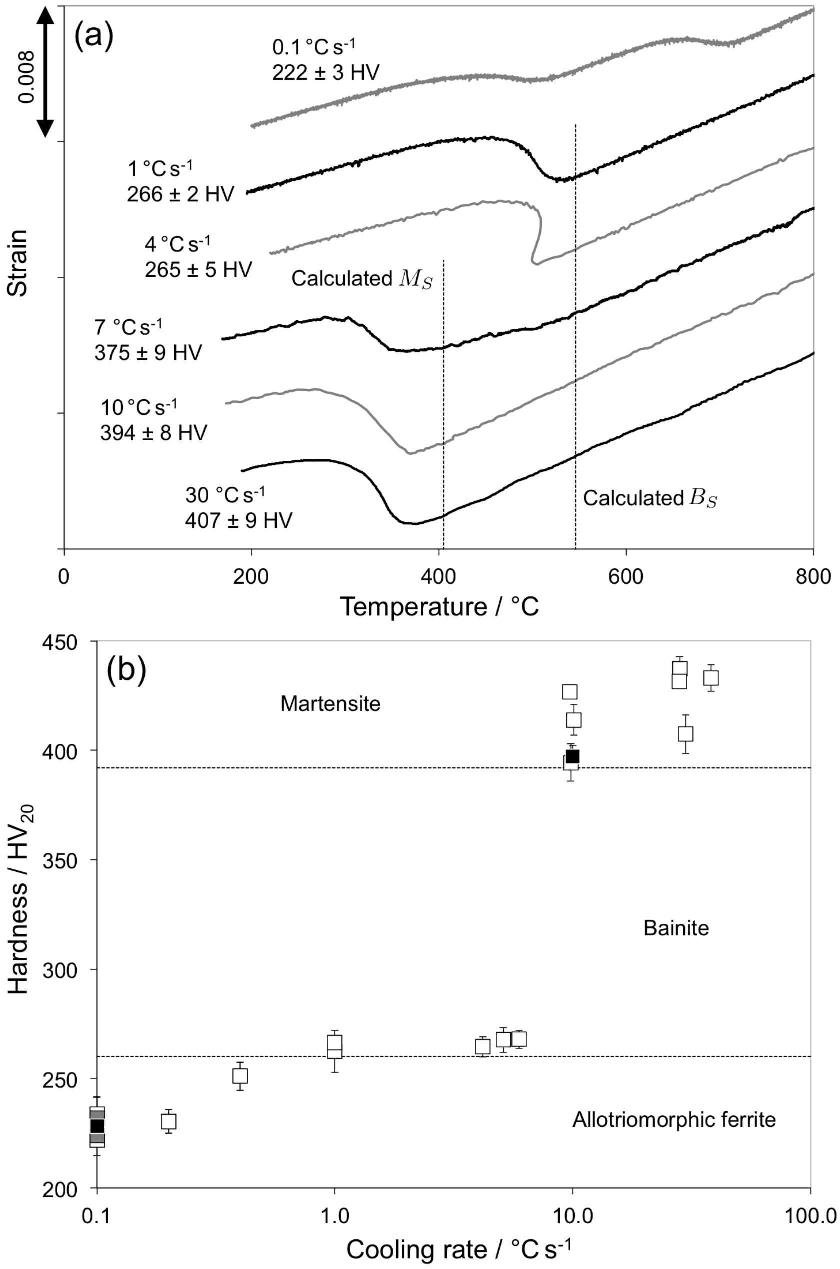

Figure 4.42: Cooling rate effects on transformation behaviour of SA508 Gr 3 steels. a) Dilatometric curve for Alloy A. Hardness Vickers (HV), calculated bainite-start (B_S) and martensite-start temperatures (M_S) also shown. b) Hardness values. White, black and grey colours represent Alloys A, B and C respectively.

Table 4.12: Bainite-start (B_S) and martensite-start temperatures (M_S) calculated using the MUCG83 software, which is based on the classical nucleation theory to calculate the time period before the onset of a detectable amount of isothermal transformation, a description of this model can be found in the work of Bhadeshia [147, 148]

Alloy	B_S / °C	M_S / °C
A	546	405
B	545	404
C	549	408

The equation used to convert strain to volume fraction is as follows:

$$\text{Volume fraction} = \frac{\text{Strain - Strain Austenite}}{\text{Strain Martensite - Strain Austenite}} \tag{4.19}$$

The Strain, Strain Austenite and Strain Martensite are as defined in Fig. 4.43

4.3.1 Phase transformation behaviour on slow cooling rates (up to $1\,^{\circ}\mathrm{C\,s^{-1}}$)

Dilatometric curves during continuous cooling from 0.1 to $1\,^{\circ}\mathrm{C\,s^{-1}}$ are presented in Fig. 4.44, revealing three transformations, the formation of allotriomorphic ferrite at about 700 °C, a second transformation at ≈ 540 °C which is consistent with the calculated start of the bainite reaction (Table 4.12), and finally, the formation of martensite from carbon-enriched residual austenite at temperatures below 160 °C. The volume percent of martensite detected was, within the limits of experimental error, insensitive to the cooling rate or austenite grain size, at 4 ± 2, 6 ± 1 and 6 ± 2 % for alloys A, B, and C respectively.

The amount of allotriomorphic ferrite obtained is in contrast, quite sensitive to the austenite gain size and the cooling rate, Fig. 4.45. An increase in the austenite grain size ($\overline{L}_\gamma$) from 4 to 17 μm reduces the quantity by 56 %, for the

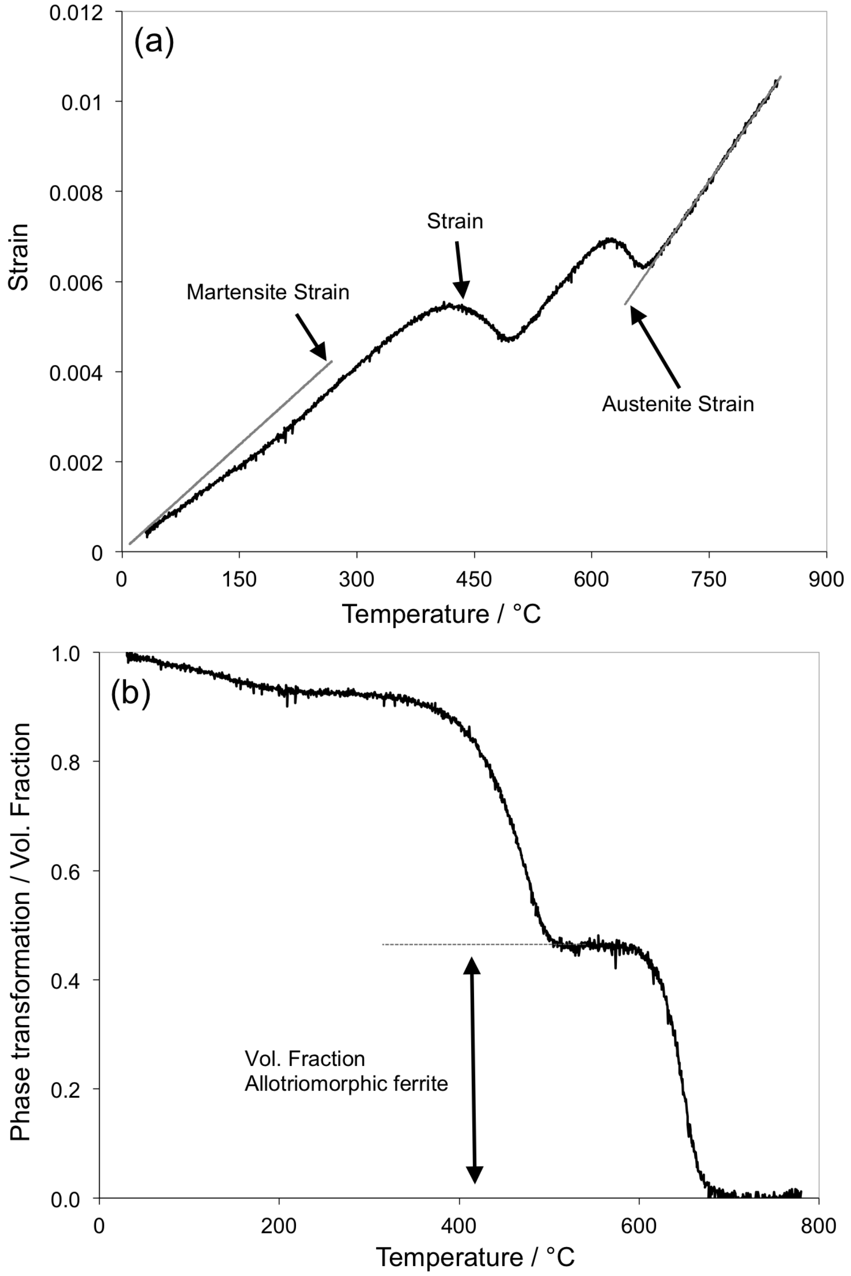

Figure 4.43: Converting strain to volume fraction. a) Strain - Temperature curve. b) Phase transformation - Temperature curve.

slowest cooling rate. Smaller grain sizes promote the phase because of the larger number density of nucleation sites and the fact that allotriomorphs thickness increases parabolically with time so that it becomes ever more difficult to con-

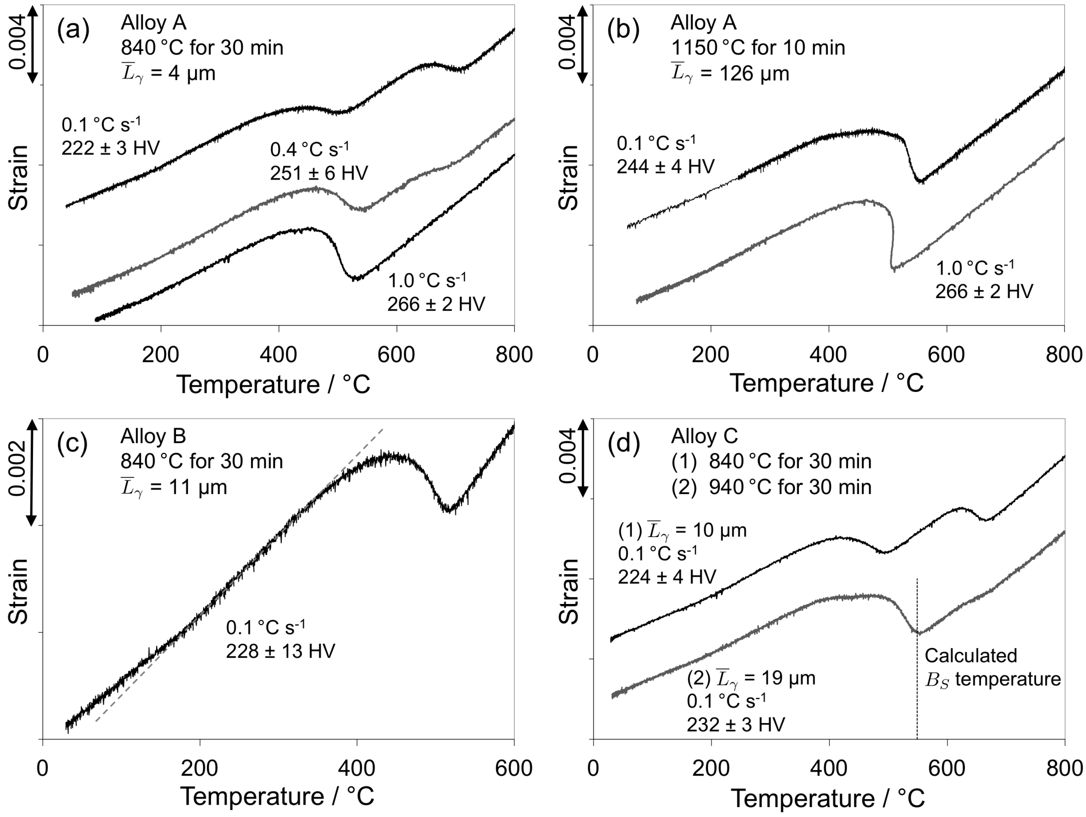

Figure 4.44: Austenite grain size and cooling rate effects on transformation behaviour of SA508 Gr. 3 steels. a) Alloy A; b) Alloy A; c) Alloy B; d) Alloy C. Austenite grain sizes ($\overline{L}_\gamma$) and Hardness Vickers (HV) values also shown.

sume the cores of austenite grains when the latter are large [149, 150]. Cooling rates greater than 0.4 °C s^{-1} suppress the formation of allotriomorphic ferrite for austenitic grain sizes above 13 µm; this defines the cooling rate for avoiding this phase in RPVs where the austenite grain size is comparable.

RPV components are commonly austenitised at 880 °C for up to 8 h (for example in [36, 37, 40, 42, 52, 69]) a temperature where AlN precipitates prevent grain coarsening so that the grain size rapidly reaches a limiting value as earlier demonstrated. Table 4.6 shows the measured austenite grain size after several hours at 880 °C for the three studied alloys. The differences observed in grain sizes are consistent with the calculated amount of AlN, Fig. 4.22, alloy A with the least

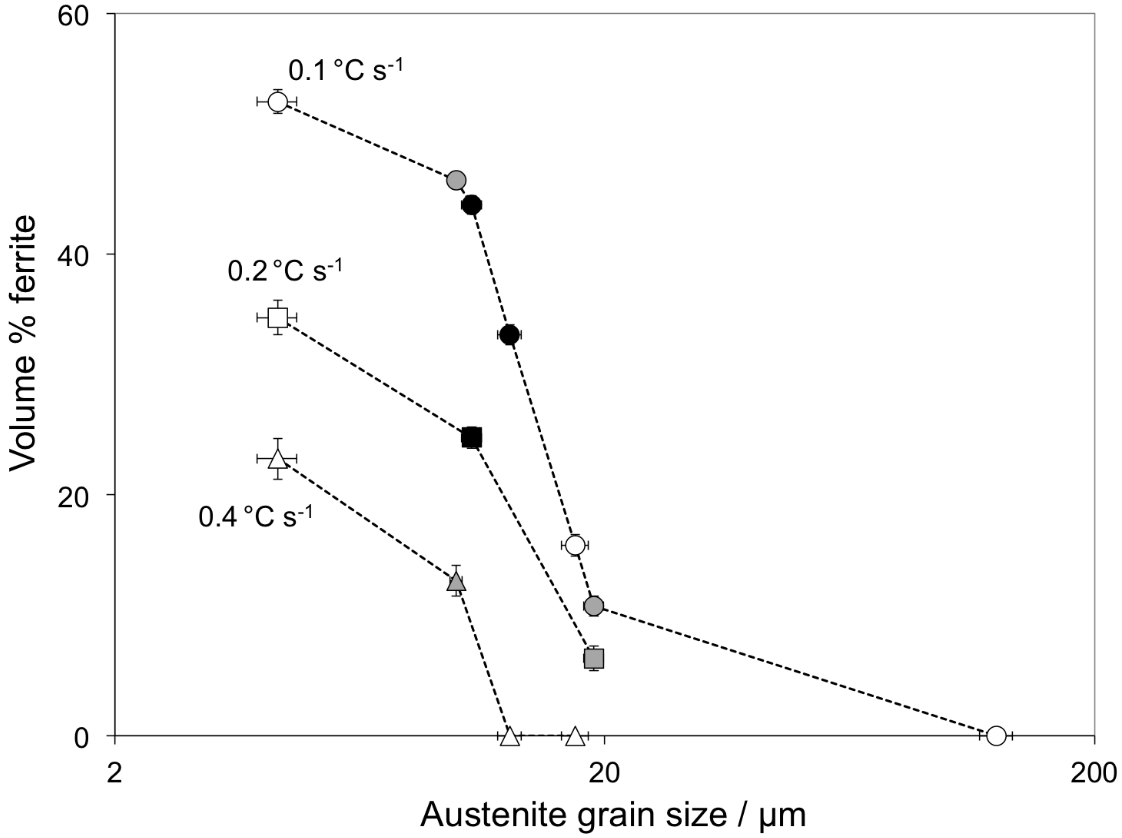

Figure 4.45: Austenite grain size versus volume of allotriomorphic ferrite at different cooling rates. White, black and grey colours represent Alloys A, B and C respectively.

AlN exhibiting the largest grain sizes. The range of austenite grain sizes studied here between 4 and 126 µm (see Table 4.6) is larger than would be achieved by the commercial heat-treatments, but it is used to understand the transformation behaviour if SA508 Gr. 3 steels. It has therefore been demonstrated here that at the mid-wall of RPVs, where the cooling rates are slowest, allotriomorphic ferrite is likely to form under common industrial processing conditions. This conclusion differs from the majority of reports on the microstructure of similar pressure vessels steels, where there appears to be a consensus that the structure following quenching is fully bainitic, and that this becomes tempered bainite with cementite and M_2C particles [25, 35, 37–41, 43–48, 67, 68]. As mentioned, Kim et al. studied the effects of cooling rate on microstructural formation on SA508 Gr. 3

steels, reporting that at cooling rates of $0.2\,^\circ\mathrm{C\,s^{-1}}$ the microstructure was fully bainitic [32]. However, their work did not consider the hardenability effects of the austenite grain size, which as presented here are very relevant. Therefore, their conclusion was influenced by the large austenitic grain size, 50 μm.

There is only one record of a study in the literature [32], that reported the presence of about 20 % of allotriomorphic ferrite in SA508 Gr. 3, after slow cooling at $0.02\,^\circ\mathrm{C\,s^{-1}}$. But they did not explicitly realise its significance. However, an examination of their toughness data, shows that the cooling rate associated with the formation of allotriomorphic ferrite also leads to a five fold reduction in the Charpy impact energy at 4 °C compared to fully bainitic samples, cooled at $0.2\,^\circ\mathrm{C\,s^{-1}}$ (11 and 57 joules respectively) [32], in spite of the fact that the latter are expected to be stronger.

Microstructural examination of the continuously cooled samples is consistent with the results obtained by dilatometry, Fig. 4.46. The final microstructure obtained for the cooling rate ($|\dot{T}|$) of $0.4\,^\circ\mathrm{C\,s^{-1}}$ and $\overline{L}_\gamma \leq 13\,\mu\mathrm{m}$, after slow cooling will be a mixture of allotriomorphic ferrite, bainite and martensite, with carbides lying parallel to the direction of habit plane traces of the bainitic ferritic plates, clearly seen in Figs. 4.46e and 4.46f. The structures obtained after quenching at $|\dot{T}| = 1\,^\circ\mathrm{C\,s^{-1}}$ are mostly bainitic, with 4-6 Vol. % of martensite, irrespective of the austenite grain size within the range studied, Fig. 4.47.

As earlier mentioned, displacive transformation products are desired since the steel is severely tempered, and martensitic or bainitic regions remain relatively fine during this process ensuring the required level of toughness. Allotriomorphic ferrite should be avoided as it is in relative terms, detrimental to toughness as each ferrite grain presents a homogeneous crack path of size equivalent to the allotriomorphic ferrite grain size to propagate cracks [150].

Experimental results have shown that allotriomorphic ferrite can be suppressed in SA508 Gr. 3 steels for all conditions where $|\dot{T}| > 1\,^\circ\mathrm{C\,s^{-1}}$. However, under current production methods for large pressure vessel components, where

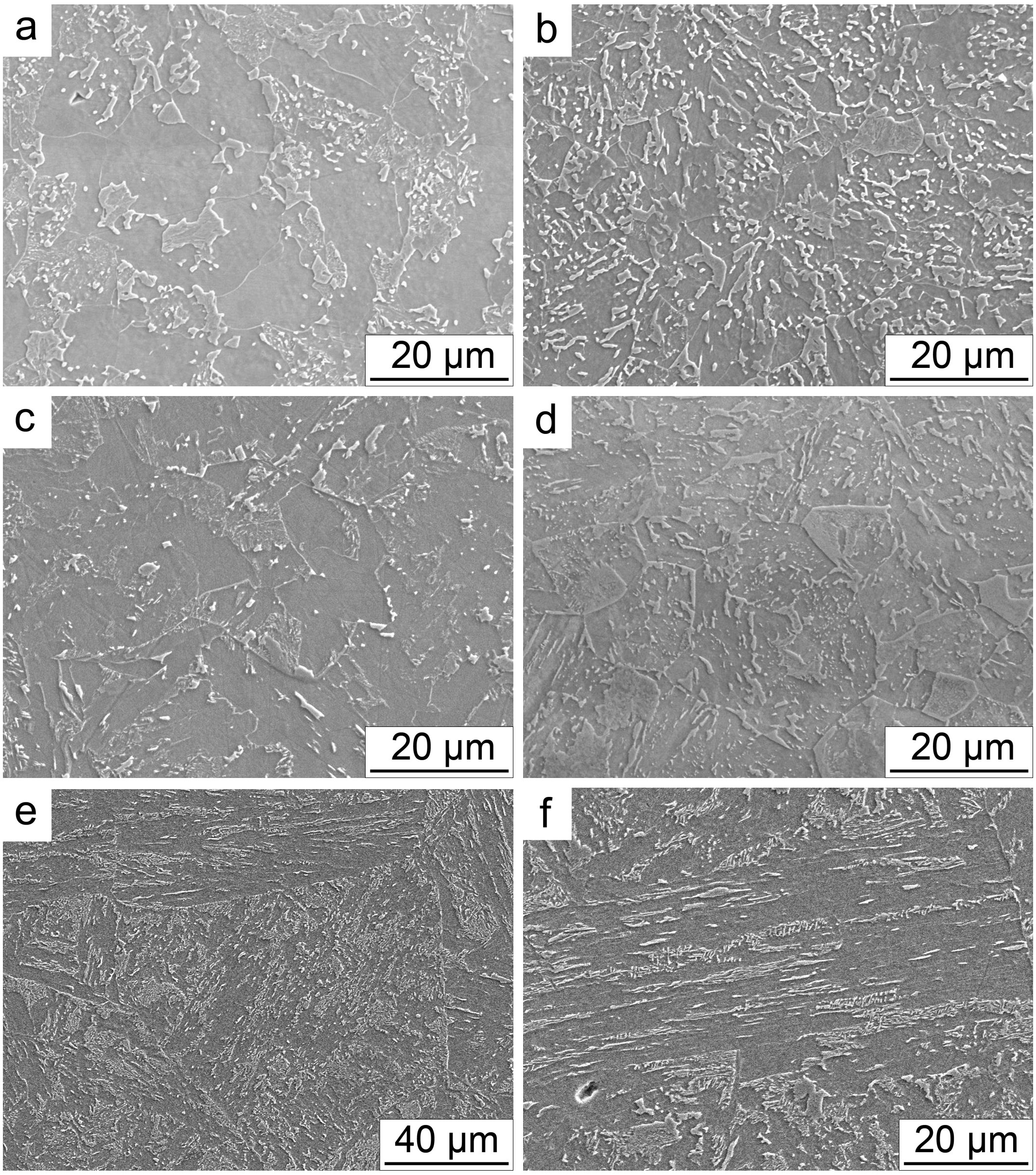

Figure 4.46: SEM microstructures of Alloy A after slow cooling. a) Austenitised at 840 °C for 30 min and cooled at 0.1 °C s^{-1}. b) Austenitised at 840 °C for 30 min and cooled at 0.4 °C s^{-1}. c) Austenitised at 940 °C for 30 min and cooled at 0.1 °C s^{-1}. d) Austenitised at 940 °C for 30 min and cooled at 0.4 °C s^{-1}. e) Austenitised at 1150 °C for 10 min and cooled at 0.1 °C s^{-1}. f) Austenitised at 1150 °C for 10 min and cooled at 0.1 °C s^{-1}.

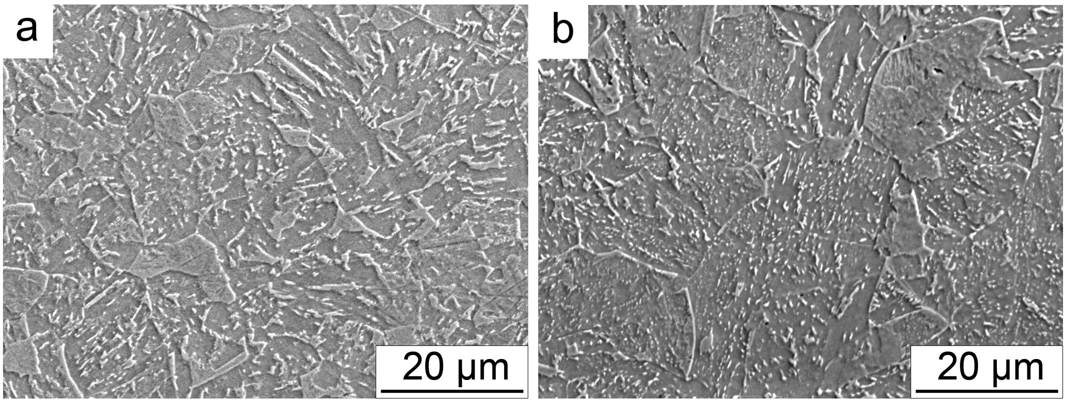

Figure 4.47: SEM microstructures of Alloy A after quenching at 1 °C s^{-1}. a) Austenitised at 840 °C for 30 min. b) Austenitised at 940 °C for 30 min.

the forgings are already quenched in highly agitated water [10], there is no room to enhance the available cooling rates, and indeed it may not be desirable to do so given other consequences of non-uniform cooling on the structural integrity of large components. Consequently, the formation of allotriomorphic ferrite could be suppressed by controlling the austenitic grain size prior quenching. This can be achieved by modifying the heat treatment, by increasing austenitisation times or temperatures, or by reducing the residual levels of aluminium and nitrogen to diminish the amount of AlN. A minimum grain size to avoid the formation of significant quantities of allotriomorphic ferrite in SA508 Gr. 3 steels, at cooling rates as low as 0.1 °C s^{-1}, is estimated by linear extrapolation of the experimental data, as seen in Fig. 4.48. Therefore, it is proposed that in order to avoid the formation of significant quantities allotriomorphic ferrite the austenite grain size should be kept to a minimum of ≈ 25 μm.

An experiment to validate this minimum grain size consistent with avoiding allotriomorphic ferrite has been performed, whereby a sample of Alloy C, austenitised at 965 °C for 30 min, with a measured $\overline{L}_\gamma = 25 \pm 1$ μm, was cooled continuously at 0.1 °C s^{-1} without showing a high temperature diffusive transformation. Fig. 4.49 shows the austenitic grain size revealed by thermal etching and the dilatometric curve, where the first transformation is clearly at temperatures where bainite forms.

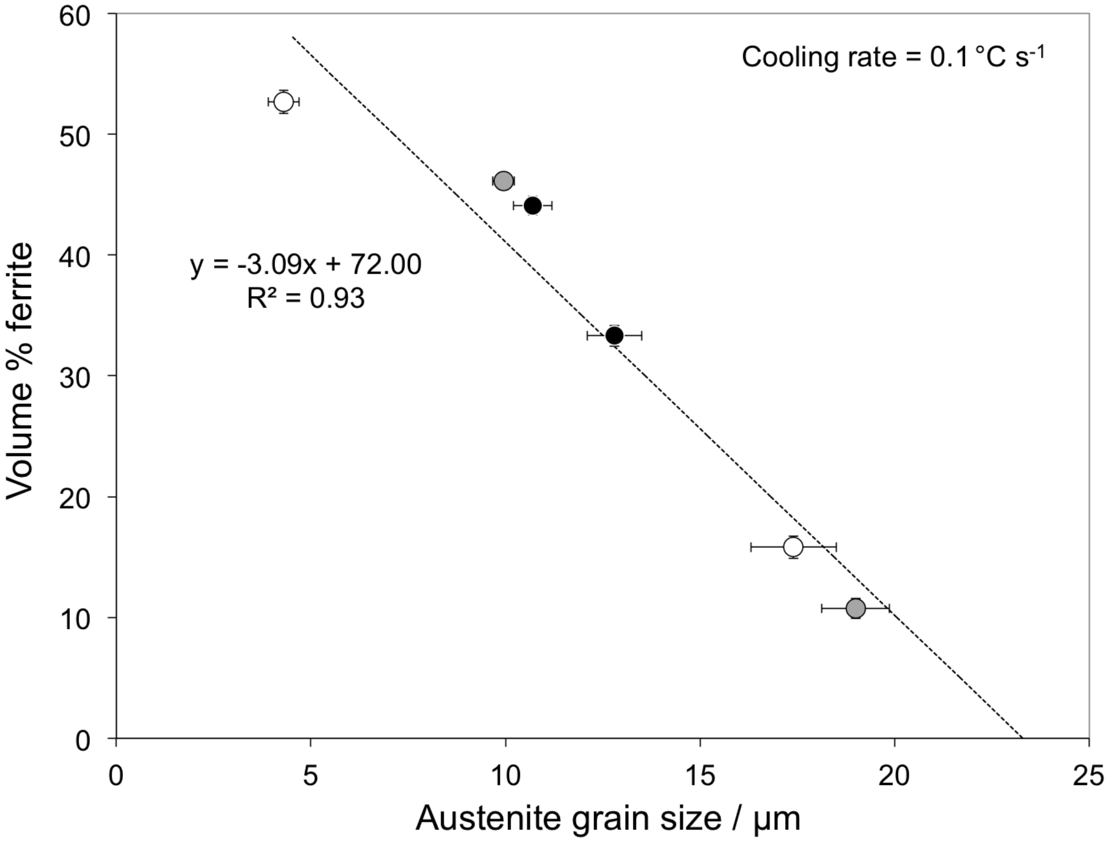

Figure 4.48: Grain size versus volume of allotriomorphic ferrite of SA508 Gr. 3 steels cooled at 0.1 °C s^{-1}. White, black and grey colours represent Alloys A, B and C respectively.

Experimental results prove that austenitising temperatures may be used to control the austenitic grain size which will affect hardenability. Furthermore, predictive tools could be used to map the material transformation behaviour of large components by means of location dependent austenitic grain size and cooling rate.

To definitely conclude that allotriomorphic ferrite forms under current processing conditions, further experiments, where samples from the 3 alloys studied were austenitised at a common heat treatment, 880 °C for up to 8h and cooled at 0.1 and 0.2 °C s^{-1}. Results prove that at the mid-wall of current RPVs, where the measured cooling rate is 0.2 °C s^{-1} (as shown in Fig. 4.41), the microstruc-

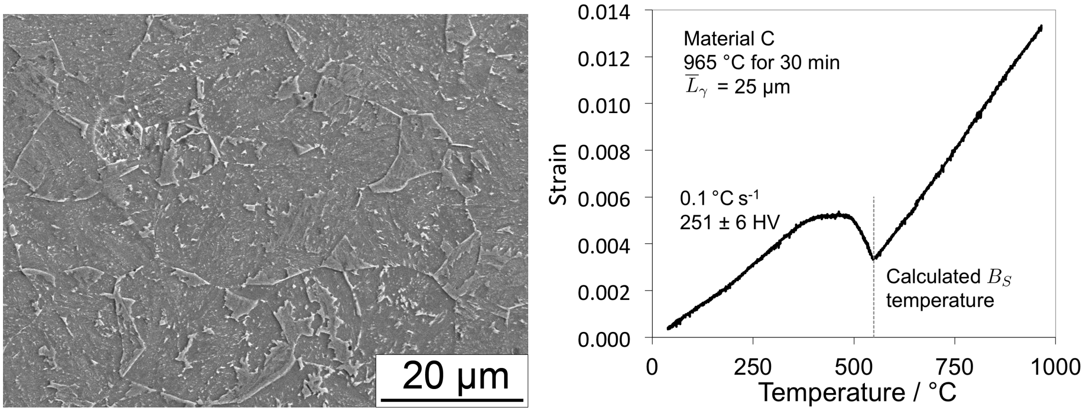

Figure 4.49: SEM microstructure and dilatometric curve of Alloy C during continuous cooling at 0.1 °C s^{-1} austenitised at 965 °C for 30 min. Austenite grain sizes ($\overline{L}_\gamma$) and Hardness Vickers (HV) values also shown.

tures at room temperature after austenitising treatment contain 4 - 5 volume % of allotriomorphic ferrite, Figs. 4.50 and 4.51.

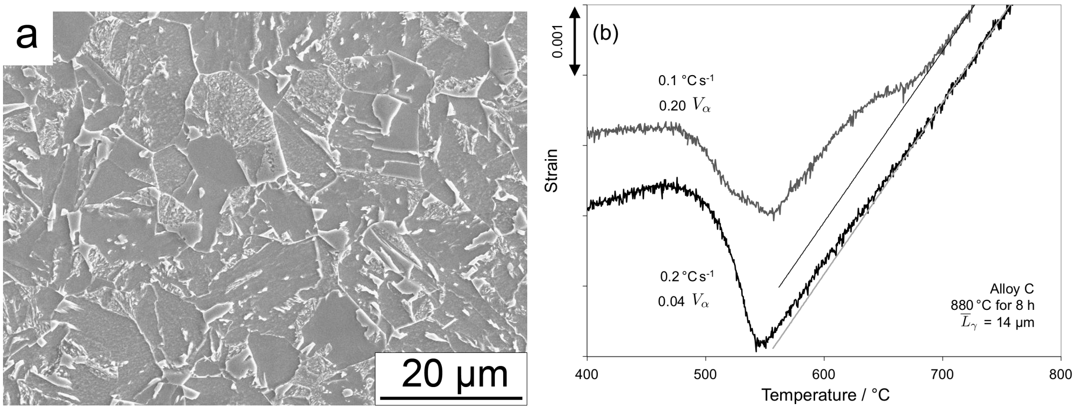

Figure 4.50: a) SEM microstructure of Alloy C cooled at 0.2 °C s^{-1} after austenitisation at 880 °C for 8 h. b) Corresponding dilatometric curve for continuous cooling at 0.1 and 0.2 °C s^{-1}. Austenite grain sizes ($\overline{L}_\gamma$) and volume fractions of allotriomorphic ferrite (V_α) also shown.

Figure 4.52 summarises the experimental data where an operational framework to avoid the formation of allotriomorphic ferrite in SA508 Gr. 3, in terms of austenitic grain size and cooling rate can be seen.

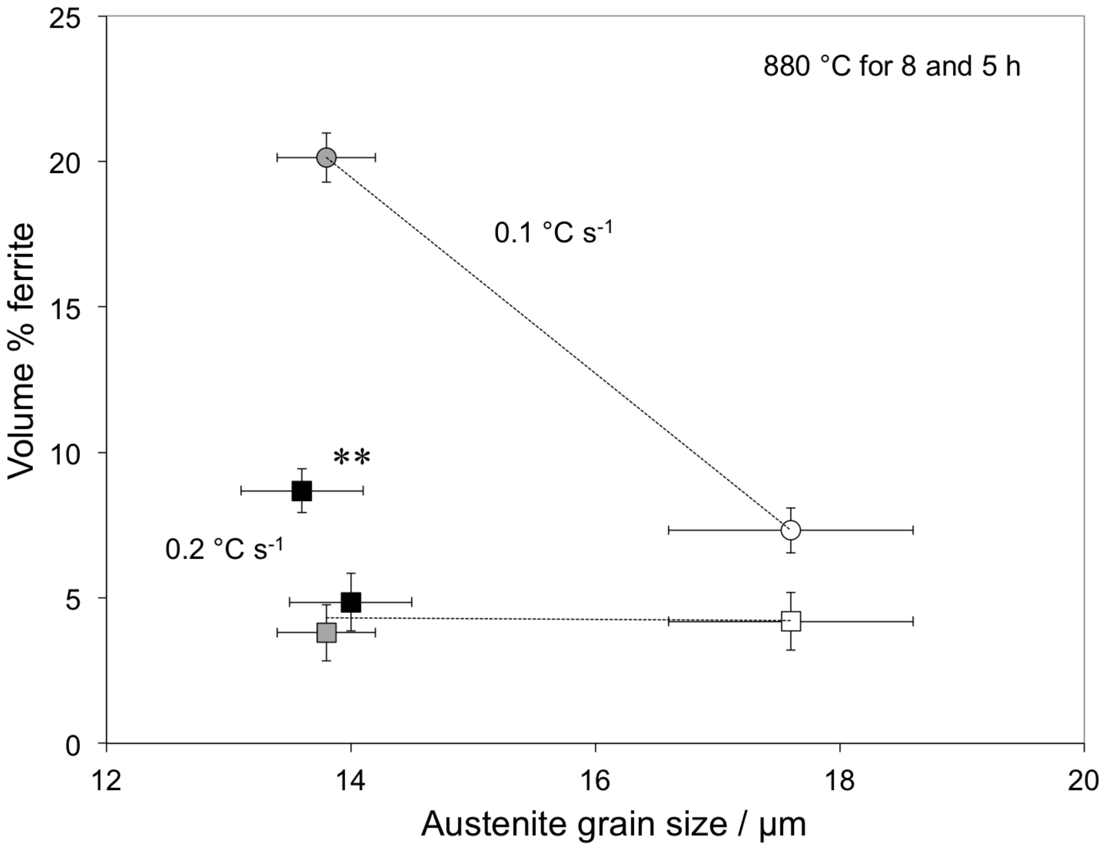

Figure 4.51: Grain size versus volume of allotriomorphic ferrite of SA508 Gr. 3 steels after austenitisation at 880 °C for 5 and 8 h. White, black and grey symbols represent alloys A, B and C respectively. ** Sample austenitised for 5 h.

4.3.1.1 Allotriomorphic ferrite transformation

The influence that $\overline{L}_\gamma$ and the magnitude of the cooling rate have on the allotriomorphic ferrite transformation is well known [151]. A larger number density of nucleation sites is obtained as $\overline{L}_\gamma$ is reduced so that the onset of allotriomorphic ferrite occurs at a smaller undercooling ($Ae3$-$Ar3$) where $Ar3$ is the onset temperature during cooling[1]. An increase in cooling rate has the opposite effect,

---

[1] The subscript r is henceforth used to identify transformation temperatures for bainite (B_{Sr}) and martensite (M_{Sr}) as well, recorded during continuous cooling. These will differ from the fundamental B_S and M_S temperatures either because undercooling occurs due to kinetic reasons or because the chemical composition of austenite is altered by prior transformation into other phases.

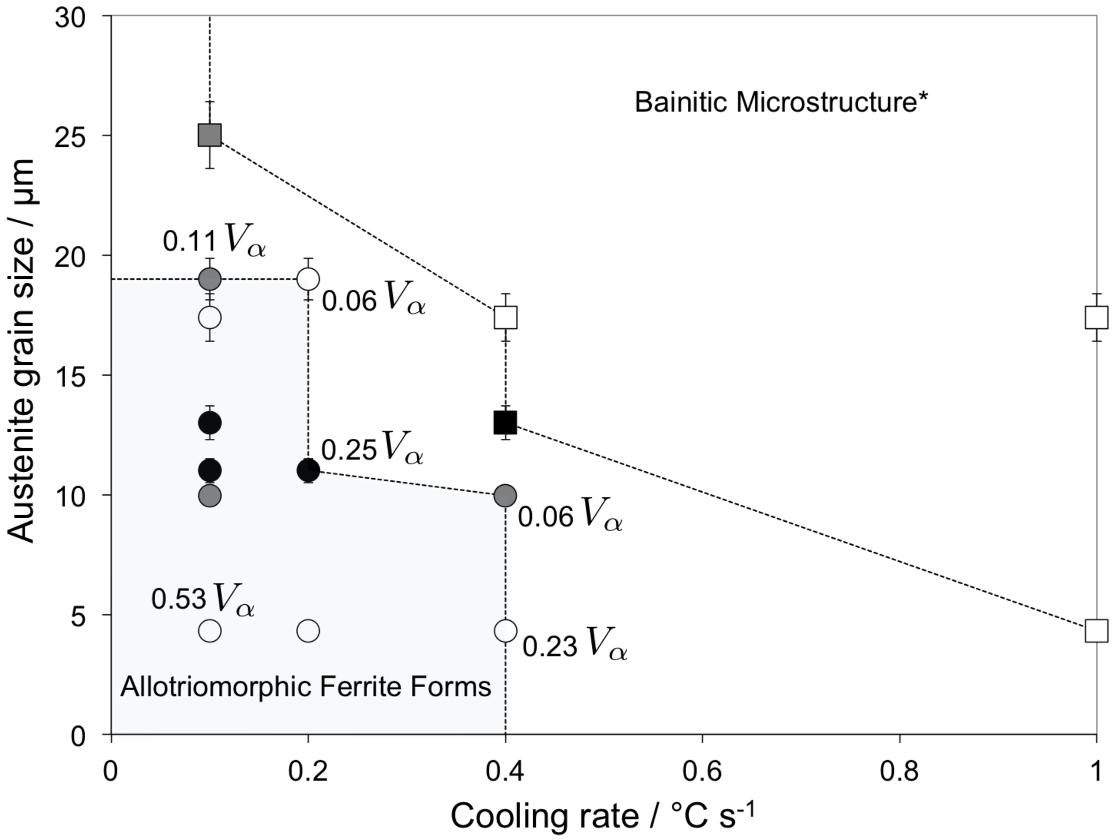

Figure 4.52: Operational framework to avoid allotriomorphic ferrite in terms of austenitic grain size and cooling rate. Volume fractions of allotriomorphic ferrite (V_α) also shown. White, black and grey colours represent Alloys A, B and C respectively. *Bainitic microstructures include a small percentage of martensitic phase.

suppressing the transformation to greater undercoolings. These effects are seen in Figs. 4.53a and b. The trends for bainite and martensite involve an additional, indirect cooling rate effect, due to the change in the austenite carbon concentration caused by preceding transformations. Therefore, a larger volume fraction of allotriomorphic ferrite (V_α) causes a greater reduction in the bainite and martensite start-temperatures, Fig. 4.53c.

The trend of B_{Sr} as a function of V_α as illustrated in Fig. 4.53c, is particularly significant from an industrial point of view. When large RPVs are manufactured,

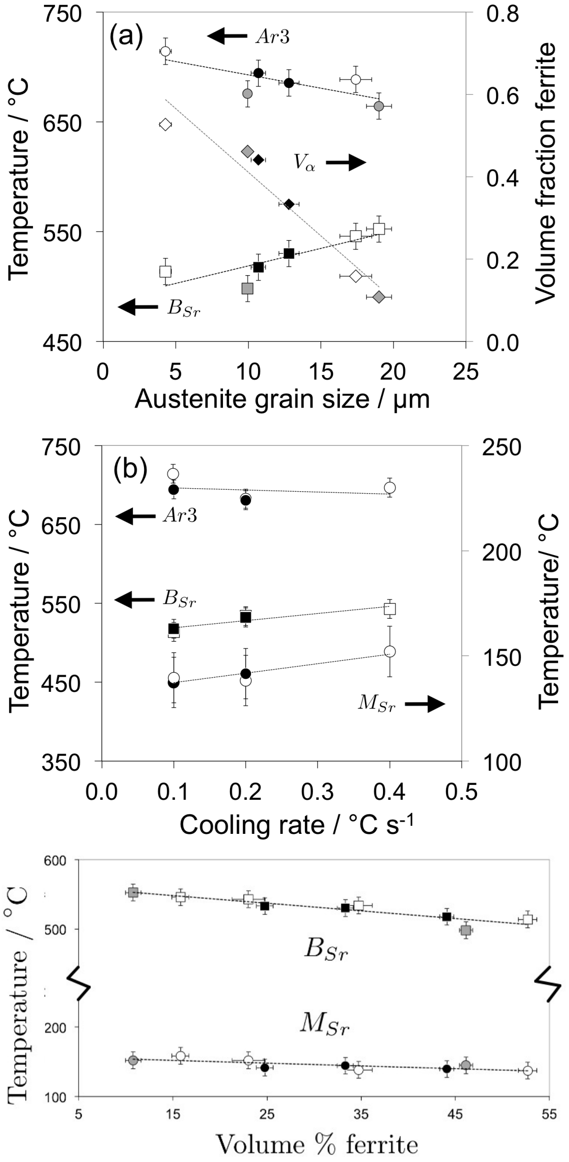

Figure 4.53: (a) Influence of the austenite grain on the onset temperatures $Ar3$ and B_{Sr} for allotriomorphic ferrite and bainite respectively, during cooling at $0.1\,°\mathrm{C\,s^{-1}}$. Volume fraction of allotriomorphic ferrite (V_α) is also plotted. (b) Cooling rate effects on transformation temperatures. M_{Sr} represents the martensite-start temperature of residual austenite, recorded in the presence of preceding phases such as allotriomorphic ferrite and bainite. (c) Volume of ferrite versus transformation temperatures. White, black and grey colours represent Alloys A, B and C respectively.

it is a common practice to attach thermocouples at different locations to record the cooling rates through the thickness. By observing typical data, it is clear that there is a pronounced reduction in cooling rate which appears in the cooling curve at bainitic transformation temperatures, Fig. 4.41. The enthalpy of transformation evolved when bainite forms modifies the natural cooling curve of the component. Figure 4.54 shows the cooling and dilatometric curves during natural cooling of Alloy A, confirming that the reduction in the cooling rate observed is due to the bainitic transformation.

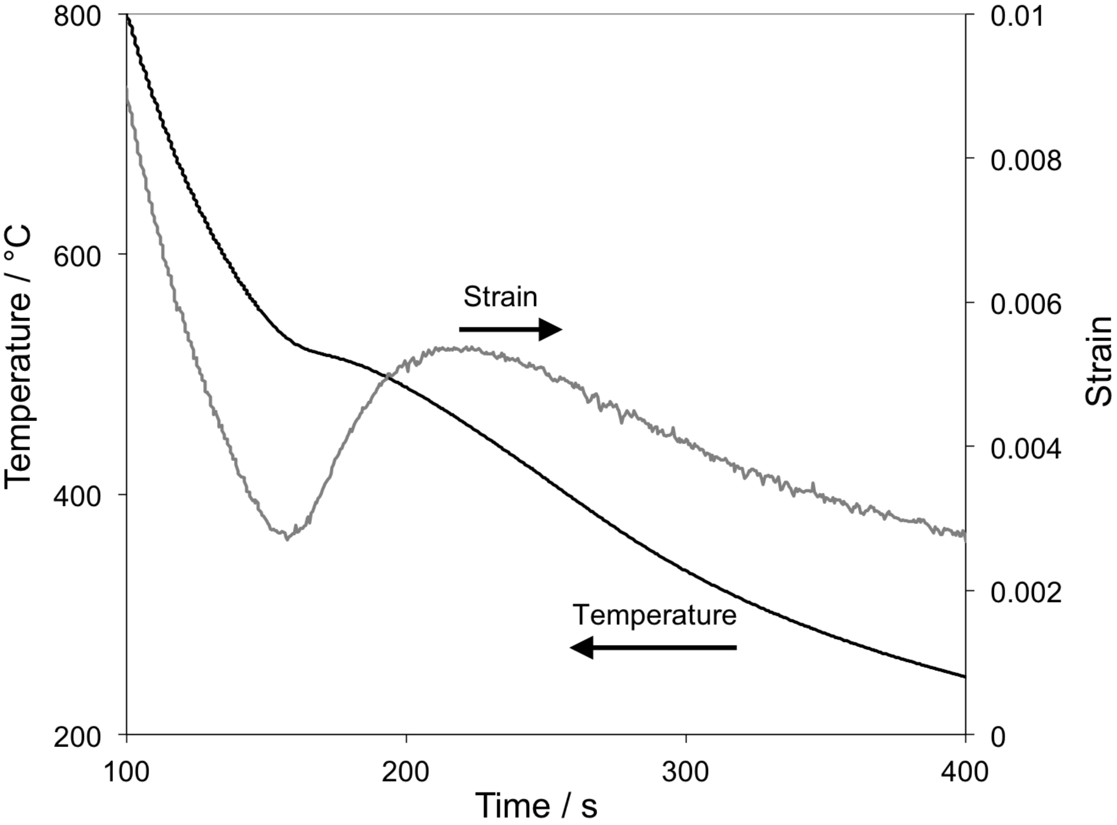

Figure 4.54: Cooling and dilatometric curves of Alloy A during natural cooling.

An entirely empirical equation based on Fig. 4.53c is proposed to help determine the volume fraction of allotriomorphic ferrite from the observed B_{Sr}

temperature in the cooling curve:

$$V_\alpha = \frac{561.53 - B_{Sr}}{102.30} \pm 0.07 \qquad \text{for} \qquad |\dot{T}| \leq 0.4\,^\circ\mathrm{C\,s^{-1}},\ \overline{L}_\gamma \leq 19\,\mu\mathrm{m} \qquad (4.20)$$

where B_{Sr} is expressed in °C.

It is necessary to justify that the observed recalescence is primarily due to bainite, without interference from allotriomorphic ferrite. Recalescence only occurs when the rate of enthalpy evolution exceeds the ability of the material to dissipate heat, i.e., when the transformation rate is large. Allotriomorphic ferrite formation is slower than the bainite reaction. Fig. 4.55 shows that even when the majority of the structure that forms is allotriomorphic ferrite, recalescence is observed only at temperatures where bainite forms.

An approximate measurement of the B_{S_r} from the cooling curve is $\sim 530\,^\circ$C. Applying Eq. 4.20, the calculated V_α is 0.31 ± 0.07. This result is coherent when compared with a sample austenitised to the same condition and cooled slightly faster, at $0.1\,^\circ\mathrm{C\,s^{-1}}$. In the case of furnace cooling, both the transformation temperature and the volume of allotriomorphic ferrite are higher, since when cooling at $0.1\,^\circ\mathrm{C\,s^{-1}}$ bainite starts to form at 545°C, and V_α is 0.16 ± 0.01 (measured using dilatometry).

4.3.2 Phase transformation behaviour on intermediate cooling rates (between 1 to $5\,^\circ\mathrm{C\,s^{-1}}$)

At intermediate cooling rates from 1 to $5\,^\circ\mathrm{C\,s^{-1}}$, the resultant microstructures after quenching from austenitisation are fully bainitic (with the mentioned small amount of martensite) independently of the austenite grain size, as seen in Figs. 4.42 and 4.56.

However, there is a clear inverse relation between $\overline{L}_\gamma$ and the B$_s$ temperature, Fig. 4.56. A grain size increase from 4 to 55 µm decreases B$_s$ by 44 °C for the case of Alloy A. As the grain size increases, there are fewer nucleation sites, hence the

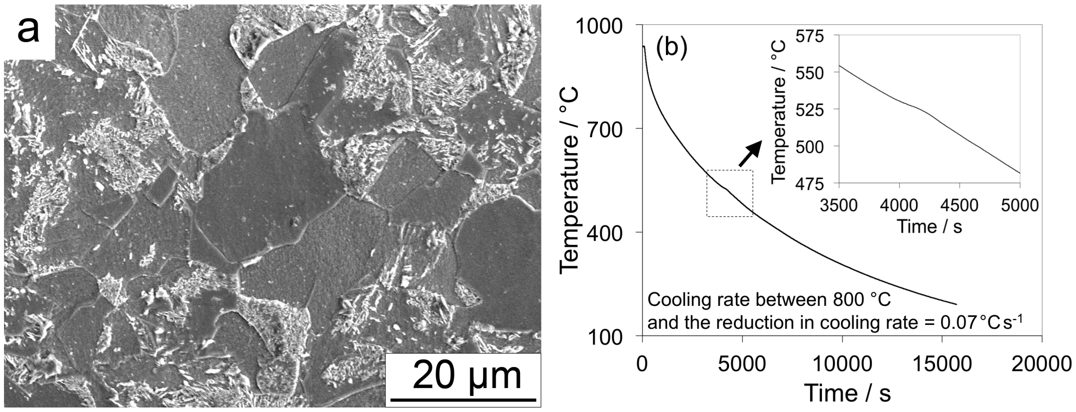

Figure 4.55: (a) SEM image of Alloy A, furnace cooled after austenitisation at 940 °C for 30 min. (b) Corresponding cooling curve measured at the surface of a cylindric (Ø 8 × 12 mm) sample. The inset is an expansion of the region of reduction in cooling rate.

temperature at which the transformation can be detected decreases. However, it is also experimentally demonstrated that for grain sizes above 60 μm, B_s is not sensitive to $\overline{L}_\gamma$ anymore, Fig. 4.56b.

SEM analyses confirm that these transformations are associated with the formation of bainite, Fig. 4.47. Microstructures reveal carbides lying parallel to the direction of habit plane traces of the bainitic ferritic plates and small austenite/martensite (M-A) islands present mostly at grain boundaries. These M-A islands are formed by the carbon rejected from the bainitic ferrite which enriches the residual austenite, thus partially stabilizing it to room temperature [152].

No consistent effect on hardness with austenite grain size is found, with all the data lying in the overall scatter band of 270 ± 6 HV for Alloy A. Similar results of independent hardness and tensile properties with austenite grain size in these nuclear pressure vessel steel have also been previously reported [65]. The lack of change in hardness with austenite grain size may be the result of the counteracting effect of decreasing transformation temperature with the increase of grain size or that the phase mixture remaining at room temperature is not function of austenite grain size.

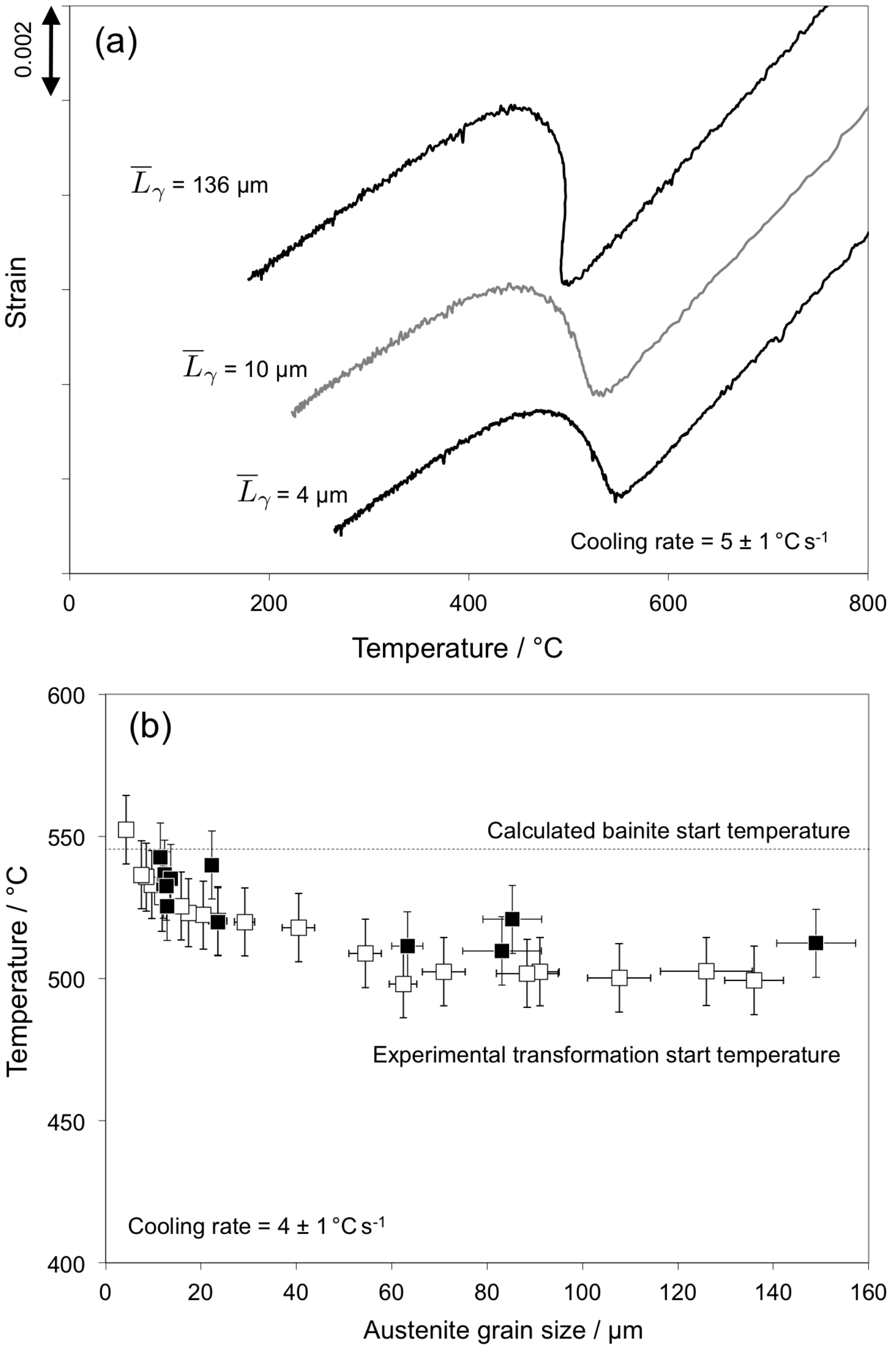

Figure 4.56: Effect of austenite grain size on transformation behaviour at intermediate cooling rates. a) Dilatometric curves for Alloy A. b) Transformation temperature. White and black symbols represent alloys A and B respectively.

4.3.3 Phase transformation behaviour on fast cooling rates ($10\,^{\circ}\mathrm{C\,s^{-1}}$ and above)

As previously described, fully martensitic structures will form at fast cooled regions, $10\,^{\circ}\mathrm{C\,s^{-1}}$ and above, in SA508 Gr. 3 steels. This phase is conventionally recognised to consist of fine platelets, each of which is approximately 0.2 μm in thickness; enhancing strength and leading to good toughness properties. However, during the course of this investigation, some extremely coarse plates of martensite were observed, which according to recent theory, result from the coalescence of, separately nucleated, adjacent laths [153–156].

It has been discovered that there are circumstances where adjacent platelets of bainite or martensite that share the same habit plane and variant of the orientation relationship with austenite tend to impinge and coalesce in the absence of intervening phases to form much coarser structures [153–155]. These coarser structures, referred to as *coalesced bainite or martensite*, form during the course of phase transformation by the merger of finer plates, each of which is separately nucleated but in the same crystallographic orientation, during prolonged growth [153, 154]. This creates a strong bimodal size distribution of plates, where coarser structures of several micrometres thick are surrounded by much finer plates, as seen in Fig. 4.57

The coalescence of martensitic structures has hardly been reported when compared to bainite for which there is a firm theoretical framework [153, 155, 157]. It is quite recent that attempts have been made to explain the formation of coalesced martensite [158]. Fat plates are associated with large strain energies since the latter scales with the thickness to length ratio [159]; the driving force for transformation must be greater than this strain energy for the coalescence to occur. It has been demonstrated, for example, that supplementing the chemical driving force by a mechanical component due to applied stress, increases the propensity for martensite plates to combine [158]. Stress-affected transformations can cause

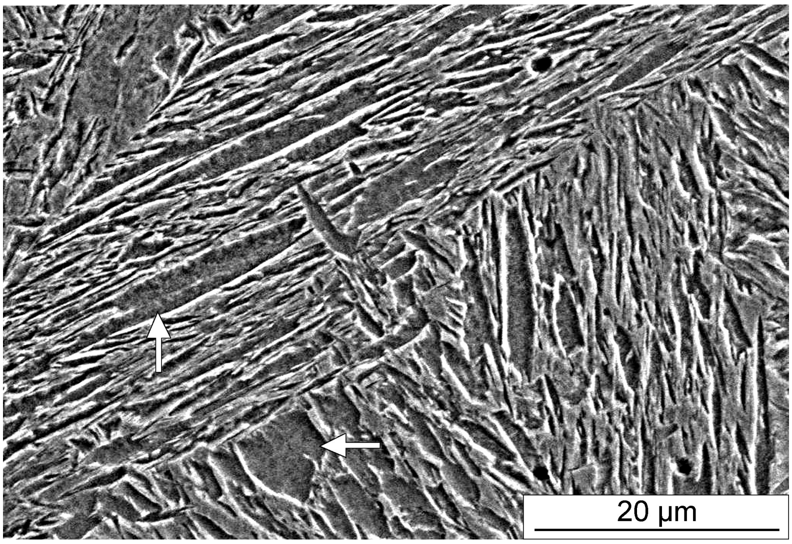

Figure 4.57: SEM of Alloy A showing clear bimodal size distribution of martensitic plates. Sample austenitised at 1200 °C for 48 h and water quenched. The arrows indicate regions where structures have coalesced.

major plate alignment with as little as 40 MPa, while stresses of 50 MPa have shown to increase significantly the formation of coalesced structures [160, 161]. Stresses of this level are quite feasible during the heterogeneous cooling of large components, such as RPV, due to thermal contractions. The effect of these combined and large driving forces during transformation can be seen in Fig. 4.57, where there is evidence that transformation under stress caused the coarse plates to align.

Such coalesced structures are known in other contexts to be detrimental to toughness, since each of the coarse plates is essentially crystallographically homogeneous and hence offers little resistance to cleavage crack propagation [153, 162, 163]. Previous studies have suggested that the process of coalescence is favoured by large undercooling below the equilibrium transformation temperature and that large austenite grain sizes must assist the process of coalescence [153]. However, it remains the case that experimental verification of the ideas is still minimal.

Therefore a systematic study of the effects of cooling rate and austenite grain

Table 4.13: Measured austenite grain sizes for the different austenitising conditions

Austenitising condition	Grain size / μm
860 °C for 1 h	7 ± 1
1150 °C for 10 min	126 ± 10
1200 °C for 48 h	221 ± 19

size on the formation of coalesced structures, and a report for the first observations of coalesced martensite in SA508 Gr. 3, with the aim of understanding the structure in order to to mitigate its consequences in an otherwise fine dispersion of martensite laths, is undertaken.

Specimens from Alloy A in the as-received condition were reheated at three different austenitising conditions; 860 °C for 1 h, 1150 °C for 10 min and 1200 °C for 48 h. Table 4.13 summarises the measured austenite grain sizes for the different austenitising conditions. The large difference in $\overline{L}_\gamma$ was intentionally engineered to gain an understanding of the consequences of grain size on the formation of coalesced martensite in SA508 Gr. 3 steels. Following austenitisation, samples were continuously cooled to obtain fully martensitic structures at cooling rates from 10 to 665 $°\mathrm{C\,s^{-1}}$.

Figure 4.58 shows the martensite obtained after austenitising at 1150 °C for 10 min, where abnormally large martensitic structures can be differentiated from an otherwise fine dispersion of martensite platelets. Figure 4.58c shows that the coalesced plates of martensite retain vestiges of their origins from individual platelets, which are the boundaries between the individual units which participated in the coalescence. This proves that the gross structure was formed by the merging of smaller plates, not the coarsening of a single plate in isolation.

Comparing the data for different cooling rates, there is evidence that changing from 10 to 40 $°\mathrm{C\,s^{-1}}$, does not increase the likelihood of finding coalesced structures or their size, when the austenite grain size is maintained, as coalesced plates with a length $\sim 20\,\mu$m and thickness $\sim 3\,\mu$m have been found regardless of the cooling rate. This agrees with the fact that the mechanism of coalescence is controlled by the driving force during transformation, and therefore, the transformation temperature [158]. Figure 4.59 shows the calculated relationship between transformation temperature and driving force for Alloy A.

Analysis of the formation of coalesced martensite reveals that the coarse structures form independently of the austenite grain size over the range examined. Figure 4.60 shows the resultant martensitic microstructure after water quenching ($80\,^{\circ}\mathrm{C\,s^{-1}}$) of SA508 Gr. 3 steel after austenitisation at 860 °C for 1 h and at 1200 °C for 48 h. Experimental results show a clear relationship between austenite grain size and the dimensions, specially the length, of coalesced plates, as suggested by Bhadeshia [153]. As the austenite grain size is reduced from 221 to $7\,\mu$m, the length of the coarse structures is reduced, from $\sim 45\,\mu$m to $\sim 7\,\mu$m, while the thickness remains similar for both cases at $\sim 3\,\mu$m (these are *apparent* values since they have not been assessed for sectioning effects). Therefore the propensity to form coalesced martensite in SA508 Gr. 3 steel is insensitive to the austenite grain size, at cooling rates where fully martensitic microstructures are formed.

This is the first report of the existence of coalesced martensite in this nuclear pressure vessel steel. However, an examination of the literature shows that these structures have appeared associated with fast cooling rates in other publications but have not been recognised as such [41, 48, 52, 164].

It is particularly interesting the case of a totally independent study on the toughness of heat affected zones of SA508 Gr. 3 steels, which reported the case of a very low value of upper shelf Charpy impact energy, 67 J, while normal values were in the order of 170 J [41]. The authors identified the structure as a coarse grained martensitic structure. However, there was no explanation given for the observed low value of impact energy. The lack of crack surface investigation from the authors in the cited article, makes it difficult to determine the specific reasons

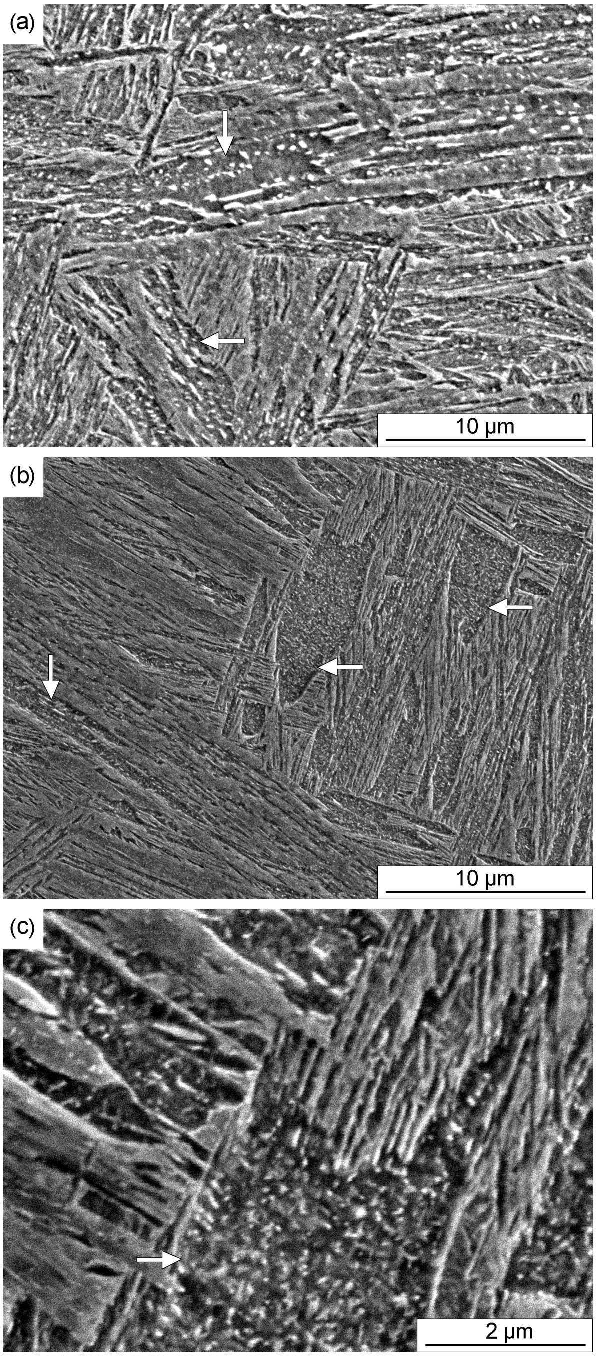

Figure 4.58: SEM micrographs of Alloy A austenitised at 1150 °C for 10 min showing coalesced martensite. A) Cooled at $10\,^{\circ}\mathrm{C\,s^{-1}}$. B) Cooled at $30\,^{\circ}\mathrm{C\,s^{-1}}$. C) High magnification image of Fig. B showing serrated edges.

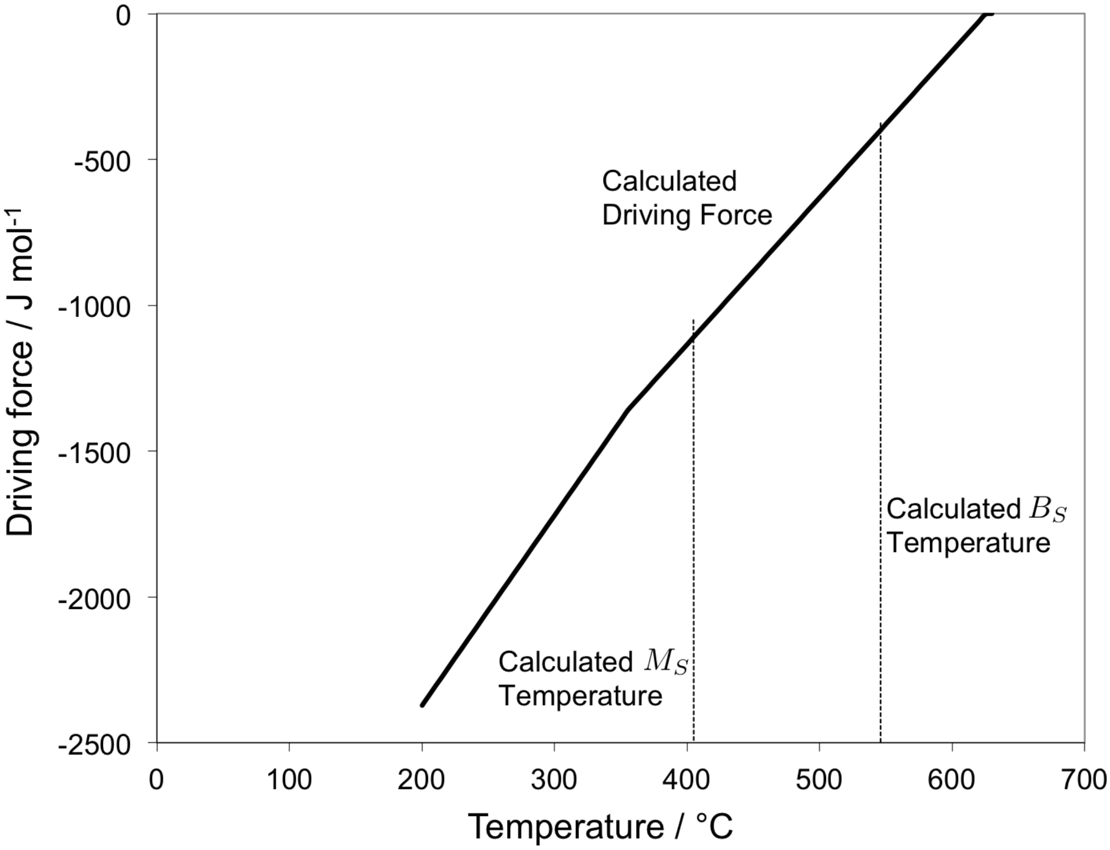

Figure 4.59: Calculated driving force versus transformation temperature for Alloy A calculated using MUCG83.

for the low value of Charpy impact energy. Nevertheless, after the findings made in the present work, it is clear that the microstructure corresponding to the sample of low impact energy (67 J) appears to be coalesced martensite, being possibly this the reason of such low toughness, Fig. 4.61. Although coarser structures are associated with lower toughness, it is noted that even the 67 J value must contain substantial ductile fracture. It is therefore necessary to understand the relation between this structure and the toughness in SA508 Gr. 3 steels.

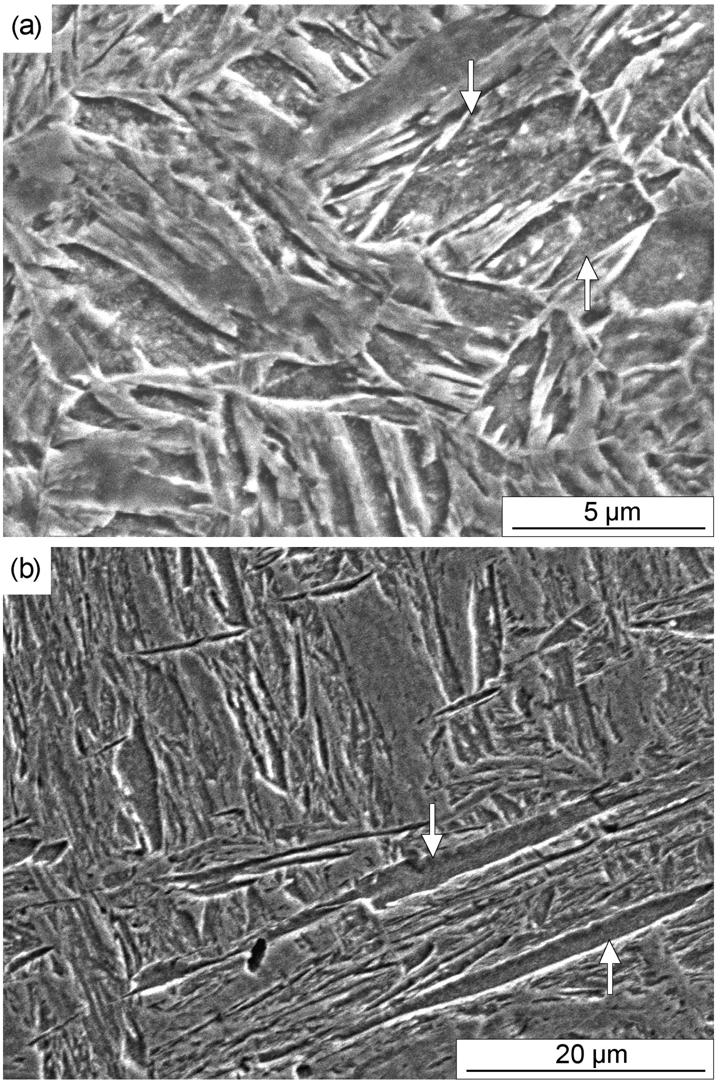

Figure 4.60: Size differences in coalesced martensite plates for different austenitic grain sizes. A) Austenitised at 860 °C for 1 h. B) Austenitised at 1200 °C for 48 h.

4.3.3.1 Coalesced martensite effects on toughness

In order to gain understanding between the size of the coarse plates and toughness, four blocks with dimensions 65×35×30 mm from Alloy C were austenitised at two very different conditions, 860 °C for 1 h and 1200 °C for 48 h, in an inert atmosphere furnace. Blocks were icy-water quenched following austenitisation, and thermocouples attached to the surface and at the centre of the blocks confirmed

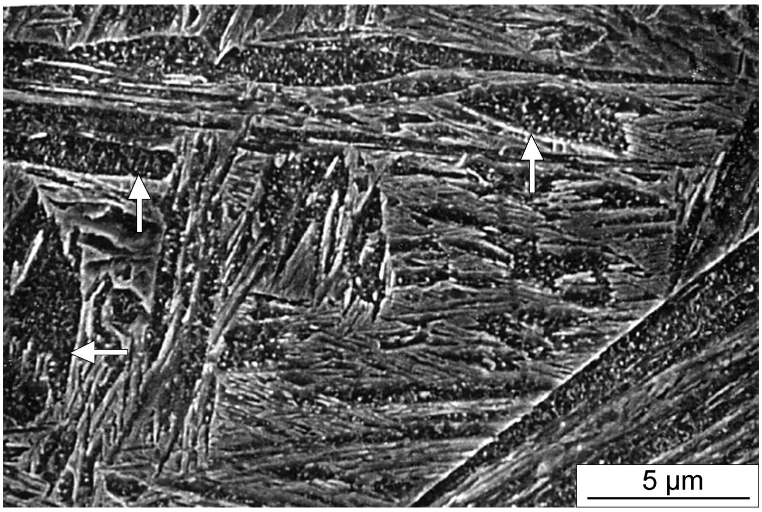

Figure 4.61: Unnoticed case of coalesced martensite in the heat affected zone of a SA508 Gr. 3 steel [41].

cooling rates in excess of 20 °C s^{-1} throughout, therefore it is assumed that the resultant microstructure was fully martensitic. Two blocks, each from a different austenitising condition, were tempered at 640 °C for 6.3 h (TP of 19 K h as defined in Eq. 2.9). Four Charpy V-notch samples were machined from each block and tested at different temperatures. Table 4.14 presents the impact energy values of the samples prior and after tempering.

Prior tempering, toughness seems to be controlled by the grain size as the small grained samples almost double in impact energy when compared with the coarse grained structures, 95 and 50 J respectively. Examination of the fracture surfaces before tempering shows two distinct fracture modes, micro-void ductile failure for the small grained samples, and cleavage brittle fracture for the coarse grained microstructures, Fig. 4.62. The transgranular failure mode observed for the two austenitising conditions may be an indication that the austenite grain size is not the unique determining factor controlling the toughness of the steel, and that the size of the coarse plates may have an effect of reducing the impact energy.

After tempering, the impact energy for the small grained samples is considerably increased to values above 250 J, even at temperatures of -50 °C, indicating

Table 4.14: Charpy impact energy for fully martensitic structure Alloy C at different conditions and temperatures. Hardness values also shown.

Austenitising condition	Austenite grain size / µm	Tempering condition	Test temperature / °C	Impact energy / J	Hardness Vickers
860 °C for 1 h	9 ± 1	-	20	95 ± 4	441 ± 4
1200 °C for 48 h	345 ± 26	-	20	50 ± 10	419 ± 3
860 °C for 1 h	9 ± 1	640 °C for 6.3 h	20	258 ± 6	234 ± 6
860 °C for 1 h	9 ± 1	640 °C for 6.3 h	-50	257 ± 3	234 ± 6
1200 °C for 48 h	345 ± 26	640 °C for 6.3 h	20	243 ± 20	240 ± 3
1200 °C for 48 h	345 ± 26	640 °C for 6.3 h	-50	251 & 56	240 ± 3

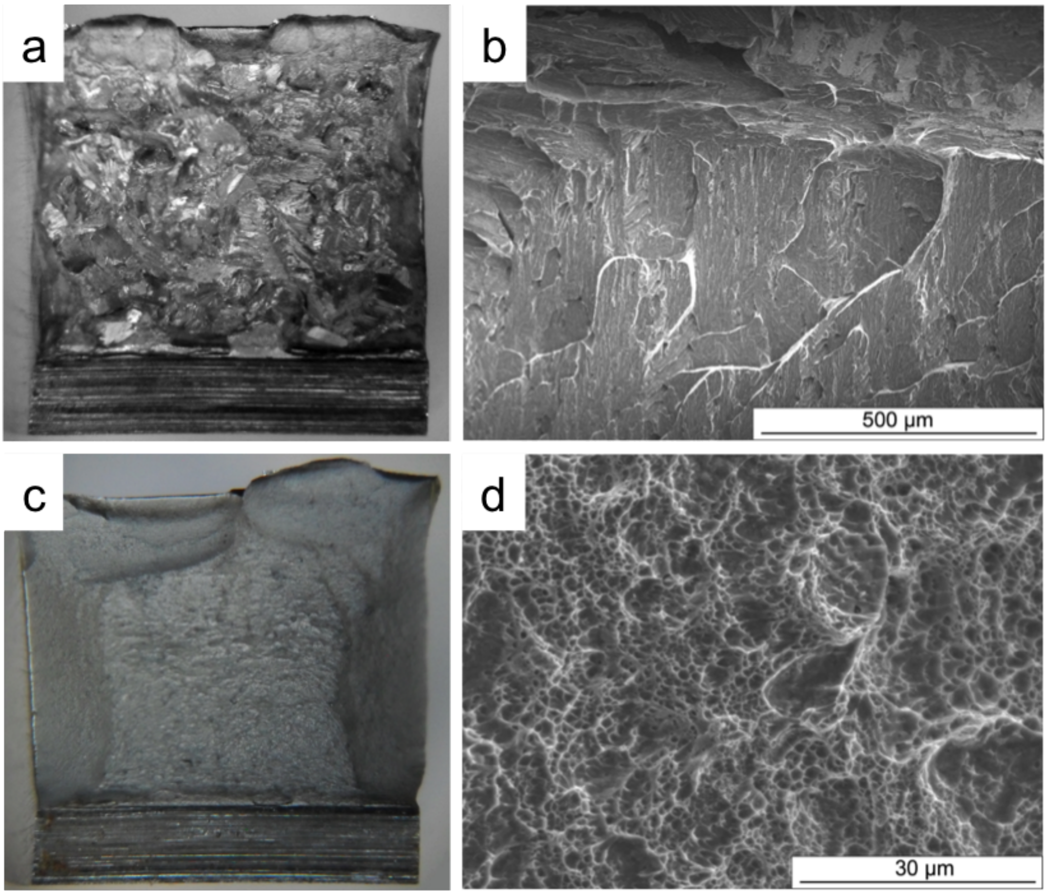

Figure 4.62: Fracture surfaces of as-quench samples prior tempering. a) Macrograph of sample austenitised at 1200 °C for 48. b) SEM of sample austenitised at 1200 °C for 48h. c) Macrograph of sample austenitised at 860 °C for 1. d) SEM of sample austenitised at 860 °C for 1.

that martensite could be a desirable microstructure in terms of toughness. This increase is the result of the combined reduction of the dislocations and the softening of the material, from 441 down to 234 HV. For the large grained case, $\overline{L}_\gamma > 300\,\mu\text{m}$, there is also an evident reduction in hardness and a general increase in toughens after tempering. However, there is a particular case in which a very low value of 56 J is obtained.

By observing the cross-section of the large grained samples with impact energies below 60 J, prior and after tempering, it is clear that the largest cleavage fracture facets are found where the coalesced plates are aligned in the direction of the crack, Fig 4.63. This is evidence that the size of the coalesced martensite plates has an effect on controlling toughness on SA508 Gr. 3 steels.

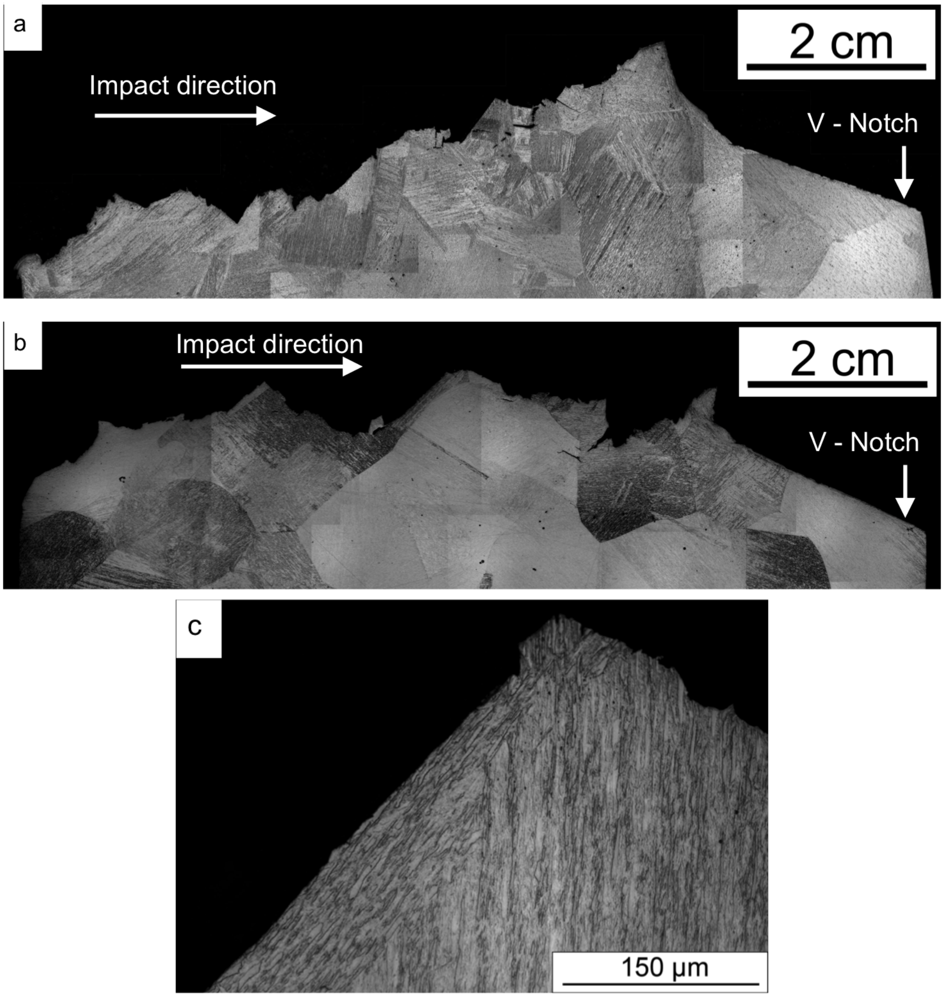

Figure 4.63: Cross-section of the fracture surfaces for the large grained microstructures, austenitised at 1200 °C for 48 h. a) As-quench sample. b) Tempered specimen. c) High magnification image showing coalesced martensite aligned in the direction of the crack.

Therefore, according to the experimental results obtained in the present investigation, by reducing the austenitic grain size, the dimensions of the coalesced martensite plates are considerably reduced. It is therefore tentatively proposed that to reduce the detrimental effect that coalesced martensite has on toughness, the austenite grain size should be maintained to a minimum, specially in the heat affected zone (HAZ) zones where large grains are present.

4.3.4 Modelling phase transformations during quenching

Phase transformation calculations during continuous cooling from austenitisiting temperatures have been performed using STRUCTURE software [165]. The theory behind the microstructure predictor model is based on decades of research at the University of Cambridge, and large parts of it have been validated independently through a variety of experimental and theoretical assessments [149, 151, 166, 167].

This software has adapted the classical Johnson-Mehl-Avrami theory for transformation kinetics, reviewed thoroughly in the work of Christian [168], to predict simultaneous transformations from austenite to allotriomorphic ferrite, pearlite and Widmanstätten ferrite as a function of the chemical composition, cooling rate and austenite grain size. Table 4.15 shows the parameters of the program.

The nucleation and growth rate for the transformation products vary as the composition of austenite and the temperature change with time during the cooling. The number of particles of phase α, nucleated at time t, is the product of the nucleation rate $I_{\alpha,t}$, the time interval Δt and the total volume of the sample V. Hence the growth of α phase particles nucleated from a boundary in a time interval t to $t+\Delta t$ becomes [151]:

$$\Delta V_{\alpha}^{e} = \sum_{t} \big(I_{\alpha,t} \, V \, \Delta t \, \nu_{\alpha,t} \, \Delta t \big) \tag{4.21}$$

where $\nu_{\alpha,t}$ is the growth rate of phase α at the current time t.

Accounting for growth of other phases and allowing for impingement with

Table 4.15: Parameters in STRUCTURE software. Adjustable parameters labelled as “Adjustable”.

Parameter	Value
Austenite Ferrite interfacial energy	Adjustable
Fraction of effective boundary sites	Adjustable
Shape factor for boundary nucleation	0.333
Mn concentration fluctuation around the mean value	0 wt%
Activation energy for atomic transfer	$200\ \mathrm{kJ\,mol^{-1}}$
Shape factor for nucleation from an inclusion	0.45
Mean inclusion diameter	0.1×10^{-12}
Total volume fraction of inclusions	0
Fraction of effective inclusions	0
Maximum number of planes parallel to grain boundary	15000
Aspect ratio of Widmastätten ferrite	0.05
Aspect ratio of allotriomorphic ferrite	3
Aspect ratio of pearlite	1
Stored energy due to deformation of austenite	0 J

particles originating from other boundaries [151]:

$$\Delta V_\alpha = \left(1 - \frac{\sum_i V_i}{V}\right) \Delta V_\alpha^e \tag{4.22}$$

where $\sum_i V_i$ is the total volume of phases transformed and V is total volume of the sample. Then the total volume of each phase at a time t can be calculated by [151]:

$$V_{i,t} = V_{i,t-1} + \Delta V_i \tag{4.23}$$

Experimental work has not given any indication of pearlite or Widmanstätten ferrite formation in SA508 Gr. 3 for the conditions studied here. Consequently, formation of pearlite or Widmanstätten ferrite has bee suppressed in the STRUCTURE software allowing only formation of allotriomorphic ferrite at high temperatures. According to theory from Cristian, the formation of a nucleus is not an homogeneous process occurring with equal probability in all parts, this is unlikely to happen [168]. During continuos cooling and depending of the difference in free energy between the austenite and the allotriomorphic ferrite, nucleation will dominate at grain boundaries, at edges (where three grains meet) or at corners (where four grain meet) [168].

The model in STRUCTURE used to calculate the nucleation and growth of allotriomorphic ferrite assumes that the nucleation of this phase occurs at austenite grain boundaries. In order to enhance the observed influence of the austenitic grain size on the final amount of the displace phase, the effect of nucleation from edges and corners has been implemented into the exiting software. Thus two new fitting parameters, factor for nucleation from edges and from corners, have been added to the previously described in Table 4.15.

To find the best combination of fitting parameters to represent the transformation behaviour of this low alloy steel, more than 34,000 combinations for the adjustable parameters were compared against experimental results, Table 4.16. Experiments have proven that allotriomorphic ferrite may form in SA508 Gr. 3

Table 4.16: Range of adjustable parameters used to find the best representation of allotriomorphic ferrite formation in SA508 Gr. 3 steels.

Parameter	Range	Interval	Best combination transformation modelling	Best combination final amount modelling
Austenite Ferrite interfacial energy	0.01 to 0.03 $\mathrm{J\,m^{-2}}$	5×10^{-4}	0.0325 $\mathrm{J\,m^{-2}}$	0.0400 $\mathrm{J\,m^{-2}}$
Fraction of effective boundary sites	2.5×10^{-12} to 1×10^{-8}	5×10^{-12}	6.5×10^{-12}	5.5×10^{-10}
Factor for nucleation from edges	0 to 0.25	0.05	0.05	0.20
Factor for nucleation from corners	0 to 0.25	0.01	0.02	0.02

steels at cooling rates up to 0.4 °C s^{-1} when the austenite grain size is less than 13 μm. During the course of this investigation, 13 tests for different austenitic grain sizes with cooling rates up to 0.4 °C s^{-1} have been performed for the three alloys under investigation. This seemed a rather small number of tests to be used to optimise the fitting parameters of the STRUCTURE software for the total amount of allotriomorphic ferrite as a function of composition, austenite grain size and cooling rate. Then, with the aid of the valuable data obtained from dilatometric tests, the kinetics of the formation of allotriomorphic ferrite from 720 to 600 °C have been modelled and compared to the experimental. In particular for each of the 13 testing curves, 122 points have been extracted, making a total of 1586 data points to compare between experimental and calculated to build a robust model to represent the data. The best combination of parameters to calculate the final amount and the evolution of allotriomorphic ferrite during cooling are given in Table 4.16. The error, measured as the root mean square error, for the calculated vol. fraction is 8×10^{-2} for both cases.

Figure 4.64a shows the comparison between the predicted and experimental formation of allotriomorphic ferrite during slow cooling, where transformation trends are appropriately represented even for unseen data. Figure 4.64b compares the measured and calculated final amounts of this phase.

Another output obtained in the STRUCTURE software is the carbon enrichment of the untransformed austenite as the ferritic transformation progresses. As previously discussed in Section 4.3.1.1, the increase in carbon content in the residual austenite plays a role in suppressing the following transformations to lower temperatures. By using the calculated carbon enrichment for a given volume fraction of allotriomorphic ferrite, it is possible to estimate, with MUCG83, the B_s temperature. Figure 4.65 shows the calculated carbon enrichment in the untransformed austenite as the allotriomorphic ferrite transformation progresses. Furthermore, the figure also compares the calculated and experimental B_s temperatures showing reasonable agreement.

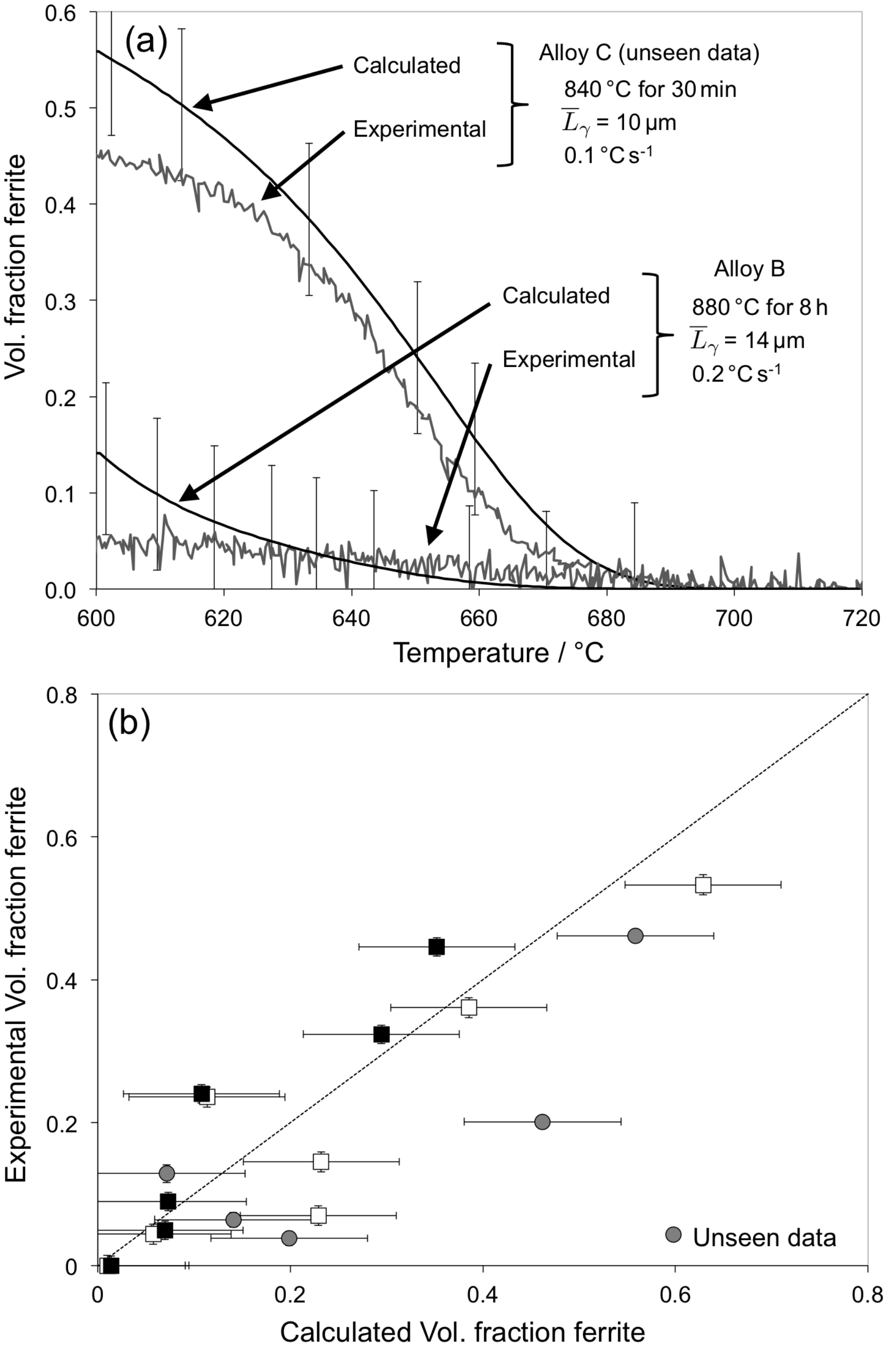

Figure 4.64: Calculated and experimental volume fraction of allotriomorphic ferrite. a) Evolution of ferrite with temperature. b) Final amount at room temperature. White, black and grey colours represent Alloys A, B and C respectively.

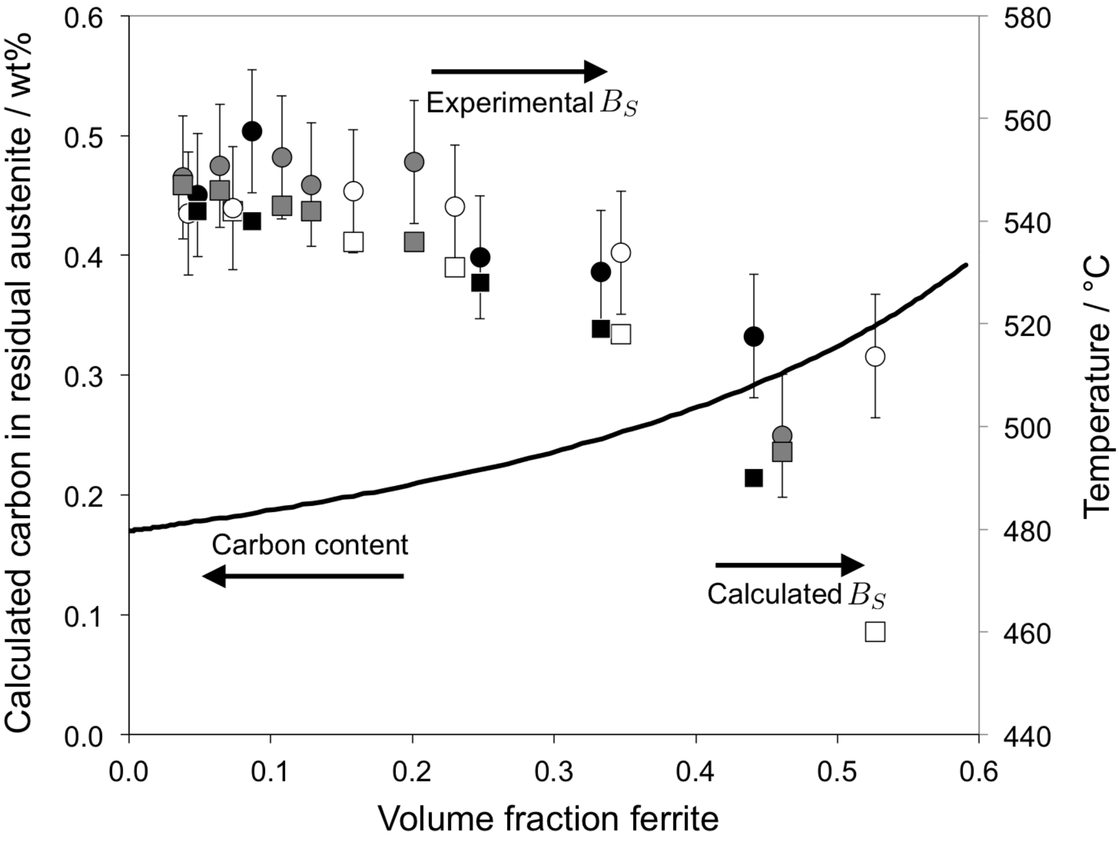

Figure 4.65: Calculated carbon in the residual austenite as a function of volume fraction of ferrite. Calculated and experimental B_s also shown. White, black and grey colours represent Alloys A, B and C respectively.

4.4 Tempering

The last stage in the quality heat treatment is the tempering, typically at 640 °C for many hours. There is an extensive literature on the microstructural evolution of fully bainitic samples of SA508 Gr. 3 steels after tempering as seen in Section 2.7. Thus, an analysis of the new structural features found during the course of this investigation is undertaken.

4.4.1 Tempering microstructures containing allotriomorphic ferrite

The study of samples containing a mixture of bainite and allotriomorphic ferrite reveals that the small austenite/martensite islands present mostly at grain boundaries have disappeared after the tempering process, and also there is a noticeable increase in cementite precipitation at the allotriomorphic ferrite/bainite interface.

Fig. 4.66 compares the microstructure of Alloy C after austenitisation at 840 °C for 30 min cooled at $0.1\,^{\circ}\mathrm{C\,s^{-1}}$, before and after tempering at 640 °C for 6.3 h. It is evident that the small austenite/martensite islands present mostly at grain boundaries have disappeared after the tempering process, and also there is an increase in cementite precipitation at the allotriomorphic ferrite/bainite interface. Cementite along grain or lath boundaries has been claimed to be detrimental to the toughness of pressure vessel steels [38, 46].

Detailed TEM investigation of the tempered sample revealed large cementite precipitates at the ferritic grain boundaries, Fig. 4.67. Furthermore, several aligned rows of precipitates are observed inside the allotriomorphic ferrite. This may be a sign of *interphase precipitation* that occurs at the α/γ interface during the course of transformation [169]. This may harden the ferrite but any consequences on properties such as toughness is the basis of the future extensive programme of mechanical testing as a function of structure.

4.4.2 Tempering of coalesced structures

It has been shown that coalesced martensite will form in rapidly cooled regions of the SA508 Gr. 3 forgings. It is important to understand how these coarse structures evolve after tempering. Therefore, a sample from Alloy A austenitised at 1150 °C for 10 min and icy-water quenched was tempered at 660 °C for 6.2 h. Scanning electron microscopy confirmed the presence of coarse structures following tempering, Fig. 4.68. The larger carbides tended to decorate the plate boundaries, thus revealing the coarse scale of some of the tempered coalesced-martensite. The results show that the large coalesced martensite plates are re-

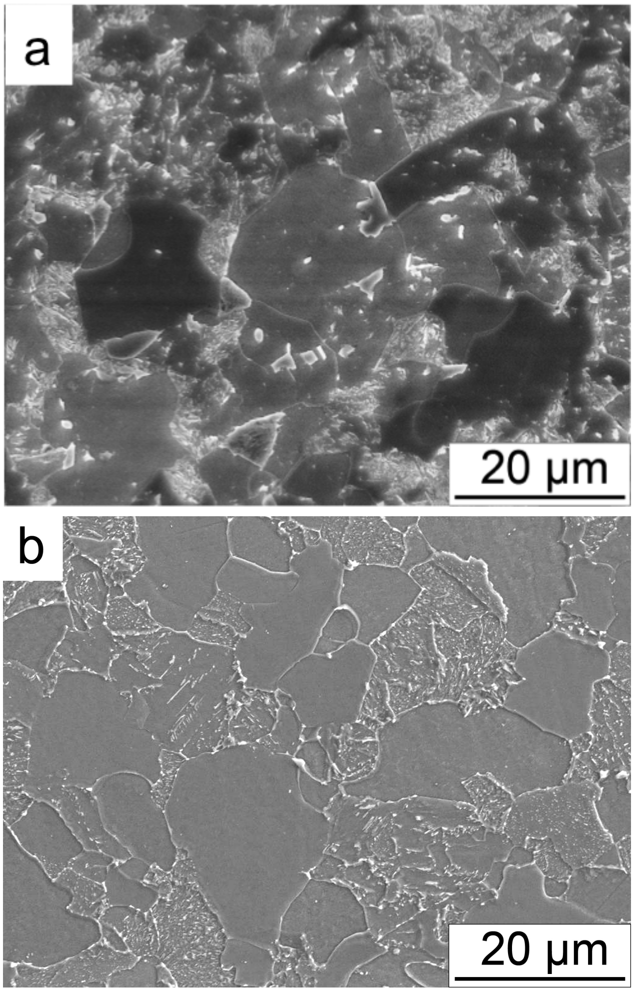

Figure 4.66: Microstructure of Alloy C austenitised at 840 °C for 30 min and cooled at 0.1 °C s^{-1}. a) Before tempering. b) After tempering at 640 °C for 6.3 h.

tained in the tempered microstructure.

4.4.3 Re-austenitisation during tempering

Thermodynamic calculations predict that austenite phase starts to form at 660 °C in SA508 Gr. 3 steels. Pressure vessel can be tempered at temperatures as high as 660 °C (as for example in [41, 42, 48, 67]). Consequently, there is a concern that the material may re-austenitise during the tempering, particularly as heating rates for large components are very low, ~ 0.01 °C s^{-1} . Hence, understanding the

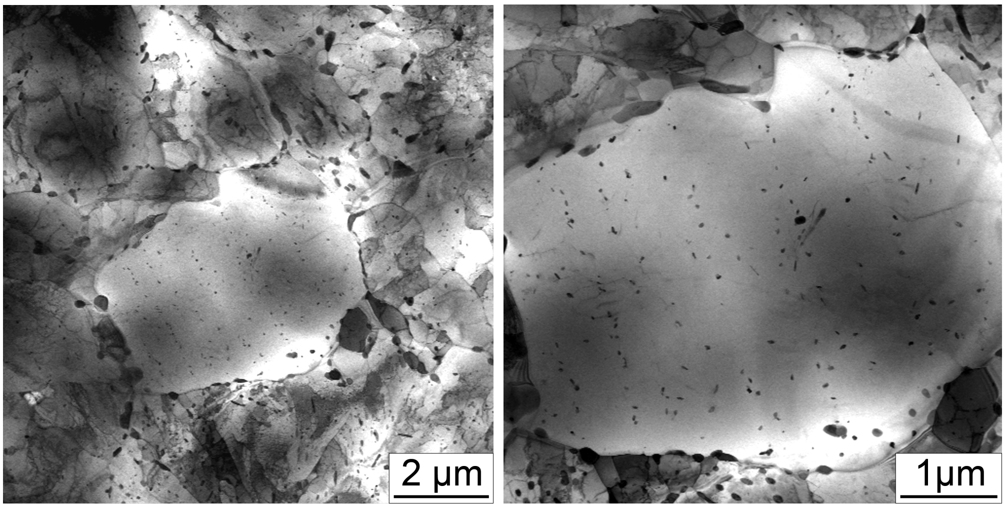

Figure 4.67: TEM microstructure of Alloy C austenitised at 840 °C for 30 min and cooled at 0.1 °C s^{-1} after tempering.

effect that the heating rate has on the austenite transformation temperature Ac$_1$ is crucial to avoid austenite formation during the tempering stage. Dilatometric tests were performed during heating of Alloy A to austenitisation temperatures and the transformation temperatures recorded for various conditions.

Experimental results show that even for the slow commercial heating rate (0.01 °C min^{-1}) there is a safety margin above 50 °C between the tempering temperature and the initial temperature for austenite formation. When increasing the heating rate, less time is available for austenite formation as a thermally activated process to take place, leading to a shift to higher transformation temperatures. This phenomenon is more noticeable at heating rates above 1 °C s^{-1}, where the transformation temperature Ac$_1$ increases by 24 and 46 °C, respect previous heating rates. These effects are summarised in Fig. 4.69.

4.5 Mechanical properties programme

An extensive programme of mechanical properties has been undertaken to understand how findings from this thesis may affect properties. Effects of austenite grain size, cooling rate and tempering parameter have been assessed by means

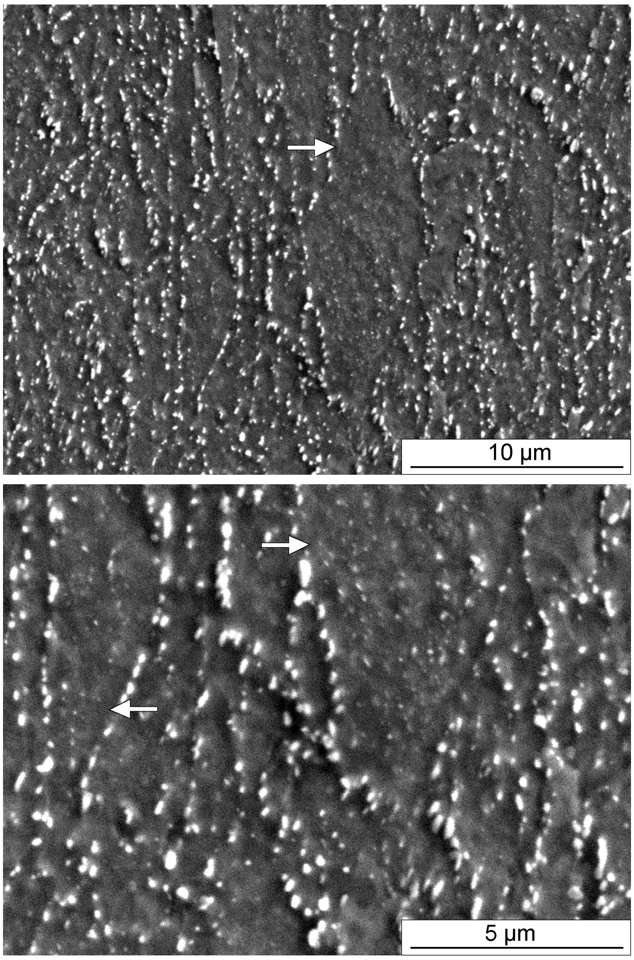

Figure 4.68: SEM micrographs of SA508 Gr. 3 Alloy A austenitised at 1150 °C for 10 min showing coalesced martensite after tempering.

of tensile strength, Charpy impact energy and hardness. 200 mm diameter discs, with different thicknesses, were quality heat treated at 18 conditions, varying austenitisation temperature, cooling media and tempering time, as summarised in Fig. 4.70. Testing was performed for Alloy C.

Austenitisation temperatures were chosen to reflect the current industrial processing (880 °C for 8 h) and a high temperature case to accelerate austenite grain growth (965 °C for 8 h). The measured austenite grain sizes for the two conditions under investigation were 14 ± 1 and 68 ± 4 μm, respectively. Figure 4.71

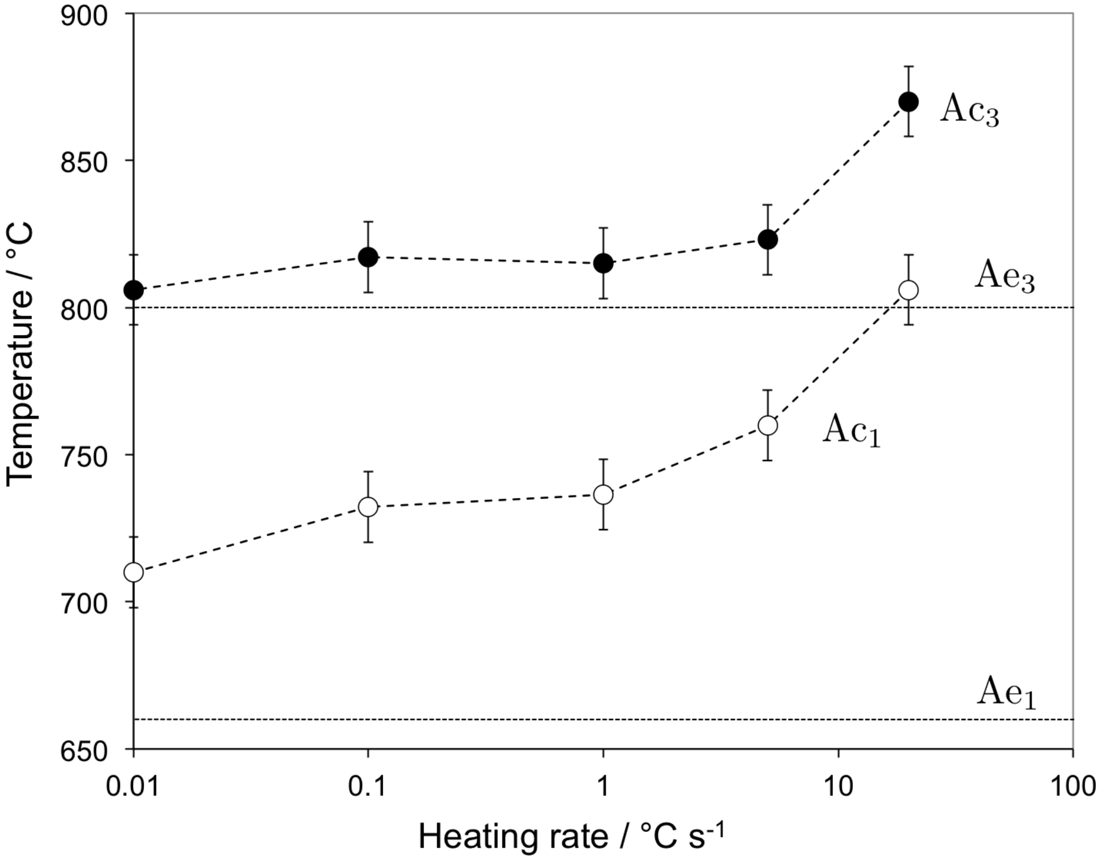

Figure 4.69: Effects of heating rate on austenite transformation temperatures on as-received Alloy A.

shows the thermal etching images revealing the difference in grain sizes. Cooling rates reproduce the conditions through the thickness of a RPV. The tempering is aimed to cover a range of TP from 18.5 K h to 19.5 K h (as defined in Eq. 2.9). This range is larger than would be achieved by commercial heat treatments, but it is used to understand the tempering behaviour in SA508 Gr. 3 steels. The tempering was carried out at 640 °C and the different tempering parameters were achieved by varying the holding time.

In order to asses the influence of the tempering on the properties, the full heat treatment given to the components during the tempering stage has to be accurately determined. It is common practice to asses the TP from the isothermal

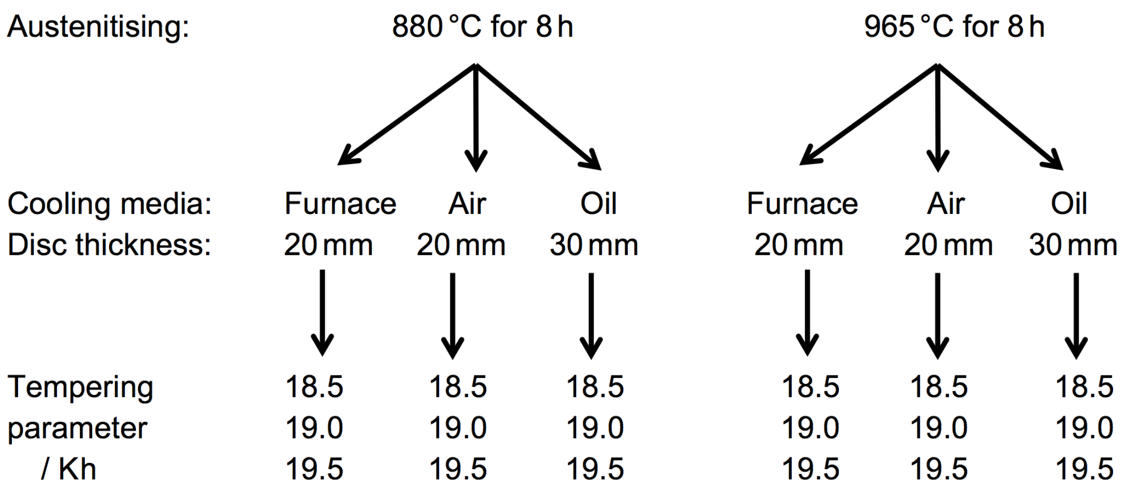

Figure 4.70: Summary of the mechanical properties experimental programme.

holding time and temperature (as presented in Eq. 2.9). However, it is necessary to account for the effect that the heating/cooling may have on the time that components have to be maintained at the isothermal tempering temperature to achieve a specific TP. Tsuchiyama proposed a model to account for the effect of a non-linear thermal cycle, such as heating and cooling, has on the TP, obtaining an equivalent time at the tempering temperature. The model is as follows [170]:

$$\begin{gathered} \mathrm{TP} = T_{max}(\log(t_{eq} + t_{th}) + 20) \times 10^{-3} \\ \text{with } t_{eq} = \sum_{i=1}^{t} 10^{\left[(T(t_{i-1})\,/\,T_{max}) \times (20 + \log(t_i - t_{i-1}) - 20\right]} \end{gathered} \tag{4.24}$$

where, T_{max} is the tempering temperature in Kelvin, t_{th} the isothermal holding time in hours, t_{eq} the equivalent time at tempering temperature due to the heating/cooling cycles in hours, t_i the time step in hours and T the temperature for each time step in Kelvin. When considering the effects of the heating and cooling the isothermal holding times are reduced.

Accounting for the effects of slow heating and coolings cycles on large components such as RPVs, where commercial heating rates up to reaching the tempering temperatures are about $40\,^{\circ}\mathrm{C\,h^{-1}}$, should became a standard practice as design

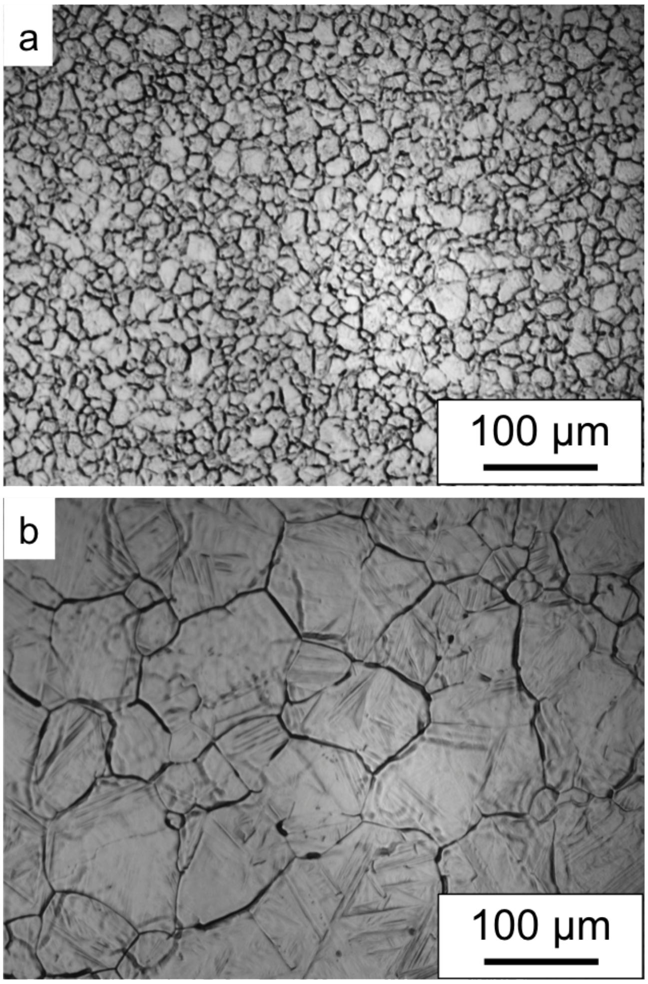

Figure 4.71: Thermal etching images revealing austenite grain size for Alloy C. a) Austenitised at 880 °C for 8 h. b) Austenitised at 965 °C for 8 h

properties may not be met due to the extended tempering as a result of not considering heating/cooling cycles.

In the present programme, Eq. 4.24 has been used to assess the effects of heating and cooling cycles on the tempering parameter. Table 4.17 summarises the isothermal times to achieve the desired TP.

From each disc, 20 standard Charpy V-notch samples (ASTM E23 [171]) and two tensile samples (ASTM A370 [172]) were obtained. To avoid orientation

Table 4.17: Isothermal tempering times and TP achieved by considering the heating and cooling steps.

Design TP / K h	Isothermal holding time / h	Experimental TP / K h
18.5	1.75	18.5
19.0	6.35	19.0
19.5	22.58	19.5

Table 4.18: Recorded cooling rates for the different conditions.

Austenitising temperature / °C	Cooling media	Cooling rate / °C s^{-1}
880	Furnace	0.17
880	Air	1.61
880	Oil	12.30
965	Furnace	0.23
965	Air	1.81
965	Oil	11.47

dependence of properties, test specimens were machined following the original axial direction of the forging. Charpy specimens were tested at temperatures between -196 to 250 °C to obtain ductile-brittle transition curves. Tensile tests were performed at room temperature and at 354 °C, the design temperature of reactors. Cooling rates were monitored by thermocouples attached to the mid-thickness of the discs, Table 4.18 gives the different cooling rates for the three cooling medias.

4.5.1 As-quenched microstructure

For detailed microstructural analyses after cooling in different media, specimens were observed by SEM, Fig. 4.72. As predicted by the previous finding in this thesis, allotriomorphic ferrite forms at the slowest cooling rate for the low austenitisation temperature. By contrast, by austenitising at 965 °C, the austenite grain size increases up to 68 µm suppressing the formation of allotriomorphic ferrite for slower furnace cooling, $0.23\,°\mathrm{C\,s^{-1}}$. Samples air cooled present a bainitic microstructure as rates are above $1\,°\mathrm{C\,s^{-1}}$, the previously determined limit to avoid formation of allotriomorphic ferrite at all austenite grain size. Although recorder temperatures in the thermocouple for the oil quenched samples are above $10\,°\mathrm{C\,s^{-1}}$, the specific cooling rate for the individual samples is $9.62 \pm 0.4\,°\mathrm{C\,s^{-1}}$ and $8.71 \pm 0.5\,°\mathrm{C\,s^{-1}}$ for the low and high austenitisation temperatures respectively. Consequently, the microstructure will be a mixture of bainite and martensite. Due to the smaller size of the austenite, samples heated to 880 °C appear to contain less amount of martensite as the decrease in the austenite grain size leads to acceleration of grain boundary nucleated bainite reaction.

4.5.2 Tempered microstructures

The morphology of the microstructures does not change much after tempering, although the carbide precipitation is somewhat increased, Fig. 4.73 to 4.75. Increased tempering times, also increase the inter-granular precipitation for the bainitic and martensitic samples. Interphase precipitation is observed inside the allotriomorphic ferrite grains in specimens tempered for short times (TP of 18.5 and 19.0 K h), however, at long tempering times (TP 19.5 K h $\sim$23 h) these precipitates tend to disappear, Figs. 4.73a, 4.73c and 4.73d. The apparition of large precipitates at the allotriomorphic ferrite grain boundaries may suggest that the precipitates have been reabsorbed and the excess of carbon has precipitated out at grain boundaries.

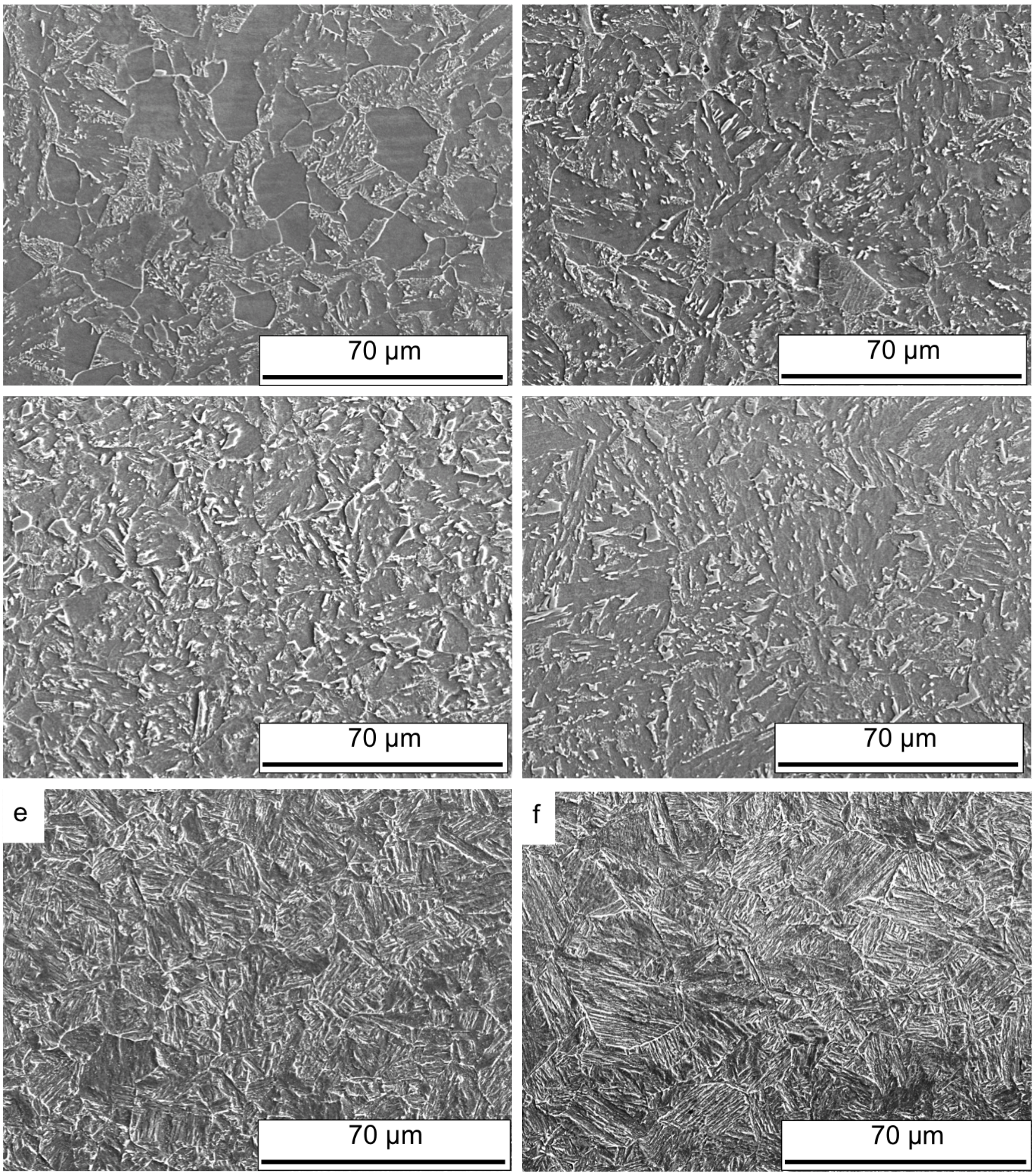

Figure 4.72: As quench SEM microstructures. a) Austenitised at 880 °C and furnace cooled. b) Austenitised at 965 °C and furnace cooled. c) Austenitised at 880 °C and air cooled. d) Austenitised at 965 °C and air cooled. e) Austenitised at 880 °C and oil quenched. f) Austenitised at 965 °C and oil quenched.

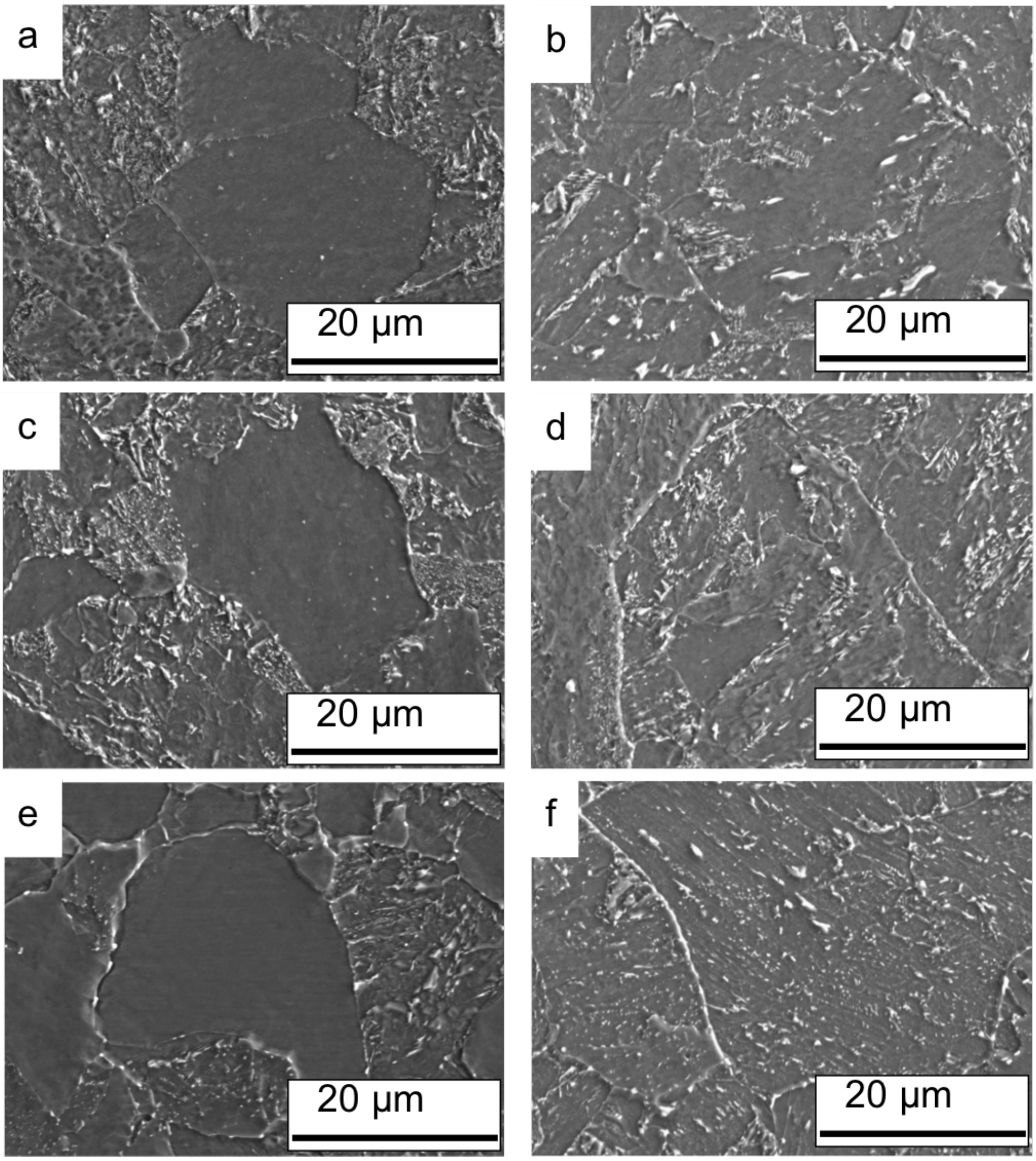

Figure 4.73: SEM microstructures of the vacuum cooled samples after tempering. a) Austenitised at 880 °C, TP = 18.5 K h. b) Austenitised at 965 °C, TP = 18.5 K h. c) Austenitised at 880 °C, TP = 19.0 K h. d) Austenitised at 965 °C, TP = 19.0 K h. e) Austenitised at 880 °C, TP = 19.5 K h. f) Austenitised at 965 °C, TP = 19.5 K h.

4.5.3 Mechanical properties

Figure 4.76 presents the hardness evolution for the different cooling medias and austenitising conditions as a function of tempering time. As a general trend,

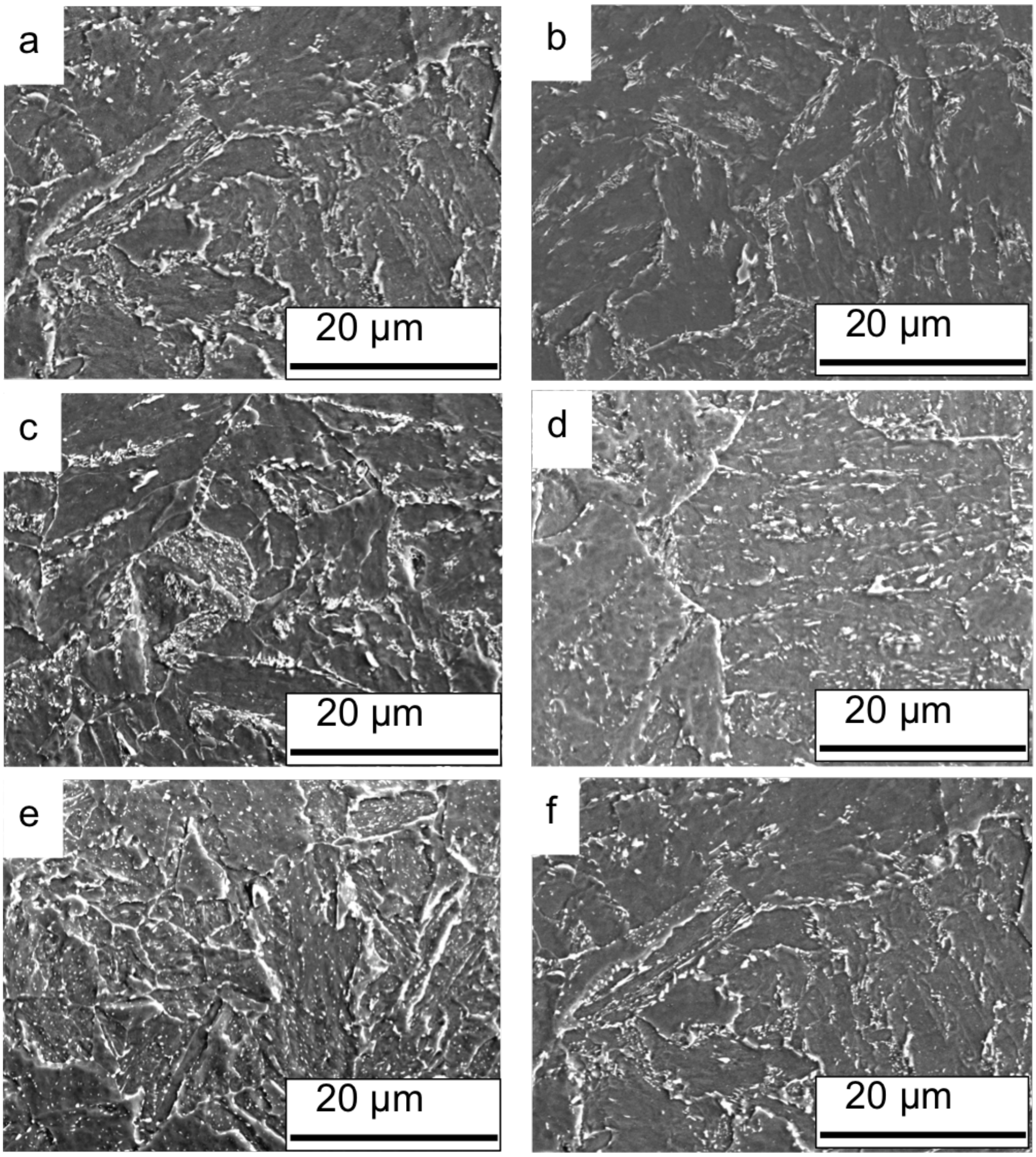

Figure 4.74: SEM microstructures of the air cooled samples after tempering. a) Austenitised at 880 °C, TP = 18.5 K h. b) Austenitised at 965 °C, TP = 18.5 K h. c) Austenitised at 880 °C, TP = 19.0 K h. d) Austenitised at 965 °C, TP = 19.0 K h. e) Austenitised at 880 °C, TP = 19.5 K h. f) Austenitised at 965 °C, TP = 19.5 K h.

increasing the tempering time reduces the hardness of the steel as a result of dislocation reduction and carbide precipitation. Experimental results have shown

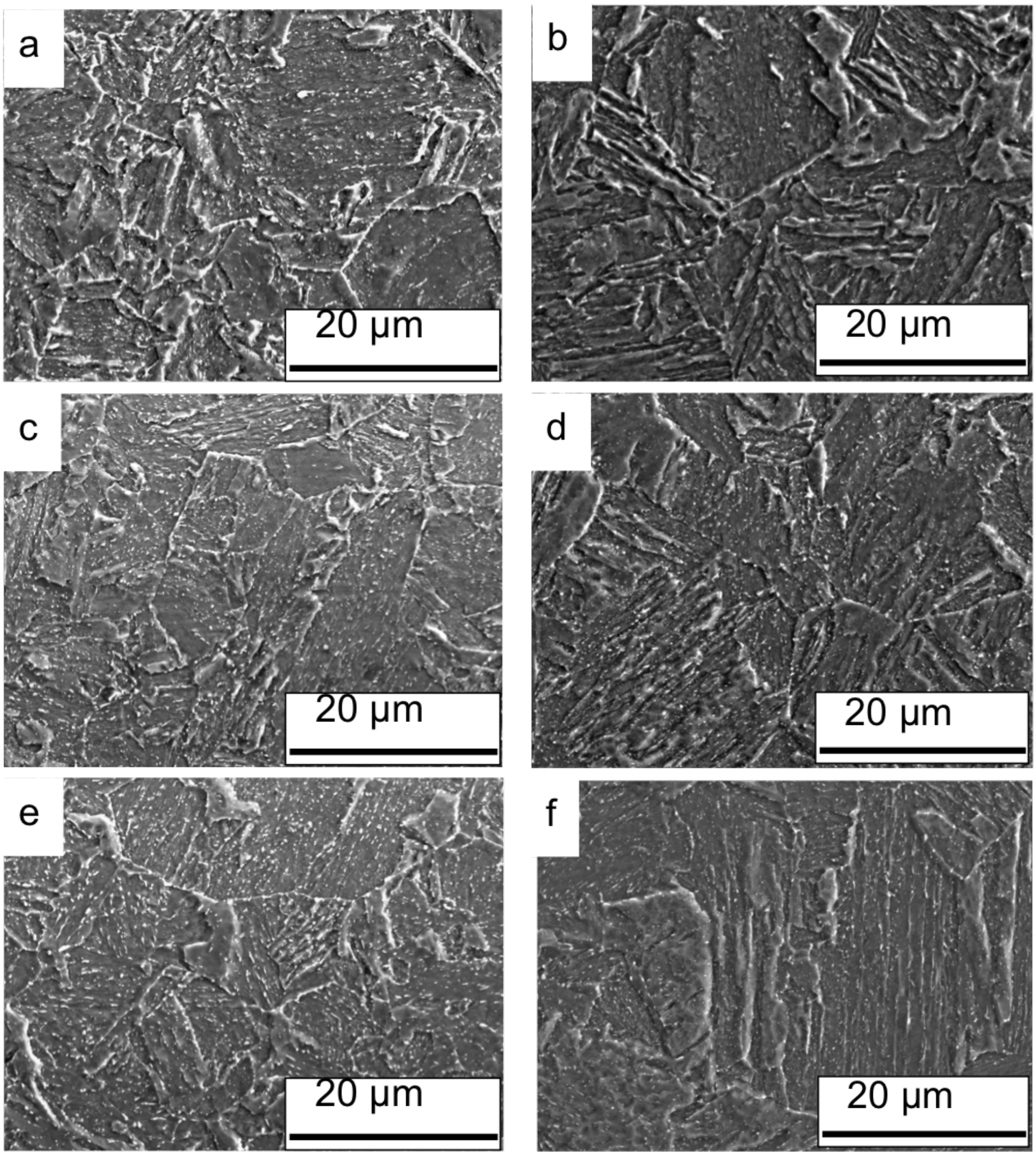

Figure 4.75: SEM microstructures of the oil quenched samples after tempering. a) Austenitised at 880 °C, TP = 18.5 K h. b) Austenitised at 965 °C, TP = 18.5 K h. c) Austenitised at 880 °C, TP = 19.0 K h. d) Austenitised at 965 °C, TP = 19.0 K h. e) Austenitised at 880 °C, TP = 19.5 K h. f) Austenitised at 965 °C, TP = 19.5 K h.

that the largest reduction in hardness is found between the state prior tempering and the sort tempering time of just below two hours. When comparing the material hardness for the different austenitising temperatures, results are linked to the microstructures.

For the furnace cooled samples, the lower hardness measured for the 880°C samples is due to the the formation of allotriomorphic ferrite. The hardness differences for the two austenitising conditions after air cooling, which present bainitic microstructures, are minimal and between the experimental error. This agrees with previous observations in this thesis, that for fully bainitic samples the hardness is not dependent on the grain size. For the oil quenched samples, the larger austenitic grained samples present slightly harder. This is direct result of the amount of martensite in the microstructure, larger austenitic grain sizes will produce more martensite upon transformation.

Material strength, at room and at elevated temperatures, decreases with increasing tempering time, as a result of dislocation reduction. The resultant phases present in the microstructure are the key parameter controlling yield and ultimate tensile strength (UTS). For the case of the slow furnace cooled samples, the occurrence of allotriomorphic ferrite for the low austenitisation temperature, decreases yield and UTS between 20 and 30 MPa at room temperature, for the tempering parameters studied. Although the observed reduction in strength due to the formation of allotriomorphic ferrite, which proportionates an homogeneous crack path, tested conditions fulfil the minimum required yield strength of 345 MPa and minimum UTS of 550 MPa at room temperature from ASTM standards [24]. The strength for fully bainitic samples, obtained after air cooling, is governed by grain size. Austenitising at lower temperatures produces a strengthening effect by grain refinement. For the fast cooled samples, which reproduce conditions near the external wall of components, the microstructure is a mixture of bainite and martensite. The ratio of mixture is sensitive to the $\overline{L}_\gamma$, larger austenitic grains will produce more martensite for a given cooling rate, thus higher strength. The UTS for the short tempering time, TP = 18.5 K h, is above the maximum limit of 725 MPa, hence fast cooled areas with short tempering times should be identified during design stages of components. These effects are seen in Figs. 4.77 and 4.78.

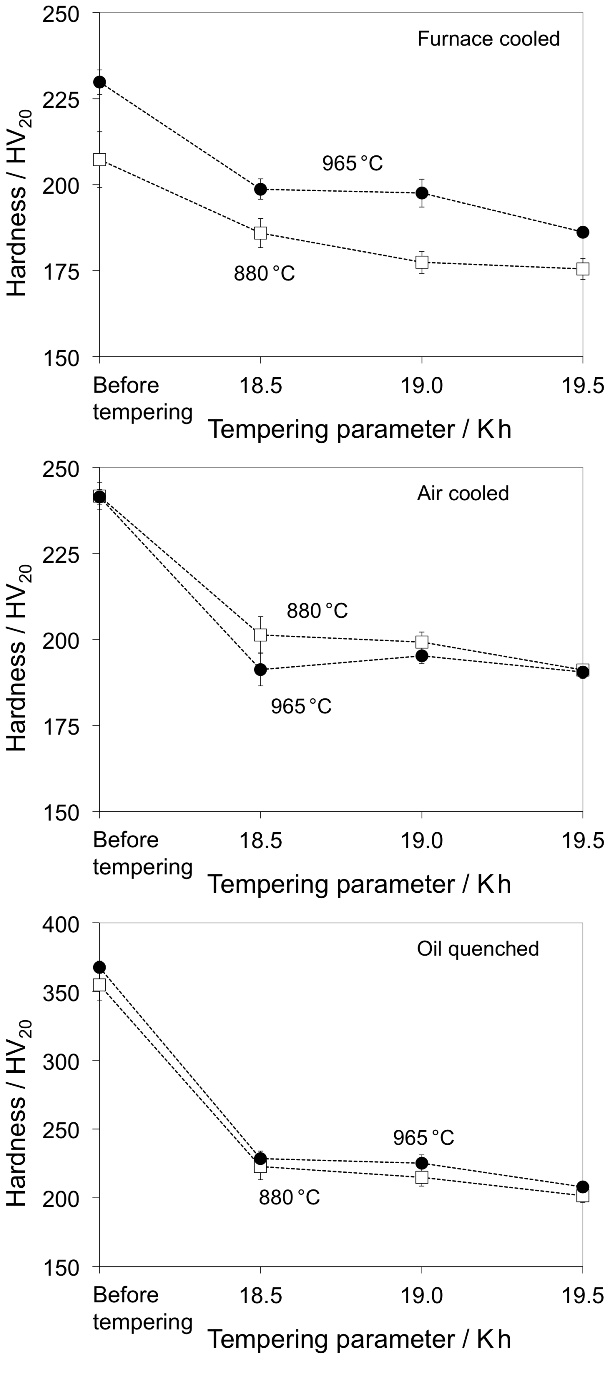

Figure 4.76: Hardness evolution as a function of tempering time, austenitisation temperature and cooling media. Values for Vickers hardness before tempering are also shown.

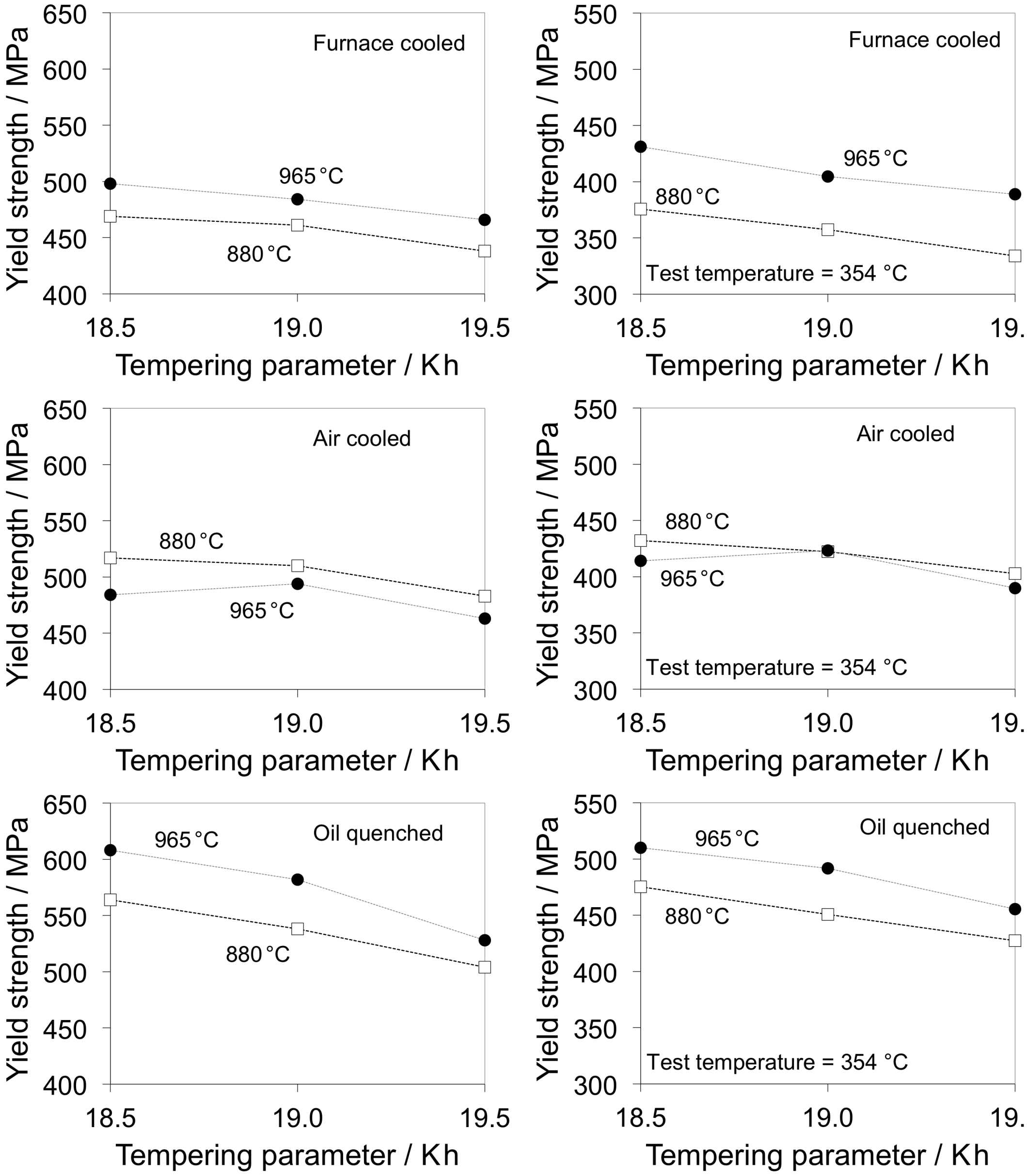

Figure 4.77: Yield strength evolution as a function of tempering time, austenitisation temperature and cooling media.

Hardness measurements in the tested tensile specimens, away from the gauge section, reveals a clear hardness - strength correlation, harder samples will result in stronger material, Fig. 4.79. The simple linear regression equations in Fig. 4.79 could be used as a quick non-destructive in situ assessment method to estimate

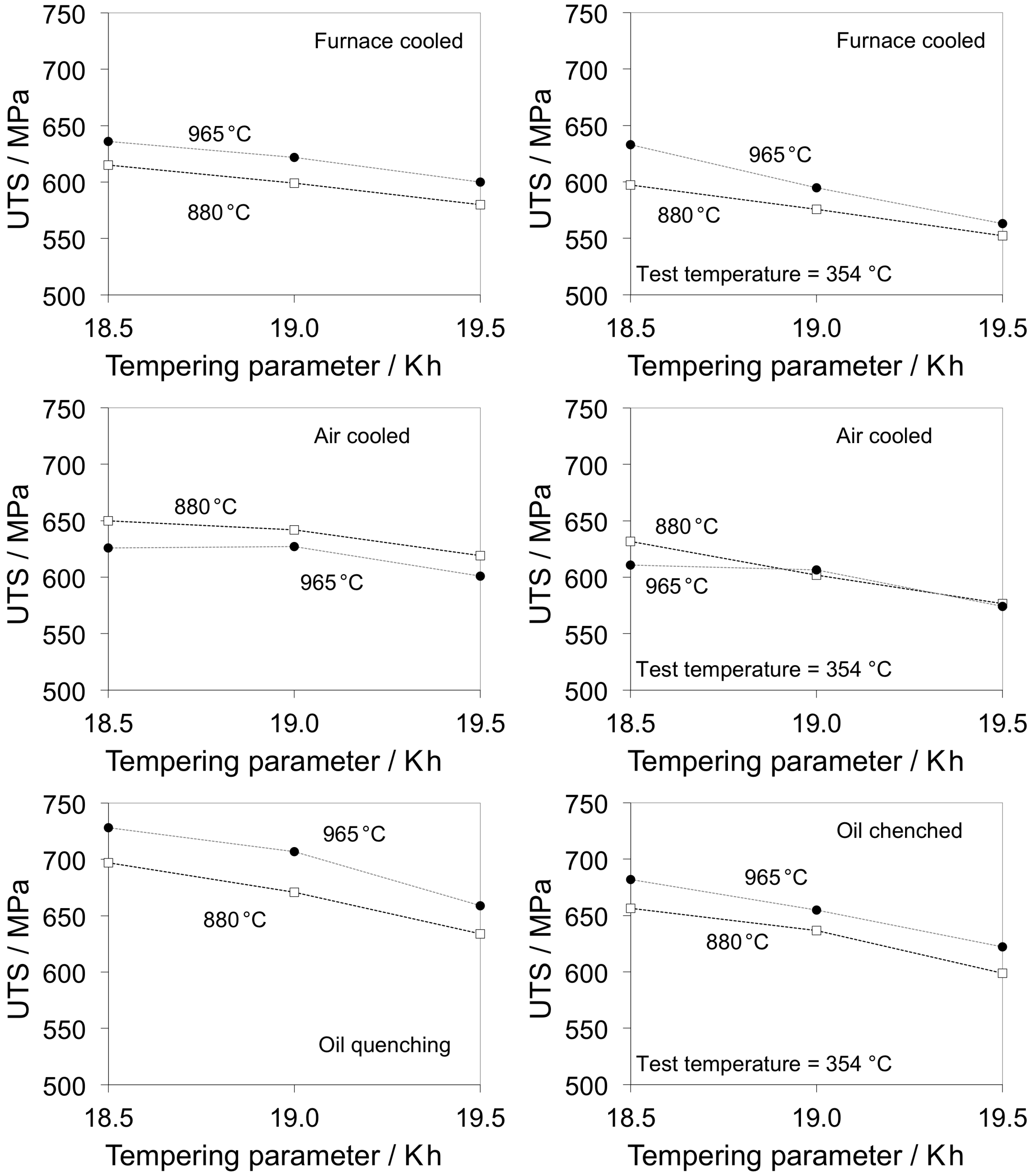

Figure 4.78: Ultimate tensile strength (UTS) evolution at room temperature as a function of tempering time, austenitisation temperature and cooling media.

strength in SA508 Gr. 3 thought the thickness. Although unseen data from the literature is in the range of values observed experimentally in the present study, it is recommended to perform similar measurements on a wider range of compositions within the standard to build up a more representative model.

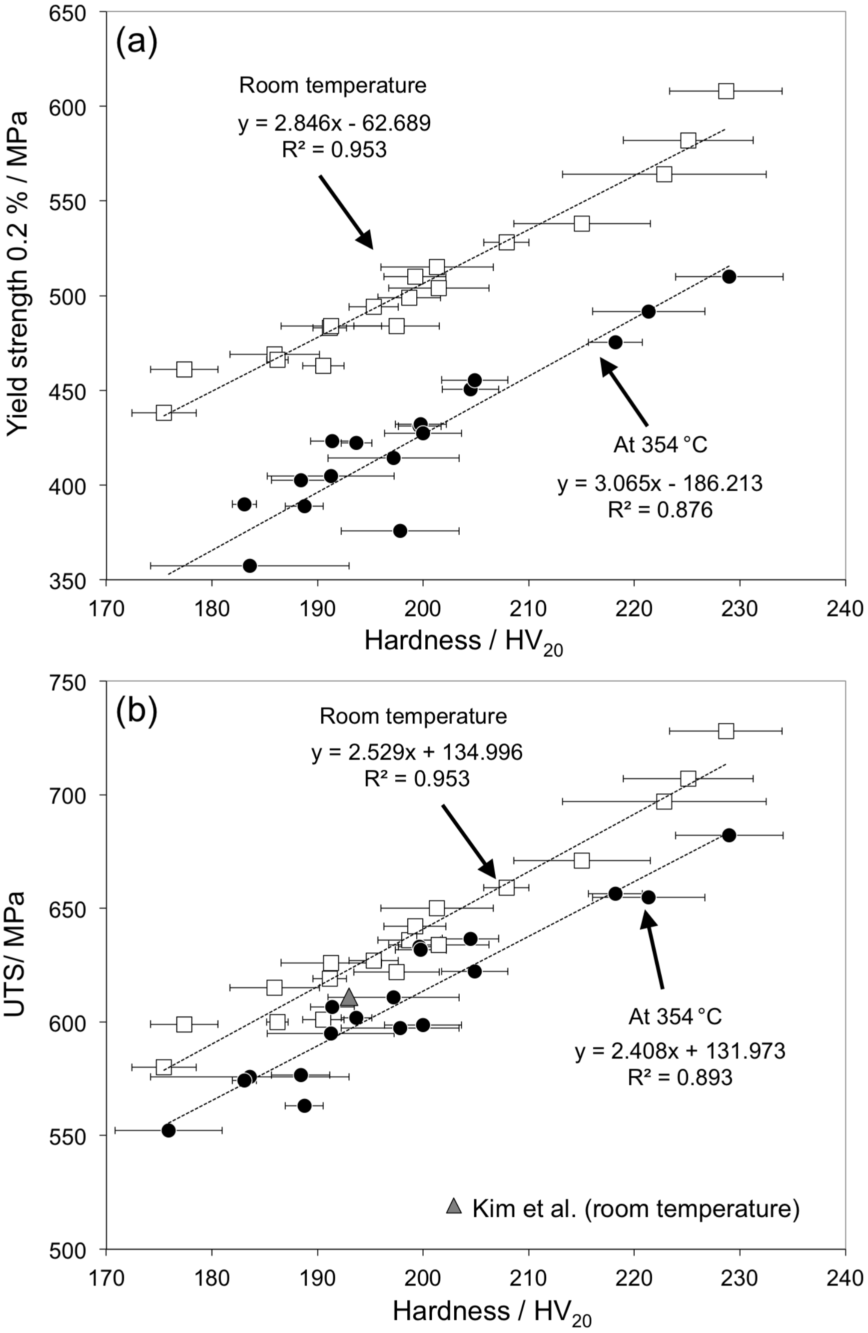

Figure 4.79: Relationship between strength and hardness in SA508 Gr. 3. a) Yield strength. b) Ultimate tensile strength (UTS). R^2 refers to the linear correlation. Data from the literature included for comparison [52].

To assess toughness performance, 20 V-notch impact Charpy tests where performed at different temperatures to construct a ductile-brittle transition curve for each condition. It is common practice, as a method of analysis, to fit a curve to the Charpy dataset to provide estimates of the temperature for a specific Charpy energy value, a percentage of shear measured in the fracture surface or a value of lateral expansion.

Various types of curve fitting equations have been proposed in the literature, a two parameter exponential curve [173], the Burr function [174], the Weibull distribution [175] and the most widely used hyperbolic tangent function [176]. A common weakness of these fitting functions is their empirical nature and lack of mechanistic basis. Cao et al. compared the goodness of fit for the different methods for a given set of data, concluding that the Burr and the hyperbolic tangent methods offer the best fit for large well distributed data and also for sparse data [177].

In the present work, the hyperbolic tangent function has been used to fit the data as follows:

$$H_f = A_h + B_h \left[1 + \tanh\left(\frac{T - C_h}{D_h} \right) \right] \tag{4.25}$$

where, H_f is the parameter being fitted, T is the temperature in °C and A_h, B_h, C_h and D_h are the fitting parameters.

Parameters used to evaluate the different conditions are the temperature for a 50 % shear in the fracture surface, for Charpy energy value of 28 and 41 J and the upper shelf energy (USE). Furthermore, the fitting parameter A_h in Eq. 4.25 takes the value of 3 J and 0 % for fitting impact energy and shear fracture area, respectively. The hyperbolic function is fitted to the Charpy datasets using non-linear least squares and the error between the line and the experimental data is calculated as the root mean square error, Fig. 4.80.

Toughness interpretation from the fitted curves is a difficult task as several

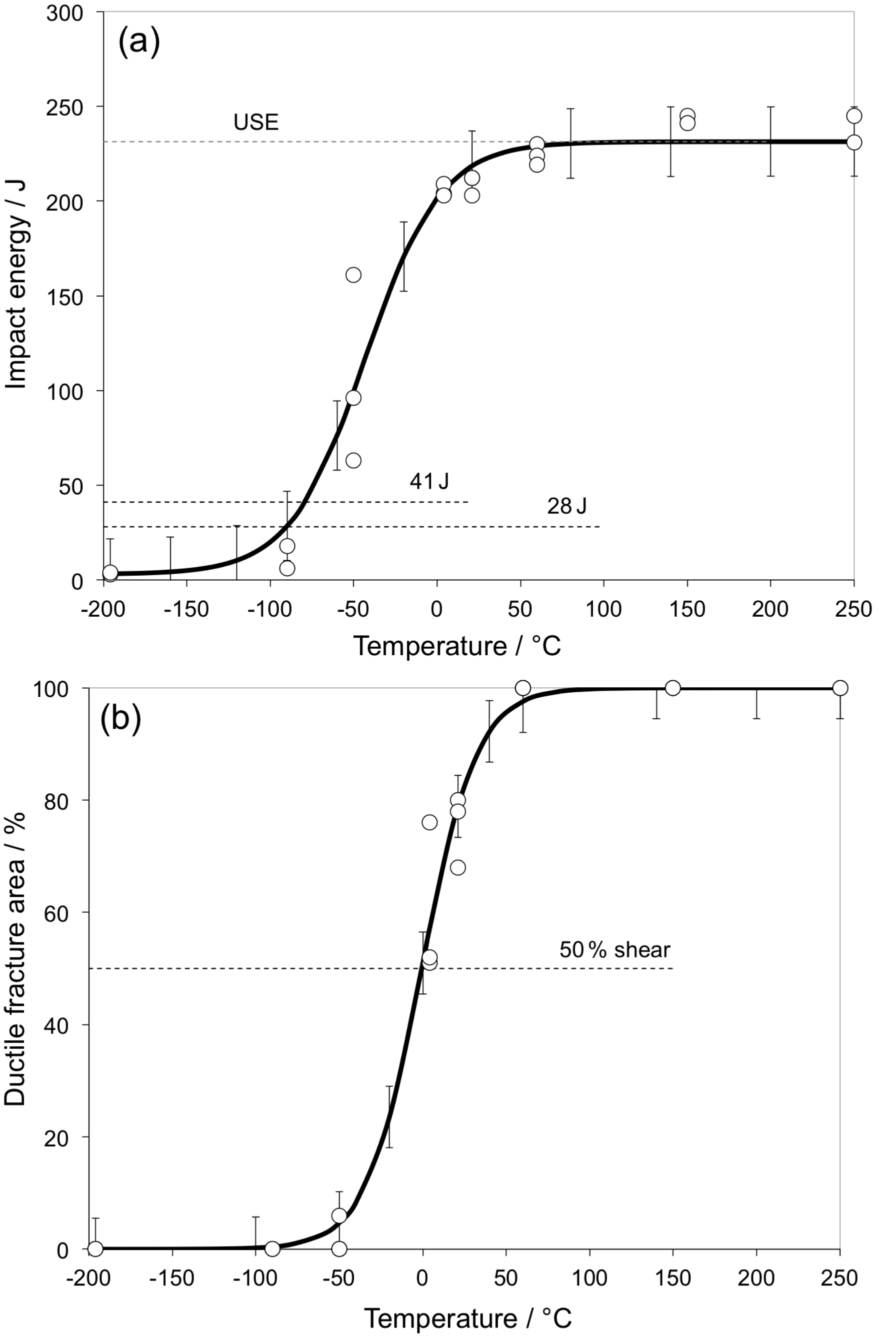

Figure 4.80: Fitted curves to Charpy dataset. a) Indicating the values of 28 J, 41 J and the upper shelf energy (USE). b) Indicating a 50 % of shear in the fracture surface. Error in the fitted lines calculated as root mean square error.

factors, such as phases present, hardness, precipitates and grain size are interrelated. As a general trend toughness decreases, the temperature to obtain a Charpy value of 28 and 41 J increases, with longer tempering parameters, due to the increased precipitation of cementite particles (voids are formed at elongated cementite/matrix interfaces or the fracture of a coarse carbides develops into a void [37, 41, 45, 46]). By contrast, as increasing the tempering time softens the material, the absorbed energy increases during at high temperatures, thus the USE is increased, Fig. 4.81.

Results confirm that the best microstructure for toughness purposes is a mixture of bainite and martensite, obtained after fast cooling, as it presents the lowest temperature for Charpy values of 28 J, 41 J and 50 % of shear in the fracture surface than a fully bainitic or a bainitic - allotriomorphic ferrite microstructure, Figs. 4.82 and 4.83. This may be explained by the refinement of the structure as it is formed at lower temperatures. More testing to construct a complete ductile-brittle transformation curve would be needed to asses fully martensitic samples with grain sizes commonly found in RPV components.

A larger austenite grain size results in more martensite than bainite, so that the toughness is improved. These results are in agreement with early work from Haverkamp et al. [68], where it was reported that as the bainite volume fraction increased, the DBTT increased and the impact values decreased at volume fractions exceeding 0.5 of bainite.

For the case of fully bainitic samples and or mixtures of bainite with allotriomorphic ferrite, smaller austenitic grain sizes would produce samples with improved toughness. The effect of grain size reduction for toughness improvement is well known for single phase microstructures, but as shown previously SA508 Gr. 3 samples cooled at a rate of $0.4\,^{\circ}\mathrm{C\,s^{-1}}$ and an austenite grain size below $13\,\mu\mathrm{m}$, a mixture of allotriomorphic ferrite and bainite is found at the microstructure. Small grained structures with a mixture of allotriomorphic ferrite and bainite present improved toughness when compared to the larger grained fully bainitic structures (austenitised at 965 °C).

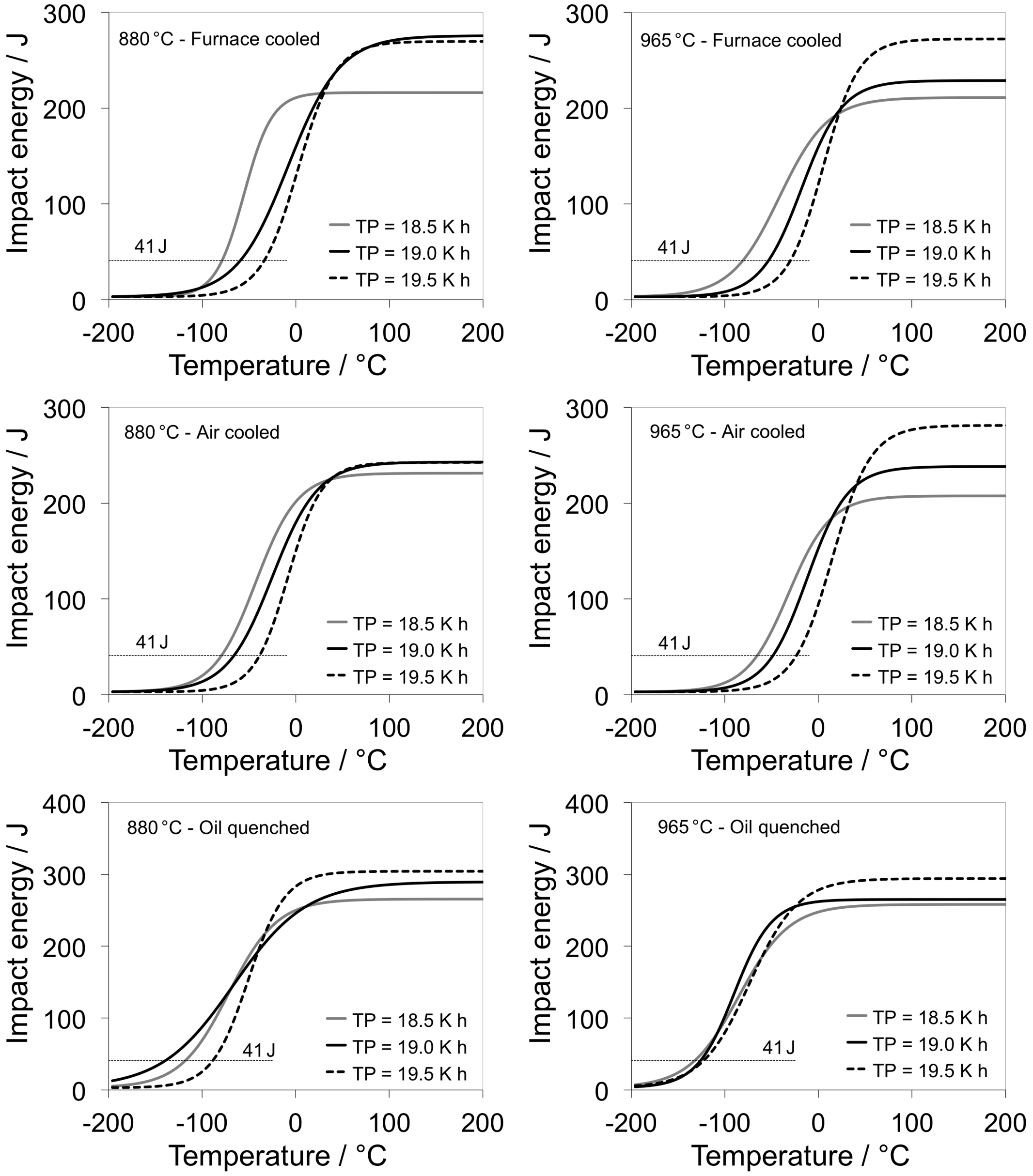

Figure 4.81: Hyperbolic tangent function fitted for the different conditions. Value of 41 J shown as reference. Errors no included in the fitted curves to ease interpretation.

Allotriomorphic ferrite formation in RPVs has been tried to avoid by constant drive to increase cooling rates from austenitisation, as it was assumed to be detrimental to toughness as each ferrite grain presents crack path equal to the grain size [150]. However, experimentens have confirmed that toughness is not reduced when allotriomorphic ferrite is present in the microstructure. An explanation, could be in the morphology of the ferrite. The observed arrays of precipitates inside the ferrite grains may hinder the crack propagation, thus maintaining an acceptable level of toughness. Hence, it is proposed that to improve toughness, austenitic grain sizes should be kept to a minimum by austenitising at lower temperatures or short times.

As it was detailed in the literature review, Section 2.5.2, reported empirical observations have shown that the strength is reduced with increased tempering parameters and that the toughness increases steadily up to reaching a maximum value at a relatively early state of tempering, decreasing significantly afterwards. This has had and impact in the nuclear industry where the tempering parameter commonly approaches 19.4 K h, the assumed value at which the impact energy reaches its maximum [28, 37, 47, 68].

Observations in the present study agree with previous observations that the strength is reduced as the TP is increased, due to a reduction in the material hardness. Toughness in SA508 Gr. 3 follows a more complex relationship, as microstructure and tempering parameter are interrelated. For the case of a mixture of allotriomorphic ferrite/bainite and for fully bainitic microstructures, increasing the tempering parameter reduces the values of absorbed energy, Figs. 4.84 to 4.86. While for the case of samples with bainitic/martensitic structures increasing the TP results in an increase in toughness. This effects are related to the precipitates as previously discussed. Therefore, according to experimental results, it is recommended to increase the integrity of the medium/slow cooled regions of components to reduce the TP to values below 19 K h.

Figure 4.87 shows that contrary to the strength, the impact energy does correlate well with the hardness.

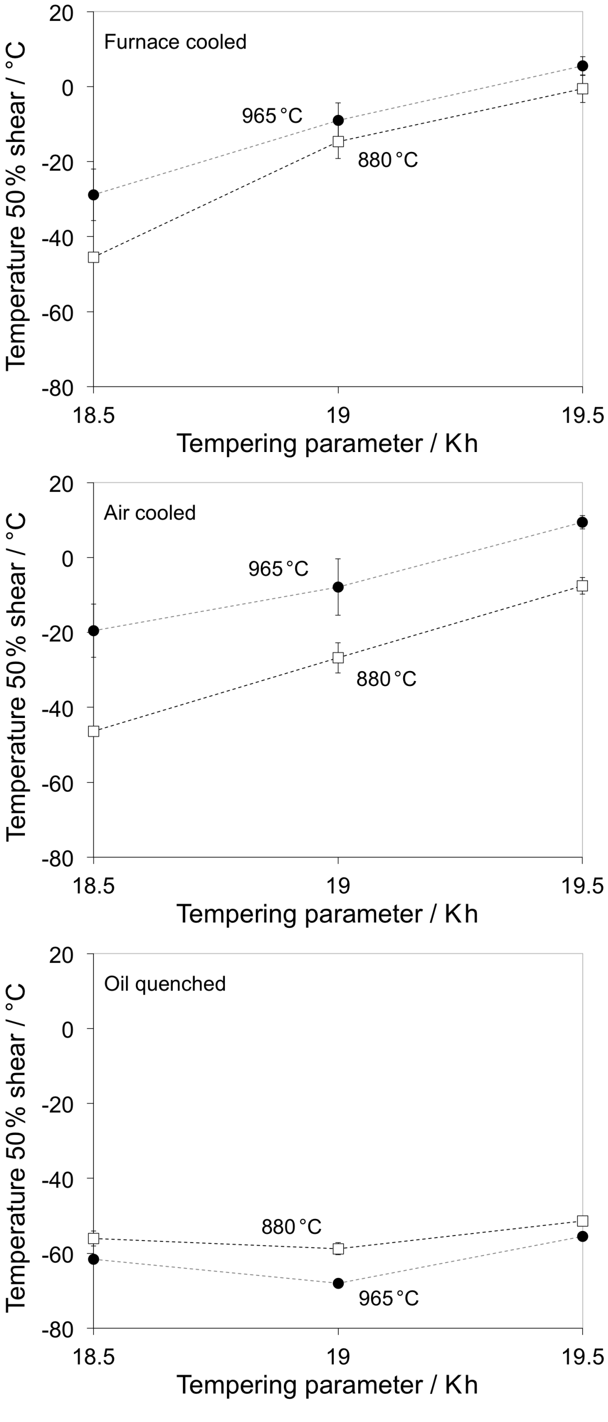

Figure 4.82: Temperature for a 50 % shear in the fracture surface

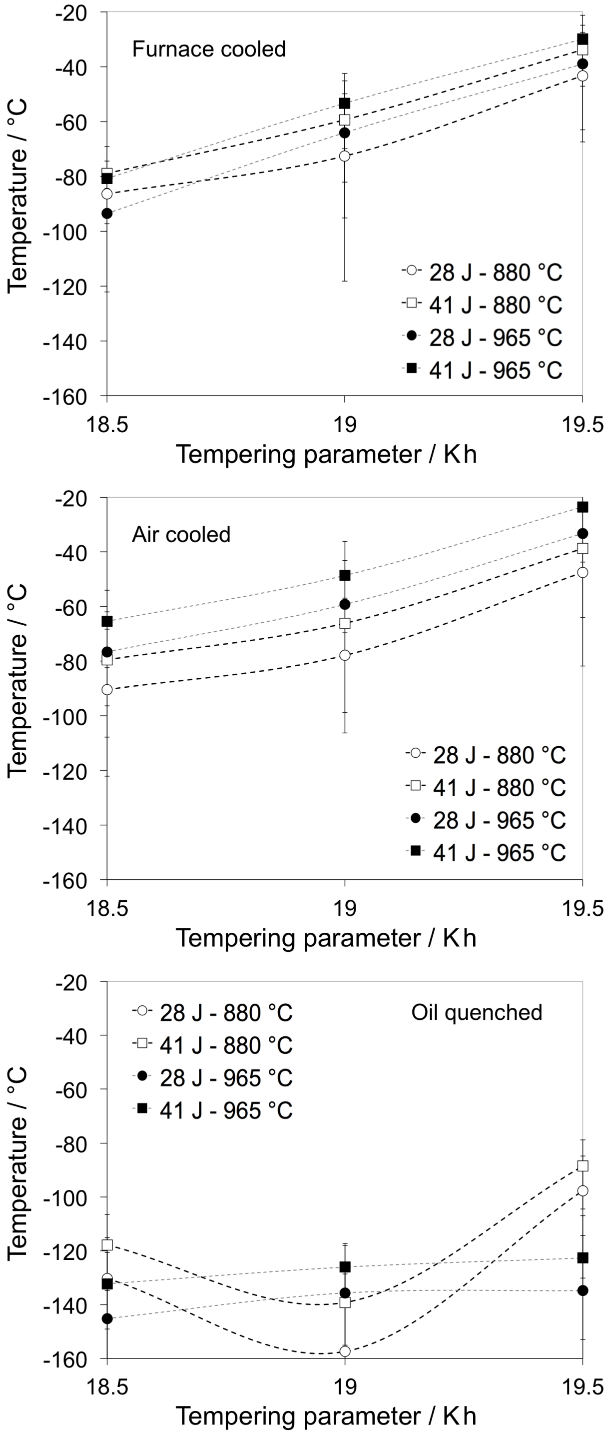

Figure 4.83: Temperature for a Charpy impact value of 28 and 41 J.

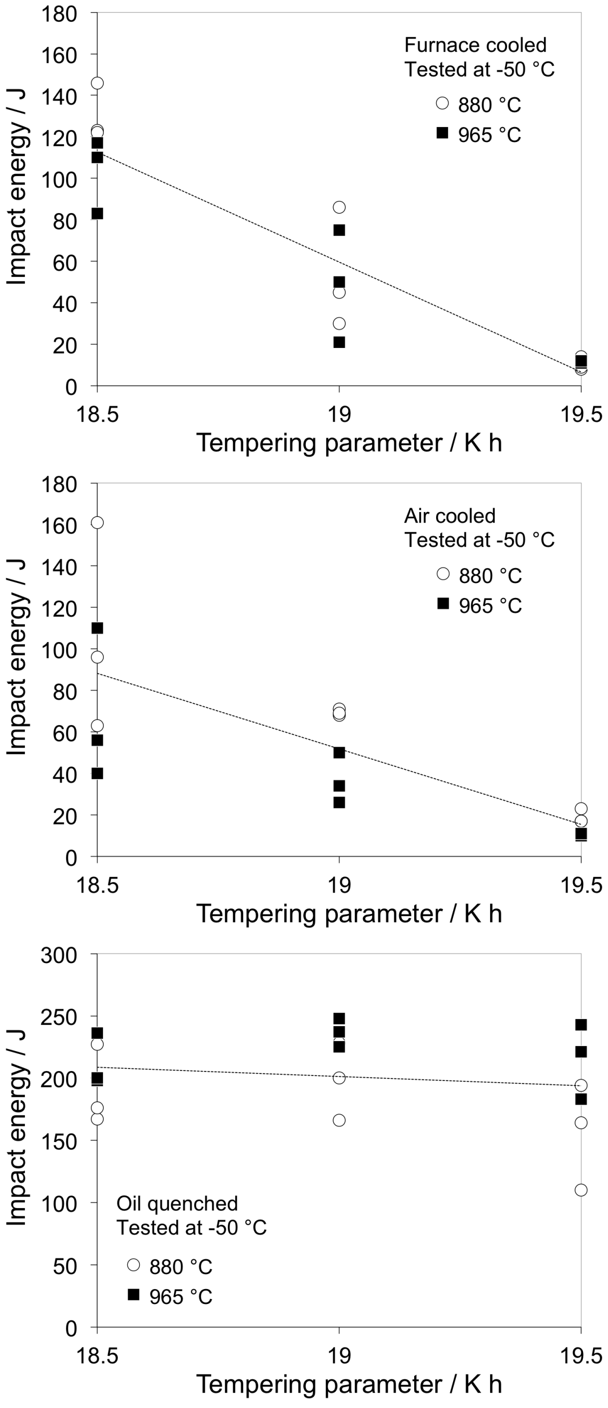

Figure 4.84: Change in absorbed impact energy at -50 °C with increase tempting parameter.

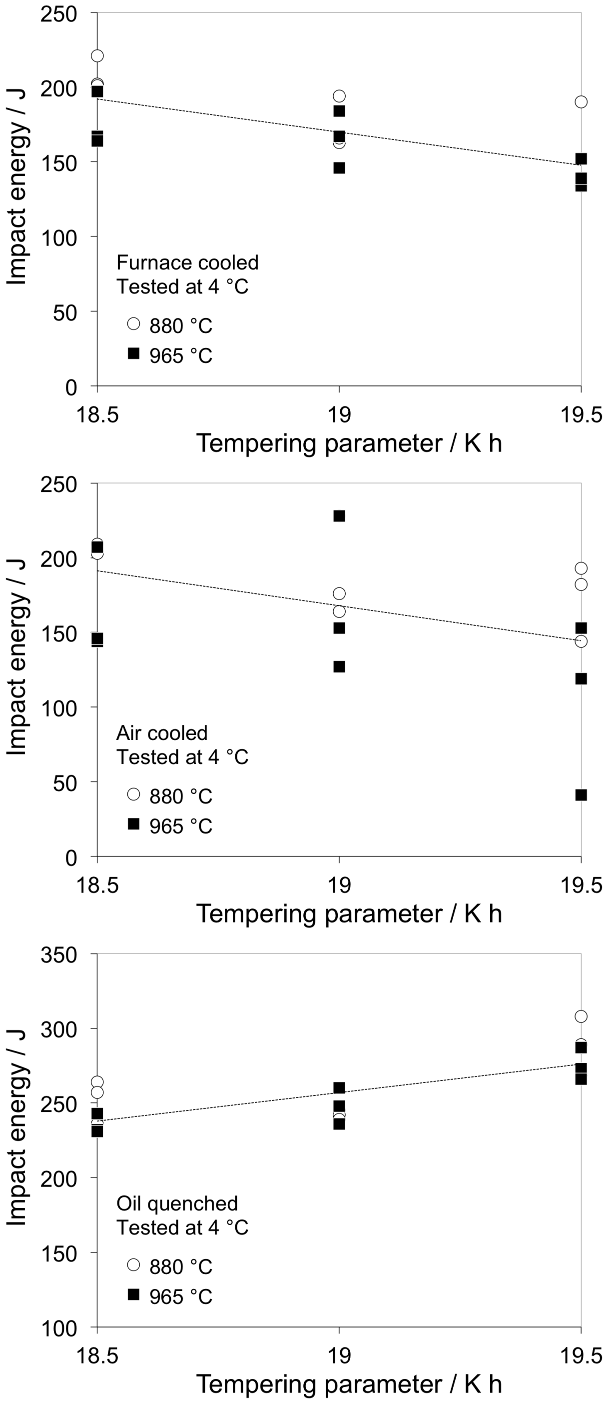

Figure 4.85: Change in absorbed impact energy at 4 °C with increase tempting parameter.

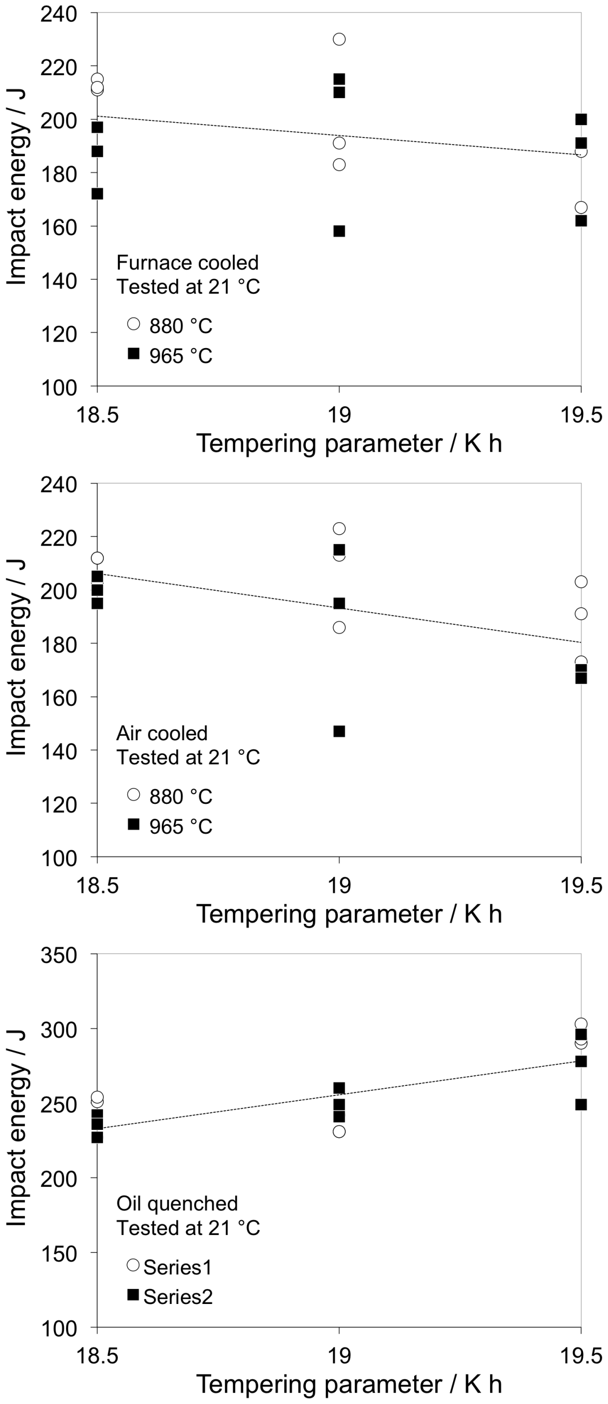

Figure 4.86: Change in absorbed impact energy at 21 °C with increase tempting parameter.

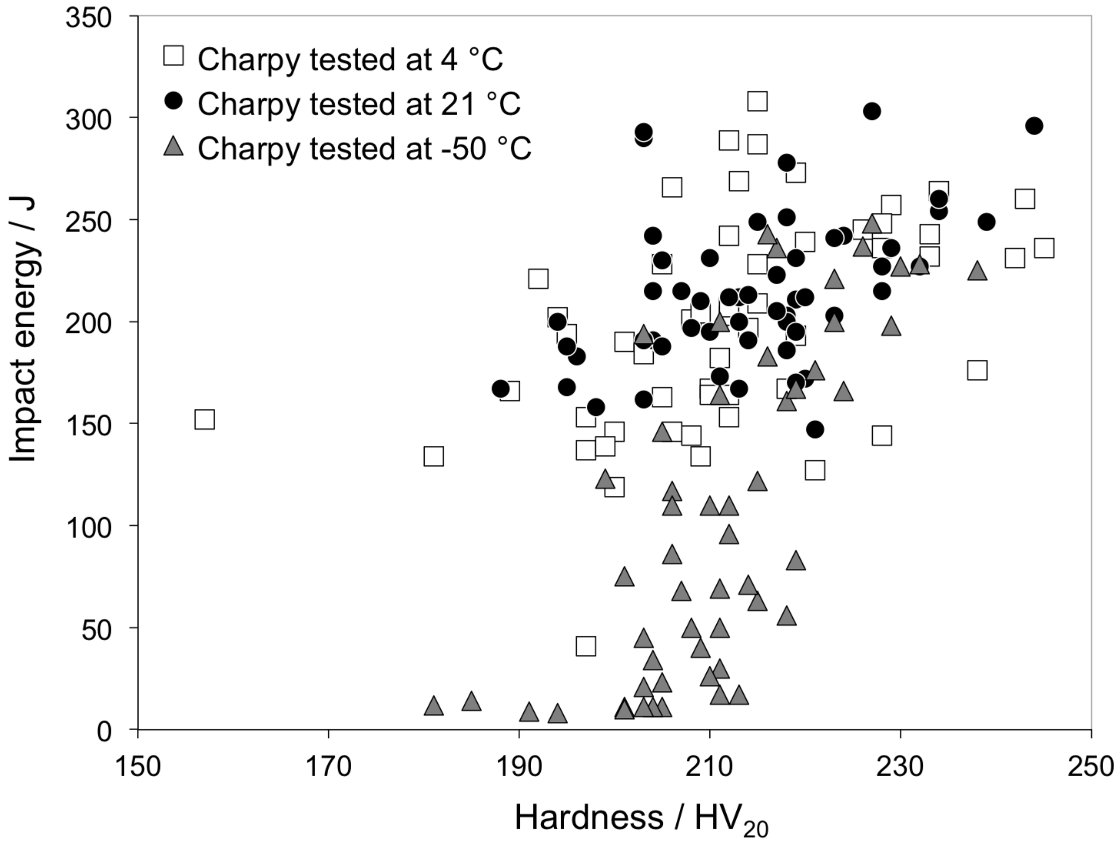

Figure 4.87: Relationship between hardness and impact energy at different temperatures.

4.6 Mechanical properties modelling

It is, of interest to find a reliable method to accurately predict the mechanical properties of large vessels as a function of thermal processing parameters. As neural networks provide an approach by which a quantitative prediction can be made in situations where the complexity of the problem makes a physically rigorous treatment difficult.

The cooling rate is a key factor determining the phase transformation mechanism and thus the resultant mechanical properties in SA508 Gr. 3 steel. Samples used for the mechanical properties programme included a thermocouple to monitor temperatures. However, due to the size of the heat treated components, the

22 testing samples obtained from each disc, have not been subjected to the same cooling rate. Therefore, a more accurate determination of the specific cooling rate for each testing sample has been undertaken by simulating the heat transfer of the disc during cooling in different media using the finite element software ABAQUS.

The boundary condition available in ABAQUS for a heat transfer calculation is the temperature exchange with the environment, which replicates the workpiece temperature loss during cooling. Particularly, for heat transfer simulation, ABAQUS requires the material density (7600 $\mathrm{kg\,m^{-3}}$ from Ref. [178]), thermal conductivity, specific heat capacity, the heat transfer coefficient, the component initial temperature (880 and 965 °C) and the ambient temperature (20 °C for all media).

The thermal conductivity and the specific heat capacity of the material were calculated for the composition of Alloy C as a function of temperature using MTDATA [112] and the MAP_STEEL_THERMAL [179] software respectively. Figure 4.88 shows the variation of these parameters as a function of temperature. Values of thermal conductivity for other SA508 steels from the literature are similar to the ones calculated in this study.

During cooling the rate of the heat extraction from the material is commonly expressed in terms of a heat transfer coefficient (h) which is function of the steel and cooling media. The heat flux across the steel/media interface is given by $q = h\,\Delta T_d$ where ΔT_d is the temperature difference between the component and the sink. The variation of heat transfer with temperature can be calculated by monitoring the cooling rate of a small probe during cooling, and is given by [180, 181]:

$$h = \frac{\rho\, V\, C_P\, |\dot{T}|}{A_s\,(T_s - T_\infty)} \tag{4.26}$$

where C_P is the specific heat capacity at constant pressure, $|\dot{T}|$ the instantaneous cooling rate, ρ the density, V_p the probe volume, A_s the probe surface area, T_s

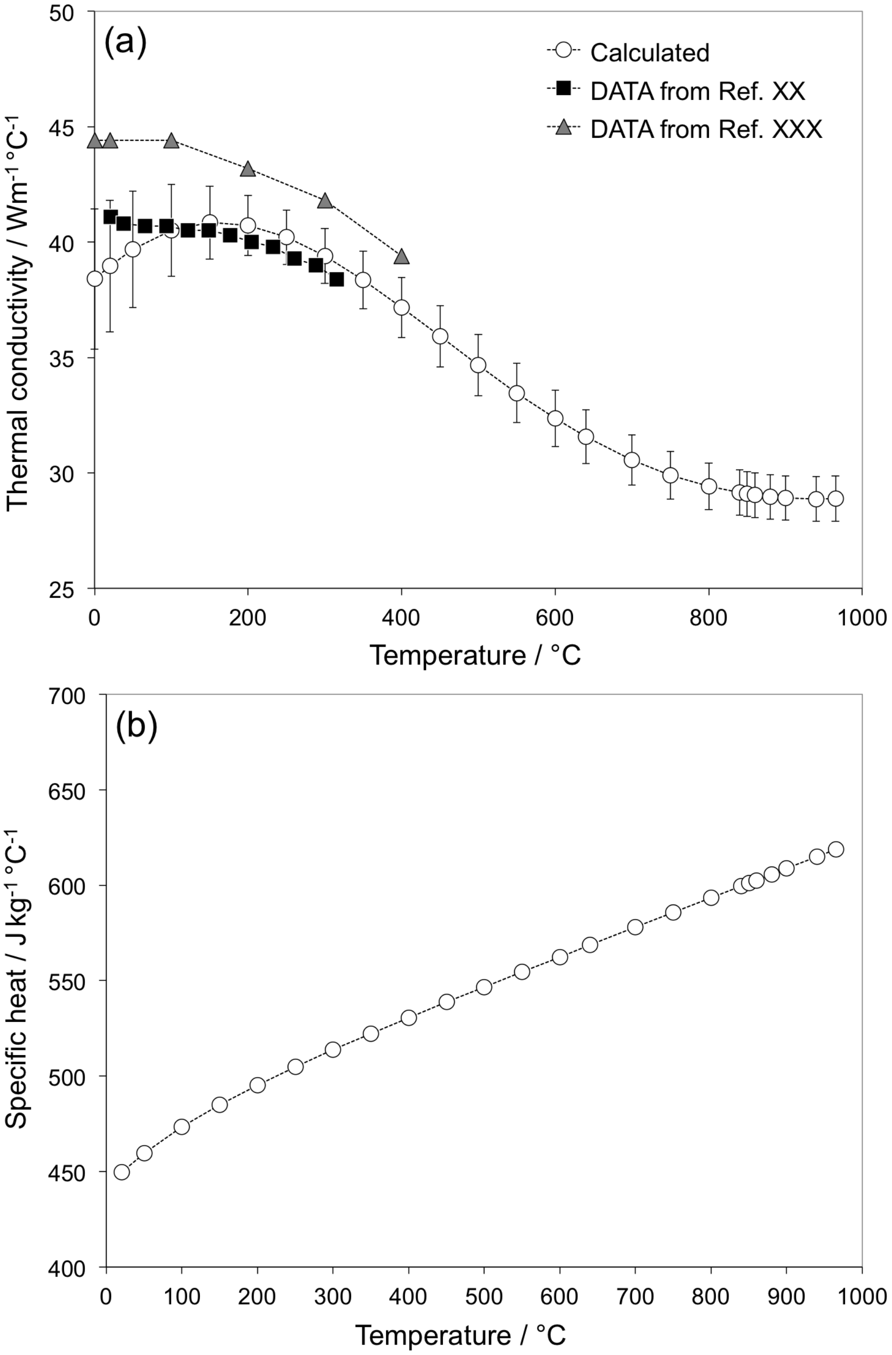

Figure 4.88: Calculation of parameters as a function of temperature. a) Thermal conductivity. b) Specific heat capacity.

Table 4.19: Experimental and calculated cooling rates for the known position of the thermocouple.

Austenitising temperature / °C	Coling media	Experimental cooling rate / $^\circ\mathrm{C\,s^{-1}}$	Calculated cooling rate / $^\circ\mathrm{C\,s^{-1}}$
880	Furnace	0.17	017
880	Air	1.61	1.61
880	Oil	12.30	12.28
965	Furnace	0.23	0.23
965	Air	1.81	1.76
965	Oil	11.47	11.46

the probe surface temperature and T_∞ the external temperature.

In the present study, the heat transfer has been fitted to reproduce accurately the cooling curve recorded experimentally by the thermocouple. It is then assumed that if the experimental cooling curve, for the known position of the thermocouple, is correctly represented, the heat transfer for the whole disc should be also representative of the actual cooling. Table 4.19 gives the experimental and the calculated cooling rates which represent cooling rates prior any reduction in cooling rate due to a phase transformation.

As the position of the 22 test samples (20 Charpy V-Notch and two tensile) in each disc is known, Fig. 4.89, the cooling rate for each individual sample has been obtained from the thermal simulation using ABAQUS. The average of eight points forming an area of $1\,\mathrm{cm}^2$ around the notch and a further point in the centre of the notch has been used to determine the cooling rate of each sample. Figure 4.90 shows a thermal simulation with ABAQUS and the positions of the nine points used to calculate the cooling rate for each sample.

To investigate the dependence of yield strength, ultimate tensile strength and impact energy at different test temperatures databases were collated and three

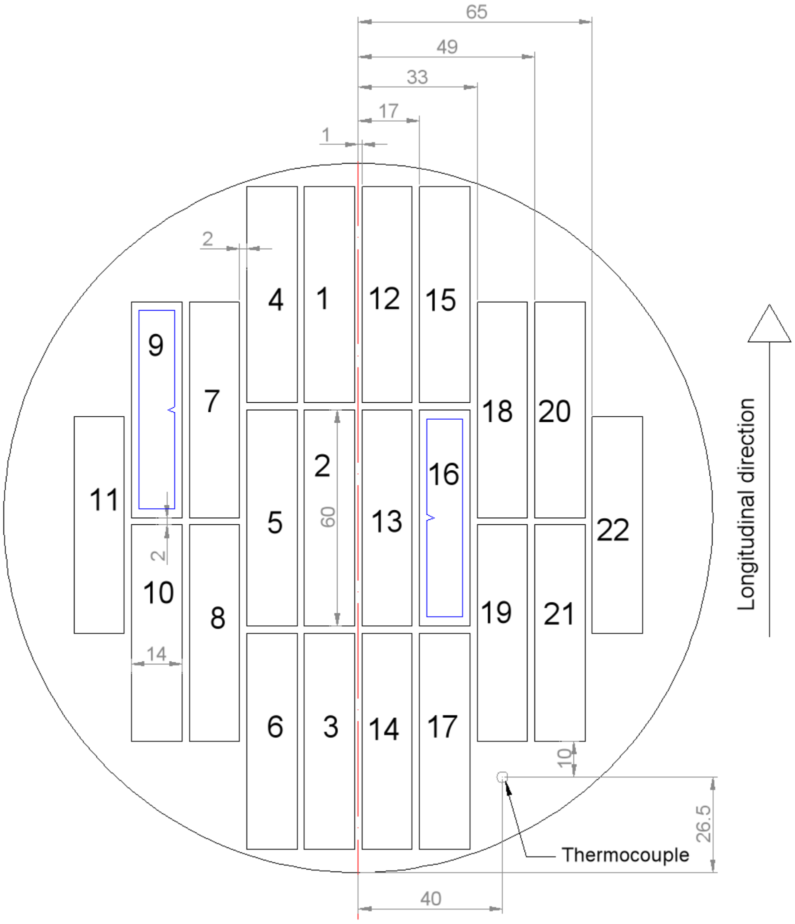

Figure 4.89: Distribution of the samples in the disc. Showing location for the sample blanks and the position of the Charpy samples in blue.

neural networks produced in the Bayesian framework following MacKay [138–140]. The database for the impact energy contained 360 values representing 78 different conditions in terms of austenite grain size, cooling rate and TP at various temperatures. The databases for the yield strength, ultimate tensile strength incorporated 36 values representing 18 different conditions, for each case. Databases were generated from the experimental data of Alloy C used for the mechanical properties programme. Details of composition of the steel have been omitted from the models so as to make it more generally applicable to SA508 Gr. 3 steels where there is relatively small compositional range. Differences due to microstructure can be regarded as being incorporated into the uncertainty which accompanies

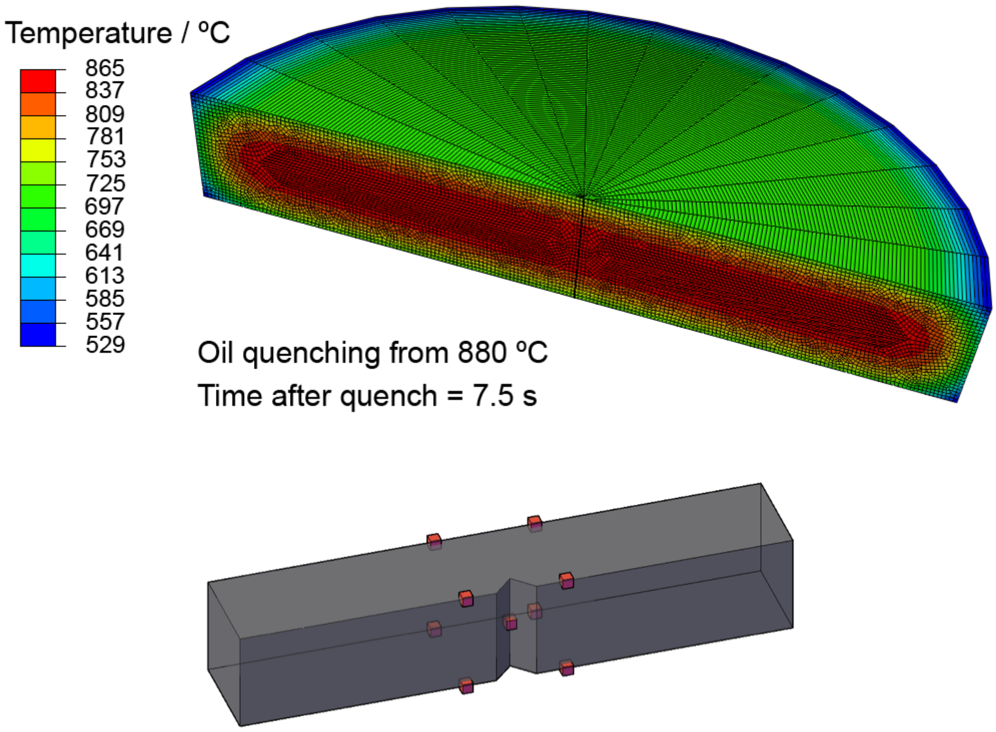

Figure 4.90: ABAQUS simulation of a disc oil quenched from 880°C and the position of the nine points used to calculate the cooling rate for each sample.

the predicted values. Table 4.20 summarises the range in the input data used to create the models.

The data were randomly divided in two groups, a training set and a testing set. In the training stage of the neural networks, different sub-models were trained allowing a maximum of 25 hidden units. Nine different random seeds were used to control the initial weights of each input parameter, so as to ensure convergence from different positions in weight space. This meant a total of 225 initial conditions in each case, resulting in 224, 222 and 221 sub-models being successfully trained for the impact energy, yield strength and ultimate tensile strength models respectively. To test for over fitting, each of the sub-models is tested to predict the unseen testing set, allowing a ranking by the log predictive error. A committee of the best models as ranked by log-predictive-error was selected to minimise the combined test error, with two sub-models for the impact

Table 4.20: Summary of the databases input data for neural network modelling.

	Impact energy	Yield strength	Ultimate tensile strength
Austenite grain size / μm	14 & 68	14 & 68	14 & 68
Cooling rate / °C s^{-1}	0.17 to 9.96	0.17 to 10.45	0.17 to 10.45
Tempering parameter / K h	18.5 to 19.5	18.5 to 19.5	18.5 to 19.5
Test temperature / °C	-196 to 250	21 & 354	21 & 354

energy model and one sub-model for the yield and ultimate strength models as best solutions. The significances of the input parameters are shown in Fig. 4.91.

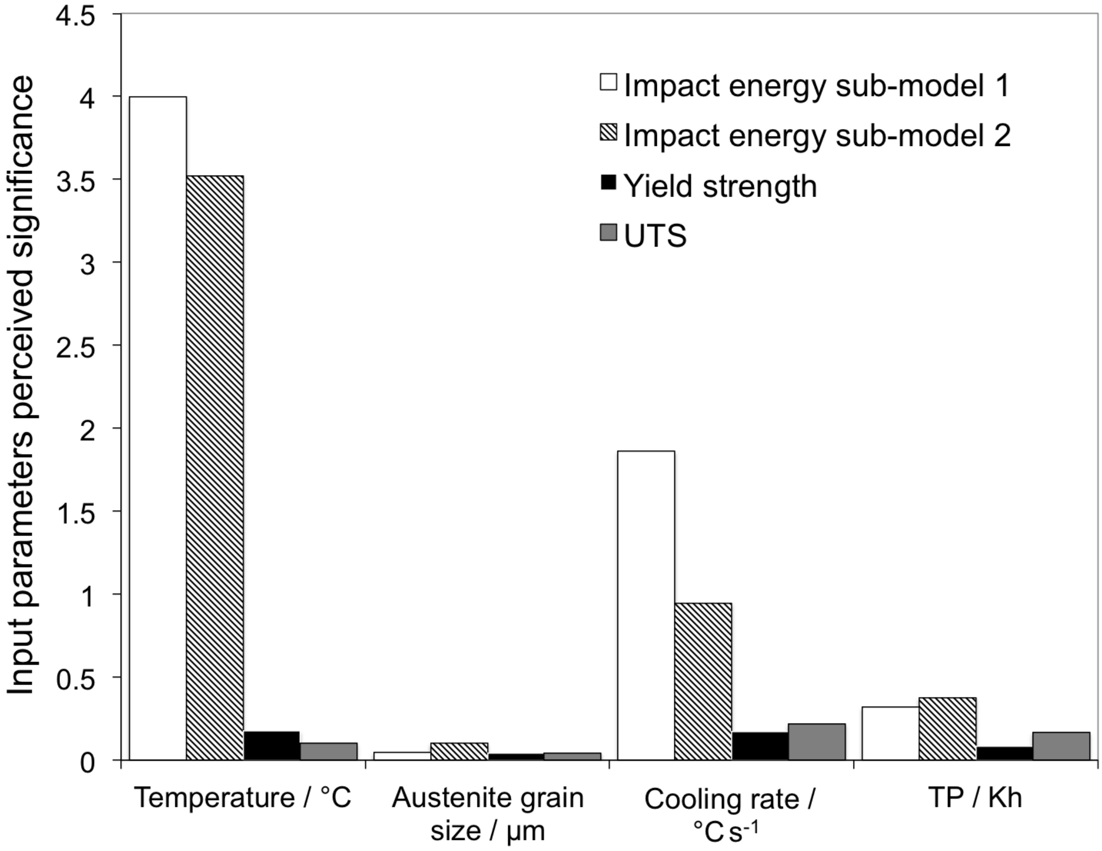

Figure 4.91: Significance for the input parameters.

Figure 4.92 shows reasonable agreement between the experimental data and the data used to generate the databases. However, to asses the the models unseen data were tested. The predictions compare favourably with independent data from the literature even outside the range seen in the database, Figs. 4.93 and 4.94. Furthermore, the neural network models could be used with the aid of thermal processing data from finite element software to map the distribution of strength and toughness in large components.

A final experiment where samples from Alloy C were heated to 965 °C for 3 h,

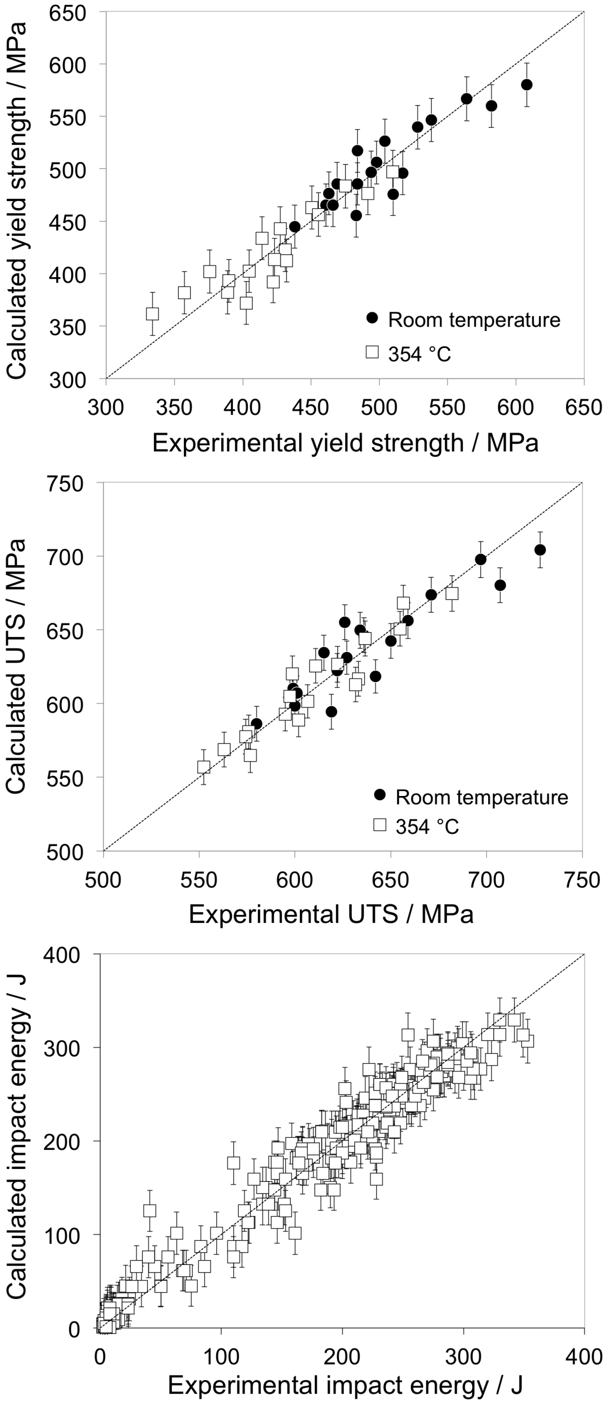

Figure 4.92: Neural network prediction of the data used to generate the databases.

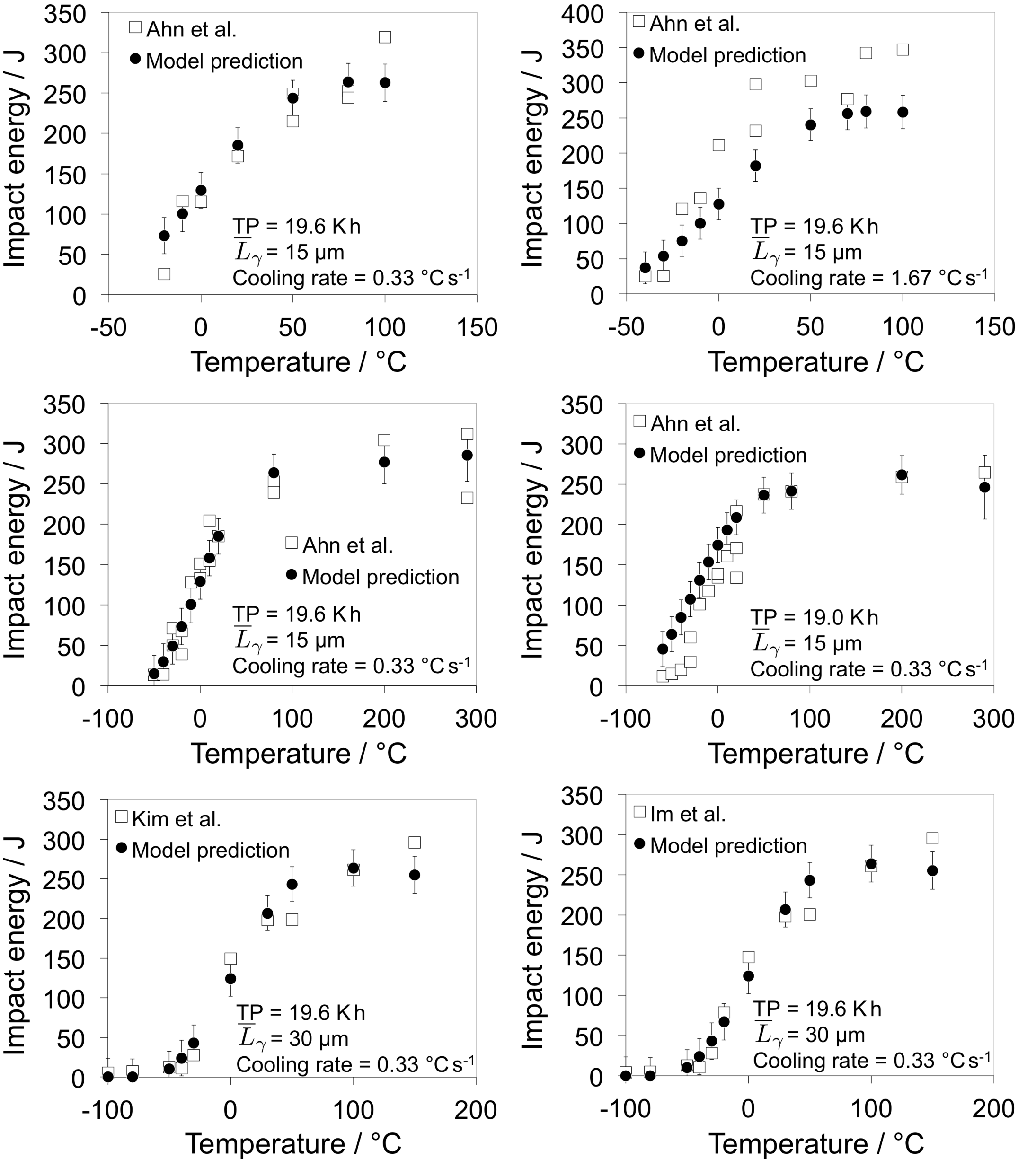

Figure 4.93: Predictions for unseen data from various authors [40, 41, 46]

cooled at a rate of $0.12\,°\mathrm{C\,s^{-1}}$ and tempered to a TP of 19.0 K h were Charpy and tensile tested. Experimental data is not available for this particular condition, thus the different models developed during the course of this investigation have been implemented to calculate the limiting grain size (Eq. 4.18) and

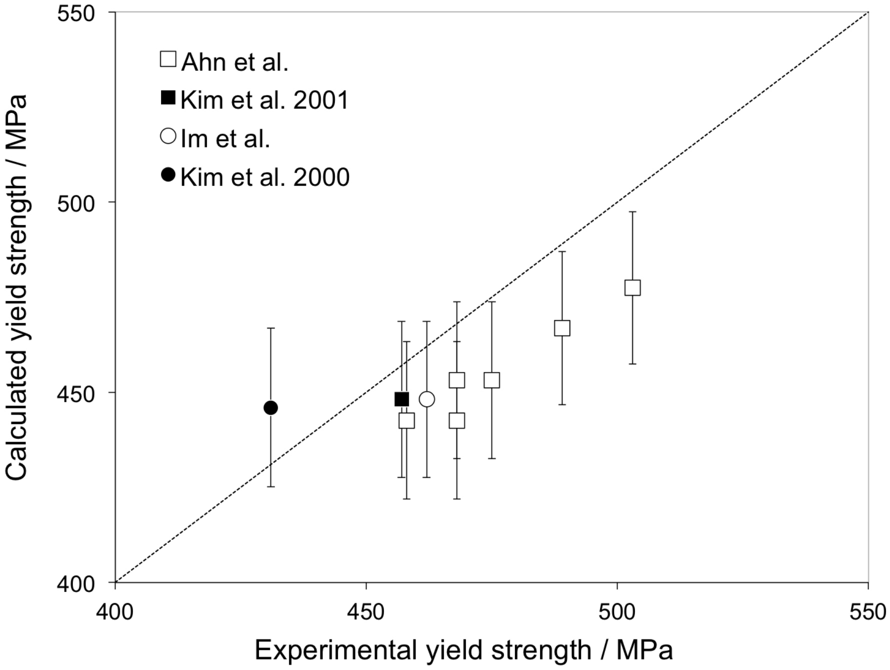

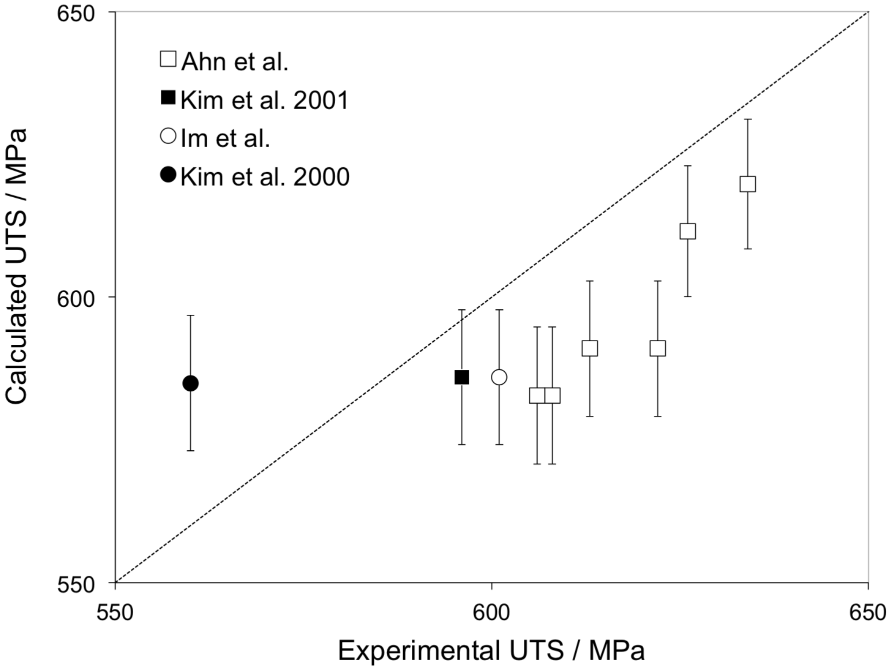

Figure 4.94: Yield strength and ultimate tensile strength (UTS) predictions for unseen data from various authors [38, 40, 41, 52]

the austenite grain size (Eq. 4.14) and used as inputs for the neural network to predict impact energy and strength. Measured yield strength and UTS are 451 and 595 MPa respectively, which compare closely to the predicted values of 473 ± 20 and 615 ± 15 MPa. Figure 4.95 shows good correlation between experimental impact data and the model predictions at different temperatures. Results have proved that combining the models developed it is possible to make a prediction for toughness and strength with a high level of confidence for SA508 Gr. 3 steels by knowing the material composition (levels of Al and N) and the heat treatment parameters. This presents a potential benefit during the design stage of components to optimise material composition, heat treatment or geometry to assure the desired level of properties.

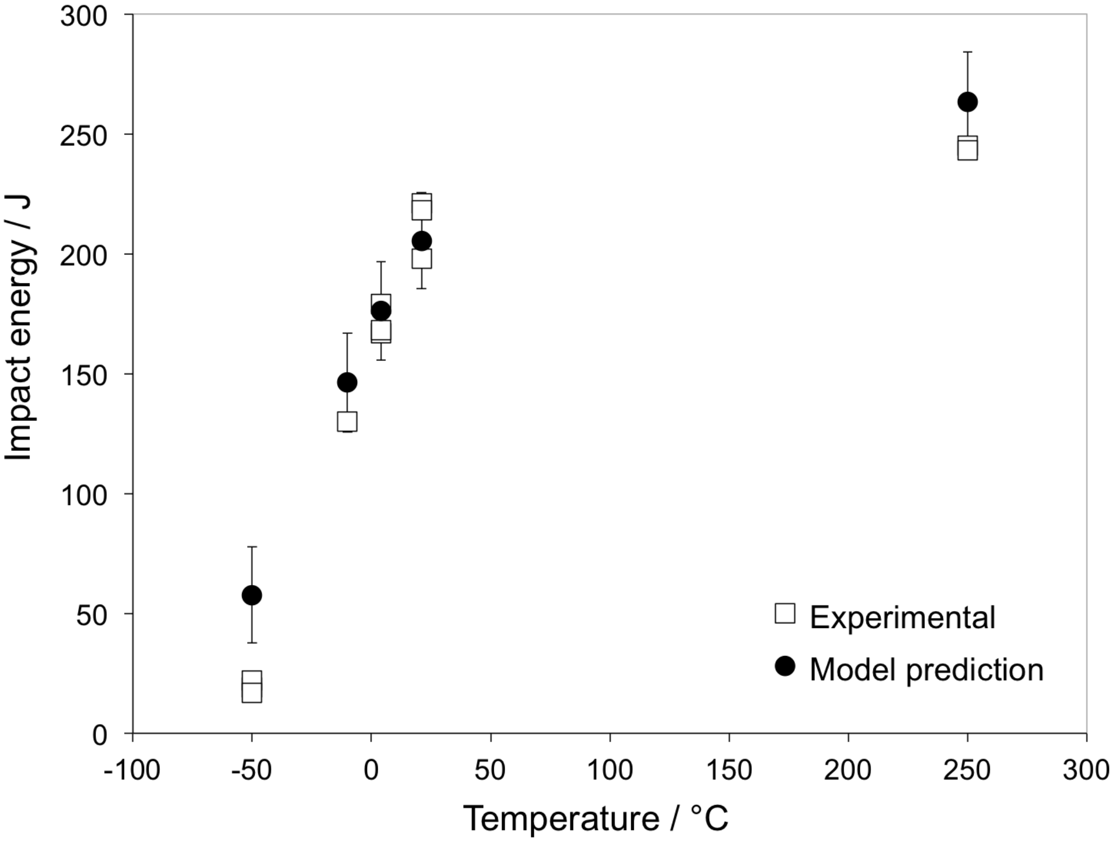

Figure 4.95: Predictions for unseen data. Inputs calculated using models developed in this work.

Chapter 5

Conclusions and further work

A methodic approach to address experimental observations in SA508 Gr. 3 steels has been undertaken in which the different stages in the quality heat treatment, consisting of austenitising followed by water quenching and tempering, are individually investigated. The essential conclusions for each stage in the heat treatment are summarised below.

5.1 Austenitising

Austenite grain growth in nuclear pressure vessel steels, SA508 Gr. 3, has been studied with the aim of deriving a physically reasonable expression which generalises well. The kinetics of the isothermal growth of austenite grains can be categorised into two temperature regimes, one in which the boundaries experience a pinning force due to precipitates so that the grain size rapidly reaches a limiting value. In contrast, at higher temperatures where the precipitates are expected to dissolve, not only is the rate of grain growth dramatically increased but also does not reach a limiting value within the time scale of the experiments reported here. Austenite grain growth kinetics have been demonstrated to be related to the amount of pinning particles present at a certain temperature. It has been established using thermodynamic calculations, high-energy X-ray diffraction, transmission electron microscopy and microanalysis, that the pinning particles at the temperatures of interest are aluminium nitrides. The standard theory for grain growth has been adapted to account for the initial grain size generated as the steel reaches its fully austenitic state, and for the evolution of this size as the sample is heated continuously to the isothermal annealing temperature. It is demonstrated that the activation energy for grain growth is, as expected, about half that for the self-diffusion of iron in austenite, once the data are interpreted to avoid over-fitting. The activation energy is thus found to be about $190\,\mathrm{kJ\,mol^{-1}}$, a value much smaller than most reported data on nuclear pressure vessel steels.

In the proposed austenite grain growth model, the final austenite grain size is a function of the initial size of the austenite grain when the sample is fully austenitised at $\mathrm{Ac_3}$ and the limiting grain size which varies with the temperature and with the level of AlN. This limiting grain size may be experimentally determined for each condition. However, a function to estimate the limiting grain size has been proposed, by simply considering the levels of Al and N in the alloy. Microstructural and dilatometric findings suggest that the initial prior-austenitic structure has little effect on the phase transformation during reheating to austenite and then on the austenitic grain size once the sample becomes fully austenitised.

It has been discovered during the course of the experimental work that there are circumstances in which there is an exaggerated grain growth of individual grains when the average grain size has reached the limiting grain. This is known as secondary recrystallisation. To avoid the formation of these few disproportionally large grains, which may affect the local properties of the component, the level of AlN in the alloy should be reduced, by controlling the amount of Al and N, to increase the limiting grain size.

5.2 Quenching from austenitisation temperatures

Although most of previous studies conclude that large components made from SA508 Gr. 3 steels are, following heat treatment, fully bainitic, it has been demonstrated with the help of a variety of experimental techniques, that the microstructures are far from homogeneous when considered in the context of the cooling rates encountered in practice through a typical component wall section.

It has ben demonstrated that allotriomorphic ferrite can be present in the microstructure of SA508 alloys under circumstances that are consistent with current industrial practice. Dilatometric and microstructural observations confirm the formation of allotriomorphic ferrite, at cooling rates below $0.4\,^{\circ}\mathrm{C\,s^{-1}}$. While at cooling rates of $1\,^{\circ}\mathrm{C\,s^{-1}}$, microstructures are mostly bainitic. The formation of allotriomorphic ferrite is greatly influenced by the austenite grain size and the cooling rate from austenitisation temperatures. A minimum austenite grain size of $25\,\mu\mathrm{m}$, as defined by a mean lineal intercept, is recommended in order to avoid the formation of significant quantities of allotriomorphic ferrite at cooling rates as low as $0.1\,^{\circ}\mathrm{C\,s^{-1}}$. During natural cooling, the bainite transformation is more clearly observed as a cooling rate reduction than the ferrite transformation because the rate of bainite formation is greater than the rate of allotriomorphic ferrite formation. An empirical equation has been developed to estimate the volume fraction of allotriomorphic ferrite from recorded or calculated cooling curves from which the reduction in cooling rate at bainitic transformation temperatures can be observed. The STRUCTURE software, adapted from the classical Johnson-Mehl-Avrami theory for transformation kinetics, has been modified to represent the evolution of allotriomorphic ferrite with temperature as a function of material composition, austenite grain size and cooling rate.

Coarse plates of martensite have been discovered at fast cooling rates. These plates could lead to a deterioration in toughness given that they would be more effective at initiating cleavage failure and less effective in deflecting the propagation of cleavage cracks. The coalescence of the martensite plates could not be avoided for cooling rates that exceed $10\,^{\circ}\mathrm{C\,s^{-1}}$, where fully martensitic microstructures are formed. Indeed, the cooling rate over the range studied, did not seem to affect the number density or thickness of the coalesced structures. A clear relationship between austenite grain size and the dimension of the coalesced structures is found. Smaller austenitic grains will result in a significant reduction in the length of the coalesced martensite plates. Unexplained cases of very low toughness reported in previous studies of SA508 Gr. 3 steels may be attributed to the presence of coalesced martensite in the microstructure, as adjacent platelets produce thicker crystallographically homogeneous grains. Severe reduction in toughness has been experimentally observed in cases combining large austenitic grain sizes and the coalesced plates aligned with the crack. Therefore, the detrimental effect on toughness could be mitigated by minimising the austenite grain size, since this in turn limits the scale of the martensite. Severe tempering does not destroy the bimodal plate-size distribution resulting from the coalescence of some of the plates. The coalesced regions are clearly delineated by the precipitation of carbides at the boundaries of the coalesced plates.

5.3 Tempering

There is a concern that the material may re-austenitise during the tempering, as thermodynamic calculations predict that austenite phase starts to form at around the 660 °C, temperature at which pressure vessels are tempered. Dilatometric results have shown that even for the slow commercial heating rate, $0.01\,^{\circ}\mathrm{C\,min^{-1}}$, there is a safety margin above 50 °C between the tempering temperature and the initial temperature for austenite formation. Furthermore, it has been demonstrated that contrary to common practice, shorter tempering parameters improve strength and toughness by reducing the temperature for a 50 % shear in the fracture surface and for Charpy energy values of 28 and 41 J. Reduction in properties are linked with an increased precipitation associated with longer tempering parameters. Although, due to the softening effect of the material at longer tempering times, the upper shelf energy of the material increases.

5.4 Mechanical properties

Effects of austenite grain size, cooling rate and tempering parameter have been assessed by means of tensile strength, Charpy impact energy and hardness for 18 different conditions. These parameters have been found to be dependent on the microstructure and present complex relations with the processing conditions. As a general trend, the best properties are found for the fast cooled microstructures containing a mixture of bainite - martensite, within the scope of the experiments reported here.

The development of methods to increase coolings rates from austenitisation temperatures, to avoid allotriomorphic ferrite formation, has been a common practice in the fabrication of large RPVs, since it has been assumed to be detrimental to toughness, as each ferrite grain presents crack path of size equivalent to the grain size. However, experimental findings from the present work have confirmed that toughness is not reduced when allotriomorphic ferrite is present in the microstructure. An explanation, could be in the morphology of the ferrite. The observed arrays of precipitates inside the allotriomorphic ferrite grains may hinder crack propagation, thus maintaining an acceptable level of toughness. Hence, it is proposed that to improve toughness, austenitic grain sizes should be kept to a minimum by austenitising at lower temperatures or short times.

As expected material strength is reduced as the tempering parameter is increased. For the case of a mixture of bainite with allotriomorphic ferrite and for fully bainitic microstructures, increasing the tempering parameter reduces the values of absorbed energy. However, in the case of the samples with bainitic/martensitic structures, increasing the tempering parameter results in an increase in toughness. Therefore, according to experimental results, it is recommended to increase the integrity of the medium/slow cooled regions of components, it is necessary to reduce the tempering parameter to values below 19 K h.

5.5 Mechanical property modelling

Location based dissimilarity in mechanical properties in large components such as pressure vessels occurs by the variation of effective heat treatment and cooling rates. It is therefore, of great interest to find a reliable method to accurately predict the mechanical properties as a function of thermal processing parameters. This work presents a methodology that combines a large quantity of industrially relevant experimental data and neural networks. This has allowed the determination of the relationship between the previously identified key processing parameters; austenite grain size, cooling rate and tempering parameter, to develop a reliable method with high confidence for predicting strength and toughness. The predictions compare favourably with independent data from the literature even outside the range seen in the database. Therefore, the neural network models could be used with the aid of thermal processing data from finite element software to map the distribution of strength and toughness in large components. This presents a potential benefit during the design stage of components to optimise material composition, heat treatment or geometry to assure the desired level of properties.

5.6 Further work

Results and conclusions from the present work suggest several promising avenues of future work.

5.6.1 Modelling nitride dissolution and precipitation kinetics

Owing to the significant effect on austenite grain growth, which directly influence hardenability and the mechanical properties of SA508 Gr. 3 steels, the precipitation behaviour of aluminium nitride should increase its practical importance. The development of a model able to predict the precipitation kinetics, growth and dissolution, behaviours and to simulate the size distribution evolution of these nitrides undergoing various heat treatment, such as isothermal annealing, reheating or continuous cooling, would be desirable.

5.6.2 Building up databases

The aim is to build up databases, or use experimental data from industrial manufactures to include in the models to construct more robust models able to reproduce more accurately the behaviour of SA508 Gr. 3 steels. And in the future to make them more generally applicable by including compositional effects.

5.6.3 Mapping properties

Neural networks models developed here appear to compare well for tensile strength and toughness from unseen data. Therefore, these models have the potential to map the distribution of strength and toughness in large components, by linking them with the thermal processing data from finite element software. Work is being undertaken to link the neural networks with Deform, the most common finite element software used during the development of large RPVs.

It is hoped that these results, with the aid of microstructural observations, will set the importance of the processing parameters, through the heat treatment process to obtain materials with the best combination of properties.

References

[1] S. M. Goldberg and R. Rosner. *Nuclear reactors: Generation to generation.* Amerian Academy of arts & Sciences, 2011.

[2] S. J. Zinkle and G. S. Was. Materials challenges in nuclear energy. *Acta Materialia*, 61:735–758, 2013.

[3] Nuclear power reactors in the world. Technical report, International Atomic Energy Agency, 2013.

[4] D. Cogswell, D. Swan, R. Mitchell, and S. Garwood. Materials and structureal integrity challenges for the next nuclear generation. In *63rd Annual Assembly and International Conference of the International Institute of Welding*, 2010.

[5] J. Talamantes-Silva, P. Bates, S. Al-Bermani, P. Davies, A. Hambleton, and D. Bunney. PVP2013-97927: New challenges in the production of ultra large forgings for the manufacturing of pressure vessels. In *Proceedings of the ASME 2013 Pressure Vessels and Piping Division Conference*, 2013.

[6] K. Suzuki. Neutron irradiation embrittlement of ASME SA508 Cl. 1 steel. *Journal of Nuclear Materials*, 109:443–450, 1982.

[7] S. G. Park, M. C. Kim, B. S. Lee, and D. M. Wee. Correlation of the thermodynamic calculation and the experimental observation of Ni-Mo-Cr low alloy steel changing Ni, Mo, and Cr contents. *Journal of Nuclear Materials*, 407:126–135, 2010.

[8] Z. Chen, Z. Zeng, and Y. J. Chao. Effect of crack depth on the shift of the ductile-brittle transition curve of steels. *Engineering Fracture Mechanics*, 74:2437–2448, 2007.

[9] J.R. Hawthorne. Composition influences and interactions in radiation sensitivity of reactor vessel steels. *Nuclear Engineering and Design*, 89:223–232, 1985.

[10] D. Cogswell. PVP2011-57563: The development of processing to mechancial mechanical property relationships via quantitative microstructure assesment in low alloy steels heavy section forgins materials. In *Proceedings of the ASME 2011 Pressure Vessels and Piping Division Conference*, 2011.

[11] D. Cooper. *Enrico Fermi: And the Revolutions in Modern physics.* Oxford University Press, 1999.

[12] U. S. Department of Energy. The history of nuclear energy.

[13] H. J. Krappe and K. Pomorski. *Theory of Nuclear Fission: A Textbook.* Springer, 2012.

[14] R. Vandenbosch. *Nuclear Fission.* Elsevier, 2012.

[15] A. Einstein. Ist die trägheit eines körpers von seinem energieinhalt abhängig? *Annalen der Physik*, 18:639–641, 1905.

[16] S. B. Patel. *Nuclear Physics: An Introduction.* New Age International, 1991.

[17] N. L. Char and B. J. Csik. Nuclear power developement: History and outlook. Technical Report 3/1987, International Atomic Energy Agency, 1987.

[18] I. O. Kessides. Nuclear power: Understanding the economic risks and uncertainties. *Energy Policy*, 38:3849–3864, 2010.

[19] A. Adamantiades and I. Kessides. Nuclear power for sustainable development: Current status and future prospects. *Energy Policy*, 37(5149–5166), 2009.

[20] C. Karakosta, C. Pappas, V. Marinakis, and J. Psarras. Renewable energy and nuclear power towards sustainable development: Characteristics and prospects. *Renewable and Sustainable Energy Reviews*, 22:187–197, 2013.

[21] S. Chu and A. Majumdar. Opportunities and challenges for a sustainable energy future. *Nature*, 488(494–303), 2012.

[22] R. K. Nanstad and W. L. Server. Reactor pressure vessel task of light water reactor sustainability program: Initial assessment of thermal annealing needs and challenges. Technical report, U.S. Departament of Energy, 2011.

[23] www.astarmat.hsandphysics.com, December 2013.

[24] ASTM. *Standard Speficifaction for Quenched and Tempered Vacuum-Treated Carbon and Alloy Steel Forgings for Pressure Vessels A 508/A 508M*, 2004.

[25] B. S. Lee, M. C. Kim, J. H. Yoon, and J. H. Hong. Characterization of high strenght and high toughness Ni-Mo-Cr low alloy steels for nuclear application. *International Journal of Pressure Vessels and Piping*, 87:74–80, 2010.

[26] Y. A. Nikolaeva, A. V. Nikolaeva, and Y. I. Shtrombakh. Radiation embrittlement of low-alloy steels. *International Journal of Pressure Vessels and Piping*, 79:619–636, 2002.

[27] J.W. Kim, K. Lee, J.S. Kim, and T.S. Byun. Local mechanical properties of alloy 82/182 dissimilar weld joint between SA508 Gr.1a and F316 SS at RT and 320 °C. *Journal of Nuclear Materials*, 384:212–221, 2009.

[28] H.P Seifert and S. Ritter. Corrosion fatigue crack growth behaviour of low-alloy reactor pressure vessel steels under boiling water reactor conditions. *Corrosion Science*, 50:1884–1899, 2008.

[29] Y. Sakai, K. Miya, I. Takahashi, A. Kosaki, and Y. Ando. Properties of heavi section steel plates and forgins for nuclaer vessels produced in Japan - Part 1. General properties. *International Journal of Pressure Vessels and Piping*, 22:57–75, 1986.

[30] K.H Lee, M.C. Kim, B.S. Lee, and D.M. Wee. Master curve characterization of the fracture toughness behavior in SA508 master curve characterization of the fracture touugness behavior in SA508 Gr.4n low alloy steels. *Journal of Nuclear Materials*, 403:68–74, 2010.

[31] F.M. Beremin. A local criterion for cleavage fracture of a nuclear pressure vessel steel. *Metallurgical Transactions A*, 14A:2277–2287, 1984.

[32] J. T. Kim, H. K. Kwon, H. S. Chang, and Y. W. Park. Improvement of impact toughness of the SA508 Class 3 steel for nuclear pressure vessel through steel-making and heat-treatment practices. *Materials Engineering and Design*, 174:51–58, 1997.

[33] W. J. Yang, B. S. Lee, M. Y. Huh, and J. H. Hong. Application of the local fracture stress model on the cleavage fracture of the reactor pressure vessel steels in the transition temperature region. *Journal of Nuclear Materials*, 317:234–242, 2003.

[34] B. J. Lee, H. D. Kim, and J. H. Hong. Calculation of α/β equilibria in SA508 Grade 3 steels for intercritical heat treatment. *Metallurgical and Materials Transactions A*, 29A:1441–1447, 1998.

[35] S.H. Chi and G.E. Lucas. Differences in mechanical properties and microstructure of SA508 CL. 3 reactor pressure vessel steels manufactured by different steel refining process. *Transactions of the 15th International Conference on Structural Mechanics in Reactor Technology*, pages 223–230, 1999.

[36] X. Q. Wu and Y. Katada. Strain-amplitude dependent fatigue resistance of low-alloy pressure vessel steels in high-temperature water. *Journal of Materials Science*, 40:1953–1958, 2005.

[37] X.Q. Wu and I.S. Kim. Effects of strain rate and temperature on tensile behavior of hydrogen-charged SA508 Cl.3 pressure vessel steel. *Materials Science and Engineering*, A348:309–318, 2003.

[38] Y.R. Im, B.J. Lee, Y. J. Oh, J.H. Hong, and H.C. Lee. Effect of microstructure on the cleavage fracture strength of low carbon Mn-Ni-Mo bainitic steels. *Journal of Nuclear Materials*, 324:33–40, 2004.

[39] B.S. Lee, J.H. Hong, W.J. Yang, M.Y. Huh, and S.H. Chi. Master curve characterization of the fracture toughness in unirradiated and irradiated RPV steels using full- and 1/3-size pre-cracked Charpy specimens. *International Journal of Pressure Vessels and Piping*, 77:599–604, 2000.

[40] Y. S. Ahn, H. D. Kim, T. S. Byun, Y. J. Oh, G. M. Kim, and J. H. Hong. Application of intercritical heat treatment to improve toughness of SA508 Cl.3 reactor pressure vessel steel. *Nuclear Engineering and Design*, 194:161–177, 1999.

[41] S. Kim, Y. Im, S. Lee, H. Lee, Y. J. Oh, and J. H. Hong. Effects of alloying elements on mechanical and fracture properties of base metals and simulated HAZ of SA508 steels. *Metallurgical and Materials Transactions A*, 32A:903–911, 2001.

[42] S. Xu, X. Q. Wu, E. H. Han, and W. Ke. Effects of dynamic strain aging on mechanical properties of SA508 Class 3 reactor pressure vessel steels. *Journal of Materials Science*, 44:2882–2889, 2009.

[43] T. S. Byun, J. H. Hong, F. M. Haggag, K. Farrell, and E. H. Lee. Measurement of through-the-thickness variations of mechanical properties in SA508 Gr.3 pressure vessel steels using ball indentation test technique. *International Journal of Pressure Vessels and Piping*, 74:231–238, 1997.

[44] M. S. Garcia-Redondo, M. L. Castano-Marin, and D. Gomez-Briceno. Comportamiento del acero de baja aleacion SA508 y del acero al carbono A410b en las condiciones de operacion y parada del circuito primario de los reactores de agua ligera tipo PWR. *Revista de Metalurgia Madrid*, 36:88–99, 2000.

[45] S. Lee, S. Kim, B. Hwang, B. S. Lee, and C. G. Lee. Effect of carbide distribution on the fracture toughness in the transition temperature region of an SA508 steel. *Acta Materialia*, 50:4755–4762, 2002.

[46] Y. R. Im, Y. J. Oh, B. J. Lee, J. H. Hong, and H. C. Lee. Effects of carbide precipitation on the strength and charpy impact properties of low carbon Mn-Ni-Mo bainitic steels. *Journal of Nuclear Materials*, 297:138–148, 2001.

[47] K. Suzuki, I. Kurihara, Sasaki, Y. Koyoma, and Y. Tanakaca. Application of high strength MnMoNi steel to pressure vessels for nuclear power plant. *Nuclear Engineering and Design*, 206:261–278, 2001.

[48] S. Kim, S. Lee, Y. R. IM, S. J. Kim H. C. Lee, and J. H. Hong. Effects of alloying elements on fracture toughness in the transition temperature region of base metals and simulated heat-affected zones of Mn-Mo-Ni low alloy steels. *Metallurgical and Materials Transactions*, 35A:2027–2037, 2004.

[49] M. Erve, F. Papouscheck, K. Fischer, and C. Maidorn. State of the art in the manufacture of heavy forgins for reactor componnts in the federal republic of Germany. *Nuclear Engineering and Design*, 108:487–495, 1988.

[50] Y. Tanaka and I. Sato. Development of high purity large forgings for nuclear power plants. *Journal of Nuclear Materials*, 417:854–859, 2011.

[51] P. Bocquet, A. Cheviet, and R. Dumont. Examples of the evolution of materials for nuclear applications: metallurgical improvement of 16MND5 steel and new technologies for manufacturing heavy components. *Nuclear Engineering and Design*, 151:503–511, 1994.

[52] S. Kim, S. Y. Kang, S. J. Oh, S. Kwon, S. Lee, J. H. Kim, and J. H. Hong. Correlation of the microstructure and fracture toughness of the heat-affected zones of an SA508 steel. *Metallurgical and Materials Transactions A*, 31A:1107–1119, 2000.

[53] D. Cogswell. *Statistical Modelling of the Transition Toughness Properties of Low Alloy Pressure Vessel Steels Volume 1: Main Body*. PhD thesis, Department of Metallurgy and Materials, School of Engineering, The University of Birmingham, 2010.

[54] H. Kakimoto, T. Arikawa, Y. Takahashi, T. Tanaka, and Y. Imaida. Development of forging process design to close internal voids. *Journal of Materials Processing Technology*, 210:415–422, 2010.

[55] P. Bocquet, R. Blondeau, I. Poitrault, J. P. Badeau, and R. Dumont. Improvement in the reliability of shells for light water reactors by manufacture from hollow ingots. *Nuclear Engineering and Design*, 130:467–475, 1991.

[56] N. Ohashi, T. Enami, H. Wanaka, and K. Aso. Manufacturing process and properties of nuclear RPV shell ring forged from hollow ingot. *Nuclear Engineering and Design*, 81:193–205, 1984.

[57] K. Suzuki, I. Sato, and H. Tsukada. Manufacturing and material properties of ultralarge size forgings for advanced BWRPV. *Nuclear Engineering and Design*, 151:513–522, 1994.

[58] K. Shibata, S. Seo, M. Kaga, and H. Uchino. Suppression of hot shortness dur to Cu in recycled steels. *Materials Transactions*, 43(3):292–300, 2002.

[59] M. Torkar. Effect of the trace and residual elements on the hot brittlenes, hot shotness and properties of 0.15-0.3% C Al-killed steels with a solidification microstructure. *Matererials and Technology*, 44(6):327–333, 2010.

[60] C. P. Sharma. *Engineering Materials: Properties and Applications of Metals and Alloys*. Prentice-Hall of India, 2004.

[61] S. Kwon, S. J. Oh, J. H. Kim, S. Kim, and S. Lee. Mössbauer analysis of heat affected zones of an SA508 steel weld. *Scripta Materalia*, 40:191–137, 1999.

[62] L. Vanherpe, N. Moelans, B. Blanpain, and S. Vandewalle. Pinning effect of spheroid second-phase particles on grain growth studied by three-dimensional phase-field simulations. *Computational Materials Science*, 49:340–350, 2010.

[63] Association Iron Steel Technology, editor. *Prediction of Grain Size, Precipitation and Crack Susceptibility in Continuous Casting*, volume 1, 2009.

[64] D. Chakrabarti, C. L. Davis, and M. Strangwood. The effect of precipitate distributions on HLSA grain structures. Technical report, International Symposium of Research Students on Material Science and Engineering, 2004.

[65] S. G. Druce. Effects on austenitisation heat treatment on the fracture resistance and temper embrittlement of MnMoNi steels. *Acta Materialia*, 34(2):219–232, 1986.

[66] E. T. Turkdogan, S. Ignatowicz, and J. Pearson. The solubility of sulphur in iron and iron-manganese alloys. *Journal of the Iron and Steel institute*, 180:349–354, 1955.

[67] K. Lee, M. C. Kim, W. J. Yang, and B. S. Lee. Evaluation of microstructural parameters controlling cleavage fracture toughness in Mn-Mo-Ni low alloy steels. *Materials Science and Engineering A*, 565:158–164, 2013.

[68] K. D. Haverkamp, K. Forch, K. H. Piehl, and W. Witte. Effect of heat treatment and precipitation state in toughness of heavy section Mn-Mo-Ni-steel for nuclear power plants components. *Nuclear Engineering and Design*, 81:207–217, 1984.

[69] L. Hao, M. Sun, and D. Li. The effect of quenching media on the microstructure and mechanical properties of SA508-3 steel. *Advanced Materials Reseach*, 311–313:974–977, 2011.

[70] L. M. Fu, H. R. Wang, W. Wang, and A. D .Shan. Austenite grain growth prediction coupling with drag and pinning effects in low carbon Nb microalloyed steels. *Materials Science and Technology*, 27(6):996–1001, 2011.

[71] S. Lee and Y. Lee. Prediction of austenite grain growth during austenitization of low alloy steels. *Materials and Design*, 29:1840–1844, 2008.

[72] S. Uhm, J. Moon, C. Lee, J. Yoon, and B. Lee. Prediction model for the austenite grain size in the coarse grained heat affected zone of Fe-C-Mn steels: Considering the effect of initial grain size on isothermal growth

behavior. *Iron and Steel Institute of Japan International*, 44(7):1230–1237, 2004.

[73] H. R. Wang and W. Wang. Simple model for austenite grain growth in microalloyed steels. *Materials Science and Technology*, 24(2):228–232, 2008.

[74] P. A. Manohar, D. P. Dunee, T. Chandra, and C. R. Killmore. Grain growth predictions in microalloyed steels. *Iron and Steel Institute of Japan International*, 36(2):194–200, 1996.

[75] C. M. Sellars and J. A. Whiteman. Recrystallization and grain growth in hot rolling. *Metal Science*, pages 187–194, 1979.

[76] G. Shen, J. Rollins, and D. Furrer. Microstructure modeling of forged waspaloy discs. In R. D. Kissinger, D. J. Deye, and D. a. Woodford, editors, *Superalloys 1996*. The Minerals, Metals and Matrials Society, 1996.

[77] P. D. Hodgson and R. K. Gibbs. A matematical model to predict the mechanical properties of hot rolled C-Mn and microalloyed steels. *Iron and Steel Institute of Japan International*, 32(12):1329–1338, 1992.

[78] J. Wang, J. Chen, Z. Zhao, and X. Y. Ruan. Modeling of microstructural evolution in microalloyed steel during hot forging process. *Acta Materialia*, 19(4):279–286, 2006.

[79] Y. Zhao, J. Shi, W. Cao, M. Wang, and G. Xie. Kinetics of austenite grain growth in medium-carbon niobium-bearing steel. *Applied Physics and Engineering*, 12:171–176, 2011.

[80] S. Nanba, M. Kitamura, M. Shimada, M. Katsumata, T. Inoue, H. Imamura, Y. Maeda, and S. Hattori. Prediction of microstructure distribution in the through-thicknesss direction during and after hot rolling in carbon steels. *Iron and Steel Institute of Japan International*, 32(3):377–386, 1992.

[81] S. S. Zhang, M. Q. Li, Y. G. Liu, J. Luo, and T. Q. Liu. The growth behavior of austenite grain in the heating process of 300M steel. *Materials Science and Engineering A*, 528:4967–4972, 2011.

[82] M. Sun, L. Hao, D. Li, and Y. Li. Modeling flow stress constitutive behavior of SA508-3 steel for nuclear reactor pressure vessels. *Journal of Nuclear Materials*, 418:269–280, 2011.

[83] A. Yoshie, M. Fujioka, Y. Watanabe, K. Nishioka, and H. Morikawa. Modelling of microstructurak evolution and mechanical properties of steel plates produced by thermo-mechanical control process. *Iron and Steel Institute of Japan International*, 32(3):395–404, 1992.

[84] J. H. Hollomon and L. D. Jaffe. Time-temperature relations in tempering steel. *Transactions of The Metallurgical Society of the American Institute of Mining, Metallurgical and Petroleum Engineers*, 162:223–249, 1945.

[85] S. Sato, T. Enami, S. Matsui, K. Asoh, and Y. Kusuhara. Temper embrittlement of Cr-Mo pressure vessel steels. Technical report, Kawasaki Steel, 1981.

[86] R. A. Swift and J. A. Gulya. Temper embrittlement of pressure vessel steels. *Welding Research Supplement*, 52:57–68, 1973.

[87] J. Grosse-Wordemann and S. Dittrich. Prevention of temper embrittlement in 2 1/4 Cr-1 Mo weld metal by metallurgical actions. *Welding Research Supplement*, 62(5), 1983.

[88] J. A. Francis, H. K. D. H. Bhadeshia, and P. J. Withers. Welding residual stresses inferritic power plant steels. *Materials Science and Technology*, 23(9):1009–1020, 2007.

[89] C. Fukuoka, Y.G. Nakagawa, J.J. Lance, and R.N. Pangborn. Conditioning monitoring by microstructural evaluation of cumulative fatigue damage. *Metallurgical and Materials Transactions A*, 27A:3841–3851, 1996.

[90] C. Chauvy, L. Coudreuse, and P. Toussaint. PVP2010-25: Potential detrimental consequences of excessive PWHT on pressure vessel steels properties. In *Proceedings of the ASME 2013 Pressure Vessels and Piping Division Conference*, 2010.

[91] T. L. Anderson. *Fracture Mechanics: Fundamentals and Applications.* Taylor & Francis, 2005.

[92] P. Bowen, S. G. Druce, and J. F. Knott. Effects of microstructure on cleavage fracutre in pressure vessel steel. *Acta Metallurgica*, 34(6):1121–1131, 1986.

[93] B. Tanguy, J. Besson, and A. Pineau. Comment on "effect of carbide distribution on the fracture toughness in the transition temperature region of an SA508 steel". *Scripta Materalia*, 49:191–197, 2003.

[94] G. Z. Wang and J. H. Chen. A comparison of fracture behavior of low alloy stees with different sizes of carbide particles. *Metallurgical and Materials Transactions A*, 27A:1909–1917, 1996.

[95] D. A. Canonico. Transition temperature considerations for thick-wall steel nuclear pressure vessels. *Nuclear Engineering and Design*, 17:149–160, 1971.

[96] G. R. Odette and G. E. Lucas. Embrittlement of nuclear reactor pressure vessels. *Journal of the Minerals, Metals and Materials Society*, 53(7):18–22, 2001.

[97] Lendell E. Steele, editor. *Radiation embrittlement of nuclear reactor pressure vessel steels. An International Review.* ASTM Publication, fourth edition, 1993.

[98] K. Hatesan, S. Majumdar, P. S. Shankar, and V. N. Shah. Preliminary materials selection issues for the next generation nuclear plant reactor pressure vessel. Technical report, Argonne National Laboratory, 2006.

[99] A. V. Nikolaeva, Y. A. Nikolaev, and A. M. Kryukov. The contribution of grain boundary effects to low-alloy steel irradiation embrittlement. *Journal of Nuclear Materials*, 218:85–93, 1994.

[100] C. Bouchet, B. Tanguy, J. Besson, and S. Bugat. Prediction of the effects of neutron irradiation on the Charpy ductile to brittle transition curve of an A508 pressure vessel steel. *Computational Materials Science*, 32:294–300, 2005.

[101] K. Dohi, T. Onchi, F. Kano, K. Fukuya, M. Narui, and H. Kayano. Effect of neutron flux on low temperature irradiation embrittlement of reactor pressure vessel steel. *Journal of Nuclear Materials*, 265:78–90, 1999.

[102] Y .A. Nikolaev, A. V. Nikolaeva, A. M. Kryukov, V. I. Levit, and Y. N. Korolyov. Radiation embrittlement and thermal annealing behavior of Cr-Ni-Mo reactor pressure vessel materials. *Journal of Nuclear Materials*, 226:144–155, 1995.

[103] M. A. Ericksonkirk, M. T. Ericksonkirk, S. Rosinski, and J. Spanner. A comparision of the tanh and exponential fitting methods for Charpy V-Notch energy data. *Journal of Pressure Vessel Technology*, 131:1–13, 2009.

[104] T. J. Griesbach and W. L. Server. Management of neutron radiation embrittlement a view from the united states. In Lendell E. Steele, editor, *Radiation embrittlement of nuclear reactor pressure vessel steels. An International Review*, volume Fourth. ASTM Publication, 1993.

[105] A. Ballesteros J. Bros and A. Lopez. Radiation embrittlement of Spanish nuclear reactor pressure vessel steels. In Lendell E. Steele, editor, *Radiation embrittlement of nuclear reactor pressure vessel steels. An International Review*. ASTM Publication, 1993.

[106] Pressurized thermal shock in nuclear power plants: Good practices for assessment. Technical Report IAEA-TECDOC-1627, International Atomic Energy Agency, 2010.

[107] C. Garcia de Andrés, F. G Caballero, C. Capdevila, and D. San Martín. Revealing austenite grain boundaries by thermal etching: advantages and disadvantages. *Materials Characterization*, 49:121–127, 2003.

[108] ASTM. *Standard Test Methods for Determining Average Grain Size E 112 - 96*, 2004.

[109] ImageJ software, http://rsbweb.nih.gov/ij/.

[110] ASTM. *Standard Test Methods and Definitions for Mechanical Testing of Steel Products A370*, 2004.

[111] ASTM. *Standard Test Methods for Notched Bar Impact Testing of Metallic Materials E 23*, 2004.

[112] MTDATA - Phase Diagram Software from the National Physical Laboratory, http://resource.npl.co.uk/mtdata/mtdatasoftware.htm.

[113] C. Garcia de Andrés, M. J. Bartolomé, C. Capdevila, D. San Martín, F. G Caballero, and V. Lopez. Metallographic techniques for the determination of the austenite grain size in medium-carbon microalloyed steel. *Materials Characterization*, 46:389–398, 2001.

[114] M. Takahashi and H. K. D. H. Bhadeshia. The interpretation of dilatometric data for transformaions in steels. *Journal of Materials Science Letters*, 8:477–478, 1989.

[115] H. S. Yang and H. K. D. H. Bhadeshia. Uncertainties in dilatometric determination of martensite start temperature. *Materials Science and Technology*, 23(5):556–560, 2007.

[116] MAUD - Materials Analysis Using Diffraction, http://www.ing.unitn.it/ maud/.

[117] L. Zhang and D. C. Guo. A general etchant for revealing prior-austenite grain boundaries in steels. *Materials Characterization*, 30:299–305, 1993.

[118] A. O. Benscoter and M. J. Perricone. Marshall's reagent: Origins, modifications, and new applications. *Microscopy and Microanalysis*, 11:76–77, 2005.

[119] F. J. Humphreys. Review grain and subgrain characterisation by electron backscatter diffraction. *Journal of Materials Science*, 36:3833–3854, 2001.

[120] T. Maitland and S. Sitzman. *Electron Backscatter Diffraction (EBSD) Technique and Materials Characterization Examples.* Springer, 2006.

[121] W. W. Mullins. Effect of thermal grooving on grain boundary motion. *Acta Metallurgica*, 6:414–427, 1958.

[122] F. G. Wilson and T. Gladman. Aluminun nitride in steel. *International Materials Review*, 33(5):211–283, 1988.

[123] R. Radis and E. Kozeschnik. Kinetics of AlN precipitation in microalloyed steel. *Modelling and Simulation in Materials Science and Engineering*, 18:1–16, 2010.

[124] M. Hansen and K. Anderko. *Constitution of binary alloys.* 2nd Edition. McGraw-Hill, 1958.

[125] G. A. Jeffrey, G. S. Parry, and R. L. Mozzi. Study of the Wurtzite type binary compounds. structures os aluminum nitride and beryllium oxide. *The Journal of Chemical Physics*, 25(5):1024–1031, 1956.

[126] A. Taylor and B. J. Kagle. *Crystallographic data on metal and alloy structures.* Dover Publications, 1962.

[127] J. D. H. Donnay and H. M. Ondik. *Crystal Data Determinative Tables: Inorganic Compounds*, volume 2 of *3rd Edition.* National Standard Reference Data System, 1973.

[128] M. Militzer, A. Gumelli, E. B. Hawbolt, and T. R. Meadowcroft. Austenite grain growth kinetics in a-killed plain carbon steels. *Metallurgical and Materials Transactions A*, 27A:3399–3496, 1996.

[129] T. Gladman and F. B. Pickering. Grain coarseing of austenite. *Journal of the Iron and Steel institute*, 205:653–664, 1967.

[130] M. Gómez and S. F. Medina. Role of microalloying elements in the microstructure of hot rolled steels. *International Journal of Materials Reserch*, 102(10):1197–1207, 2011.

[131] R. J. Bruls, H. T. Hintzen, G. de With, R. Metselaar, and J. C. van Miltenburg. The temperature dependence of the Grueneisen parameters of MgSiN2, AlN and B-Si3N4. *Journal of Physics and Chemistry of Solids*, 62:783–792, 2001.

[132] X. G. Lu, M. Selleby, and B. Sundman. Assessments of molar volume and thermal expansion for selected BCC, FCC and HPC metallic elements. *Computer Coupling of Phase Diagrams and Thermochemistry*, 29(1):68–89, 2005.

[133] J. W. Martin, R. D. Doherty, and B. Cantor. *Stability of microstructure in metallic systems*. Cambridge University Press, 2 edition, 1997.

[134] J. W. Christian. *Theory of Transformations in Metal and Alloys, Part I*. Pergamon Press, Oxford, U. K., 3 edition, 2003.

[135] I. Andresen and Ø. Grong. Analytical modelling of grain growth in metals and alloys in the presence of growing and dissolving precipitates-I. Normal grain growth. *Acta Metallurgica et Materalia*, 43(7):2673–1688, 1995.

[136] J. Friedberg, L. E. Tomdahl, and M. Hillert. Diffusion in iron. *Jernkont. Annlr*, 153:263–276, 1969.

[137] G. P. Krielaart, J. Sietsma, and S. van der Zwaag. Ferrite formation in Fe-C alloys during austenite decomposition under non equilibrium interface conditions. *Materials Science and Engineering A*, 237:216–223, 1997.

[138] D. J. C. MacKay. Practical Bayesian framework of backpropagation networks. *Neural Computation*, 4:448–472, 1992.

[139] D. J. C. MacKay. Bayesian interpolation. *Neural Computation*, 4:415–447, 1992.

[140] H. K. D. H. Bhadeshia. Neural networks in materials science. *Iron and Steel Institute of Japan International*, 39:966–979, 1999.

[141] P. D. Allison. *Fixed Effects Regression Methods for Longitudinal Data: Using SAS*. SAS Institute, 2005.

[142] James F. Epperson. *An Introduction to Numerical Methods and Analysis*. John Wiley & Sons, 2014.

[143] N. C. Law and D. V. Edmonds. The formation of austenite in low-alloy steel. *Metallurgical transactions A*, 11A:33–46, 1980.

[144] H. Azizi-Alizamini, M. Militzer, and W. J. Poole. Austenite formation in plain low-carbon steels. *Metallurgical and Materials Transactions A*, 42A:1544–1557, 2011.

[145] R. E. Reed-Hill and R. Abbaschian. *Physical metallurgy principles.* PSW-KENT, 3rd edition, 1991.

[146] C. P. Poole Jr. *Encyclopedic Dictionary of Condensed Matter Physics, Volume 1.* Academic Press, 2004.

[147] M. Peet and H. K. D. H. Bhadeshia. Software for transformations in steels. http://www.msm.cam.ac.uk/map/steel/programs/mucg83.html, 1982.

[148] H. K. D. H. Bhadeshia. Thermodynamic analysis of isothermal transformation diagrams. *Metal Science*, 16:159–165, 1982.

[149] S. J. Jones and H. K. D. H. Bhadeshia. Kinetics of the widmanstätten ferrite transformation in steel. In *Displacive Phase Transformations and their applications in materials engineering*, pages 419–426, Materials Park, Ohio, USA, 1998. The Minerals, Metals & Materials Society.

[150] H. K. D. H. Bhadeshia, L. E. Svensson, and B. Gretoft. A model for the development of microstructure in low-alloy steel (Fe-Mn-Si-C) weld deposits. *Acta Materialia*, 33(7):1271–1985, 1985.

[151] S. J. Jones and H. K. D. H. Bhadeshia. Kinetics of simultaneous decomposition of austenite into several transformation products. *Acta Materialia*, 45(7):2911–2920, 1997.

[152] F. G. Caballero, H. Roelofs, St. Hasler, C. Capdevila, J. Chao, J. Cornide, and C. Garcia-Mateo. Influence of bainite morphology on impact toughnessof continuously cooled cementite free bainitic steels. *Materials Science and Technology*, 28(1):95–102, 2012.

[153] H. K. D. H. Bhadeshia, E. Keehan, L. Karlsson, and H. O. Andrén. Coalesced bainite. *Transactions of the Indian Institute of Metals*, 29:689–694, 2006.

[154] J. H. Pak, H. K. D. H. Bhadeshia, and L. Karlsson. Mechanism of misorientation development within coalesced martensite. *Materials Science and Technology*, 28(8):918–923, 2012.

[155] J. H. Pak, H. K. D. H. Bhadeshia, L. Karlsson, and E. Keehan. Coalesced bainite by isothermal transformation of reheated weld metal. *Science and Technology of Welding and joining*, 13(7):593–597, 2008.

[156] F. G Caballero, J. Chao, J. Cornide, C. García-Mateo, M. J. Santofimia, and C. Capdevila. Toughness deterioration in advanced high strength bainitic steels. *Materials Science and Engineering A*, 525:87–95, 2009.

[157] L. C. Chang and H. K. D. H. Bhadeshia. Microstructure of lower bainite formaed at large undercooling below bainite start temperature. *Materials Science and Technology*, 12:233–236, 1996.

[158] J. H. Pak. *Coalesced Bainite and Martensite.* PhD thesis, GIFT, POSTECH, 2012.

[159] J. W. Christian. Accommodation strains in martensite formation, the use of the dilatation parameter. *Acta Metallurgica*, 6:377–379, 1958.

[160] H. K. D. H. Bhadeshia, S. A. David, J. M. Vitek, and R. W. Reed. Stress induced transformation to bainite in Fe-Cr-Mo-C pressure vessel steel. *Materials Science and Technology*, 7:686–698, 1991.

[161] J. Pak, D. W. Suh, and H. K. D. H. Bhadeshia. Promoting the coalescence of bainite platelets. *Scripta Materalia*, 66:951–953, 2012.

[162] E. Keehan, H. K. D. H. Bhadeshia, and M. Thuvander. Electron backscatter diffraction study of the coalesced bainite i high strength steel weld metals. *Materials Science and Technology*, 24(10):1183–1188, 2008.

[163] E. Keehan, L. Karlsson, and H. O. Andrén. Influence of carbon, mandanese and nickel on microstructure and properties of strong steel weld metal. part 1 - Effect of nickel content. *Science and Technology of Welding and joining*, 11(1):1–8, 2006.

[164] H. Jang, J-H. Kim, C. Jang, J. G. Lee, and T. S. Kim. Low-cycle fatigue bahaviours of two heats of SA508 Gr.1a low alloy steel in 310 °c ais deoxygenated water - Effects of dynamic strain aging and microstructures. *Materials Science and Engineering A*, 580:41–50, 2013.

[165] S. J. Jones and H. K. D. H. Bhadeshia. Structure, http://www.msm.cam.ac.uk/map/steel/programs/structure.html.

[166] S. J. Jones and H. K. D. H. Bhadeshia. Competitive formation of inter- and intragranularly nucleated ferrite. *Metallurgical and Materials Transactions A*, 28A:1997–2005, 1997.

[167] J. Chen. *Modelling of Simultaneous Transformations in Steels.* PhD thesis, University of Cambridge, 2009.

[168] J. W. Christian. *The theory of transformations in metals and alloys. Part I.* Pergamon, 2002.

[169] R. W. K. Honeycombe. Ferrite. *Metal Science*, 14:201–214, 1980.

[170] T. Tsuchiyama. Physical meaning of Tempering Parameter and its application for continuous heating or cooling heat treatment process. *Journal of the Japan Society for heat Treatment*, 42:163–168, 2002.

[171] ASTM. *Standard Test Methods for Notched Bar Impact Testing of Metallic Materials*, 2003.

[172] ASTM. *Standard Test Methods and Definitions for Mechanical Testing of Steel Products*, 2003.

[173] O. M. Akselsen and Ø. Grong. Prediction of weld metal Charpy V-notch toughness. *Materials Science and Engineering*, A159:187–192, 1992.

[174] P. L. Windle, M. Crowder, and R. Moskovic. A statistical model for the analysis and prediction of the effect of neutron irradiation on charpy impact energy curves. *Nuclear Engineering and Design*, 165:43–56, 1996.

[175] M. T. Todinov. Fitting impact fracture toughness data in the transition region. *Materials Science and Engineering*, A265:1–6, 1999.

[176] W. Olfield. Curve fitting impact test data: A statistical procedure. Technical Report 11, ASTM Standardization News, 1975.

[177] L. W. Cao, S. J. Wu, and P. E. J. Flewitt. Comparison of ductile-to-brittle transition curve fitting approaches. *International Journal of Pressure Vessels and Piping*, pages 12–16, 2012.

[178] G. Qian and M. Niffenegger. PVP2013-98161: Investigation on constraint effect of a reactor pressure vessel subjected to pressurized thermal shocks. In *Proceedings of the ASME 2013 Pressure Vessels and Piping Conference*, 2013.

[179] H. Salman Hasan and M. Peet. Map_steel_thermal 10, 2010.

[180] H. S. Hasan, M. J. Peet, J. M. Jalil, and H. K. D. H. Bhadeshia. Heat transfer coefficients during quenching of steels. *Heat and Mass Transfer*, 47(3):315–321, 2011.

[181] J. P. Holman. *Heat transfer*. McGraw-Hill, 9th edition, 2004.